Universitat Autònoma de Barcelona

Electrolyte-gated organic field-effect transistors based on organic semiconductor: insulating polymer blends

Qiaoming Zhang

Universitat Autònoma de Barcelona

Electrolyte-Gated Organic Field-Effect Transistors based on Organic Semiconductor : Insulating Polymer Blends

Qiaoming Zhang

Doctoral Thesis

PhD Programme in Materials Science

Thesis Directors:

Dr. Marta Mas-Torrent and Dr. Francesca Leonardi

Thesis Tutor:

Prof. Jordi Sort Viñas

Institut de Ciència de Materials de Barcelona

Department of Physics

Science Faculty

Universitat Autònoma de Barcelona

2019

La present memòria es presenta per aspirar al Grau de Doctor per:

Qiaoming Zhang

Vist i plau:

Dr. Marta Mas-Torrent

Dr. Francesca Leonardi

Prof. Jordi Sort Viñas

Bellaterra, 23 de Abril de 2019

MARTA MAS-TORRENT, Research Scientist and **FRANCESCA LEONARDI**, Senior Postdoctoral Research, of the Spanish Council of Research at the Materials Science Institute of Barcelona (ICMAB-CSIC), and **JORDI SORT VIÑAS**, Professor of Universitat Autònoma de Barcelona (UAB)

CERTIFY

That **Qiaoming Zhang**, Master in Physical, has performed, under their management, the research work entitled "**Electrolyte-Gated Organic Field-Effect Transistors based on Organic Semiconductor : Insulating Polymer Blends**". This work has been carried out under the mark of the Materials Science Ph. D. program of the Physics Department of the Autonomous University of Barcelona.

And in witness whereof this is signed by

Suprvisors:	Tutor:
Dr. Marta Mas-Torrent	Prof. Jordi Sort Viñas
Dr. Francesca Leonardi	

April 23, 2019

Acknowledgments

At this point, it is my pleasure to thank many people who made this thesis possible. I would like to express my deepest gratitude to Prof. Jaume Veciana and Prof. Concepció Rovira for allowing me to work in NANOMOL group full of many wonderful and nice friends.

It is a great honor for me to thank my supervisor, Dr. Marta Mas-Torrent, for giving me the opportunity to work and perform my thesis in her amazing group, and my co-supervisor, Dr. Francesca Leonardi, for teaching me all things and skills related to research. During my doctoral period, they always gave me strong supports and provided me almost everything I need with their professional supervision, bright ideas and strategic guidance at every stage. Special and sincere thanks to Marta for her patience, immense knowledge, fruitful discussions. Due to her guidance, my project and PhD life went well. No matter how busy she is, she always answers my questions and solves my problem as fast as she could. I would also like to give my grateful thanks to Francesca, who had to read and correct my papers starting from the beginning and I can imagine that it was not so easy due to my poor English.

My sincere thanks go to Dr. Stefano Casalini, who introduced me to the field of the EGOFETs, taught me how to do experiment hand by hand at the beginning of my PhD career and solves the problems I met in both research and personal life. I would also like to give my warm thanks to Dr. Raphael Pfattner, Dr. Tommaso Salzillo and Dr. Antonio Campos Garcia, for their clear explanations of the fundamental basics about OFET and in general for their help in my day to day routine, such as the careful design of experiments in order to obtain the key findings for my research.

I would like to give my gratefulness to our group members, Dr. Sergi Riera-Galindo, Dr. Adriana R. Kyvik, Dr. Francesc Bejarano, Dr. Maria Serena Maglione, Dr. Paula Mayorga, Ines Temiño, Adrian Tamayo and Simona Ricci, who were always so helpful and shared their friendships and supports with me. Because all of you, my past four years in Barcelona were memorable and full of happiness. Thanks again to Toni, Ines, Adrian and Simona for their help in the lab and on practical things of my daily life.

I would like to thank all the rest of the people in NANOMOL group, especially Dr. Nuria Crivillers, Dr. Nora Ventosa, Dr. Imma Ratera, and Dr. José Vidal-Gancedo, for their suggestions during the group meetings, assistances and supports in the lab when I needed.

Thanks all my Chinese friends in ICMAB and UAB, Ziliang Li, Yanan Zhu, Changyong Lu, Wenjie Qian, Mengdi Qian, Yu Chen, Fangchang Tan, Songbai Zhang, Lu Lu, Jie Liu, Yaxing Wang and others no explicitly mentioned here, who supported me during my studies and life in the past four years. A special thanks to Jinghai Li, who studied in the same group with me. I wish you success in your PhD study. I would like to thank the China Scholarship Council for the financial supports.

最后也是最重要的，我要特别感谢我的家人。首先，谢谢父母的养育，给我的理解和支持。即使在我们家最困难的时候，二老也没有放弃让我读书，给了我他们能给的最好的教育。正是由于您们的辛勤付出，才有了我的今天。其次，我的妻子，陈丽佳，谢谢你对我无微不至的照顾。在我出国留学的四年时间里，你一边承担家庭的重担，一边还要完成自己的科研，付出很多。最后，我可爱的女儿，张雨晨(Cristina)。感谢上天将你赐给了我。你的到来给我们整个家族都带来了欢乐。特别是你的爷爷奶奶，你的一个笑容能够让他们开心一整天，你感受到了吗？虽然我没能在你的婴儿时期陪伴你，但我知道我不会再错过你的其他成长阶段。

Thank you very much to all of you again!

Contents

List of Abbreviations and symbols

Abbreviations

MOSFET	Metal Oxide Semiconductor Field-Effect transistor
OLED	Organic Light-Emitting Diode
OFET	Organic Field-Effect Transistors
OECT	Organic Electrochemical Transistor
RFID	Radio Frequency Identification
HOMO	Highest Occupied Molecular Orbital
LUMO	Lowest Unoccupied Molecular orbital
VRH	Variable Range Hopping
BGBC	Bottom-Gate Bottom-Contact
BGTC	Bottom-Gate Top-Contact
TGBC	Top-Gate Bottom-Contact
TGTC	Top-Gate Top-Contact
S	Source electrode
D	Drain electrode
G	Gate electrode
OSC	Organic Semiconductor
PVD	Physical Vapor Deposition
BAMS	Bar-Assisted Meniscus Shearing
EGOFET	Electrolyte-Gated Organic Field-Effect Transistor
EDL	Electrical Double Layer
GCS	Gouy-Chapman-Stern Model
SAM	Self-Assembled Monolayer
PE-CVD	Plasma Enhanced Chemical Vapor Deposition
LoD	Limit of Detection
PS	Polystyrene
AFM	Atomic Force Microscopy

DCM	Displacement Current Measurement
EIS	Electrochemical Impedance Spectroscopy
KPFM	Kelvin Probe Force Microscopy
CPD	Contact Potential Difference
HYGOFET	Hydrogel-Gated Organic Field-Effect Transistor
SEM	Scanning Electron Microscopy
SHE	Standard Hydrogen Electrode
NHE	Normal Hydrogen Electrode

Symbols

V_{GS}	gate-source voltage
V_{DS}	drain-source voltage
I_{DS}	drain-source current
V_{th}	threshold voltage
E_F	fermi level
W	channel width
L	channel length
μ	field-effect mobility
C_i	gate capacitance
C_{dl}	double layer capacitance
P	pinch off
V_{on}	switch on voltage
I_{on}/I_{off}	on/off ratio
I_{on}	on-current
I_{off}	off-current
SS	subthreshold swing
SiO_2	silicon dioxide
λ_D	debye length
d	double layer thickness

ε_0	permittivity of vacuum
ε_r	relative permittivity
e	elementary charge
N_A	Avagadro’s number
T	the absolute temperature
k_B	boltzmann constant
M_w	molecular weight
τ_{on}	switch-on speed
τ_{off}	switch-off speed
n	charge carrier (hole) density
g_m	transconductance
V_{GS}^{eff}	effective gate voltage
V_{offset}	offset voltage

Chapter 1. Introduction

Abstract: The first chapter of this thesis aims to give a general introduction on organic electronics, some basic concepts on organic semiconductors (OSCs) and a brief description of fundamental mechanisms governing organic field-effect transistors (OFETs) and electrolyte-gated organic field-effect transistors (EGOFETs). First of all, a short overview of organic electronics and OSCs, including the development of organic electronics, the electrical structure and charge transport mechanisms of OSCs, OSCs materials and the solution-based techniques used to process them, is presented. Then, OFETs are described with a focus on device architecture, operating principles and the main electrical characteristics. Subsequently, the fundamental mechanisms of EGOFETs, such as the role of the electrolyte, the electrical double layer and the principles of operation are described. EGOFETs, which represent the focus of this thesis, have displayed a great potential to become novel sensing platforms thus, the last part of the chapter, deals with a short description of their state-of-the-art as sensors. Finally, the objectives of this thesis are described.

1.1 Organic Electronics

In 1947, John Bardeen, Walter H. Brattain and William Shockley, at that time at Bell Laboratories, created the first germanium-based transistor[1] that is actually recognized as the most important invention of the 20th century. Germanium was soon replaced by silicon and, since then, transistors technology has attracted great attention in both academic and industry communities.

Due to their pioneering work on semiconductors and the invention of the transistor, Bardeen, Brattain and Shockley were awarded the Nobel Prize in Physics in 1956.[1] Important milestones towards what is commonly called "information age", were achieved when back in 1954 the first operative silicon (Si) transistor was fabricated by Morris Tannenbaum[2,3] and in 1960 the first integrated circuit (Metal Oxide Semiconductor Field-Effect transistor (MOSFET)) was invented by Atalla and Kahng[4]. Nowadays, transistors are mainly based on silicon and they are the building blocks of almost all the modern electronic devices, which surround our daily life, starting from simple devices (*i.e.* an electronic timer) to more complex circuits (*i.e.* computer, mobile phone and even medical instrumentations). However, some drawbacks related to inorganic semiconductor technologies (such as their high-cost and the environmental impact of their production processes) have moved scientific research towards other alternatives. Furthermore, several issues regarding flexibility and lightness limit the application of traditional silicon technology into the so-called conformable electronics.[5] Therefore, the advent of organic semiconductors and the concept of plastic electronics have risen in our modern society.

The term "organic" was firstly introduced in the late 19th century, when it was believed that organic compounds could only be formed in living organisms.[6,7] However, it is known that organic molecules can also be synthesized artificially. In general, the organic materials, either natural or synthetic, consist of carbon atoms in combination with other elements such as hydrogen (H), nitrogen (N), phosphorus (P), oxygen (O), sulfur (S) and halogens or even metals.[6,7] The mechanical, electrical and optical properties of organic materials have shown numerous applications. Some organic materials are applicable in technologies based on semiconductors and have been topic of research since the late 1940's.[8] Some milestones of organic electronics are hereby highlighted: (1) in the 1950s, the discovery of polycyclic aromatic compounds forming semi-conducting charge-transfer complex salts with halogens;[9,10] (2) in 1973, Anderson *et al.* observed metallic conductivity in the organic metal tetrathiafulvalene-tetracyanoquinodimethane (TTF-TCNQ) complex;[11] (3) in 1977, the first application of organic semiconductors started from the controlled doping of a synthetic conjugated polymer, which was demonstrated by Alan J. Heeger, Alan G. MacDiarmid and Hideki Shirakawa,[12] who were awarded the Nobel prize in Chemistry in 2000 for "the discovery and development of conductive polymers".[13] These findings demonstrated that organic semiconductors/conductors could be used as electrically active materials and promoted the development of a new research field called organic electronics.

This field includes all the devices having an active component based on organic material. In particular, organic semiconductors, have been applied in organic light-emitting diodes (OLEDs)[14–17], organic solar cells[18–20] and organic field-effect transistors (OFETs)[21–24].

OLEDs are diodes used to directly convert current into visible light. Their structure consists of an organic active layer sandwiched between two electrodes where at least one of them is transparent to allow light emission.[25] The basic operation principle is based on the recombination of injected holes and electrons to form excitons, which decay through radiative emission to ground states. The first practical OLED was fabricated by Teng *et al.*[16] in 1987 and it consisted of a bilayer structure containing an electron transporting layer (ETL) and a hole transporting layer (HTL), as shown in **Figure 1.1**. Interestingly, the color of the emitted light (*i.e.* red, green and blue) could be modulated by selecting the appropriate OSCs.[25] Due to the impressive improvements in this field, commercial products started to invade the market, such as RGB digital displays, where color contrast is determined by the presence of three OLEDs of different colors for each pixel, are nowadays a consolidated technology.[25] It is also of recent release the flexible smart phone from Huawei Mate X (**Figure 1.2**) which demonstrates how flexible electronics is playing an increasing role in our daily life.

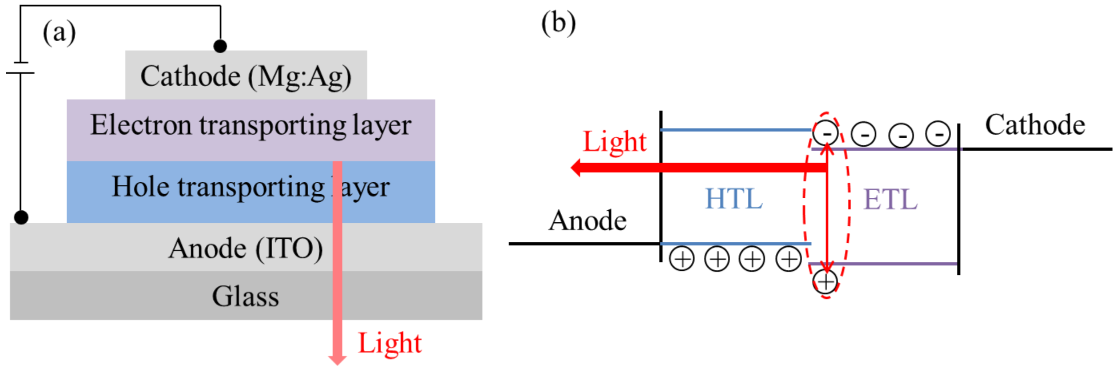

Figure 1.1: Schematic illustration of a typical bilayer OLED and its corresponding energy levels.[16]

Figure 1.2: Flexible smart phone with OLEDs displays. Images taken from the website of Huawei (https://consumer.huawei.com)

In contrast to OLEDs, organic solar cells are devices that convert light into direct current (DC). Their structure is similar to OLEDs and it includes an organic active layer sandwiched between two electrodes where at least one is transparent to visible light. As shown in **Figure 1.3**, the working principle behind an organic solar cells comprises five key steps:[26] (1) photo capture and exciton generation, (2) exciton diffusion to the donor/acceptor interface, (3) exciton dissociation at the interface, (4) carrier diffusion to the respective electrodes, (5) carrier collection by the respective electrodes. Although organic solar cells exhibit an acceptable power conversion efficiency, whose at present reaches 17 %,[19] the technology has not yet reached the market due to the relative low lifetime of these devices.

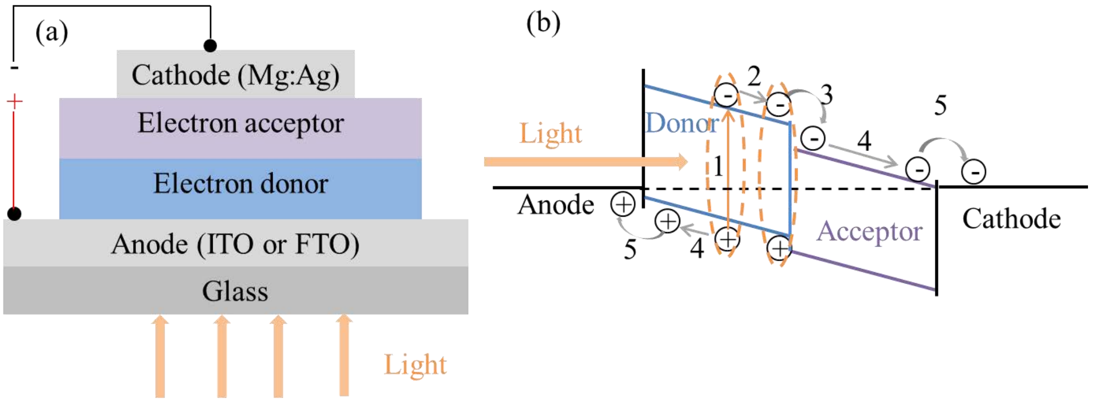

Figure 1.3: Schematic illustration of a bilayer organic solar cell and its corresponding energy levels.[26]

The third type of organic electronic device is the organic field-effect transistor (OFET). In this case, the current between the source and drain electrodes is modulated by the third (gate) electrode due to the field-effect (details regarding its operation principle can be found in the next section).[24] The first OFET based on thiophene polymer was fabricated by Tsumura *et al.* in 1986.[27] OFETs can potentially be integrated in flat panel displays based on flexible matrix elements and complementary circuits[28–31] where large area coverage and low-cost production play an important role. In addition, OFETs can be applied on small integrated circuits,[32] Radio Frequency Identification (RFID) tags[33] or chemical and pressure sensing device.[34–41]

Other important field of research are the organic spin valves, which take advantage of the weak spin-orbit interaction due to the relative long spin relaxation time of OSCs compared to their inorganic counterpart,[42,43] and organic lasers, which exploit the high optical gain of organic materials.[44] Actually, the field of organic electronics is still attracting great attention from the research community which is pursuing the following goals: i) the design and synthesis of new organic materials to improve their solubility and electrical properties; ii) the development of new deposition methodologies aiming at large scale manufacturing; iii) the improvement of devices stability and iv) the investigation of new geometries and structures for the development of new applications.

1.2 Organic Semiconductors

1.2.1 Electronic Structure of Organic Semiconductors

Atoms are the basic units of all matter and their structure contains a positive dense nucleus (including the protons and neutrons) surrounded by a negative charged cloud of electron. According to quantum mechanics, each electron is described by a wave-function. The square of wave-function represents the possibility to find it in a specific region. These wave-functions are called atomic orbitals. The energy and the shape of the atomic orbitals are characterized by three quantum numbers: n is the principal quantum number which determines the energy, l is the quantum number describing the orbital angular momentum and m is the magnetic quantum number that represents the orientation of the angular momentum. *S*-orbital and *p*-orbital represent the orbitals with angular momentum $l = 0$ and 1, respectively. In general, the *s*-orbital is symmetric spherical-shaped, while the *p*-orbital is dumbbell-shaped along three axis direction.[45,46]

When two or more atoms become closer, their atomic orbitals overlap to form molecular orbitals, which can be represented by a mathematical function describing the wave-like behavior of an electron in a molecule. In general, the molecular orbital can be estimated by the linear combination of atomic orbitals defined through the LCAO-MO method.[47] The molecular orbital in a simple diatomic molecule (hydrogen) results on a bonding molecular orbital and an antibonding molecular orbital, that are lower and higher in energy compared to the single atomic orbitals as displayed in **Figure 1.4**. Therefore, there is a splitting of the original atomic energy levels into two molecular energy levels where the two electrons occupy the orbital of lower energy, *i.e.* the bonding molecular orbital, assuming an anti-parallel spin configuration. The occupied orbital of highest energy is named the Highest Occupied Molecular Orbital (HOMO), whereas the unoccupied orbital of lowest energy is called the Lowest Unoccupied Molecular orbital (LUMO). The energy difference between the HOMO and LUMO is the energy gap.[48]

Similar to the atomic orbital, the molecular orbitals can be defined through labels. If the orbital is symmetric with respect to the axis joining the two nuclear centers, the corresponding bond is called a σ-bond, whereas if it is asymmetric with a nodal plane containing the inter-nuclear axis, the bond is called π-bond. In general, the π-bond is weaker than the σ-bond, and π-bond contains high energy orbitals. The corresponding antibonding orbitals are labeled as σ*, π*.

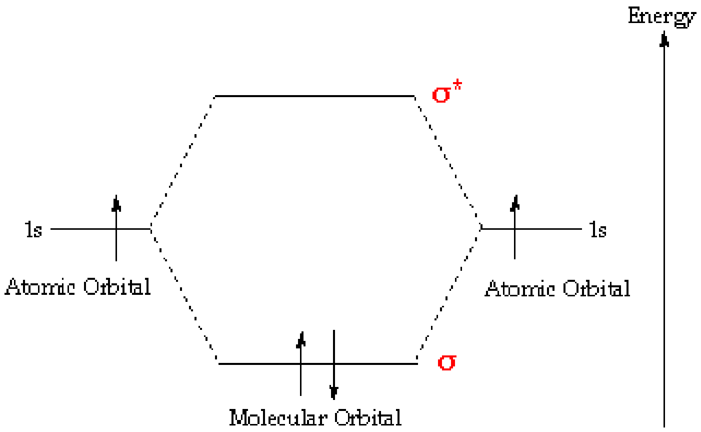

Figure 1.4: Formation of bonding and antibonding molecular orbitals in hydrogen molecule.

As previously defined, the structure of organic materials is based on carbon which possess a ground state ($1s^2 2s^2 2p^2$) containing just two unpaired electrons available for forming two covalent bonds.

However, this theory called valence bond theory fails to predict even the simplest hydrocarbon compound, *i.e.* methane (CH_4), thus L. C. Pauling proposed the concept of orbital hybridization which is elucidated in **Figure 1.5.** Hybrid orbitals originate from the combination of atomic orbitals and can explain the molecular geometry of carbon compounds; according to this theory in fact, methane is correctly predicted and assumes a tetrahedral structure. In sp^3 hybridization, the 2s orbitals and all three of the 2p orbitals hybridize to form four *sp* orbitals, each consisting of 75% *p* character and 25% *s* character. As example, in saturated compounds (*i.e.* CH_4), these four sp^3 hybrid orbitals are overlapped with hydrogen 1s orbitals yielding four strong σ-bonds of equal length and strength arranged in a tetrahedral configuration. In the case of unsaturated carbon species like ethylene (C_2H_4), three σ-bonds are formed ($2s$, $2p_x$ and $2p_y$) arranged in three coplanar sp^2 hybrid orbitals, whereas the fourth unpaired electron ($2p_z$) can form a π-bond which arranges perpendicular with respect to the molecular plane. In the π-bonds, the electrons are delocalized below and above the molecule plane inducing a lowering of the energy gap between HOMO and LUMO, which characterizes the optical and electronic properties of conjugated organic materials. In carbon compounds having a triple bond (C_2H_2), two *sp* hybrid orbitals arrange along opposite directions and two uncharged $2p_y$ and $2p_z$ orbitals are perpendicular to the molecular plane.

As mentioned above, ethylene represents the precursor of the family of conjugated molecules and it is characterized by a chemical structure consisting of alternating single and double C-C bonds. The $2p_z$ orbitals form π-bonds that are delocalized along the chain and are responsible for all electrical and optical properties of these materials.

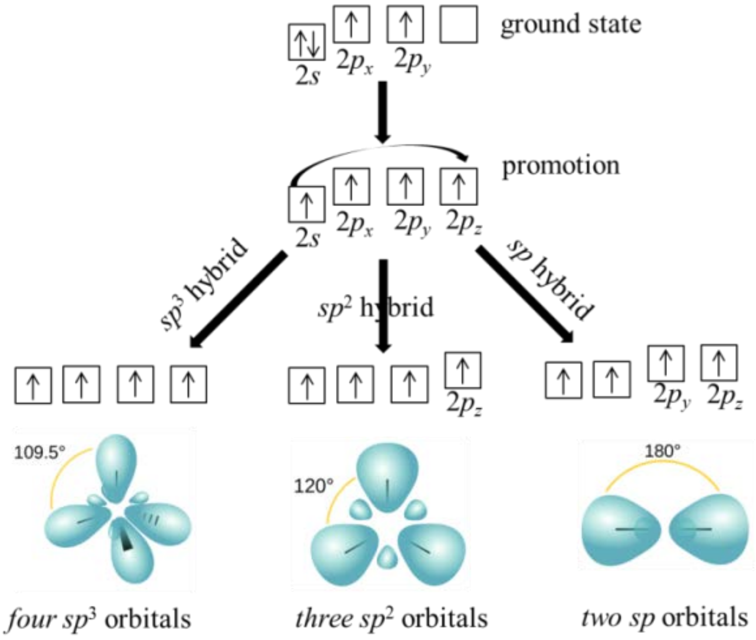

Figure 1.5: Electron configurations of the C atom in the ground state, hybridization state of (left) sp^3, (center) sp^2 and (right) *sp*, and their corresponding hybridized orbitals.

By increasing the number of carbon atoms, electrons delocalization extends over the whole molecule and the discrete π and π* orbitals observed for short chain unsaturated hydrocarbons (left part **Figure 1.6**) become progressively a continuum forming a band-like energetic structure (right part **Figure 1.6**). Furthermore, the increasing of electron delocalization reduces the energy gap between HOMO and LUMO which is a fundamental characteristic for charge carrier transport of conjugated materials as reported in the following section.

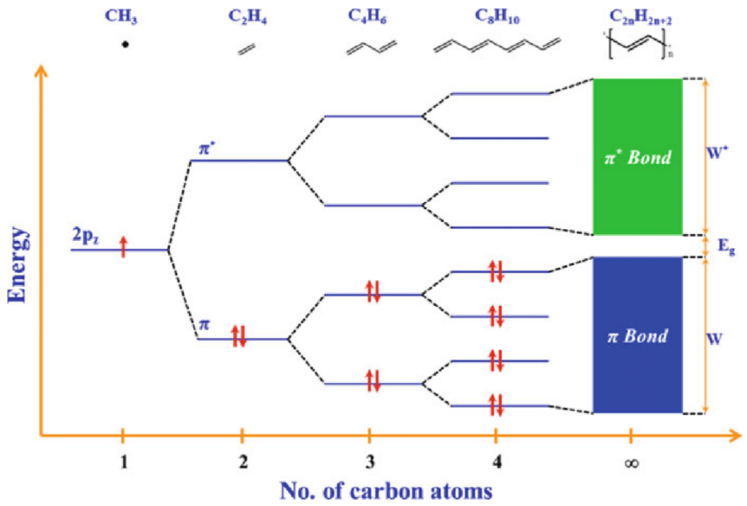

Figure 1.6: Energy level splitting and band formation in conjugated molecules.[49]

1.2.2 Charge Carriers and Transport in Organic Semiconductors

In conjugated organic molecules, the two most interesting molecular orbitals are HOMO and LUMO. In the ground state, all the energy levels below the HOMO are fully filled with electrons and all the energy levels above the LUMO are empty. This situation guarantees the neutrality of the molecule. In this class of molecules, the energy gap between HOMO and LUMO is relatively small so, thermal excitation of electrons from HOMO to LUMO is possible. When an electron is removed from the HOMO level, a positive charge "hole" is induced and can contribute to the current. In contrast, when an electron is added to the LUMO level, the negative charge "electron" can also contribute to the current. The introduction of a charge (hole or electron) into the molecule chain deforms locally its structure which results in the lowering of the electronic energy of the added charge. These local lattice vibrations are called phonons, which are quasiparticles describing the elementary vibrational motion in a crystal lattice.[50] The combination of charges and phonons are called polarons which can be either positive or negative. **Figure 1.7** describes the energy diagram relative to the formation of polarons and bipolarons. In fact, a more energetically stable situation can be reached when two close polarons combine into a bipolaron.[50]

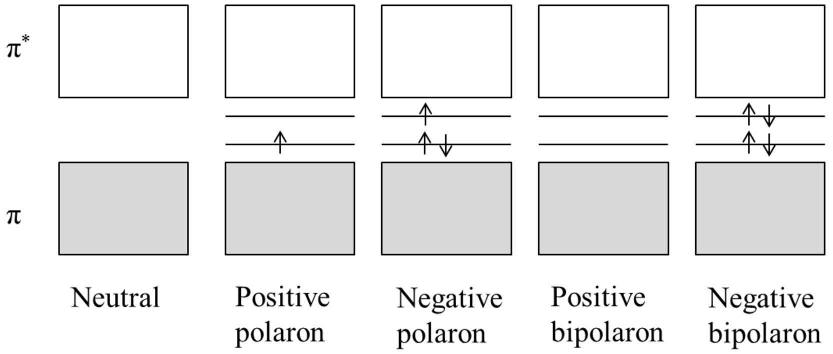

Figure 1.7: Energy levels of the neutral molecule, positive and negative polaron, the positive and negative bipolaron.[49]

Charge transport mechanism in organic semiconductors has to face up the abundant structural defects and strong lattice vibrations that originate from the weak van der Waals interactions between organic semiconductors molecules. Up to now, several different transport mechanisms, such as band-like transport model, multiple thermal trapping and release model and hopping transport model have been proposed for both organic thin-film (amorphous and polycrystalline) and organic single crystals (**Figure 1. 8**). In the case of high quality organic crystals, a classic band-like transport is expected due to the strong delocalization of charge carriers that can travel in extended Bloch-waves through the periodic lattice structure. The band-like transport could also be used to explain the transport within a single grain or for some conjugated polymers displaying extreme torsions of chain.[51–53] In the case of polycrystalline OSCs, in which the crystallites are separated by grain boundaries, the multiple thermal trapping and release model has been proposed based on the assumption that charge carriers travel in narrow, delocalized bands but most of them are trapped by localized states within the energy gap.[52,54] In this model, trapping and thermally activated release of the carriers determines the effective mobility and their thermally activated behavior.[55,56] For the charge transport in the amorphous or highly disorder OSCs, the hopping model has been introduced assuming that a charge carrier jump from an occupied localized site to an adjacent unoccupied localized site due to a phonons-assisted mechanism that permit to overcome the energy barriers. When the electron-phonon coupling is weak (*i.e.*, charge carriers are strongly localized), simple phenomenological Miller-Abrahams model can be used to describe the charge transport.[55] According to this model, the carrier jump rate

(W_{ij}) strongly depends on the distance and energy difference between the starting site and the target site. The above hopping model was further extended into the "variable range hopping" (VRH) model,[57] which assumes the charges hop short distances with high activation energies or long distances with low activation energies. On the other hand, Marcus theory can be used for systems with a strong electron-phonon adiabatic coupling.[58,59] The strong electron-phonon coupling could lead to carrier self-trapping and then weakens the energy of the charge creating a big barrier for charge removal.[54,60] In the Marcus theory, two major parameters determine self-exchange rates: (i) the electronic coupling, estimated by the transfer integral (J) between adjacent molecules, which needs to be maximized, and (ii) the reorganization energy, which needs to be small for efficient charge transport.[60] In summary, although a lot of efforts have been devoted to understanding the transport mechanisms taking place in organic semiconductors, some basic aspects still remain unclear.

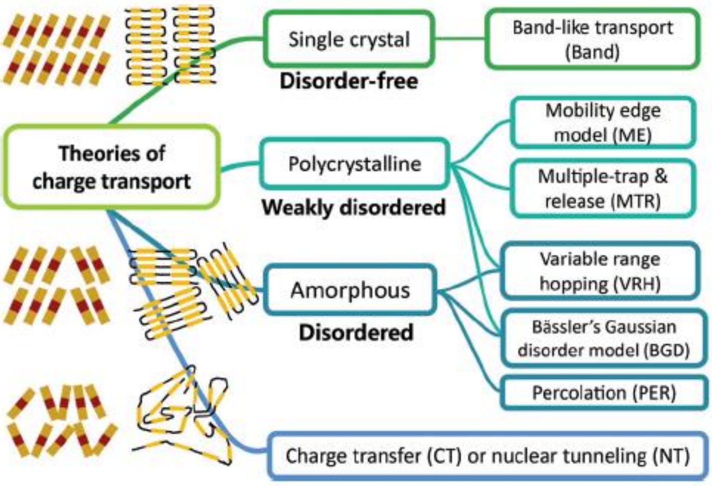

Figure 1.8: A brief summary of charge transport theories in organic semiconductors/polymers.[53]

1.2.3 Organic Semiconductor Materials

In general, organic semiconductors are electroactive small conjugated molecules or polymers with a strong π-conjugated system where the electrons are delocalized over the whole molecule structure.[24,61] OSCs can be divided into three classes according to the type of carrier that are able to transport:[24] *p*-type, where the majority of charge carriers are holes, *n*-type, if electrons are the main carriers and ambipolar, where charge transport happens through both holes and electrons. In this thesis only *p*-type OSCs have been employed, so we will focus our attention solely on this kind of materials.

Another important distinction has to be done regarding the nature of the OSC. In fact the family of organic semiconductors can be divided into small conjugated molecules or conjugated polymer semiconductors.[24,62–64] The conductivity is mainly determined by the relative position of the π-π orbitals, and thus the molecular ordering is very important to achieve high performance OFET.

Regarding conjugated polymer semiconductors, their compatibility with solution processing technique (*i.e.* spin-coating, dip-coating and bar-coating) due to the inherent good solubility in organic solvents and their excellent film-forming properties is often counter-balanced by a low degree of crystallinity. In other terms, solution processed polymer OSCs result in amorphous or poorly crystalline thin films where microcrystalline domains are embedded in an amorphous matrix in most cases. As example, poly(3-hexylthiophene) (P3HT) (**Figure 1.9**) is probably the most studied polymer OSC and it has exhibited a mobility of 0.1 $cm^2 V^{-1} s^{-1}$ in OFETs.[65] In general, high disorder limits the charge transport resulting in low electrical performance of OFETs[66] so one widely exploited strategy consists in the increasing of structural order by the careful design of the molecules structure. For instance, polymer OFETs based on poly(2,5-bis(3-alkylthiophen2-yl)thieno(3,2-b)thiophene) (PBTTT) (**Figure 1.9**) reported by McCulloch *et al.*,[67] have reached a mobility of 1.1 $cm^2 V^{-1} s^{-1}$ due to the improved crystallinity of the film caused by the better side-chain packing. In addition, Kim *et al.* reported a random copolymer consisting of diketopyrrolopyrrole-thienothiophene (DPP-TT) and DPP-selenophene-vinylene-selenophene (DPP-SVS), whose field effect mobility reached 5 $cm^2 V^{-1} s^{-1}$ when processed as thin film from non-chlorinated solvent thanks to the side pendant groups which improve its solubility.[67,68]

Apart from this strategy, there is extensive research on novel formulation based on donor-acceptor copolymers where the polymer backbone is composed of alternating electron deficient and electron rich units resulting in a significant increase of the performance.[61] In fact, 2D Nuclear Magnetic Resonance has demonstrated the existence of attractive forces between donor and acceptor units which definitely improve the charge transport.[69] One example of high mobility donor-acceptor copolymer is the cyclopentadithiophene-benzothiadiazole (CDT-BTZ) (**Figure 1.9**), which has exhibited mobilities up to 3.5 cm^2 V^{-1} s^{-1} in dip-coated thin films and up to 5.5 cm^2 V^{-1} s^{-1} in single fibers grown by a solvent vapor enhanced drop casting technique.[69,70] Another interesting example is the donor-acceptor copolymer based on the electron-deficient units of diketopyrrolopyrrole (DPP) and thienothiophene acceptor unit, which exhibited ambipolar behavior with both electron and hole mobility exceeding 1 cm^2 V^{-1} s^{-1}.[71]

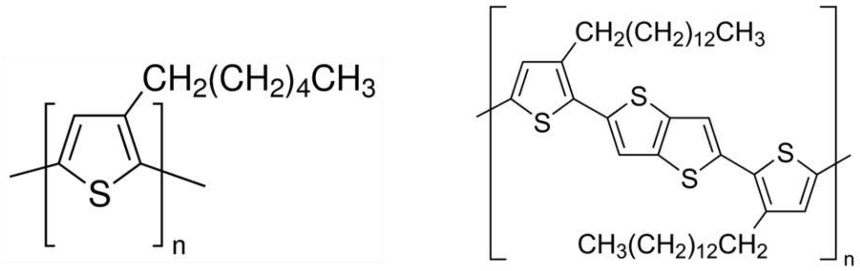

P3HT PBTTT

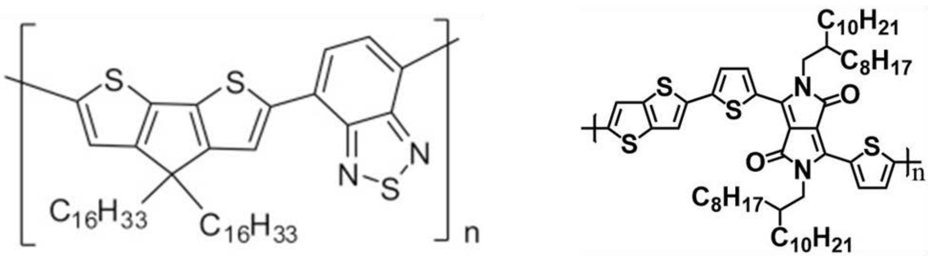

CDT-BTZ DPPT-TT

Figure 1.9: Chemical structure of conjugated polymer OSCs.

On the contrary, small molecule OSCs tend to form more ordered structures and highly crystalline films *via* high vacuum deposition but they are hardly processed in solution due to their poor solubility properties.[24] The problem has been partially overcome with the addition of side groups to the conjugated and rigid cores for improving the solubility without compromising the electronic properties of the material.[61] Many benchmark small molecule OSCs belong to the family of acene and heteroacene and some examples are shown in **Figure 1.10**. A model small molecule semiconductor is triisopropyl-silylethynyl. 6,13-bis(triisopropylsilylethynyl) pentacene (TIPS-pentacene) that was first synthesized by Anthony *et al.* by adding soluble side chains to the central 6- and 13- position of a pentacene core.[69] Neat TIPS-pentacene films exhibited a high degree of crystallinity once processed by spin-coating technique and displayed a mobility exceeding 1 cm^2 V^{-1} s^{-1}.[69] In addition, various heteroacene derivatives, such as 2,8-difluoro-5,11-bis(triethylsilylethynyl)anthradithiophene (diF-TES-ADT)[72] or (triethylsilylethynyl)anthradithiophene (TES-ADT)[73], exhibit similar performance.

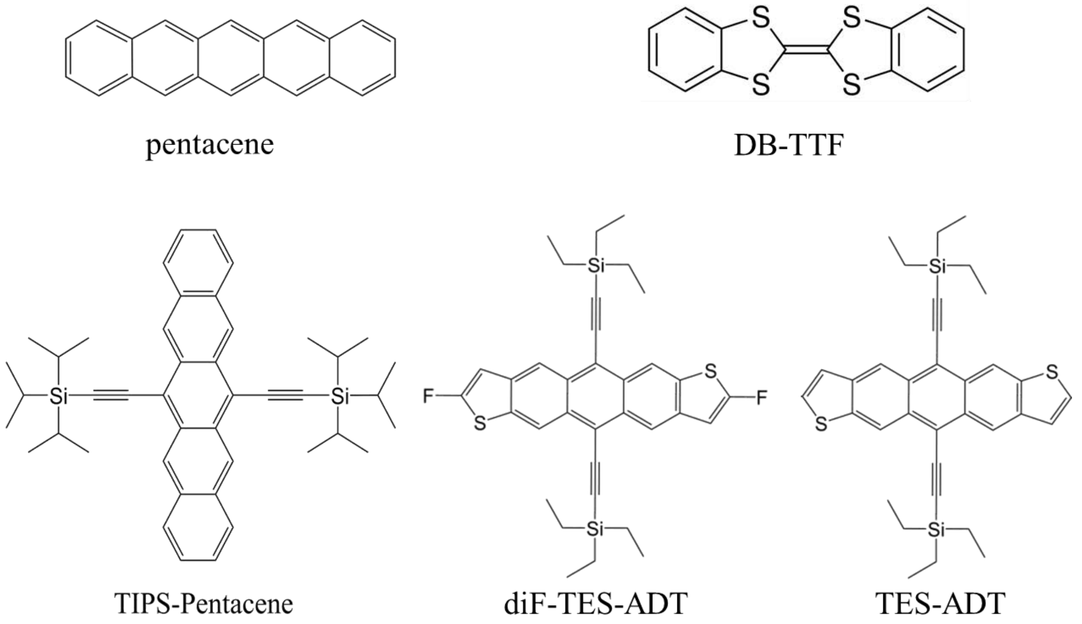

Figure 1.10: Molecular structures of benchmark small molecule OSCs.

However, the preparation of large area uniform and reproducible films based on small molecule OSCs is still challenging due to the low viscosity of the inks. To circumvent this, a promising route consists in blending small molecule OSCs with an insulating binder polymer aiming to exploit the advantages of both types of materials: uniform film-forming properties of the binder polymer component and high carrier mobility of the OSC.[74–76] Furthermore, this strategy has demonstrated several advantages even when the OSC component is a polymer semiconductor due to the improved electronic performance reported by several authors.[77,78] Hence, this approach not only facilitates the processing of these OSC materials but provide additional advantages such as the reduction of the amount of the semiconductor required, an improved crystallization, a high device-to-device reproducibility and the enhancement of the operational stability.[75]

The first example of a solution processed OSC:polymer blend was reported by Stingelin-Stutzmann *et al.* who employed a rubrene-based blend for the fabrication of OFETs with a saturated mobility of 0.7 cm^2 V^{-1} s^{-1}.[79] It should be highlighted that prior to this work, this small molecule OSC were mainly studied by the controlled growth of single crystals or by thermal evaporation under ultra-high vacuum conditions. Hereafter, various small molecule OSCs (*i.e.* acene derivatives, thiophene derivatives) blended with insulating polymers have been systematically investigated with several solution processing techniques for achieving robust performance OFETs.[80–83] Some typical examples are summarized below: TIPS-pentacene with polystyrene (PS),[83,84] poly(α-methylstyrene) (PαMS)[80] and poly (methyl methacrylate) (PMMA),[80] diF-TES-ADT with PS and PMMA,[81,84] dibenzo-tetrathiafulvalene (DB-TTF) with PS,[82] 2,7-Dioctyl[1]benzothieno[3,2-b][1]benzothiophene (C8-BTBT) with PS,[84] and meso-diphenyltetrathia (22) annulene (2,1,2,1) (DPTTA) with PS.[85]

Thanks to the binder polymer, homogeneous and continuous crystalline films are achieved with large and well-connected domains, which is beneficial for improving the electrical performance of OFETs.[83,86] For example, OFETs based on TIPS-pentacene:PS blend thin film exhibiting ribbon-like crystals, has resulted in an outstanding OFET mobility of 8.3 cm^2 V^{-1} s^{-1} due to the excellent film quality and the continuous growth of the crystals in the shearing direction.[83] Moreover, the use of polymer binders allow to reach more isotropic 2D crystallites leading to an improved device-to-device reproducibility and easy processing while retaining high mobility.[87,88] As reported by Kim *et al.*,[88] a narrower distribution of mobility was observed in diF-TES-ADT: PαMS blends deposited by spin coating, in which the improved reproducibility was attributed to the enhanced film uniformity. Furthermore, OFETs based on OSC/polymer blends typically exhibit an enhanced stability due to the improved crystallinity or even to the self-encapsulation of the OSC.[82,89] Our group reported a strategy to achieve OFETs of high environmental stability by mixing DB-TTF, which is a non-air-stable material, with a binder polymer (*i.e.* PS) resulting in a layered film where a thin encapsulation layer protects the polycrystalline OSC thin film.[82] The shelf stability of the OFETs was explored by measuring the devices for several weeks under ambient conditions.

Thus, blending the OSCs with a binder polymer provides an effective protocol to improve solution processing, device reproducibility and OFETs stability. These benefits are mainly ascribed to the phase separation occurring during the deposition process.[75,90–92] Due to the solvent evaporation during solution coating, the blend changes from mixed phase to two individual phases according to the free energy of the system and, as a result, a bilayer or trilayer structures are commonly observed in the resulting coating.[90,91] This phase separation phenomenon is complex and depends on a large number of factors, such as the physical and chemical properties of the materials, solvent boiling point, processing conditions, type of substrate, *etc.*[76,90,92–94] Up to now, the mechanism of the phase separation, specifically, the correlation between solution-casting conditions and the resulting thin film morphology, as well as the corresponding device performance, is still not clear. However, some of the desirable features have been clearly identified. For example, by changing the C8-BTBT:PS ratio, our group demonstrated that a tri-layers structure (PS/C8-BTBT/PS) with an ultrathin skin-like layer can be obtained which also prevent the diffusion of water and/or oxygen.[89]

1.2.4 Solution-processed Organic Semiconductors

The deposition of the OSC is a fundamental step of OFET fabrication. The techniques of deposition can be divided into two main categories: (i) physical vapor deposition (PVD) techniques and (ii) solution-processed deposition techniques.[48,95,96]

Vapor phase deposition techniques are mainly based on the thermal evaporation of the material under high-vacuum chamber (*i.e.* 10^{-6}~10^{-8} mbar) at high-temperature, Once the vapor pressure of the heated material exceeds the pressure in the chamber, the materials start to evaporate and condense on the target substrates, as shown in **Figure 1.11**.[97] This approach usually results in high quality OSC films and presents many advantages in terms of control and reproducibility of film thickness and, in addition, this method offers the possibility of multilayer deposition and the co-deposition of different materials. However, it normally requires expensive equipment and it is not suitable for large area fabrication. Field-effect transistors presented in this thesis are based on solution-processed OSCs.

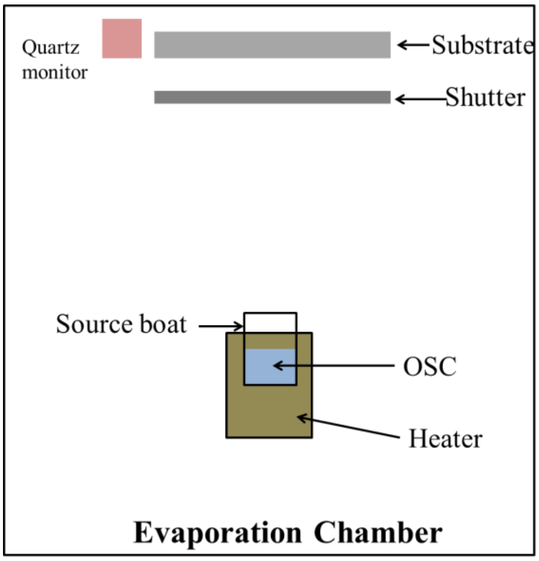

Figure 1.11: Schematic presentation of the vacuum deposition system.

Solution processing techniques are, in fact, an attractive strategy for OSC thin film deposition due to the cost-effectivness options that they offer and their suitability for large-area fabrication. According to this approach, the OSC material is firstly dissolved into an appropriate organic solvent and then processed as thin film over a target substrate. The most common solution processing techniques are spin-coating, drop-casting, dip-coating, spray-coating, blade-coating, zone-casting and bar-assisted meniscus shearing. The next section deals with a brief description of them.

Drop-casting

Drop-casting is probably the simplest approach for the deposition of organic semiconductors and it consists in dropping an OSC solution on a target substrate allowing the evaporation of the solvent. A schematic representation of this method is shown in **Figure 1.12**. Drop casting is commonly used to obtain single-crystal OSCs while its potential as thin film deposition technique is limited due to several drawbacks.

In fact, drop casting suffers of poor reproducibility and often results in not uniform films with a thickness and morphology that strongly depended on the precursor concentration and solvent evaporation rate.[98]

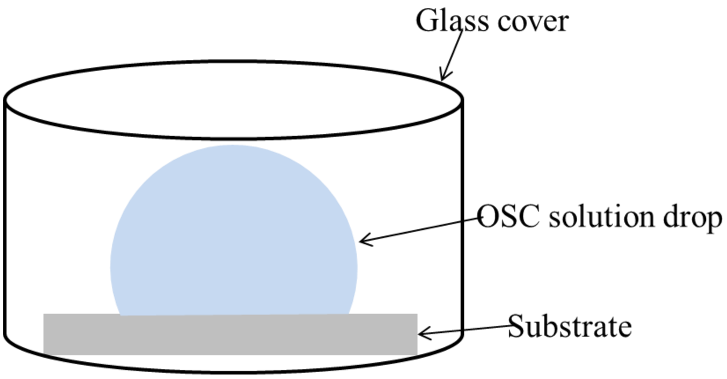

Figure 1.12: Schematic representation of the drop coasting technique.

Spin coating

Spin coating is one of the most common techniques for thin film deposition employed at laboratory scale, because it is simple and does not require any complex equipment.[99,100] This method consists in dropping an OSC solution on the target substrate and then spinning the sample at high revolutions as depicted in **Figure 1.13**. The centrifugal forces dry the film instantaneously leaving the substrate covered with a uniform thin film. The thickness of the film is controlled by the concentration of the precursors in the solution, the viscosity of the solution and the working parameters of the spin coater. However, as mentioned in the drop casting approach, this technique is not advantageous in terms of materials since it requires a lot of solvent, and is not suitable for large area fabrication.

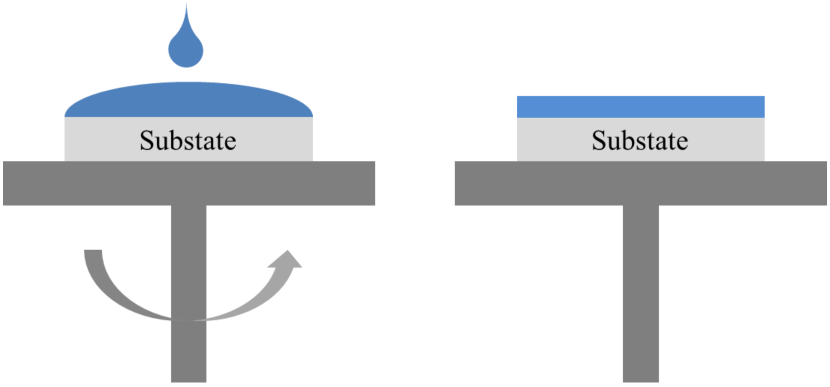

Figure 1.13: Schematic representation of a spin coating process.

Dip coating

Dip coating is another laboratory-scale technique which consists in the immersion of the substrate in a OSC solution followed by its controlled withdraw at low speed in order to grow a thin film in a controlled manner (**Figure 1.14**).[101] This method allows obtaining very thin layers with a thickness determined by the withdrawal speed and by the solution concentration. Furthermore, dip coating is suitable for covering large area samples and the resulting thin films normally display good uniformity. However, the disadvantages in terms of solution volume and its unsuitability for coating curved or flexible substrates limit this technique to a laboratory scale.

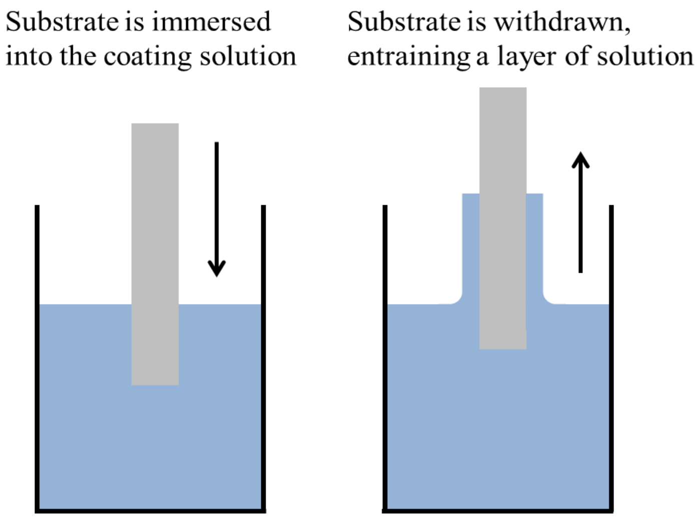

Figure 1.14: Schematic of the dip coating deposition technique.

Spray coating

Spray coating is based on the vaporization of an OSC solution with a high pressure gas carrier (usually N_2) as depicted in **Figure 1.15**. This technique is widely employed at industrial scale and it is one of the most versatile in terms of target materials (i.e. glass, metal and plastic substrate).[100,102] The film thickness and morphology can be controlled by the air pressure, solution viscosity, solvent properties, gun tip geometry and the distance between the nozzle and substrate. This technique can be employed for covering large areas but usually results in thin films of higher roughness compared with the smooth thin films normally achieved by spin coating.[100]

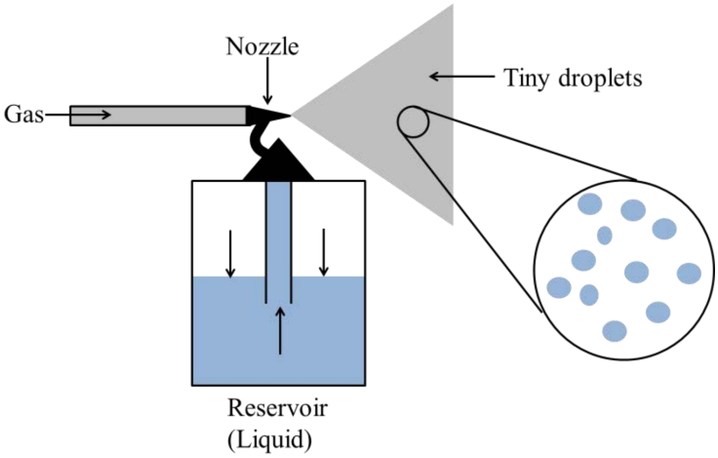

Figure 1.15: Schematic illustration of a spray coating technique.

Zone casting

Zone casting is a technique employed for the preparation of anisotropic thin films of soluble organic semiconductors.[103,104] It consists in the continuous deposition of a film through a flat nozzle that is moving over a substrate (**Figure 1.16**). The solvent evaporation from the meniscus zone can be controlled by adjusting the temperature of the machine and the thickness and the quality of the thin film are determined by the supply rate of the solution, its concentration and the speed of the nozzle. One of major advantage of this technique is its suitability for large scale manufacturing however, for obtaining films of good uniformity, the process has to be performed at very slow speed (< 1 mm/s) which often gives rise to high anisotropic polycrystalline coatings.

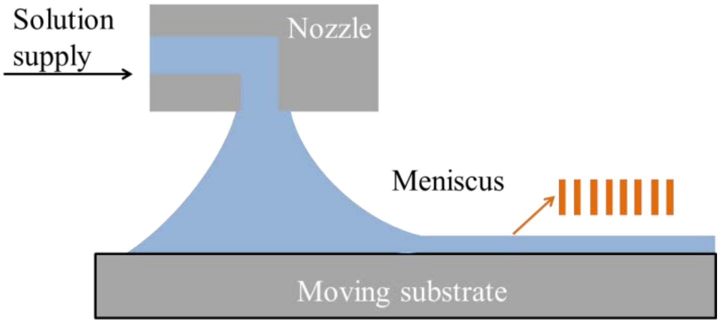

Figure 1.16: Schematic representation of zone casting technique.

Blade coating

Blade coating is a scalable method for depositing thin films which consists in the controlled spreading of an OSC solution over a substrate assisted by a blade.[100,105] In this technique, the OSC solutions are dropped on top of the substrate, and then the blade or substrate moves horizontally in order to leave a uniform wet film on the substrate, as illustrated in **Figure 1.17**. This technique can operate at high speed (*i.e.* several meters per minute) and a fine control of the temperature can allow the fast evaporation of the solvent once the film is formed.

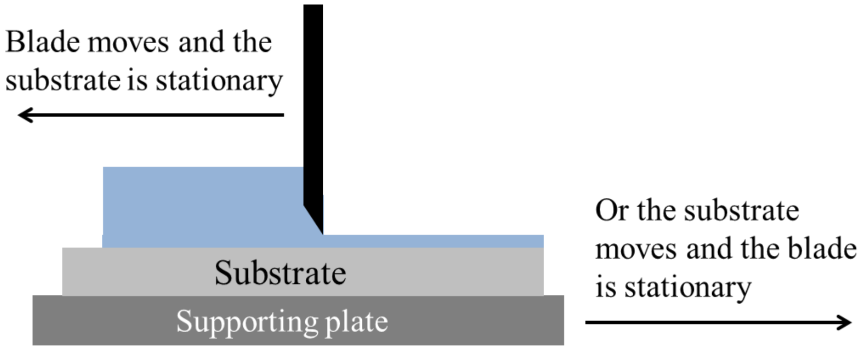

Figure 1.17: Schematic representation of the blade coating technique.

Bar-assisted meniscus shearing

Bar-assisted meniscus shearing (BAMS) differs from the conventional blade coating approach because it is based on the formation of a liquid meniscus between the substrate and a rounded bar.[82,84,106] As shown in **Figure 1.18**, the solution is gently injected between the bar and the substrate until a liquid meniscus is formed, then the horizontal movement allows the formation of a uniform thin film. The temperature of the hot plate can be controlled according to the solvent employed and the thickness of the resulting film depends on the speed of the bar/substrate, the temperature, the height of the gap between the bar and substrate, the viscosity of the OSC solution and the surface tension of the solution.[82]

The simplicity of the method and the lack of any post-coating treatment make this technique really attractive for processing OSC thin films of high crystallinity on large areas. BAMS is a technique developed in our group which has been employed for achieving high crystalline and homogeneous thin films with several benchmark semiconductors. All the thin films presented in Chapter 2 have been processed with this technique and the applications developed in Chapter 3 and 4 are also based on organic thin film transistors processed by BAMS. A typical example of a thin film coated by BAMS is given in **Figure 1.19**.

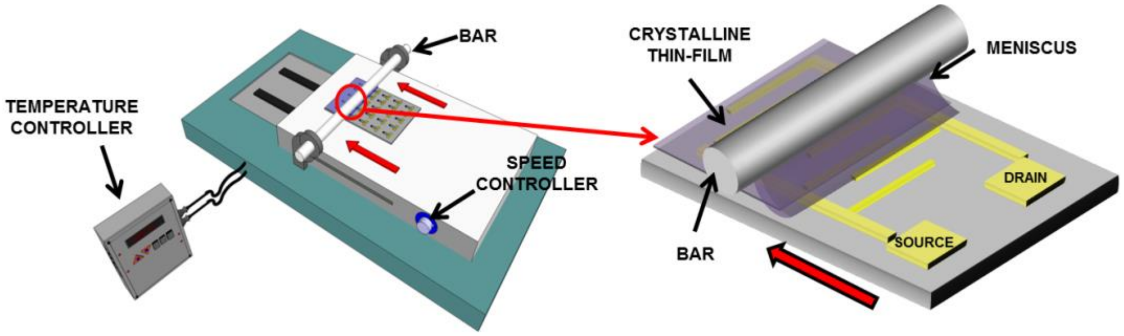

Figure 1.18: Schematic illustration of the BAMS technique.

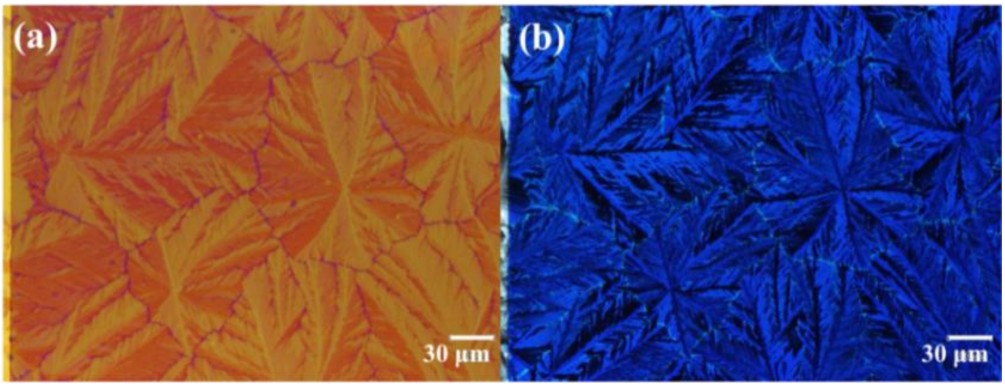

Figure 1.19: Optical microscope images of a typical thin film coated by BAMS based on a diF-TES-ADT:PS_{10K} blend. (left) polarizer/analyzer = 0° and (right) polarizer/analyzer = 90°.

1.3 Organic Field-Effect Transistors (OFETs)

An organic field-effect transistor (OFET) is a three terminal device, in which the voltage across the gate (*G*) and source (*S*) electrodes modulates the charge carrier density of the organic semiconductor (OSC) layer. A second potential applied between the drain (*D*) and *S* electrodes allows the current to flow. The region of semiconductor between the *S* and *D* is the channel area and it is defined through two geometrical parameters, the width *W* and the length *L*, which represent the extension and separation of the channel region between *S* and *D*. The *G* electrode is electrically isolated from the OSC by a gate dielectric layer arranged in a Metal/Insulator/Semiconductor (MIS) architecture.[48,107,108]

1.3.1 Device Geometry

As displayed in **Figure 1.20**, an OFET usually contains three components: a thin OSC layer, a gate dielectric and three electrodes. These elements can be assembled into four geometries, namely (a) bottom-gate bottom-contact (BGBC), (b) bottom-gate top-contact (BGTC), (c) top-gate bottom-contact (TGBC) and (d) top-gate top-contact (TGTC) architectures.[108] This nomenclature defines the position of the three electrodes, namely *S*, *D* and *G*, with respect to the OSC.

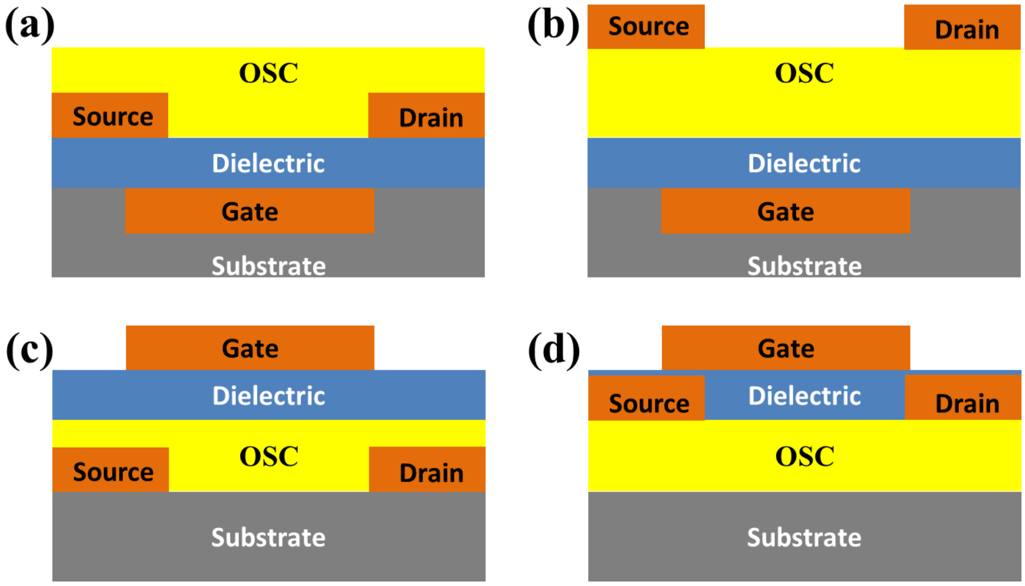

Figure 1.20: (a) Bottom-Gate Bottom-Contact (BGBC), (b) Bottom-Gate Top-Contact (BGTC), (c) Top-Gate Bottom-Contact and (d) Top-Gate Top-Contact (TGTC) architectures of an OFET.

All the above four geometries have their own advantages and disadvantages in terms of device fabrication but, BGBC architecture is the common choice when an easy and fast processing is required. For instance, the BGBC configuration is widely employed for preliminary tests of novel OSC materials since their deposition as thin film represents the last fabrication step. However, the organic material is sensitive to the different surfaces of the device during the coating which can result in different OSC morphology on the different areas of the device. This phenomenon often affects the OSC growth, the uniformity of film and its crystallinity which can in turn, impact severely the electrical performance. In contrast, when a BGTC configuration is employed, the OSC is deposited on top of the dielectric layer and *S*/*D* patterning is performed at last. In this configuration, the thin organic layer is more homogenous and smooth which is usually beneficial for the 2D conduction at the OSC/dielectric interface.[109] Furthermore, BGTC configuration typically exhibits lower contact resistance compared to the BGBC architecture due to the metal intercalation during electrodes evaporation which increases the total metal/OSC interface. However, the top contact approach could suffer of drawbacks associated with the overheating of the organic film during the contacts evaporation or the creation of short circuits.

1.3.2 Operation Principle and Main Device Characteristics

An OFET can be viewed as a capacitor assembled in MIS structure, where the OSC can either be a holes (*p*-channel) transporting or electrons transporting (*n*-channel) material depending on the nature of its charge carriers. OFET are devices that operate in a field-effect mode and the accumulation of charge carriers at the OSC/dielectric interface is induced by a potential applied at the gate-source (V_{GS}).[108] Afterwards, the transversal movement of the charges takes place due to a second potential applied at the source-drain terminals (V_{DS}) which results in the creation of a source-drain current (I_{DS}) as depicted in **Figure 1.21**. The minimum gate voltage required to create the conducting channel is called threshold voltage (V_{th}). In an ideal OFET, the V_{th} is zero but real devices generally display non-zero V_{th} due to the presence of traps at the insulator-semiconductor interface or because of the high work function difference between the gate electrode and semiconductor.

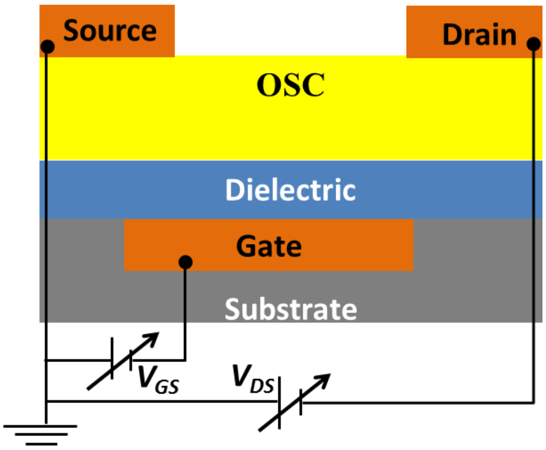

Figure 1.21: The BGTC architecture of an OFET and its corresponding measurement circuitry.

In order to understand the operating principle of the OFETs, a simplified Fermi energy level diagram is depicted in **Figure 1.22**. If no gate voltage is applied, no mobile charges are present in the OSC layer and no charge transport can occur due to the high resistance of the OSC (see **Figure 1.22 (a)**). Considering a *p*-type semiconductor, holes represent the majority charge carriers and they can be accumulated in the OSC adjacent to the gate dielectric interface when a negative gate voltage (V_{GS}) is applied (see **Figure 1.22 (b)**). The HOMO/LUMO levels of the semiconductor shift upwards in energy leading to the HOMO level close to the Fermi level (E_F) of the source electrode.[110] If the gate electric field is large enough, the HOMO will become resonant with the E_F of the electrode permitting the injection of holes and the flowing of the I_{DS} upon application of the V_{DS} (see **Figure 1.22 (c)**). In case of an *n*-type OSC, the situation is reversed and the injection happens with the LUMO level as depicted in **Figure 1.22 (d)** and **(e)**.

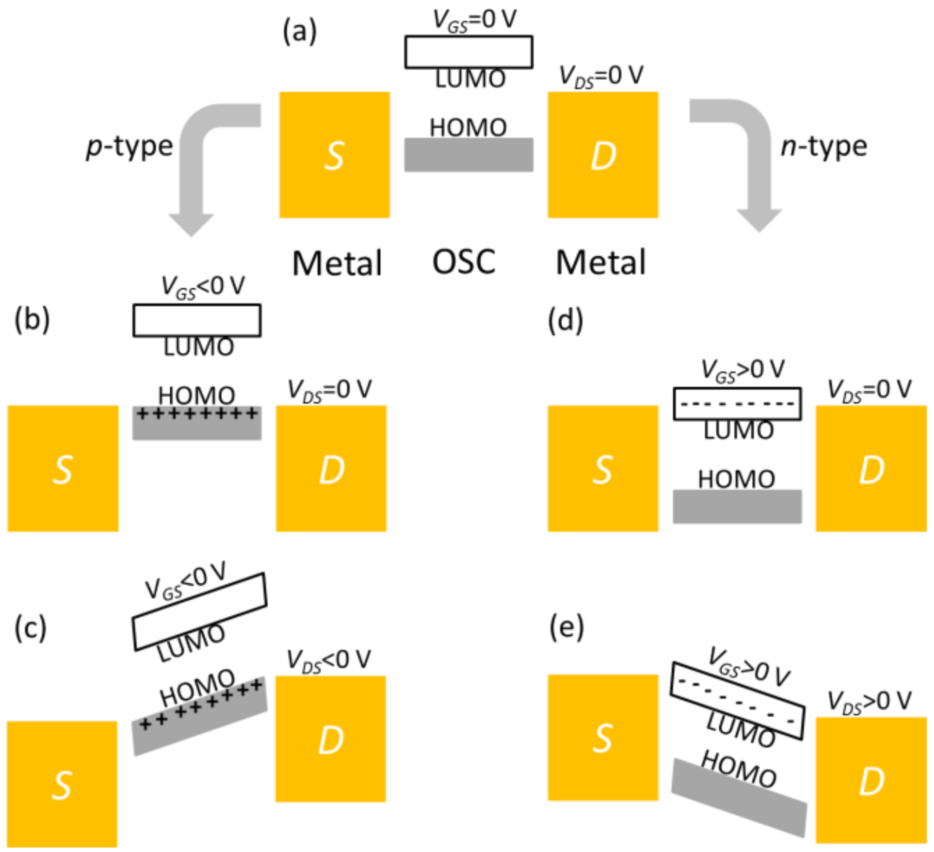

Figure 1.22: Schematic illustration of the working principle of an OFET. (a) off-state when no V_{DS} and V_{GS} applied. (b) Shifting upwards of the HOMO/LUMO level due to the negative V_{GS} applied. (c) Hole transport upon applying a negative V_{DS}. (d) Shifting downwards of the HOMO/LUMO level due to the applied positive V_{GS}. (e) Electron transport due to the positive V_{DS}.[110]

Although the energy diagrams are a useful way to demonstrate the OFET operation mechanism, they are rather simplistic and far away to understand a real device. In fact, the fabrication process of an OFET involves many additional effects that only electrical measurements can reveal like charge trapping phenomena, structural defects in the OSC film or at the OSC/dielectric interface and band bending effects.[110] To describe the current-voltage response of an OFET in a quantitative way, Horowitz *et al.* proposed a comprehensive model following the metal-oxide-semiconductor field-effect transistors (MOSFETs) theory.[111] This model is based on three assumptions: (i) the charge carrier mobility is assumed to be constant within the range of operation, (ii) the parasitic contact resistance between the electrodes and the OSC can be neglected, (iii) the electric field perpendicular to the channel created by the gate electric field is significantly stronger than the one parallel to the channel caused by the drain-source electric field.[111]

OFETs can operate in two regimes according to the distribution of charge carriers in the channel.[110] Upon the application of a small drain voltage ($V_{DS} << V_{GS}\text{-}V_{th}$), the charge carriers density distribution becomes slightly asymmetric as shown in **Figure 1.23 (a)**. Therefore, a direct proportionality between the I_{DS} current and V_{DS} exists and the transistor operates in linear regime, which can be described according to the following relation:[110]

$$I_{DS,lin} = \frac{W\mu C_i}{L}(V_{GS} - V_{th})V_{DS} \qquad \text{if} \qquad (V_{DS} << V_{GS}\text{-}V_{th}) \qquad (1.1)$$

where $I_{DS,lin}$ is the drain-source current in the linear regime, W and L are the width and length of the channel, respectively, μ is the field-effect mobility, C_i is the gate capacitance per unit area, V_{GS} is the gate-source voltage, V_{DS} is the drain-source voltage and V_{th} is the threshold voltage.

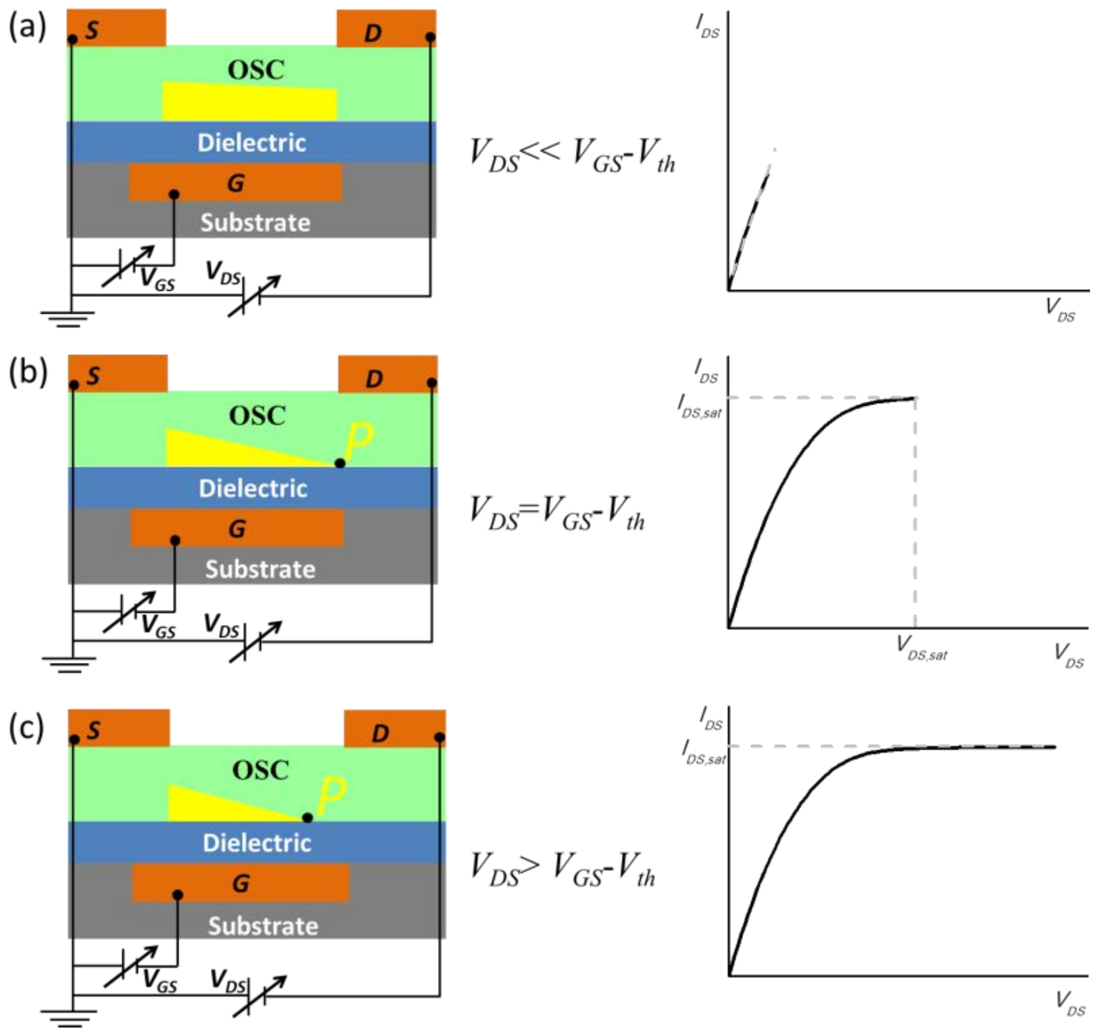

Figure 1.23: Schematic illustration of the charge distribution in the channel and their corresponding *I-V* characteristics in different operating regimes of OFETs at (a) the linear regime, (b) the start of saturation at pinch-off and (c) the saturation regime. [111]

By increasing V_{DS}, the amount of charge carriers near the drain electrode decreases and when the condition $V_{DS}=V_{GS}-V_{th}$ is satisfied, the charge density at the drain electrode is zero and the channel is "pinch off" (*P*) (**Figure 1.23 (b)**). The pinch-off point represents the maximum of I_{DS} even if the drain voltage is further increased ($V_{DS} > V_{GS}-V_{th}$) (**Figure 1.23 (c)**). In this regime, the I_{DS} current reaches a value independent on V_{DS}, and the transistor is operating in saturation regime. The saturation current ($I_{DS,\ sat}$) can be obtained through the following equation:[110]

$$I_{DS,sat} = \frac{W\mu C_i}{2L}(V_{GS} - V_{th})^2 \qquad \text{if} \qquad (V_{DS} > V_{GS}-V_{th}) \qquad (1.2)$$

OFET characterization is based on two typical current-voltage characteristics, namely transfer and output characteristics. In the output characteristics, I_{DS} current is modulated as a function of V_{DS} for different gate voltages. A typical output characteristic is displayed in **Figure 1.24 (a)**, where the linear regime (low V_{DS}) and the saturation regime (high V_{DS}) are evidenced.[110] The dashed line in the graph represents the onset of saturation for each gate voltage. In the transfer characteristics, the I_{DS} current is recorded by sweeping the V_{GS} at a constant V_{DS}. A typical OFET response recorded in linear and saturation regimes is shown in **Figure 1.24 (b)** and **(c)** where the right y-axis display I_{DS} in a log-lin scale since the I_{DS} can vary over several orders of magnitude.

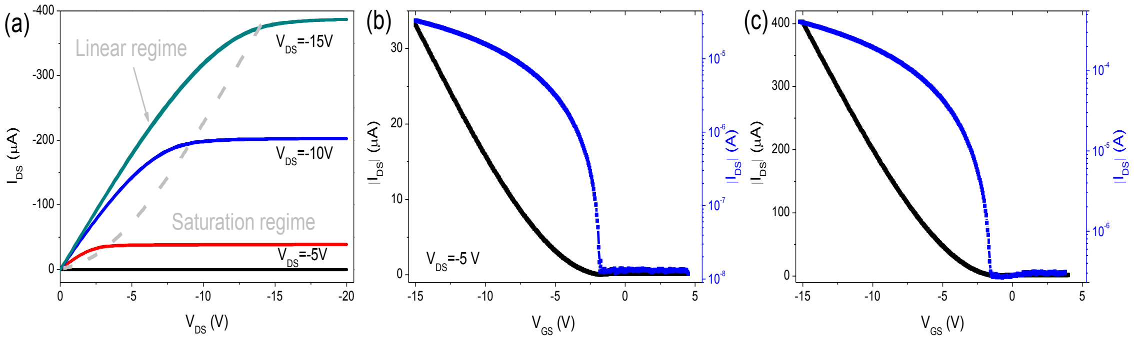

Figure 1.24: (a) Typical output characteristics of an OFET with indications of the linear and saturation regimes. Typical transfer characteristics of an OFET recorded in (b) linear and (c) saturation regimes.

1.3.3 OFET Parameters and Device Performance

OFET is a multi-parametric device and the electrical performance can be characterized by many factors which represent the figures of merits of the device and are normally evaluated in order to understand device quality and performance. Field-effect mobility, threshold voltage, switch-on voltage, on/off ratio, subthreshold swing and hysteresis are the parameters hereby discussed.

Field-effect mobility

The field-effect mobility (μ) is defined as the average drift velocity of the charge carriers in a material under an electric field. At low electric fields, the velocity appears constant and it is linearly dependent on the field magnitude so, charge carrier mobility (μ) is given by:

$$\mu = \frac{|v|}{|E|} \tag{1.3}$$

where v is the average drift velocity of charge carriers and E is the applied electric field. As a consequence, the unit is cm^2 v^{-1} s^{-1}. However, the linear relationship between the drift velocity and applied electric field is no longer valid at high electric field (at fields in excess of ~ 10^5 V cm^{-1})[107] and it displays a non-linear behavior.

In an OFET, this value should be close to the intrinsic mobility of the OSC material but real devices always display lower values due to the presence of defects and parasitic resistances. As a consequence, it is common to observe large fluctuations of μ according to OFET architecture and quality of OSC thin film, which in turn, make the comparison of measurements performed under different conditions not straightforward.

Field-effect mobility is evaluated from equations 1.1 and 1.2 in the linear and saturation regimes, respectively and μ can be extracted from the derivative of the I_{DS} *vs.* V_{GS} according to:

$$\mu_{FE,lin} = \frac{L}{WC_i|V_{DS}|}\left(\frac{\partial I_{DS,lin}}{\partial V_{GS}}\right)_{V_{DS}=const} \tag{1.4}$$

$$\mu_{FE,sat} = \frac{2L}{WC_i}\left(\frac{\partial\sqrt{I_{DS,sat}}}{\partial V_{GS}}\right)^2_{V_{DS}=const} \tag{1.5}$$

for the linear and saturation regime, respectively. An alternative method consists in the extraction of the slope of the linear part of I_{DS} *vs.* V_{GS} plot which represents a good approximation but lacks of any information about the dependence of μ_{FE} on V_{GS}.

Threshold voltage and switch-on voltage

In conventional MOSFETs theory, the threshold voltage (V_{th}) is defined as the onset of the *strong inversion*[i]. However, this behavior does not characterize organic transistor which are unipolar and operate in *accumulation mode*[ii]. Despite this difference, the term threshold voltage is generally borrowed by OFET community to specify the gate voltage at which the current increases at the onset of charge carrier accumulation. In general, a V_{th} close to zero is desirable but charge trapping and unintended doping usually shift this value. A widely used method to determine V_{th} consists in prolonging

---

[i] In classical MOSFET theory the inversion represents a region close to the dielectric where the *n*-type carriers are converted into *p*-type carriers due to the large electric field across the Metal-Insulator-Semiconductor structure. This operation mode is very specific for crystalline silicon.

[ii] The accumulation regime in a OFET is defined as the creation of a conducting channel near the dielectric interface when a negative (or a positive) gate-source bias is applied to a *p*-channel transistor (or *n*-channel transistor).

the linear part of the $|I_{DS}|^{1/2}$-V_{GS} plot in the saturation regime (or the linear part of I_{DS}-V_{GS} plot recorded in linear regime) till the V_{GS} axis, as shown in **Figure 1.25**. However, deviations from linearity in the $|I_{DS}|^{1/2}$-V_{GS} plot are common in real devices due to the dependence of field-effect mobility on gate voltage which makes it difficult the extraction of this parameter. As a consequence, this value strongly depends on the V_{GS} range employed and it remains a purely empirical parameter.

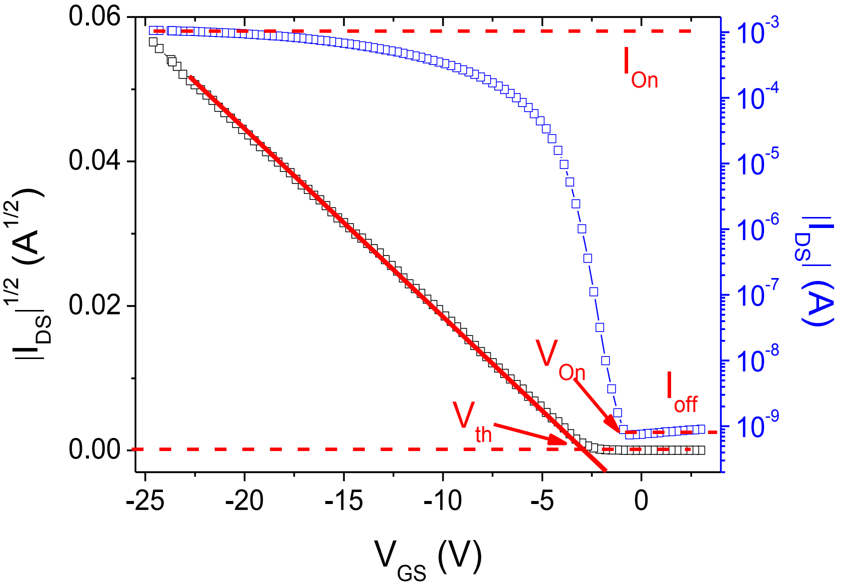

Figure 1.25: OFET parameters extraction shown in a typical transfer curve measured in the saturation regime.

The switch on voltage (V_{on}) is defined as the V_{GS} at which the conductive channel starts to form and it can be extracted from the *Log* (I_{DS})-V_{GS} plot, as shown in **Figure 1.25**. Below $|V_{on}|$, no gate voltage dependence of I_{DS} is observed, while I_{DS} abruptly increase for V_{GS} values above the V_{on}. In an ideal OFET, there should be no difference between the V_{th} and V_{on}, and both parameters should be zero.

On/off ratio

When contact resistance effects at the OSC/electrodes interface are neglected, on current (I_{on}) mainly depends on the mobility of the OSC and on the capacitance of the gate dielectric so high on-current usually reflects high electrical performance. On the contrary, a low off current (I_{off}) reflects the quality and the purity of the active OSC material and, under ideal conditions, it is mainly determined by gate leakage current

(I_{GS}). This assumption defines the On/Off ratio (I_{on}/I_{off}) of an OFET which is a technological parameter defining the switching efficacy of the OFET. High I_{on}/I_{off} ratios are normally desired because characterizes the amplification capability of the device. In **Figure 1.25**, the two parameters are evidenced.

Subthreshold swing

The subthreshold region corresponds to the I_{DS}/V_{GS} response at a gate voltage below the threshold voltage. The importance of this region relies on its information regarding the effectiveness of the charge accumulation process after the application of a gate voltage. The subthreshold swing (*SS*) is a parameter that quantifies how sharply the device is switched on by the gate voltage and, by definition, is the voltage necessary to increase the source-drain current one order of magnitude as described by:[110]

$$\mathrm{SS} = \frac{\partial \mathrm{V}_{GS}}{\partial(\log I_{DS})} \qquad (1.6)$$

Small value of *SS* would permit the switch of the device within a small voltage changes and hence, with a reduction of the power consumption of the device. In addition, *SS* is a good indicator of the density of traps present at the OSC/dielectric interface.

Hysteresis effect

Hysteresis is an undesired effect of OFET characteristics and it can be evaluated from the difference of I_{DS} values at the same V_{GS} during the forward and backward scans of the transfer characteristic. Hysteresis can appear as “clock-wise” or “anticlock-wise” according to the higher or lower current of the backward scan compared to the forward one and it strongly depends on the measurement parameters, *i.e.* sweep rate, the step width, the delay time, *etc.*[112] In addition, many physical effects can cause hysteresis in the electrical response, such as charge trapping at the OSC/dielectric and OSC/electrode interfaces or slow reaction of mobile charge carriers.[112] Thus, it is mandatory an accurate control of the surfaces of the device during the fabrication process in order to achieve a well formed OSC layer and avoid the presence of traps and defects.

1.4 Electrolyte-Gated Organic Field-Effect Transistors

OFETs have a great potential for replacing silicon-based electronics due to their versatility in terms of materials and for their possible application in flexible electronics. However, like their inorganic counterpart, OFETs operate at high voltage because their architecture is still linked to conventional dielectrics like SiO_2, PMMA, cytop, etc.,[113] which possess dielectric constants ranging from several nF to hundreds of nF limiting their application as low power devices.[114]

This constraint can be overcome by replacing conventional insulators (*e.g.* SiO_2 and polymers) with electrolytes where an electrical double layer (EDL) forming at the electrolyte/OSC interface can effectively serve as dielectric.[113–116] The devices are called electrolyte-gated organic field-effect transistors (EGOFETs) and they can operate with a significant reduction of the operation voltage (typically < 2 V) according to the electrochemical stability window of the electrolyte.[114] An electrical double layer has a thickness of tens of Angstrom and possesses a capacitance on the order of 1 -10 μF cm^{-2}.[117,118] EGOFETs are gaining attention due to their capability of work in aqueous electrolytes, of great interest for applications in the field of biosensing and bioelectronics.[113,119,120]

The following section deals with a detailed description of the EGOFETs, including the electrolyte materials, the operation mechanism and their possible applications.

1.4.1 Electrolyte

An electrolyte is a solution that generally contains ions, atoms or molecules which determines its electrical conductivity. The neutrality of an electrolyte is determined by the presence of a species which dissociate into cations and anions. Based on the degree of dissociation, electrolytes can be divided into two categories: (i) strong electrolyte where the species can totally or almost completely dissociate, and (ii) weak electrolyte where the dissociation is partial. Another important distinction is based on the physical state of the electrolytes, liquid and solid/quasi-solid-state are the two important classes of electrolytes.[121,122] Furthermore, according to the solvent employed, liquid electrolytes can be grouped into aqueous electrolytes, organic electrolytes and ionic liquids, whereas the solid or quasi-solid state electrolytes can be differentiate according to their nature (*i.e.* organic or inorganic). A brief resume of the abovementioned characteristic is displayed in **Figure 1.26**.

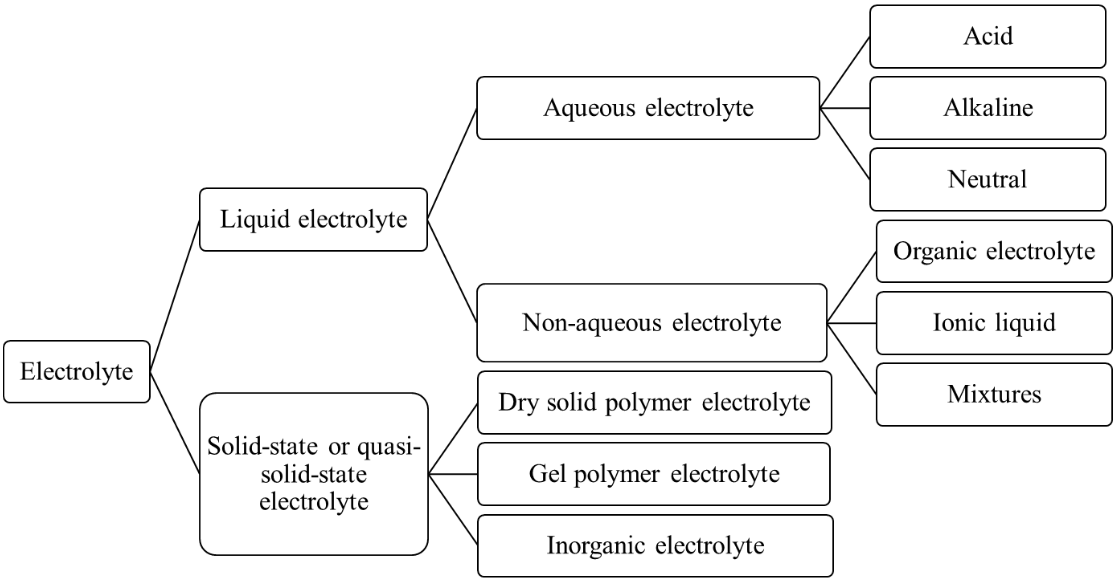

Figure 1.26: Classification of electrolytes.[121]

In general, electrolytes have a wide range of applications, starting from biomedicine to energy conversion and storage.[121,123] For instance, electrolytes are fundamental for balancing several body functions starting from muscles contraction till the movement of water throughout the whole body.[124] In addition, electrolytes are key components in batteries and supercapacitors where an intense research is ongoing in order to find possible alternatives to Li-ions batteries.[121]

Water is surely the most attractive option as working electrolyte due to its abundance, easy availability and environmental impact. In recent years, several EGOFETs have been reported based on different classes of electrolytes (*i.e.* electrolytic solutions, ionic liquids, ion gels, polyelectrolytes and polymer electrolytes) but the first example of a water-based EGOFET dates back to 2010 when Kergoat *et al.*[116] demonstrated the field-effect operation of a P3HT OFET gated by ultrapure water. This working electrolyte, in fact, has another interesting advantage compared to ion gels or organic electrolytes which is the capability to turn the device itself into a biochemical transducer.[116,120] Phosphate-buffered saline (PBS), 4-(2-hydroxyethyl)-1-piperazineathanesulfonic acid (HEPES) and in general any saline buffer are the common media for any biological application and the use of water or aqueous based electrolyte can change a conventional electronic component like an OFET into a real bioelectronics platform.[113,120]

Pure water itself is actually a weak electrolyte and its dissociation equilibrium can be described by the following self-ionization reaction:

$$H_2O + H_2O \rightleftharpoons OH^- + H_3O^+.$$

At room temperature, the conductivity of ultrapure water is 5.5 µS m^{-1} [125] but the exposure to air increase its acidity and hence its conductance due to the dissolution of the CO_2 from atmosphere.[122]

Water has a limited electrochemical window delimited by the hydrogen evolution reaction occurring around 0 V *vs.* standard hydrogel electrode (SHE) and the oxygen evolution at a positive potential of 1.23 V *vs.* SHE.[122,126]

When a salt, like sodium chloride (NaCl) is dissolved into the water its conductivity increases due to the dissociation equilibrium of the salt and the two resulting ions become hydrated by water molecules due to electrostatic interactions.

Salt solutions and buffers have been demonstrated to be suitable for EGOFETs sensors especially when protein and antibodies are employed.[127–130] As demonstrated by Casalini *et al.*[127,128] and Torsi *et al.*,[129,130] EGOFETs can turn into ultrasensitive platform for the detection of relevant proteins and biomarkers, however, the use of a proper electrolyte is fundamental in order to keep intact the functionality of the bio-recognition agent.

Hydrogels can be envisioned as water in a solid form because they are constituted of a polymeric network capable to swell a large amount of water due to the numerous hydrogen bonds forming during the gelling process.[131–133] Therefore, these materials can be considered “electrolytes in the form of a gel” and their application as dielectric on EGOFETs has already been demonstrated. Back in 2015, Dumitru *et al.* reported the use of calcium alginate beads as working electrolyte which performance are comparable with an analog liquid electrolyte.[134] The use of hydrogels as dielectric media for EGOFETs is still at its early days but has plenty room of improvements due to the several applications of these materials in the field of biology and biomedicine, like cell culturing and differentiation and sensing.[131,133]

1.4.2 Electrical Double Layers

As mentioned before, the electrical double layers (EDLs) formation at the OSC/electrolyte and electrolyte/gate electrode interfaces is the main reason behind the reduction of the operation voltage in the EGOFETs compared to the conventional OFETs.[113] An EDL forms when a solid electrode is in contact with an electrolyte leading to a rearrangement of the ions at the surface of the electrode.[56,118]

Several phenomenological models have been proposed to describe the structure of the EDL, but the Gouy-Chapman-Stern (GCS) theory, schematized in **Figure 1.27** is the most adopted.[56,117,118] According to this model, the EDL contains two different layers, namely the Stern layer and diffusion layer. The former consists of adsorbed dipole-oriented solvent molecules and solvated ions of opposite charge compared to the electrode where the first layer of adsorbed solvent molecules is called as “inner Helmholtz plane”, while the “outer Helmholtz plane” correspond to the center of the solvated ions. The latter instead, is the bulk of the electrolyte where ions and counter-ions extend relatively far into the electrolyte.[56,117]

The electrode and the “outer Helmholtz plane” is effectively a parallel plate capacitor where the distance of the two plates is in the order of several Angstroms. As a consequence, the potential drop across this layer is linear and very steep. On the contrary, in the diffuse layer, ions obey a Boltzmann distribution. Therefore, the potential drops exponentially. In addition, the diffuse layer would be compressed with increasing the concentration of the electrolyte due to the Boltzmann distribution.[117,118]

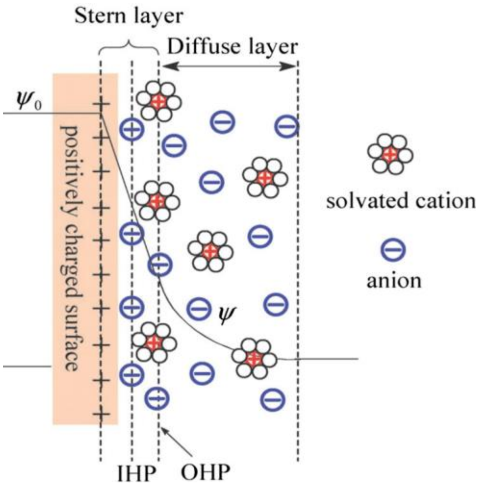

Figure 1.27: Schematic representation of EDL structure according to the GCS model.[117]

According to the GCS model, the capacitance of a single EDL consists of two contributions in series, as described in following equation:[118]

$$\frac{1}{C_S} = \frac{1}{C_S^{St}} + \frac{1}{C_S^{D}},$$

where C_S is the capacitance of EDL, C_S^{St} is the capacitance of Stern layer and C_S^{D} is the capacitance of diffuse layer. The C_S^{St} and C_S^{D} can be obtained by the following two equations:[118]

$$C_S^{St} = \frac{\varepsilon_r\varepsilon_0}{d} \text{ and } C_S^{D} = \frac{4zeN_AC_\infty\lambda_D}{\psi_D}\sinh(\frac{ze\psi_D}{2k_BT}),$$

where d is the thickness of the layer, ε_r is the relative permittivity, ε_0 is the permittivity of vacuum, z is the valence of the electrolyte, e is the elementary charge, N_A is Avagadro's number, C_∞ is the molar concentration of the electrolyte in the bulk, Ψ_D is the electric potential in the diffuse layer, T is the absolute temperature, k_B is the Boltzmann constant, and λ_D is the Debye length defined as $\lambda_D = \sqrt{\varepsilon_r\varepsilon_0k_BT}/\sqrt{2z^2e^2N_AC_\infty}$.

Due to its small thickness and the high concentration of the adsorbed ions, the EDL possesses a large capacitance (in the order of tens μF cm^{-2}).[113,117,118,135] Furthermore, the nature of the electrolyte solution, such as its ionic strength and the ion charge and size, has a significant influence on EDL formation, and in turn, on its capacitance and potential profile.[56,136] For example, M. A. Brown *et al.* demonstrated that the average thickness of the Stern layer becomes thinner as the electrolyte concentration is increased, leading to an increase of the surface charge density and of its capacitance.[56] In addition, by using accurate numerical simulation, Pilon *et al.* reported the influence of the ion size on the EDL capacitance, that it was observed to increase with decreasing the ion size.[136]

However, a remarkable difference is observed between a conventional dielectric and an electrolyte as evidenced from **Figure 1.28** where the voltage profiles and the distribution of electric fields in the two cases are reported.[46,137] In a conventional dielectric, the electrostatic potential drops gradually and upon application of a voltage, a uniform and constant electric field is generated. In the case of an electrolyte, the applied voltage drops just near the interfaces due to the formation of an EDL, while in the bulk the potential profile is constant. Therefore, the high electric field is only concentrated near the interfaces and it has a value on the order of 10^9 V m^{-1} and it drops to negligible values in the bulk.[46]

This peculiarity has increased the interest of the scientific community towards the creations of sensitive transducer by taking advantage of one of the two EDLs present in the EGOFET that result to be the most sensitive part of the whole architecture. In the next sections some sensors based on EGOFETs are described where one of these two interfaces is exploited for detecting ultra-low analyte concentrations.

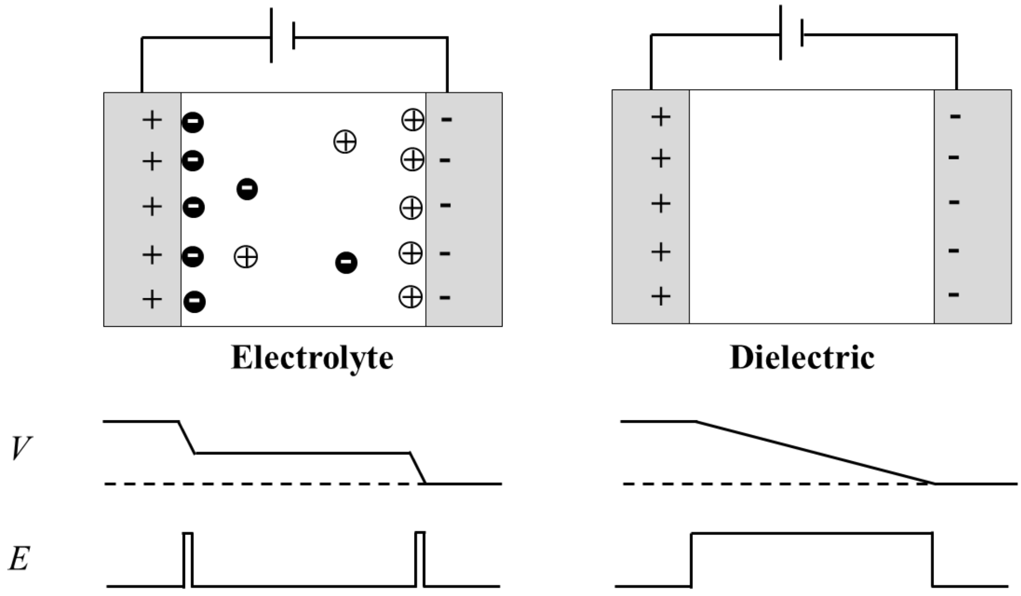

Figure 1.28: Schematic illustrations of the charge distribution, electric potential (V) and electric field (E) in the capacitor based on electrolyte layer (left) and a conventional dielectric layer (right).[46]

1.4.3 Operation Principle and Possible Applications

Once the conventional dielectric is replaced by an electrolyte, the so-called electrolyte-gated organic field-effect transistor is realized. As shown in **Figure 1.29**, the EGOFET consists of *S* and *D* electrodes and an OSC channel in electric contact with a *G* electrode *via* an electrolyte that is commonly confined through a PDMS pool.[135] For a *p*-type EGOFET, the anions of the electrolyte accumulate at the electrolyte/OSC interface while the cations migrate and accumulate at the electrolyte/gate interface due to the application of a negative V_{GS}, resulting in the formation of two EDLs at both interfaces. Holes can, therefore, accumulate at the semiconductor region and due to the high capacitance, thus high charge carrier densities can be achieved permitting the low operation voltage of the device. A typical *I-V* transfer characteristic of EGOFETs recorded in saturation regime is shown in **Figure 1.30**. Their electrical response is usually treated with the classical MOSFET theory as commonly done for OFETs,[106] which counts on different figure of merits (*i.e.* threshold voltage (V_{th}), mobility (μ), drain-source current (I_{DS})) evidenced in the graph.

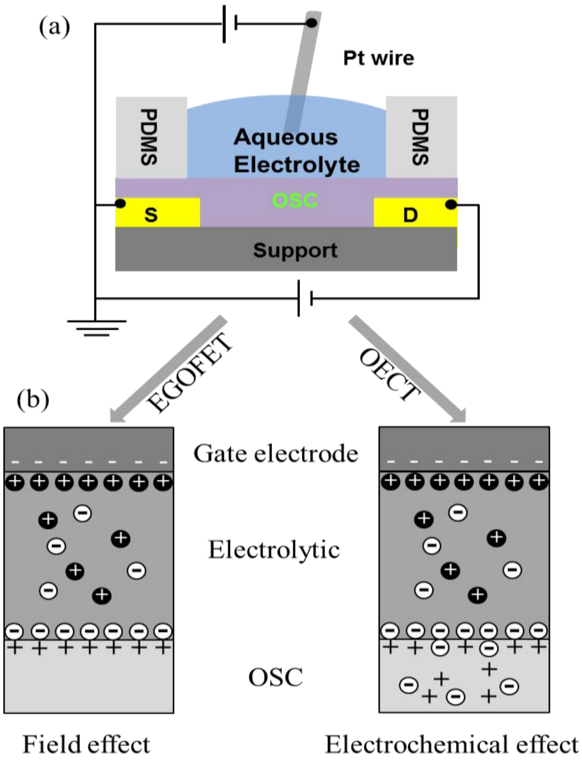

Figure 1.29: (a) BCTG architecture of an electrolyte-gated transistor. (b) Diagram of an electrolyte-gated OSC film in field effect mode (left) and electrochemical mode (right).[138]

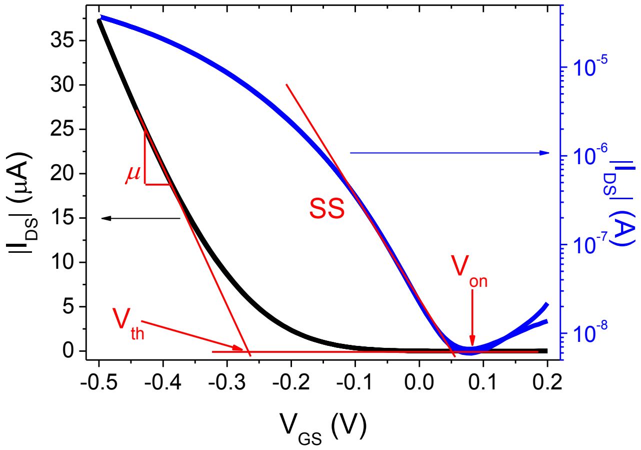

Figure 1.30: EGOFET parameters extraction shown in a typical transfer curve in saturation regime.

Since organic semiconductors cannot be considered completely impermeable to ions, current modulation in electrolyte-gated transistors can result from two gating mechanisms: field-effect mode and electrochemical mode, which is associated with the operation mode of Organic Electrochemical Transistors (OECTs).[114,138] As mentioned above, the first demonstration of a water-gated OFET (WGOFET) was from Kergoat *et al.* in 2010 who supported the field effect operation of their P3HT-based EGOFET with the two following evidences:[116] (1) a fast response speed (~ 4.6 ms) in response to a gate voltage modulation accompanied by a negligible hysteresis and (2) the narrow operation window (*i.e.* < 1 V) where no electrochemical reaction has been observed both in the I_{DS} and I_{GS}. However, later in 2017, Giridharagopal *et al.* demonstrated through AFM that P3HT can allow both types of operations according to the crystallinity of the thin film.[139] Amorphous regions, in fact, were demonstrated to be prone to electrochemical doping while crystalline domains were operating in field effect mode.[140]

Despite the intense research on this field, a solid physical model for describing EGOFETs still does not exist and their operation mechanism remain purely phenomenological. Nonetheless, the OSC/electrolyte and electrolyte/gate interfaces represent the most sensitive part of the device and any tiny change in their surface potential and/or capacitance is amplified in the transistor electrical response.[135] In addition, when the EGOFET is operated in aqueous media it can open up to a series of applications in the field of biology and sensing just by the addition of a specific functionality.[120] Several authors have modified EGOFETs interfaces in contact with the medium by using specific molecules or functional groups including Self-Assembled Monolayers (SAMs) or by incorporating biological receptors.[120141]

In 2012, Buth *et al.* reported a EGOFET sensor able to detect penicillin.[141] In this case, the recognition agent, *i.e.* the enzyme penicillinase, was added to the OSC/electrolyte interface by functionalizing the top surface of the OSC with 3-aminopropyltriethoxysilane (APTES) due to the creation of hydroxyl groups *via* UV activation (**Figure 1.31**). Their proof-of-concept device had a limit of detection (LoD) of ca. 5 µM towards penicillin. A similar approach was also developed by Torsi *et al.* through the modification of P3HT surface with plasma enhanced vapor chemical deposition (PE-CVD).[142] The authors have further incorporated a phospholipid (PL) layer and detected streptavidin protein with a LoD of 10 nM. The high sensitivity of the sensor was attributed to the capacitive effect across the PL bilayer, involving the charges carried by streptavidin.[129]

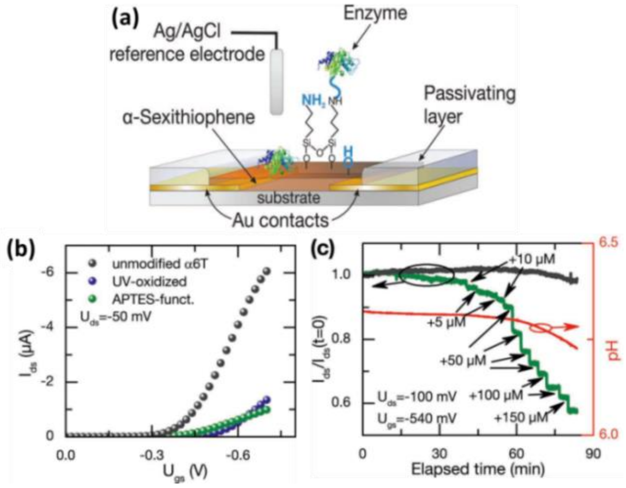

Figure 1.31: (a) Schematic illustration of the transistor layout and its functionalization steps. (b) Transfer curves of untreated, UV-oxidized and APTES-functionalized transistors recorded at pH=5. (c) I_{DS} *vs.* time test during a penicillin titration in PBS buffer. Reproduced with permission from ref. 141. Copyright © 2012 John Wiley & Sons.

Although this approach has revealed suitable for the incorporation of antibodies, enzymes and other biomolecules demonstrating good sensitivity, it inevitably affects the organic semiconductor and the reliability of the transducer.

On the other hand, several groups have mainly focused on the functionalization of the gate electrode. In 2015, Torsi *et al*. fabricated a sensor of unprecedented sensitivity with a LoD of 10 pM by modifying the gate electrode of the EGOFETs with the receptor for carvone enatiomers, odorant molecules.[130] The author anchored the receptor to the Au gate by means of a self-assembled monolayer and a capacitive modulated transduction was governing the sensor response.[130]

The functionalization of the gate electrode was also reported by Casalini *et al.*[128] who developed an Interleukin-4 (IL4) EGOFET-sensor by immobilizing IL4 antibodies. As depicted in **Figure 1.32**, the importance of the functionalization strategy on the sensitivity of the platform was pointed out and it exhibited a LoD of ca. 5 nM.[128]

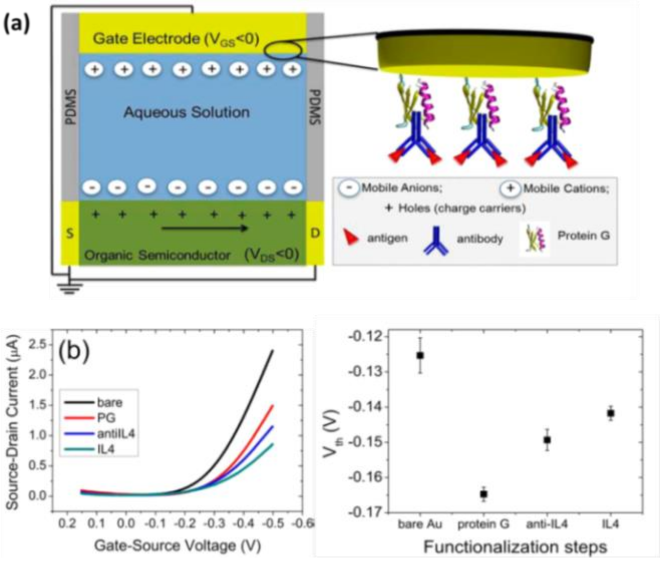

Figure 1.32: (a) Schematic illustration of EGOFET cross section along with a sketch of the magnification of the electrolyte/gate interface. (b) *I-V* transfer characteristics of PG-based protocols and its corresponding V_{th} trends according to the stepwise functionalization. Reproduced with permission from ref. 128. Copyright © 2015 American Chemical Society.

Beside bio-sensing application, EGOFETs have also employed as platform to detect metal ions and for the study of monolayer formation in aqueous media. As shown in **Figure 1.33**, Nguyen *et al.* reported a Cu^{2+} sensor by using gate area as sensing element, which has been previously functionalized with a Gly-Gly-His peptide layer.[143] The LoD of this EGOFET sensor is ca. 10^{-12} M and its sensitivity in the linear range (10^{-12} ~ 10^{-8} M) is 1 mA dec^{-1}.

In all these examples, the subsequent addition of biomolecules, *i.e.* the bio-receptor and the analyte, affects the electrical response of the EGOFET in a two-fold manner: primarily affecting the capacitance at the gate electrode/electrolyte interface and in addition, by shifting the surface potential of the electrode due to their inherent changes.

Although it is difficult to discern the degree of contribution caused by these two effects, EGOFETs can represent a valuable route for the fabrication of novel biosensors due to their versatility and sensitivity.

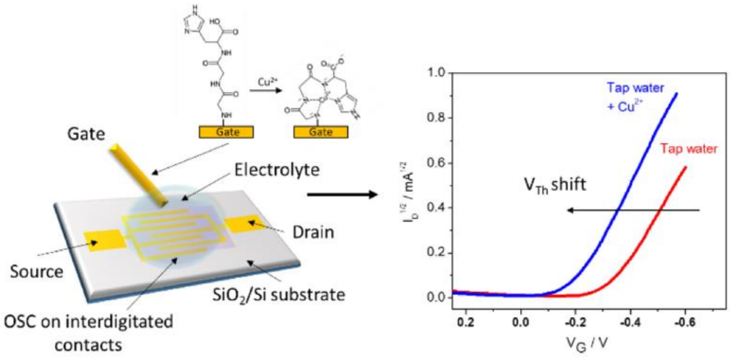

Figure 1.33: (Left) Schematic representation of the architecture of EGOFETs and the GGH-functionalization of the gate electrode. (Right) The *I-V* transfer characteristics of this EGOFETs before and after Cu^{2+} detection. Reproduced with permission from ref. 143. Copyright © 2018 Elsevier B. V.

1.4.4 State-of-the-Art of EGOFETs

Although employing EGOFETs provides many advantages for the development of multi-functional platforms interesting in the field of sensing events occurring in aqueous media, some unsolved problems are actually hindering their technological transfer, such as the poor electrical stability. Water and oxygen are aggressive media for OSC materials and since OSCs are high polarizable molecules, they can acts as trap centers.[135,144,145] The direct consequence is an electrical performance degradation already extensively reported for common OFETs. Thus, many efforts have been spent for improving the device quality. However, many reports often deal with proof-of-concept devices suitable for point of care testing while long time recording and robustness under continuous electrical stress still remain elusive.[106]

The obtainment of a robust and efficient device is crucial for the future applications of this technology outside a laboratory environment. In **Table 1.1** recent progresses of EGOFETs in terms of their active OSC materials, OSC deposition methods and main electrical output are summarized. It should be highlighted that all the OSC materials presented here were deposited by spin-coating or by Ultra High Vacuum deposition, which are not appealing in terms of upscaling and large area fabrication. According to this table, a groundbreaking EGOFETs must encompass all the following characteristics: (i) $\mu \geq 0.1$ cm^{2}V^{-1}s^{-1},[146] (ii) high on/off ratio $\geq 10^3$,[116] (iii) a potentiometric sensitivity in the range of μV,[147] (iv) operational frequency (*f*) higher than 200 Hz[147] and (v) capable to withstand prolonged (*i.e.* from hours to days) electrical stresses.[148,149] Undoubtedly, a high degree of crystallinity along with an extended homogeneity at long-range length scales (*i.e.* from few to hundreds of micrometers) is fundamental to achieve high performance EGOFETs. Therefore, the fabrication issues related to EGOFETs, the choice of the OSC and its consequent processing are pivotal.

Table 1.1: Summary of the state-of-the-art of EGOFETs.

Material	Electrolyte	Technique*	μ (cm^{2}V^{-1}s^{-1})	V_{th} (mV)	*SS* (mV/dec)	I_{On}/I_{Off}	τ (ms)	Ref
Rubrene (crystal)	Water	PVD	6.7×10^{-2}	-90	-	8×10^4	-	116
P3HT	Water	SP	3.9×10^{-3}	-200	-	160	τ_{ON}=50 τ_{OFF}=10	116
P3HT/PMMA	Water	SP	1.2×10^{-1}	250	-	$<10^3$	-	146
P3HT/phospholipid membranes	Water	SP	1.5×10^{-3}	-40	-	318	-	150
P3HT/PL membranes	$LiClO_4$ 5mM	SP	6.4×10^{-3}	-50	-	1135	-	150
P3HT/PL	KCl 100 mM	SP	1.2×10^{-2}	100	-	130	-	151
P3HT/ion-selective membrane	NaCl 10 mM	SP	2×10^{-2}	100	-	$\sim10^2$	-	152
P3HT/biotin bilay	Water	SP	7.3×10^{-3}	-100	300	~500	-	153
PII2T-Si	Water	SP	4.0×10^{-3}	-730	~100	>650	-	149
PII2T-Si	NaCl 10 µM	SP	1.4×10^{-3}	-720	-	>150	-	149
PII2T-Si (on flexible)	Seawater	SP	5.0×10^{-3}	-750	-	>380	-	149
pBTTT (on glass slide)	Water	SP	8×10^{-2}	~ 0	520	$>10^2$	-	154
α-sexithiophene	KCl 50 mM	PVD	2.2×10^{-2}	-	-	-	-	155
pBTTT-C14(flexible)	Water	SP	1.1×10^{-1}	-	-	-	-	130
CuPc (on glass slide)	Water	PVD	1.2×10^{-3}	100	≤100	$\sim10^3$	≥300	156
pentacene	Water	PVD	1.3×10^{-2}	-100	-	$\sim10^4$	~4.6	157
pBTTT	PBS 10 mM	SP	3.3×10^{-2}	-70	-	10^3	-	158
pBTTT/PAA	PBS 10 mM	SP	3.6×10^{-3}	-90	-	10^2	-	158
PNDIT2 (n-type)	Water	SP	3.7×10^{-3}	170	-	-	-	159
PNDISVS	Water	SP	1.9×10^{-2}	490	-	-	-	159
PCBM	Water	SP	7×10^{-3}	180	-	-	-	159

*PVD refers to physical vapor deposition and SP stands for spin coating.

1.5 Objective of This Thesis

As anticipated before, blending organic semiconductors with insulating polymer has revealed a valuable route for the fabrication of outperforming OFETs due to the several advantages of this approach: the reduction of the OSC material, the improved viscosity that allows the deposition of homogeneous films especially in the case of small molecules semiconductors, the higher crystallinity of the thin film, the vertical phase separation that can permit dielectric passivation and eventually, the self-encapsulation of the active material.

This thesis is focused on the fabrication of high performance EGOFETs by exploiting this blending approach in conjunction with a roll-to-roll compatible technique, *i.e.* BAMS. Different OSC: polymer blends have been selected and tested by employing EGOFET architecture and two applications have been developed: *i)* an EGOFET serving for the detection of Hg^{2+} ions in aqueous solution and *ii)* the use of agarose gel to replace the liquid medium in the EGOFET architecture for the development of a pressure sensor.

More specifically, the main objectives of this thesis are:

i. Study and development of state-of-the-art EGOFETs by selecting different OSC:insulating polymer blends processed through BAMS. Investigation of their morphology and electrical performance (including the transfer and output characteristics, potentiometric sensitivity *etc*.) in MilliQ water and high ionic strength solutions aims to select the best EGOFET device.

ii. Development of a Hg^{2+} ion sensor based on an EGOFET based on an OSC/polymer blend. Study of the interaction of this ion with the active transporting material and determination of the sensitivity and selectivity of the device.

iii. Fabrication of a solid electrolyte EGOFET by replacing the conventional liquid electrolyte with a water-based hydrogel. Study of the performance of the resulting device towards mechanical pressure.

Bibliography

1. W. B. Shockley, J. Bardeen. and W. H. Brattain. Nobel Prize in Physics 1956. Available at: https://www.nobelprize.org/prizes/physics/1956/summary/.
2. Tanenbaum, M. *Bell Labs Notebook*. (1954).
3. Tanenbaum, M., Valdes, L. B., Buehler, E. & Hannay, N. B. Silicon n-p-n Grown Junction Transistors. *J. Appl. Phys.* **26,** 686–692 (1955).
4. D. Kahng, M. M. A. Silicon-silicon dioxide field induced surface devices. in *IRE Solid-state Devices Research Conference, Pittsburgh, PA* (1960).
5. Zhang, T. *et al.* Flexible electronics: Thin silicon die on flexible substrates. *IEEE Trans. Electron. Packag. Manuf.* **32,** 291–300 (2009).
6. Pope, M. & Swenberg, C. E. *Electronic Processes in Organic Crystals and Polymers*. (Oxford University Press, 1999).
7. Clayden, J., Greeves, N. & Warren, S. *Organic Chemistry*. (Oxford University Press, 2012).
8. Meller, G. & Grasser, T. *Organic Electronics*. (Springer-Verlag Berlin Heidelberg, 2010).
9. Mulliken, R. S. Overlap Integrals and Chemical Binding. *J. Am. Chem. Soc.* **72,** 4493–4503 (1950).
10. Harver, R. G. *Polycyclic Aromatic Hydrocarbons*. (WILEY VCH, 1997).
11. Anderson, P. W., Lee, P. A. & Saitoh, M. Remarks on Giant Conductivity in TTF-TCNQ. *Solid State Commun.* **13,** 595–598 (1973).
12. Shirakawa, H., Louis, E., MacDiarmid, A., Chiang, C. & Heeger, J. Synthesis of Electrically Conducting Organic Polymers : Halogen Derivatives. *Chem. Commun.* 578–580 (1977).
13. Heeger, A. J., MacDiarmid, A. G. & Shirakawa, H. Nobel Prize in Chemistry 2000. Available at: http://nobelprize.org/nobel_prizes/chemistry/laureates/2000/press.html.
14. Bernius, M. T., Inbasekaran, M., O'Brien, J. & Wu, W. Progress with light-emitting polymers. *Adv. Mater.* **12,** 1737–1750 (2000).

15. Friend, R. H. *et al.* Electroluminescence in Conjugated Polymers and Fullerenes. *Nature* **397,** 121–128 (1999).
16. Tang, C. W. & Vanslyke, S. A. Organic electroluminescent diodes. *Appl. Phys. Lett.* **51,** 913–915 (1987).
17. Burroughes, J. H. *et al.* Light-emitting diodes based on conjugated polymers. *Nature* **347,** 539–541 (1990).
18. Grätzel, M. Photoelectrochemical cells Michael. *Nature* **367,** 1262–1270 (2001).
19. Li, C. *et al.* Organic and solution-processed tandem solar cells with 17.3% efficiency. *Science* **361,** 1094–1098 (2018).
20. Tang, C. W. Two-layer organic photovoltaic cell. *Appl. Phys. Lett.* **48,** 183–185 (1986).
21. Heilmeier, G. H. & Zanoni, L. A. Surface studies of α-copper phthalocyanine films. *J. Phys. Chem. Solids* **25,** 603–611 (1964).
22. Burroughes, J. H., Jones, C. A. & Friend, R. H. New semiconductor device physics in polymer diodes and transistors. *Nature* **335,** 137–141 (1988).
23. Horowitz, G., Fichou, D., Peng, X., Xu, Z. & Garnier, F. A field-effect transistor based on conjugated alpha-sexithienyl. *Solid State Commun.* **72,** 381–384 (1989).
24. Mas-Torrent, M. & Rovira, C. Novel small molecules for organic field-effect transistors: Towards processability and high performancens. *Chem. Soc. Rev.* **37,** 827–838 (2008).
25. Geffroy, B., le Roy, P. & Prat, C. Organic light-emitting diode (OLED) technology: Materials, devices and display technologies. *Polym. Int.* **55,** 572–582 (2006).
26. Abdulrazzaq, O. A., Saini, V., Bourdo, S., Dervishi, E. & Biris, A. S. Organic solar cells: A review of materials, limitations, and possibilities for improvement. *Part. Sci. Technol.* **31,** 427–442 (2013).
27. Tsumura, A., Koezuka, H. & Ando, T. Macromolecular electronic device: Field-effect transistor with a polythiophene thin film. *Appl. Phys. Lett.* **49,** 1210–1212 (1986).
28. Gelinck, G., Heremans, P., Nomoto, K. & Anthopoulos, T. D. Organic

Transistors in Optical Displays and Microelectronic Applications. *Adv. Mater.* **22,** 3778–3798 (2010).

29. Cantatore, E. *et al.* Flexible active-matrix displays and shift registers based on solution-processed organic transistors. *Nat. Mater.* **3,** 106–110 (2004).

30. Crone, B. K. *et al.* Design and fabrication of organic complementary circuits. *J. Appl. Phys.* **89,** 5125–5132 (2002).

31. Drury, C. J., Mutsaerts, C. M. J., Hart, C. M., Matters, M. & De Leeuw, D. M. Low-cost all-polymer integrated circuits. *Eur. Solid-State Circuits Conf.* **108,** 30–34 (1998).

32. Dodabalapur, A., Laquindanum, J., Katz, H. E. & Bao, Z. Complementary circuits with organic transistors. *Appl. Phys. Lett.* **69,** 4227–4229 (1996).

33. Baude, P. F. *et al.* Pentacene-based radio-frequency identification circuitry. *Appl. Phys. Lett.* **82,** 3964–3966 (2003).

34. Manunza, I., Sulis, A. & Bonfiglio, A. Pressure sensing by flexible, organic, field effect transistors. *Appl. Phys. Lett.* **89,** 143502 (2006).

35. Pacher, P. *et al.* Chemical control of local doping in organic thin-film transistors: From depletion to enhancement. *Adv. Mater.* **20,** 3143–3148 (2008).

36. Zang, Y., Zhang, F., Di, C. A. & Zhu, D. Advances of flexible pressure sensors toward artificial intelligence and health care applications. *Mater. Horizons* **2,** 140–156 (2015).

37. Zang, Y. *et al.* Flexible suspended gate organic thin-film transistors for ultra-sensitive pressure detection. *Nat. Commun.* **6,** 6269 (2015).

38. Mannsfeld, S. C. B. *et al.* Highly sensitive flexible pressure sensors with microstructured rubber dielectric layers. *Nat. Mater.* **9,** 859–864 (2010).

39. Schwartz, G. *et al.* Flexible polymer transistors with high pressure sensitivity for application in electronic skin and health monitoring. *Nat. Commun.* **4,** 1859 (2013).

40. Zhang, C., Chen, P. & Hu, W. Organic field-effect transistor-based gas sensors. *Chem. Soc. Rev.* **44,** 2087–2107 (2015).

41. Mirza, M., Wang, J., Wang, L., He, J. & Jiang, C. Response enhancement

mechanism of NO2 gas sensing in ultrathin pentacene field-effect transistors. *Org. Electron.* **24,** 96–100 (2015).

42. Xiong, Z. H., Wu, D., Valy Vardeny, Z. &.Shi, J. Giant magnetoresistance in organic spin-valves. *Nature* **427,** 821–824 (2004).
43. Jang, H. J. & Richter, C. A. Organic Spin-Valves and Beyond: Spin Injection and Transport in Organic Semiconductors and the Effect of Interfacial Engineering. *Adv. Mater.* **29,** (2017).
44. Kuehne, A. J. C. & Gather, M. C. Organic Lasers: Recent Developments on Materials, Device Geometries, and Fabrication Techniques. *Chem. Rev.* **116,** 12823–12864 (2016).
45. Moorthy, S. B. K. *Thin film structures in energy applications*. (Springer International Publishing AG Switzerland, 2015).
46. Herlogsson, L. Electrolyte-Gated Organic Thin-Film Transistors. *Linköping University press* (2011).
47. Wang, C. Electronic Structure of pai -Conjugated Materials and Their Effect on Organic Photovoltaics. (Linköping University Electronic Press, 2017).
48. Bao, Z. & Locklin, J. *Organic Field-Effect Transistors*. (CRC Press, 2007).
49. Sinno, H. Polyelectrolyte-Gated Organic Field Effect Transistors - Printing and Electrical Stability. (Linköpings Universitet, 2013).
50. Patil, A. O., Heeger, A. J. & Wudl, F. Optical Properties of Conducting Polymers. *Chem. Rev* **88,** 183–200 (1988).
51. Ciuchi, S. *et al.* Molecular Fingerprints in the Electronic Properties of Crystalline Organic Semiconductors : From Experiment to Theory. *Phys. Rev. Lett.* **108,** 256401 (2012).
52. Venkateshvaran, D. *et al.* Approaching disorder-free transport in high-mobility conjugated polymers. *Nature* **515,** 384–388 (2014).
53. Liu, C. *et al.* A unified understanding of charge transport in organic semiconductors : the importance of attenuated delocalization for the carriers. *Mater. Horizons* **4,** 608–618 (2017).
54. Coropceanu, V. *et al.* Charge Transport in Organic Semiconductors. *Chem. Rev.*

107, 926–952 (2007).

55. Miller, A. & Abraham, E. Impurity Conduction at Low Concentrations. *Phys. Rev.* **123,** 745–755 (1960).
56. Brown, M. A., Goel, A. & Abbas, Z. Electrical Double Layer Effect of Electrolyte Concentration on the Stern Layer Thickness at a Charged Interface. *Angew. Chemie - Int. Ed.* **55,** 3790–3794 (2016).
57. Vissenberg, M. C. J. M. & Matters, M. Theory of the field-effect mobility in amorphous organic transistors. *Phys. Rev. B* **57,** 964–967 (1998).
58. Ortmann, F., Bechstedt, F. & Hannewald, K. Charge transport in organic crystals: Theory and modelling. *Phys. Status Solidi* **248,** 511–525 (2011).
59. Klug, A. Organic Field-Effect Transistors – Process Development, Stability Issues and Sensor Applications. (Technische Universität Graz Betreuer, 2010).
60. Lu, N. *et al.* Charge carrier hopping transport based on Marcus theory and variable-range hopping theory in organic semiconductors. *J. Appl. Phys.* **118,** 045701 (2015).
61. Sirringhaus, H. 25th anniversary article: Organic field-effect transistors: The path beyond amorphous silicon. *Adv. Mater.* **26,** 1319–1335 (2014).
62. Allard, S., Forster, M., Souharce, B., Thiem, H. & Scherf, U. Organic semiconductors for solution-processable field-effect transistors (OFETs). *Angew. Chemie - Int. Ed.* **47,** 4070–4098 (2008).
63. Sirringhaus, H. Device physics of solution-processed organic field-effect transistors. *Adv. Mater.* **17,** 2411–2425 (2005).
64. Wu, W., Liu, Y. & Zhu, D. π-Conjugated molecules with fused rings for organic field-effect transistors: Design, synthesis and applications. *Chem. Soc. Rev.* **39,** 1489–1502 (2010).
65. Sirringhaus, H. *et al.* Two-dimensional charge transport in conjugated polymers. *Nature* **40,** 685–688 (1999).
66. McCullough, R. D. The Chemistry of Conducting Polythiophenes. *Adv. Mater.* **10,** 93–116 (1998).
67. Mcculloch, I. *et al.* Liquid-crystalline semiconducting polymers with high

charge-carrier mobility. *Nat. Mater.* **5,** 328–333 (2006).

68. Yun, H. J., Cho, J., Chung, D. S., Kim, Y. H. & Kwon, S. K. Comparative studies on the relations between composition ratio and charge transport of diketopyrrolopyrrole-based random copolymers. *Macromolecules* **47,** 7030–7035 (2014).

69. Tsao, H. N. *et al.* Ultrahigh Mobility in Polymer Field-Effect Transistors by Design. *J. Am. Chem. Soc.* **133,** 2605–2612 (2011).

70. Wang, S. *et al.* Organic Field-Effect Transistors based on Highly Ordered Single Polymer Fibers. *Adv. Mater.* **24,** 417–420 (2012).

71. Chen, Z. *et al.* High-Performance Ambipolar Diketopyrrolopyrrole- Thieno [3 , 2- b] thiophene Copolymer Field-Effect Transistors with Balanced Hole and Electron Mobilities. *Adv. Mater.* **24,** 647–652 (2012).

72. Gundlach, D. J. *et al.* Contact-induced crystallinity for high-performance soluble acene-based transistors and circuits. *Nat. Mater.* **7,** 216–221 (2008).

73. Lee, S. S. *et al.* Controlling nucleation and crystallization in solution-processed organic semiconductors for thin-film transistors. *Adv. Mater.* **21,** 3605–3609 (2009).

74. Smith, J. *et al.* Solution-processed organic transistors based on semiconducting blends. *J. Mater. Chem.* **20,** 2562–2574 (2010).

75. Lee, W. H. & Park, Y. D. Organic semiconductor/insulator polymer blends for high-performance organic transistors. *Polymers (Basel).* **6,** 1057–1073 (2014).

76. Riera-Galindo, S., Tamayo, A. & Mas-Torrent, M. Role of Polymorphism and Thin-Film Morphology in Organic Semiconductors Processed by Solution Shearing. *ACS Omega* **3,** 2329–2339 (2018).

77. Lei, Y. *et al.* Enhancing Crystalline Structural Orders of Polymer Semiconductors for Efficient Charge Transport via Polymer-Matrix-Mediated Molecular Self-Assembly. *Adv. Mater.* **28,** 6687–6694 (2016).

78. Goffri, S. *et al.* Multicomponent semiconducting polymer systems with low crystallization- induced percolation threshold. *Nat. Mater.* **5,** 950–956 (2006).

79. Stingelin-Stutzmann, N. *et al.* Organic thin-film electronics from vitreous

solution-processed rubrene hypereutectics. *Nat. Mater.* **4,** 601–606 (2005).

80. Niazi, M. R. *et al.* Contact-induced nucleation in high-performance bottom-contact organic thin film transistors manufactured by large-area compatible solution processing. *Adv. Funct. Mater.* **26,** 2371–2378 (2016).
81. Niazi, M. R. *et al.* Solution-printed organic semiconductor blends exhibiting transport properties on par with single crystals. *Nat. Commun.* **6,** 8598 (2015).
82. Del Pozo, F. G. *et al.* Single crystal-like performance in solution-coated thin-film organic field-effect transistors. *Adv. Funct. Mater.* **26,** 2379–2386 (2015).
83. Teixeira da Rocha, C. *et al.* Solution Coating of Small Molecule/Polymer Blends Enabling Ultralow Voltage and High-Mobility Organic Transistors. *Adv. Electron. Mater.* **4,** 1800141 (2018).
84. Temiño, I. *et al.* A Rapid, Low-Cost, and Scalable Technique for Printing State-of-the-Art Organic Field-Effect Transistors. *Adv. Mater. Technol.* **1,** 1600090 (2016).
85. Campos, A., Zhang, Q., Ajayakumar, M. R., Leonardi, F. & Mas-Torrent, M. High Performance Organic Field-Effect Transistor with a Solid and Aqueous Dielectric Based on a Solution Sheared Sulfur-Bridged Annulene Derivative. *Adv. Electron. Mater.* 1700349 (2017).
86. Zhang, K. *et al.* Crystallization Control of Organic Semiconductors during Meniscus-Guided Coating by Blending with Polymer Binder. *Adv. Funct. Mater.* **28,** 1805594 (2018).
87. Malandraki, A. *et al.* Enhanced reproducibility of inkjet printed organic thin film transistors based on solution processable polymer-small molecule blends. *J. Mater. Chem.* **20,** 9155 (2010).
88. Kim, Y. H., Anthony, J. E. & Park, S. K. Polymer blended small molecule organic field effect transistors with improved device-to-device uniformity and operational stability. *Org. Electron.* **13,** 1152–1157 (2012).
89. Pérez-Rodríguez, A., Temiño, I., Ocal, C., Mas-Torrent, M. & Barrena, E. Decoding the Vertical Phase Separation and Its Impact on C8-BTBT/PS Transistor Properties. *ACS Appl. Mater. Interfaces* **10,** 7296–7303 (2018).

90. Lee, W. H. *et al.* The influence of the solvent evaporation rate on the phase separation and electrical performances of soluble acene-polymer blend semiconductors. *Adv. Funct. Mater.* **22,** 267–281 (2012).

91. Lee, W. H. *et al.* Semiconductor-dielectric blends: A facile all solution route to flexible all-organic transistors. *Adv. Mater.* **21,** 4243–4248 (2009).

92. Shin, N. *et al.* Vertically segregated structure and properties of small molecule-polymer blend semiconductors for organic thin-film transistors. *Adv. Funct. Mater.* **23,** 366–376 (2013).

93. Nomoto, K. *et al.* Solution-processed organic thin-film transistors with vertical nanophase separation. *Appl. Phys. Lett.* **93,** 053303 (2008).

94. Sandhage, K. H. *et al.* Solvent and polymer matrix effects on TIPS-pentacene/polymer blend organic field-effect transistors. *J. Mater. Chem.* **22,** 5531 (2012).

95. Li, Y., Sun, H., Shi, Y. & Tsukagoshi, K. Patterning technology for solution-processed organic crystal field-effect transistors. *Sci. Technol. Adv. Mater.* **15,** 024203 (2014).

96. Gu, X., Shaw, L., Gu, K., Toney, M. F. & Bao, Z. The meniscus-guided deposition of semiconducting polymers. *Nat. Commun.* **9,** 534 (2018).

97. Kymissis, I. *Organic Field Effect Transistors Theory, Fabrication and Characterization*. (Springer, 2008).

98. Park, J., Lee, S. & Lee, H. H. High-mobility polymer thin-film transistors fabricated by solvent-assisted drop-casting. *Org. Electron.* **7,** 256–260 (2006).

99. Birnie, D. P. in *Sol-Gel Technologies for Glass Producers and Users* (Springer Science + Business Media, 2004).

100. Hoth, C. N., Schilinsky, P., Choulis, S. A., Balasubramanian, S. & Brabec, C. J. in *Applications of Organic and Printed Electronics* 57–81 (Springer Science + Business Media, 2013).

101. Schneller, T., Waser, R., Kosec, M. & Payne, D. in *Chemical solution deposition of functional oxide thin films* (Springer-verlag Wien, 2013).

102. Reale, A. *et al.* Spray Coating for Polymer Solar Cells: An Up-to-Date Overview.

Energy Technol. **3,** 385–406 (2015).

103. Tracz, A., Pakula, T. & Jeszka, J. K. Zone casting - a universal method of preparing oriented anisotropic layers of organic materials. *Mater. Sci.* **22,** 415–421 (2004).
104. Mas-Torrent, M. *et al.* Organic field-effect transistors (OFETs) of highly oriented films of dithiophene-tetrathiafulvalene prepared by zone casting. *Org. Electron.* **9,** 143–148 (2008).
105. Berni, A., Mennig, M. & Scmidt, H. in *Sol-Gel Technologies for Glass Producers and Users* 89–92 (1952).
106. Zhang, Q., Leonardi, F., Casalini, S., Temiño, I. & Mas-Torrent, M. High performing solution-coated electrolyte-gated organic field-effect transistors for aqueous media operation. *Sci. Rep.* **6,** 39623 (2016).
107. Malachowski, M. J. & Zmija, J. Organic field-effect transistors. *Opto-Electronics Rev.* **18,** 121–136 (2010).
108. Klauk, H. Organic thin-film transistors. *Chem. Soc. Rev.* **39,** 2643–2666 (2010).
109. Shehu, A. *et al.* Layered distribution of charge carriers in organic thin film transistors. *Phys. Rev. Lett.* **104,** 246602 (2010).
110. Newman, C. R., Frisbie, C. D., Demetrio, A., Filho, S. & Bre, J. Introduction to Organic Thin Film Transistors and Design of n-Channel Organic Semiconductors. *Chem. Mater.* **16,** 4436–4451 (2004).
111. Horowitz, G., Hajlaoui, R., Bouchriha, H., Bourguiga, R. & Hajlaoui, M. Concept of `threshold voltage' in organic field-effect transistors. *Adv. Mater.* **10,** 923–927 (1998).
112. Egginger, M., Bauer, S., Schwödiauer, R., Neugebauer, H. & Sariciftci, N. S. Current versus gate voltage hysteresis in organic field effect transistors. *Monatshefte fur Chemie* **140,** 735–750 (2009).
113. Wang, D., Noël, V. & Piro, B. Electrolytic Gated Organic Field-Effect Transistors for Application in Biosensors—A Review. *Electronics* **5,** 9 (2016).
114. Kim, S. H. *et al.* Electrolyte-gated transistors for organic and printed electronics. *Adv. Mater.* **25,** 1822–1846 (2013).

115. Schmidt, E., Shi, S., Ruden, P. P. & Frisbie, C. D. Characterization of the Electric Double Layer Formation Dynamics of a Metal/Ionic Liquid/Metal Structure. *ACS Appl. Mater. Interfaces* **8,** 14879–14884 (2016).

116. Kergoat, L. *et al.* A water-gate organic field-effect transistor. *Adv. Mater.* **22,** 2565–2569 (2010).

117. Du, H., Lin, X., Xu, Z. & Chu, D. Electric double-layer transistors : a review of recent progress. *J. Mater. Sci.* **50,** 5641–5673 (2015).

118. Burt, R., Birkett, G. & Zhao, X. S. A review of molecular modelling of electric double layer capacitors. *Phys. Chem. Chem. Phys.* **16,** 6519–6538 (2014).

119. Katz, H. E. *et al.* Chemical and Biomolecule Sensing with Organic Field-Effect Transistors. *Chem. Rev.* **119,** 3–35 (2018).

120. Manoli, K. *et al.* Printable bioelectronics to investigate functional biological interfaces. *Angew. Chemie Int. Ed.* **54,** 12562–12576 (2015).

121. Zhang, J. *et al.* A review of electrolyte materials and compositions for electrochemical supercapacitors. *Chem. Soc. Rev.* **44,** 7484–7539 (2015).

122. Yalkowsky, S. H., He, Y. & Jain, P. *Handbook of Aqueous solubility Data SECOND EDITION*. (CRC Press, 2010).

123. Zhang, H. *et al.* Review—Solid Electrolytes for Safe and High Energy Density Lithium-Sulfur Batteries: Promises and Challenges. *J. Electrochem. Soc.* **165,** A6008–A6016 (2017).

124. Felman, A. Everything you need to konw about electrolytes. *Medical News Today* (2017). Available at: https://www.medicalnewstoday.com/articles/153188.php.

125. Water, U., Controls, A. I. C., Water, H. P. & Controls, I. C. *High Purity Water Resistivity/ Conductivity Measurement*. *Thermo Scientific IC Control***,** (2012).

126. Taruta, S. *et al.* An aqueous electrolyte of the widest potential window and its superior capability for capacitors. *Sci. Rep.* **7,** 45048 (2017).

127. Foschi, G. *et al.* Electrical release of dopamine and levodopa mediated by amphiphilic β-cyclodextrins immobilized on polycrystalline gold. *Nanoscale* **7,** 20025–20032 (2015).

128. Casalini, S. *et al.* Multiscale Sensing of Antibody-Antigen Interactions by Organic Transistors and Single-Molecule Force Spectroscopy. *ACS Nano* **9,** 5051–5062 (2015).
129. Magliulo, M. *et al.* Electrolyte-gated organic field-effect transistor sensors based on supported biotinylated phospholipid bilayer. *Adv. Mater.* **25,** 2090–2094 (2013).
130. Mulla, M. Y. *et al.* Capacitance-modulated transistor detects odorant binding protein chiral interactions. *Nat. Commun.* **6,** 6010 (2015).
131. Buenger, D., Topuz, F. & Groll, J. Hydrogels in sensing applications. *Prog. Polym. Sci.* **37,** 1678–1719 (2012).
132. Ahmed, E. M. Hydrogel: Preparation, characterization, and applications: A review. *J. Adv. Res.* **6,** 105–121 (2015).
133. Bahram, M., Mohseni, N. & Moghtader, M. in *Emerging Concepts in Analysis and Applications of Hydrogels* (eds. Ghanbarzadeh, B. & Almasi, H.) 75–100 (INTECh, 2016).
134. Dumitru, L. M. *et al.* A hydrogel capsule as gate dielectric in flexible organic field-effect transistors. *APL Mater.* **3,** 014904 (2015).
135. Cramer, T. *et al.* Water-gated organic field effect transistors-opportunities for biochemical sensing and extracellular signal transduction. *J. Mater. Chem. B* **1,** 3728–3741 (2013).
136. Wang, H. & Pilon, L. Accurate simulations of electric double layer capacitance of ultramicroelectrodes. *J. Phys. Chem. C* **115,** 16711–16719 (2011).
137. Al Naim, A. Electrolyte-gated thin film transistors with solution-processed semiconductors. (UNIVERSITY OF SHEFFIELD, 2014).
138. Rivnay, J. *et al.* Organic electrochemical transistors. *Nat. Rev. Mater.* **3,** 17086 (2018).
139. Giridharagopal, R. *et al.* Electrochemical strain microscopy probes morphology-induced variations in ion uptake and performance in organic electrochemical transistors. *Nat. Mater.* **16,** 737–742 (2017).
140. Toss, H. *et al.* On the mode of operation in electrolyte-gated thin film transistors

based on different substituted polythiophenes. *Org. Electron.* **15,** 2420–2427 (2014).

141. Buth, F., Donner, A., Sachsenhauser, M., Stutzmann, M. & Garrido, J. A. Biofunctional electrolyte-gated organic field-effect transistors. *Adv. Mater.* **24,** 4511–4517 (2012).

142. Magliulo, M. *et al.* PE-CVD of hydrophilic-COOH functionalized coatings on electrolyte gated field-effect transistor electronic layers. *Plasma Process. Polym.* **10,** 102–109 (2013).

143. Nguyen, T. T. K. *et al.* Peptide-modified electrolyte-gated organic field effect transistor. Application to Cu^{2+} detection. *Biosens. Bioelectron.* **127,** 118–125 (2018).

144. Pernstich, K. P., Oberhoff, D., Goldmann, C. & Batlogg, B. Modeling the water related trap state created in pentacene transistors. *Appl. Phys. Lett.* **89,** 213509 (2006).

145. Nikolka, M. *et al.* High operational and environmental stability of high-mobility conjugated polymer field-effect transistors through the use of molecular additives. *Nat. Mater.* **16,** 356–362 (2017).

146. Kergoat, L. *et al.* Use of poly(3-hexylthiophene)/poly(methyl methacrylate) (P3HT/PMMA) blends to improve the performance of water-gated organic field-effect transistors. *Org. Electron.* **12,** 1253–1257 (2011).

147. Cramer, T. *et al.* Double layer capacitance measured by organic field effect transistor operated in water. *Appl. Phys. Lett.* **100,** 143302 (2012).

148. Yun, M. *et al.* Stable organic field-effect transistors for continuous and nondestructive sensing of chemical and biologically relevant molecules in aqueous environment. *ACS Appl. Mater. Interfaces* **6,** 1616–1622 (2014).

149. Knopfmacher, O. *et al.* Highly stable organic polymer field-effect transistor sensor for selective detection in the marine environment. *Nat. Commun.* **5,** 2954 (2014).

150. Cotrone, S. *et al.* Phospholipid film in electrolyte-gated organic field-effect transistors. *Org. Electron. physics, Mater. Appl.* **13,** 638–644 (2012).

151. Narayan, K. S. *et al.* Water-Gated Phospholipid-Monolayer Organic Field Effect Transistor Through Modified Mueller – Montal Method. *Electron Device Lett.* **34,** 310–312 (2013).
152. Schmoltner, K., Kofler, J., Klug, A. & List-Kratochvil, E. J. W. Electrolyte-gated organic field-effect transistor for selective reversible ion detection. *Adv. Mater.* **25,** 6895–6899 (2013).
153. Suspène, C. *et al.* Copolythiophene-based water-gated organic field-effect transistors for biosensing. *J. Mater. Chem. B* **1,** 2090–2097 (2013).
154. Porrazzo, R. *et al.* Improving mobility and electrochemical stability of a water-gated polymer field-effect transistor. *Org. Electron.* **15,** 2126–2134 (2014).
155. Buth, F., Kumar, D., Stutzmann, M. & Garrido, J. A. Electrolyte-gated organic field-effect transistors for sensing applications. *Appl. Phys. Lett.* **98,** 153302 (2011).
156. De Oliveira, R. F., Merces, L., Vello, T. P. & Bof Bufon, C. C. Water-gated phthalocyanine transistors: Operation and transduction of the peptide-enzyme interaction. *Org. Electron.* **31,** 217–226 (2016).
157. Cramer, T. *et al.* Double layer capacitance measured by organic field effect transistor operated in water. *Appl. Phys. Lett.* **100,** (2012).
158. Mulla, M. Y. *et al.* UV crosslinked poly(acrylic acid): a simple way to bio-functionalize electrolyte-gated OFET biosensors. *J. Mater. Chem. B* **3,** 5049–5057 (2015).
159. Porrazzo, R. *et al.* Water-Gated n-Type Organic Field-Effect Transistors for Complementary Integrated Circuits Operating in an Aqueous Environment. *ACS Omega* **2,** 1–10 (2017).

Chapter 2. EGOFETs Based on OSC:PS Blend Films[iii]

Abstract: In this chapter, four organic semiconductors (OSCs), including three small molecules and one polymer, have been selected as active materials for the fabrication of electrolyte-gated organic field-effect transistors (EGOFETs), which are considered as a promising sensing platform in the field of bioelectronics due to their ability to operate in aqueous media. Blending these four OSCs, *i.e.* TIPS-pentacene, diF-TES-ADT, DPTTA and PDPP-BTT(1)-SVS(9), with an insulating polymer (*i.e.* polystyrene, PS) and their deposition through bar-assisted meniscus shearing (BAMS) technique, are the two key strategies that have been employed in order to achieve high performance devices. For each OSC:PS blend, a careful optimization process, varying the ink formulation and deposition parameters, and their analysis on the thin film morphology have been carried out in order to select the best conditions for OFET and EGOFET preparation. Noticeably, the presence of the insulating polymer and the control of surface wettability through a self-assembled monolayer have revealed important to guarantee homogenous thin films of well-defined crystallinity and, consequently robust electrical performance. In addition, the EGOFET behavior of each OSC:PS formulation have been further studied by means of potentiometric sensitivity and switching speed. Further, an in-depth stability test has been carried out. All the devices have been characterized in MilliQ water and even in high ionic strength solutions. Among these four OSCs, diF-TES-ADT:PS blend (PS M_w = 10 000 g/mol, OSC:PS ratio=4:1 and PFBT coating on device's electrodes) has been recognized as the best EGOFET performing material for EGOFETs, being also promising for long-time electrical recording measurements.

[iii] 1) Q. M. Zhang, F. Leonardi, S. Casalini, I. Temiño and M. Mas-Torrent, *Sci. Rep*. 2016, 6, 39623. 2) F. Leonardi, S. Casalini, Q. M. Zhang, S. Galindo, D. Gutierrez, and M. Mas-Torrent, *Adv. Mater.* 2016, 28, 10311. 3) A. Campos, Q. M. Zhang, M. R. Ajayakumar, F. Leonardi, and M. Mas-Torrent, *Adv. Electron. Mater.* 2017, 1700349, 4) F. Leonardi, Q. M. Zhang, Y. H. Kim, and M. Mas-Torrent, *Mat. Sci. Semicon. Proc.* 2019, 93, 105.

2.1 Introduction

Aiming at the fabrication of low-power electronics, electrolyte-gated organic field-effect transistors (EGOFETs), whose layout consists in directly exposing the organic semiconductor (OSC) to aqueous media without the need of an encapsulation layer, have demonstrated to be excellent candidates.[1,2] Such device permits the lowering of the operation voltage (<1 V) since a very high capacitance (~ several $\mu F\ cm^{-2}$) is achieved due to the formation of two electrical double layers at the OSC/electrolyte and electrolyte/gate electrode interfaces when a V_{GS} is applied.[1,3] By modifying with specific molecules or functional groups one of these two interfaces, the surface potential will change if the species interact or absorb a target in the media, affecting the current in the semiconductor channel induced by field-effect.[2,4,5] Therefore, EGOFETs could be used as a promising platform for label-free (bio)-sensor applications since they provide the following advantages: (i) intrinsic signal amplification ability, (ii) sensitivity to small voltages, (iii) multi-parametric response and (iv) an intrinsic versatility which can turn them into a specific sensing platform.[4] Although the choice of using EGOFETs has many advantages for the development of sensing platforms interesting in the field of diagnostics[6] and healthcare[7], some unsolved problems (*i.e.* low carrier mobility, slow response time, poor stability, and fast degradation) are actually hindering their practical application. As a consequence, it is crucial to obtain robust and efficient EGOFETs technologically relevant for the electronic market.

As mentioned in Chapter 1, a groundbreaking EGOFET must encompass all the following characteristics: (i) $\mu \geq 0.1\ cm^2V^{-1}s^{-1}$,[8] (ii) high on/off ratio $\geq 10^3$,[1] (iii) a potentiometric sensitivity in the range of μV,[9] (iv) operational frequency (*f*) higher than 200 Hz[9] and (v) capability to withstand prolonged (*i.e.* from hours to days) electrical stresses.[10,11] To date, there are no precedents of EGOFETs that meet all these criteria. Undoubtedly, the choice of the OSC and its consequent processing are pivotal.[3]

In general, a high degree of crystallinity along with an extended homogeneity at long-range (*i.e.* from few to hundreds of μm) is fundamental to avoid the so-called "electrochemical doping", whose distinctive fingerprints are a marked hysteresis, electrical instability within time frame of minutes and/or hours and slow operational response.[12] With this in mind, spin-coated semi-crystalline or liquid crystalline polymer OSCs[1,13] have been chosen as active layers in EGOFETs as well as single crystals[1] or thin films of small molecule semiconductors prepared by vacuum sublimation.[9,14,15] Our approach consists of combining two widely overlooked strategies: (i) the exploitation of blends composed by an insulating polymer and an OSC[8,16–18] and (ii) the use of a solution-shearing technique, such as bar-assisted meniscus shearing (BAMS), to deposit the OSC[19,20]. The former strategy is based on the exploitation of polystyrene (PS), as insulating polymer which is blended with a soluble OSCs. The use of blends has been shown to promote material process ability and also leads to thin films with an enhanced crystallinity and environmental stability.[19–21] Furthermore our solution shearing approach is a low cost technique compatible with roll-to-roll processes that has been recently demonstrated to produce high-crystalline thin films in one single step featuring electrical performance comparable to devices based on amorphous silicon.[19–22]

- **The choice of OSC material**

To widen the library of OSC materials suitable for EGOFETs, three kinds of OSCs have been selected to blend with PS: (1) two benchmark commercial small molecule OSCs, bis(triisopropylsilylethynyl)pentacene (TIPS-pentacene) and 2,8-difluoro-5,11-bis(triethylsilylethynyl)anthradithiophene (diF-TES-ADT),[20,23,24] (2) a synthesized *p*-type OSC with a circular annulene, meso-diphenyltetrathia(22)annulene(2,1,2,1) (DPTTA),[25] and (3) a donor-acceptor random copolymer poly[2,5-bis(7-decylnonadecyl)pyrrolo[3,4-c]pyrrole-1,4(2H,5H)-dione-2,2'-bithieno[3,2-b]thiophene]-co-[2,5-bis(7-decylnonadecyl)pyrrolo[3,4-c]pyrrole-1,4(2H,5H)-dione-(E)-(1,2-bis(5-(thiophen-2-yl)selenophen-2-yl)ethene)] (PDPP-TT-SVS)[26,27]. The chemical structures of all the selected OSCs and PS are shown in **Figure 2.1**. It is worth pointing out that these four OSCs had already shown excellent performances in "standard" OFET,[25,26] however, to the best of our knowledge, all of them had never been explored as active material for EGOFETs.

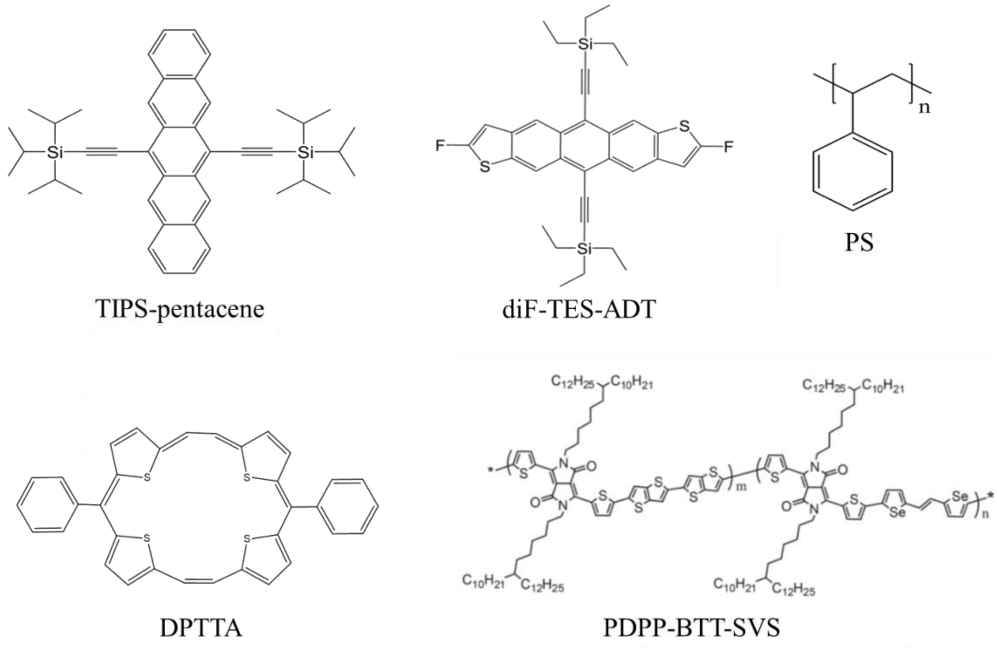

Figure 2.1: Chemical structure of selected OSCs and polystyrene.

TIPS-pentacene and diF-TES-ADT are two widely used small molecule OSCs, which normally display an OFET mobility on the order of 2.7 cm^2 V^{-1} s^{-1} and 6 cm^2 V^{-1} s^{-1}, respectively.[23,24] They belong to the family of acenes and their side chains promote their solubility in most common organic solvents. In TIPS-pentacene, two triisopropylsilylethynyl units have been added to a pentacene core while in diF-TES-ADT, the same two side chains are incorporated into a five members ring structure partially replaced by two fluorinated thiophene units. These materials have been extensively used as active components in OFETs and processed through different solution processing techniques, such as spin coating and blade coating.[21,28]

The structure of DPTTA is based on a tetratia(22)annulene(2,1,2,1), which was first synthesized by Singh *et al.* in 2011.[25] They reported a fairly good OFET field-effect mobility of 0.7 cm^2 V^{-1} s^{-1} as single-crystal and 0.29 cm^2 V^{-1} s^{-1} as evaporated thin film.[25] Lately, DPTTA was further exploited in organic electronics by different research groups.[29,30] Although the high potential of this material as active component in devices, it had not yet been processed in thin film by any solution-based processing technique, which clearly limits its further applicability.

PDPP-TT-SVS is a donor-acceptor random co-polymer which, contrarily to the previous OSCs, belongs to the class of polymer semiconductors. This polymer OSC exhibits good solubility in various non-chlorinated and chlorinated solvents due to the random copolymerization synthetic approach for incorporating the the donor-acceptor units.[27] The outstanding performance of this material have already been reported by Kim *et al.* which have studied how the co-polymer composition affects the electrical behavior once this material is employed in OFETs.[26] However, this OSC was solely processed *via* spin coating and measured under controlled atmosphere and thus, its exploitation with roll-to-roll (R2R) techniques or the electrical response recorded under ambient atmosphere were still unexplored.

- **Self-assembled monolayers (SAMs)**

Self-assembly is possibly one of the most effective and versatile strategy for surface functionalization and it is defined as the autonomous organization of components into patterns and structures, without human intervention.[5] Self-assembled monolayers (SAMs) are molecular assemblies anchored spontaneously on surfaces by adsorption and organized with large ordered structures.[31] One single unit contains three parts: the head-group (anchoring group), the backbone (main chain) and the terminal (functional) group.[5,32] SAMs can be formed on several surfaces, like metals or oxides, that are commonly employed in a variety of technological applications.[31,33] In organic electronics, the use of SAMs on electrodes, dielectrics, and even semiconductors has become a widely adopted and versatile approach for modulating the interfacial properties of organic electronic devices.[5]

2,3,4,5,6-pentafluorobenzenethiol (PFBT) is a widely used material in organic electronics and it can be anchored on gold electrodes due to its thiolated head.[21] Our group has observed that homogenous and interconnected crystallites form on PFBT-modified OFETs coated with TIPS-pentacene:PS and diF-TES-ADT:PS deposited by BAMS at 1 cm/s, which definitely displayed better electrical OFET performance when compared to those without an electrode-functionalization.[20] The reason has been attributed to the large crystalline domains extended along the whole channel region (L is in the range 25 – 100 μm).

- **Object of this chapter**

The optimization of thin film deposition is pivotal for achieving high performance devices and for understanding the structure-property relationship of the material. However, EGOFETs present a complex scenario mainly described from a phenomenological point of view but lacking of any solid physical model. These devices could represent the next generation of (bio)sensors but the creation of stable and reliable EGOFETs is the first fundamental step for the complete understanding of their operation. Thus, the objective of this chapter is to develop robust and efficient EGOFETs by combining two overlooked strategies: (i) the exploitation of blends composed by an insulating polymer and a small molecule OSC, and (ii) the use of a solution-shearing technique, *i.e.* BAMS, to deposit the OSC. To do so, three different kinds of OSCs, including two benchmark small molecule OSCs (*e.g.* TIPS-pentacene, diF-TES-ADT,) one synthesized small molecule OSC (DP-TTA) and one donor-acceptor copolymer OSC (PDPP-TT-SVS), were selected as active material and combined with an insulating polymer (*e.g.* PS).

For each blend film, the morphology and thickness have been firstly characterized by optical microscopy and atomic force microscopy (AFM). Then, a preliminary OFET electrical test was carried out to assess the quality of the device followed by the EGOFET characterization by means of MilliQ water and a saline solution (*viz.* NaCl 1M) as electrolyte media. Moreover, potentiometric sensitivity and switching speed tests have been carried out to understand the intrinsic capability of the EGOFET devices toward transient pulses. Finally, stability measurements (*i.e. in-situ* real-time monitoring, bias-stress and shelf-stability) have been carried out in order to assess the robustness of this electrical platform.

2.2 TIPS-pentacene:PS and diF-TES-ADT:PS Blends

In a previous work, our group has exploited two benchmark small molecule OSCs, TIPS-pentacene and diF-TES-ADT, in combination with polystyrene to produce thin films employing BAMS technique.[20] Devices based on TIPS-pentacene:PS and diF-TES-ADT:PS blend have displayed an OFET average mobility of ~ 1.8 $cm^2 V^{-1} s^{-1}$ and 1.5 $cm^2 V^{-1} s^{-1}$,[20] respectively, which have served as starting point for the preparation of EGOFETs. These two OSCs had been completely unexplored as active materials for EGOFETs, so a first screening varying the blend formulation (*i.e.* the OSC:PS blend ratio and the molecular weight of PS) and in presence or absence of PFBT has been carried out. Here, PFBT has been used as electrode modifier onto *S*/*D* electrodes in order to improve the electrical performances due to an ameliorated charge-injection and better morphological homogeneity of the active material coating.[20,34] The characterization details of the films prepared during the optimization process, including the optical microscopy images, typical OFET and EGOFET for each ink formulation and coating conditions can be found in **Table A. 1** and **A.2** (**Appendix A).**[*] Our screening process results in an outperforming EGOFET when the OSC:PS blend films are prepared according to the following parameters:

TIPS-pentacene:PS blend

- Ink formulation: TIPS-pentacene:PS_{10K} mixed in a 4:1 ratio, 2 wt%
- Solvent: Chlorobenzene
- S/D electrode functionalization: 2,3,4,5,6-Pentafluorothiophenol (PFBT)
- Coating parameters: 1 cm/s at 105 °C.

diF-TES-ADT:PS blend

- Ink formulation: diF-TES-ADT:PS_{10K} mixed in a 4:1 ratio, 2 wt%
- Solvent: Chlorobenzene
- S/D electrode functionalization: 2,3,4,5,6-Pentafluorothiophenol (PFBT)
- Coating parameters: 1 cm/s at 105 °C.

---

[*] The characterization data of the sample prepared during the optimization process (optical microscopy, OFET and EGOFET electrical performance with MilliQ H_2O and NaCl 1 M solution as media) can be found in **Appendix A1** and **A2**.

For sake of clarity, these two formulations are identified with the following name: TIPS:PS_{10K}(4:1)/PFBT and diF:PS_{10K}(4:1)/PFBT, respectively. This labelling protocol unequivocally identifies the preparation conditions of the precursor inks (ratio of the two components, the molecular weight of the PS and the presence of PFBT as electrode coating). All the electrical results related to various ink formulations and coating parameters reported in **Appendix A,** show lower performance compared to the TIPS:PS_{10K}(4:1)/PFBT and diF:PS_{10K}(4:1)/PFBT based EGOFETs. In addition, with the aim to gain an understanding of the role of PFBT and PS, the following 6 formulations have also been studied: TIPS:PS_{10K}(4:1), TIPS/PFBT, TIPS, diF:PS_{10K}(4:1), diF/PFBT and diF.

2.2.1 Morphological Characterization of the Blend Thin-film

A first morphological screening of thin films based on TIPS-pentacene and diF-TES-ADT has been performed by using polarized optical microscopy, as shown in **Figure 2.2** and **Figure 2.3**. The crystals of the semiconducting thin-film do not show any dependency with respect to the bar-shearing direction because of the high deposition speed (*i.e.* 1 cm · s^{-1}).[20,34] In contrast, the crystals size shows a clear dependence with respect to the surface treatment of the *S*/*D* electrodes. As a result, both TIPS:PS_{10K}(4:1)/PFBT and diF:PS_{10K}(4:1)/PFBT domains have a size as high as 30×30 μm^2 (see **Figure 2.2 (a)** and **Figure 2.3 (a)**); whereas in the thin films lacking of electrode functionalization with PFBT (TIPS:PS_{10K}(4:1) and diF:PS_{10K}(4:1)) the domains have a size almost doubled (~ 60×60 μm^2), although the films are slightly less homogenous with less regular crystallite shapes, especially in the case of TIPS (see **Figure 2.2 (b)** and **Figure 2.3 (b)**). This might be due to the higher nucleation occurring with the more interacting PFBT-Au electrodes.[34] The role of PS on the quality of the thin film seems also essential: a smaller grain size and less defined crystals have been observed in PS-free films in TIPS-pentacene based thin films (~ 5×5 μm^2 in TIPS/PFBT thin film and ~ 30×30 μm^2 in TIPS thin film, **Figure 2.2 (c)** and **(d)**). A similar scenario was observed in diF-TES-ADT based thin film in absence of PS binder (diF/PFBT and diF; see **Figure 2.3 (c)** and **(d)**), resulting in smaller and less defined crystals.

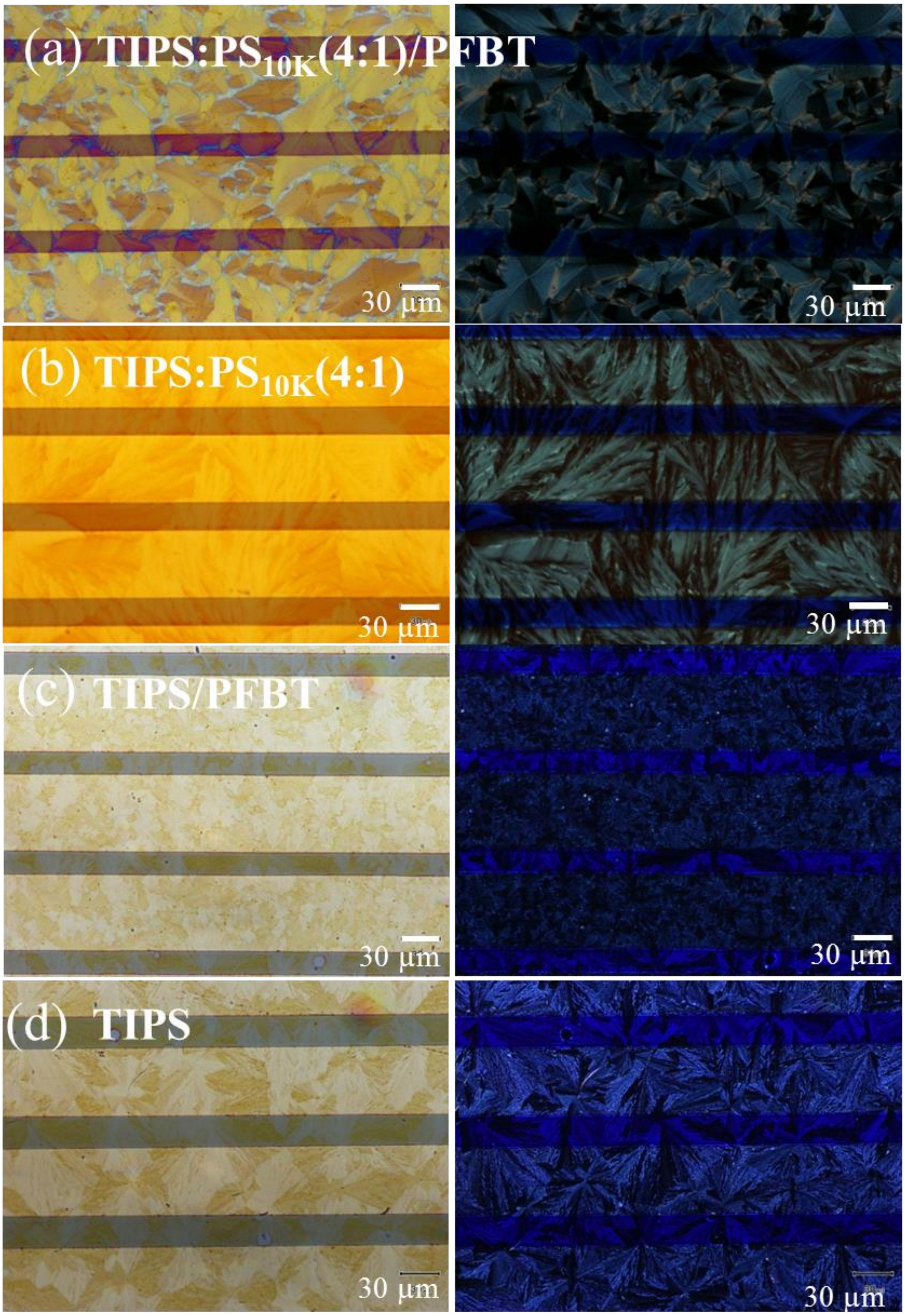

Figure 2.2: Optical microscopy images acquired with a cross polarizer of (a) TIPS:PS_{10K}(4:1)/PFBT, (b)TIPS:PS_{10K}, (c)TIPS/PFBT and (d) TIPS thin films. On the left, polarizer/analyzer = 0° and on the right, polarizer/analyzer = 90°.

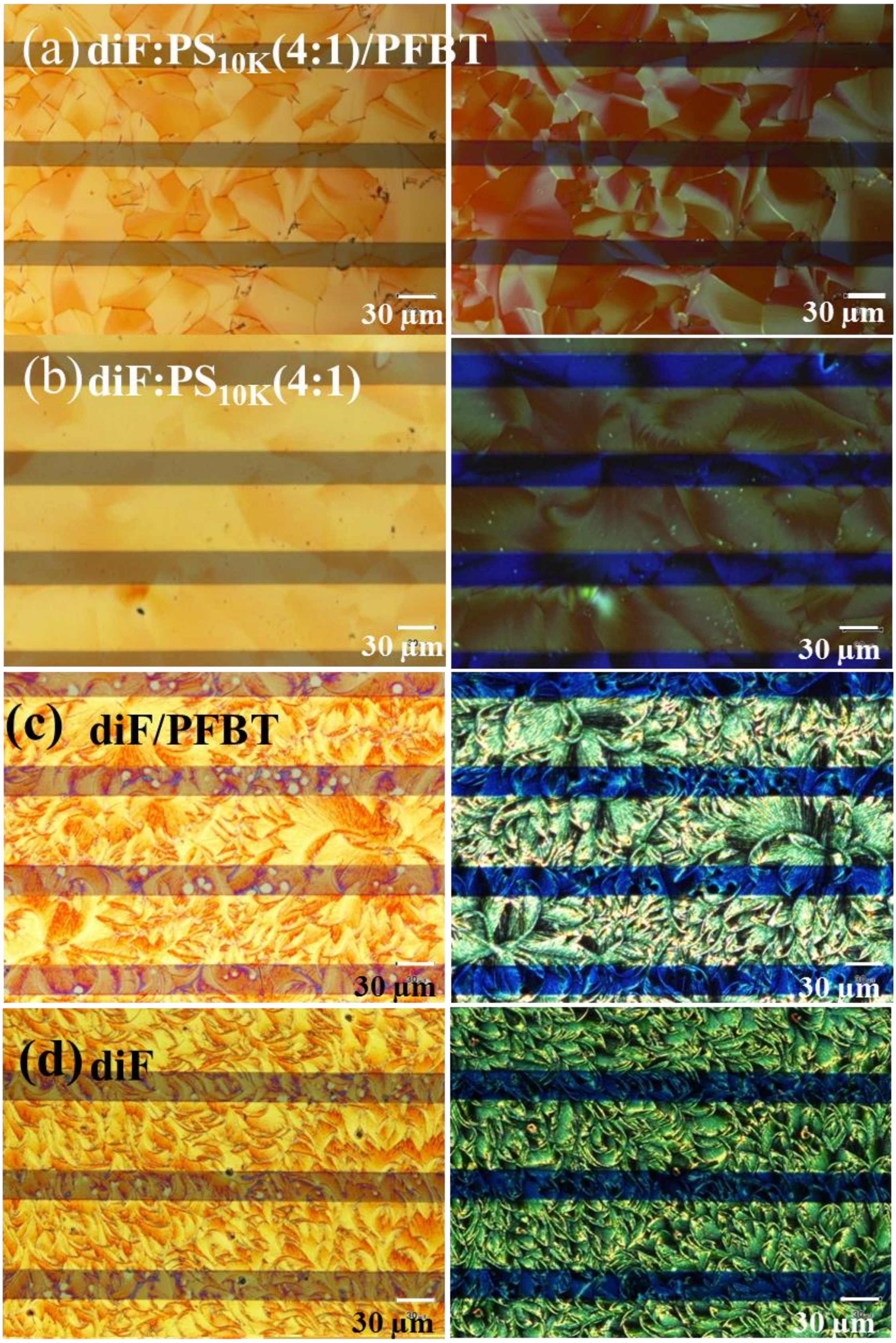

Figure 2.3: Optical microscopy images acquired with a cross polarizer of (a) diF:PS$_{10K}$(4:1)/PFBT, (b)diF:PS$_{10K}$, (c)diF/PFBT and (d) diF thin films. On the left, polarizer/analyzer = 0° and on the right, polarizer/analyzer = 90°.

By using atomic force microscopy (AFM), we have been able to study the coating morphology in terms of thickness and root mean square roughness (σ_{rms}). As shown in **Figure 2.4 (a)** and **Figure 2.5 (a)**, AFM analysis has revealed a thickness of 25 nm and σ_{rms} around 2 nm corresponding to TIPS:PS$_{10K}$(4:1)/PFBT thin films. For comparison, the same AFM test has been repeated on TIPS:PS$_{10K}$(4:1) thin film and the lack of PFBT resulted in a thinner film (~ 15 nm) with σ_{rms} ~ 3 nm, as displayed in **Figure 2.4 (b)** and **Figure 2.5 (b)**. These results suggested that the roughness of the top surface is not affected by the presence of two underlying materials, namely SiO_2 and polycrystalline Au.

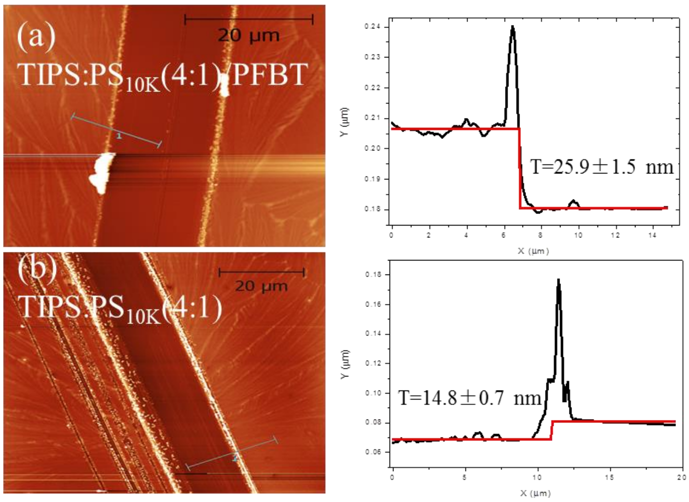

Figure 2.4: AFM profiles and their corresponding 2D fitting of (a) TIPS:PS$_{10K}$(4:1)/PFBT and (b) TIPS:PS$_{10K}$(4:1) thin film.

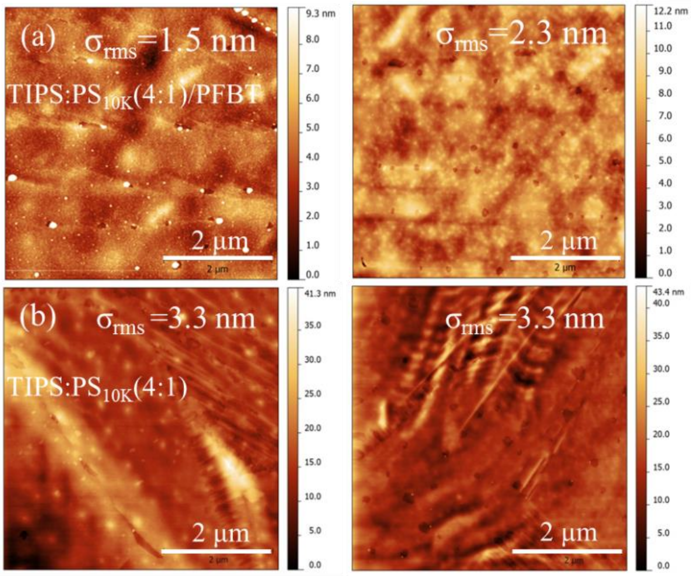

Figure 2.5: AFM images (5×5 μm^2) of (a) TIPS:PS$_{10K}$(4:1)/PFBT and (b) TIPS:PS$_{10K}$(4:1) devices. The left and right column images were acquired on the channel and electrode region, respectively.

In addition, a similar scenario was observed in diT-TES-ADT based thin films. As shown in **Figure 2.6**, the AFM profile of diF:PS$_{10K}$(4:1)/PFBT thin film reveals a thickness around 30 nm, while less than 20 nm is observed in the diF:PS$_{10K}$(4:1) film. Furthermore, an σ_{rms} value around ~ 2 nm has been extracted in diF:PS$_{10K}$(4:1)/PFBT thin film, while this value slightly increases in the PFBT-free film (σ_{rms} ~ 3 nm), as displayed in **Figure 2.7**. As previously mentioned, an extended homogeneity and crystallinity of the semiconducting thin-film are the two desirable features for EGOFETs operability, and our coatings fulfill these basic requirements.

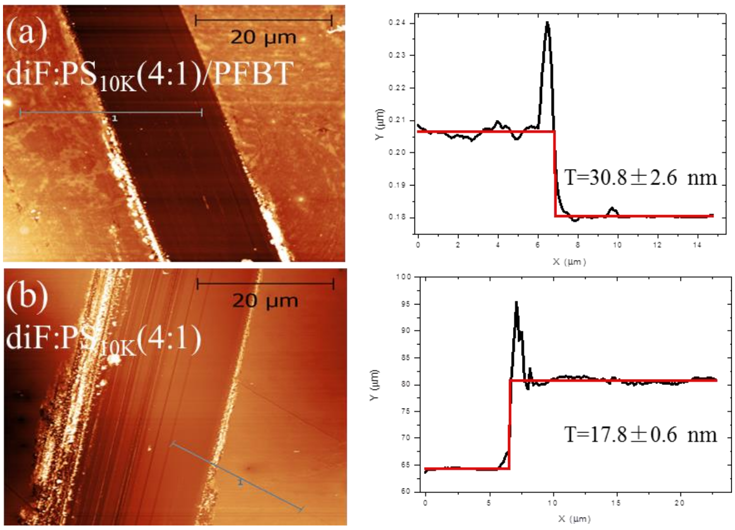

Figure 2.6: AFM profiles and their corresponding 2D fitting of (a) diF:PS$_{10K}$(4:1)/PFBT and (b) diF:PS$_{10K}$(4:1) thin film.

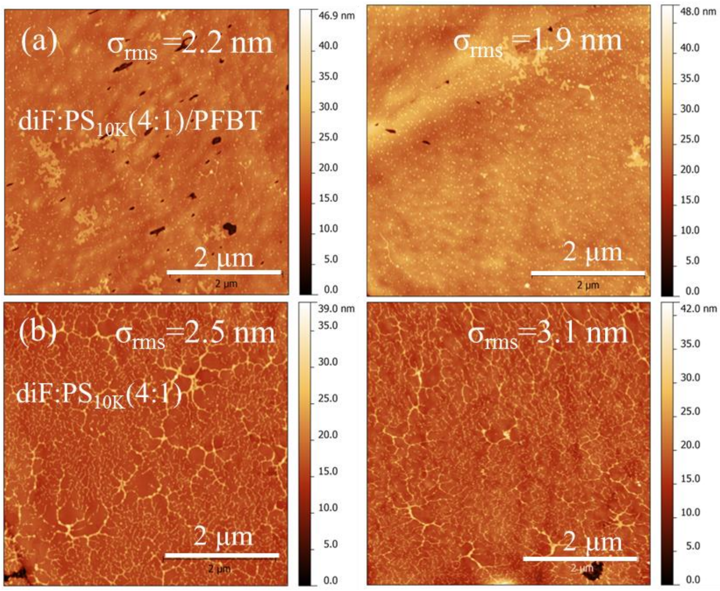

Figure 2.7: AFM images (5×5 µm^2) of (a) diF:PS$_{10K}$(4:1)/PFBT and (b) diF:PS$_{10K}$(4:1) devices. The left and right column images were acquired on the channel and electrode region, respectively.

2.2.2 Electrical Characterization

Moving from morphological to electrical characterization, we have firstly tested these blend films in the OFET configuration, whose architecture consists of Si/SiO_2 serving as gate electrode and dielectric layer, respectively (see **Figure 1.20 (a)**). The preliminary OFET electrical tests together with the optical microscopy images allow us to assess the quality of the blend thin film. As reported in **Figure 2.8**, all transfer and output characteristics of the TIPS:PS_{10K}(4:1)/PFBT-based OFETs exhibited a clear *p*-type behavior without hysteresis. In contrast, a huge hysteresis was observed in the TIPS:PS_{10K}(4:1)-based devices (see **Figure 2.9 (a)-(c)**). In addition, the I_{DS} in TIPS:PS_{10K}(4:1)/PFBT-based OFETs is two orders of magnitude higher than the one recorded in TIPS:PS_{10K}(4:1)-based ones at the same conditions (V_{GS} = -10 V and V_{DS} = -2 V). Furthermore, the I_{on}/I_{off} ratio in TIPS:PS_{10K}(4:1)/PFBT-based OFET is ~ 4×10^6, while this value drops to ~ 4×10^4 in the TIPS:PS_{10K}(4:1)-based device. As comparison, pristine TIPS-pentacene-based OFETs (namely TIPS/PFBT and TIPS-based devices, see **Figure 2.9 (d)-(f)** and **Figure 2.9 (g)-(i)**) exhibited a worse electrical performance when compared to our best OFET formulation, *i.e.* TIPS:PS_{10K}(4:1)/PFBT. Clearly, all the above mentioned results confirmed the fundamental role of PS and PFBT for improving the crystallinity of the thin film and electrical performance.[35]

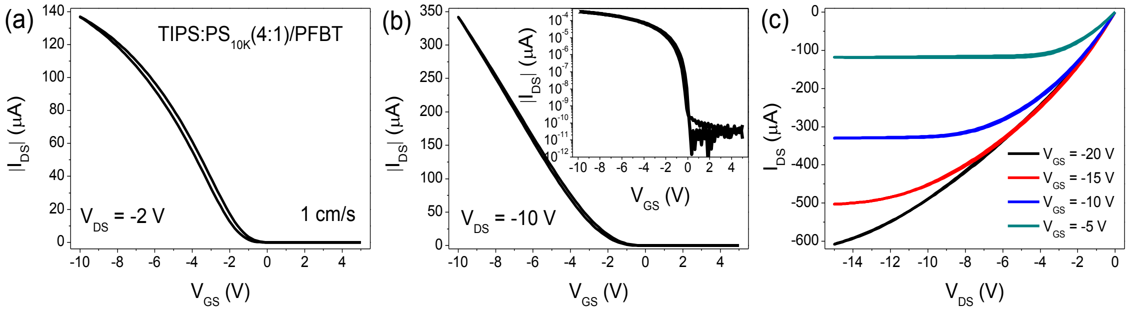

Figure 2.8: Transfer characteristics in BGBC configuration of TIPS:PS_{10K}(4:1)/PFBT-based OFETs in a) linear regime and b) saturation regime. The inset in b) is the corresponding Log-Lin plot. c) *I-V* output characteristics of the same device with V_{GS} spanning from -5 to -20 V with pace of -5 V.

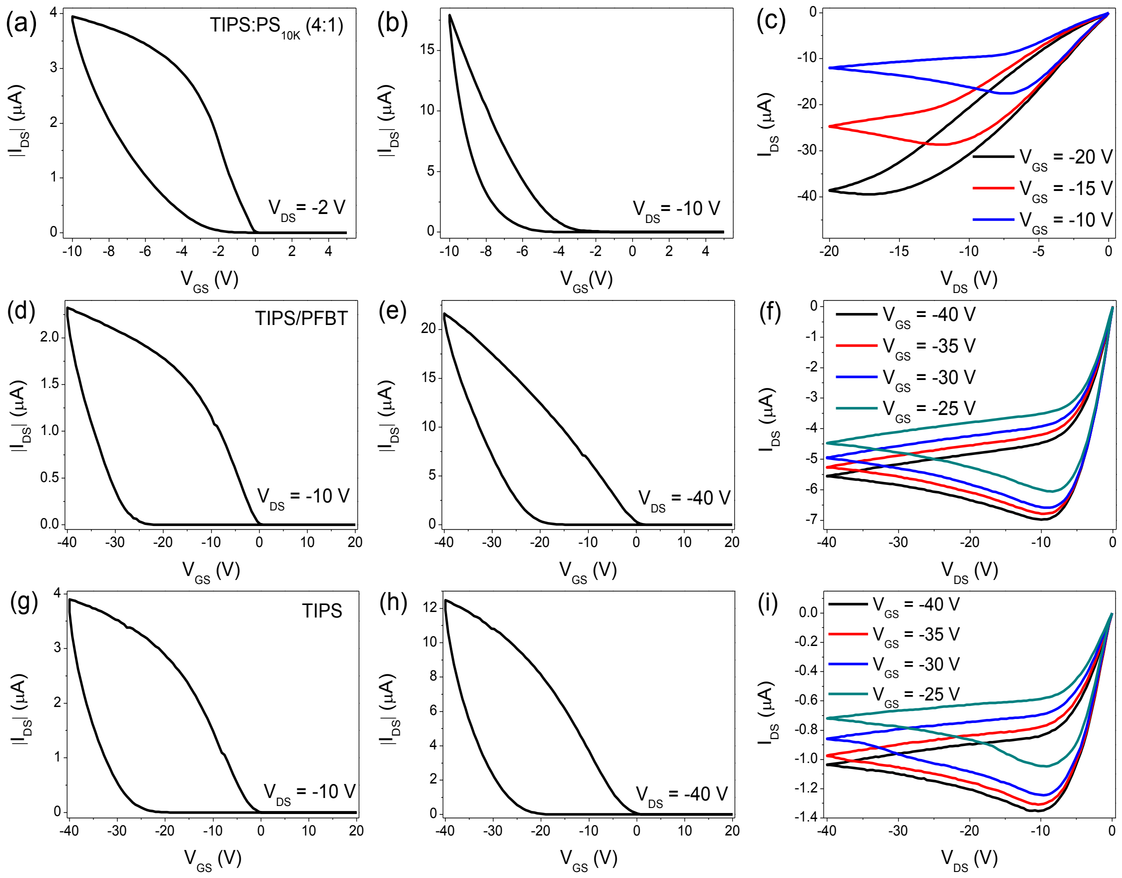

Figure 2.9: Transfer and output characteristics in BGBC configuration of (a-c) TIPS:PS$_{10K}$(4:1), (d-f) TIPS/PFBT and (g-i) TIPS based OFETs.

A similar tendency was observed in diF-TES-ADT based OFETs. As shown in **Figure 2.10**, diF:PS$_{10K}$(4:1)/PFBT-based OFETs exhibited again a typical *p*-type behavior and a small hysteresis. For comparison, the PFBT-free and PS-free characteristics have also been recorded. The I_{DS} in diF:PS$_{10K}$(4:1)/PBFT-based device is two times larger than the one obtained for diF:PS$_{10K}$(4:1) and diF/PFBT (see **Figure 2.11 (a)-(f)**), and two orders of magnitude higher than the one recorded for OFETs based on solely diF (see **Figure 2.1 (g)-(i)**) recorded in the same conditions (*i.e.* V_{GS} = -10 V and V_{DS} = -2 V). In particular, a huge hysteresis was observed in diF-based OFETs. Once again, the comparison confirmed the pivotal role of PFBT functionalization of *S/D* electrodes and the presence of PS in the precursor ink for improving crystallinity and homogeneity of the thin film which in turn, result in superior electrical performance.[20]

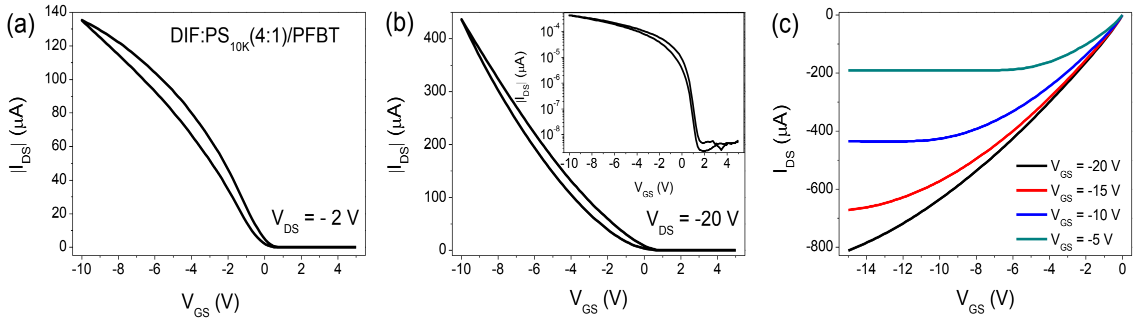

Figure 2.10: Transfer characteristics in BGBC configuration of diF:PS$_{10K}$(4:1)/PFBT-based OFETs in (a) linear regime and (b) saturation regime. The inset in (b) is the corresponding Log-Lin plot. (c) *I-V* output characteristic of the same device with V_{GS} spanning from -5 to -20 V with pace of -5 V.

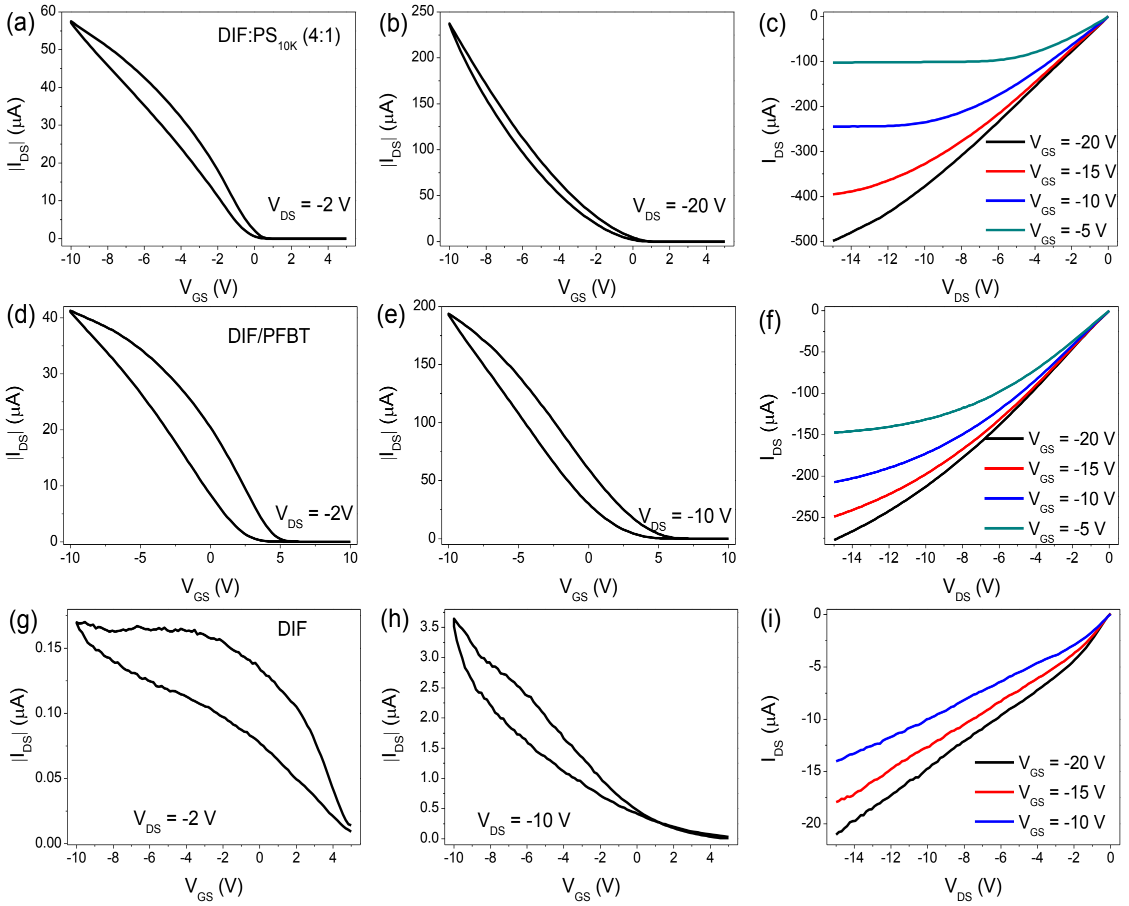

Figure 2.11: Transfer (linear and saturation regime) and output characteristics in BGBC configuration of (a-c) diF:PS$_{10K}$(4:1), (d-f) diF/PFBT and (g-i) diF based OFETs.

Moving to EGOFET configuration, the electrical performance has been recorded with two types of media: (i) MilliQ water and (ii) NaCl 1 M solution. The former allowed us to verify the field-effect mode of operation, whereas the latter enables to assess their effective exploitation in real aqueous samples whose ionic strength is more complex than MilliQ water.

As reported in **Figure 2.12** and **Figure 2.13**, *I-V* transfer and output characteristics show a *p*-type behavior in both TIPS:PS$_{10K}$(4:1)/PFBT and diF:PS$_{10K}$(4:1)/PFBT based EGOFETs in a range of V_{GS} from 300 mV to -500 mV. In MilliQ water, *I-V* transfer characteristics of both two types of EGOFETs do not show any hysteresis in both linear and saturation regime and they display an excellent amplification capability (namely both have I_{on}/I_{off} ratio centers at or closes to 10^4). In addition, the subthreshold slopes (*SS*) of TIPS:PS$_{10K}$(4:1)/PFBT and diF:PS$_{10K}$(4:1)/PFBT based devices are 87±3 mV/decade and 82±2 mV/decade, respectively, which is close to the theoretical threshold equal to 60 mV/decade.[36] When the devices were tested in NaCl 1 M solution, no electrical failures were observed in both two devices. Another noticeable effect is the negative shift of the switch-on voltage (V_{on}) in the higher ionic strength solution, which gives lower I_{DS} at a fixed voltage (*e.g.* V_{GS}= -0.4 V, V_{DS}= -0.4 V). This shift is probably caused by the drastic increase of the ionic strength which triggers the so-called “ionic screening”, already observed in other electronic devices operated in aqueous media.[36,37]

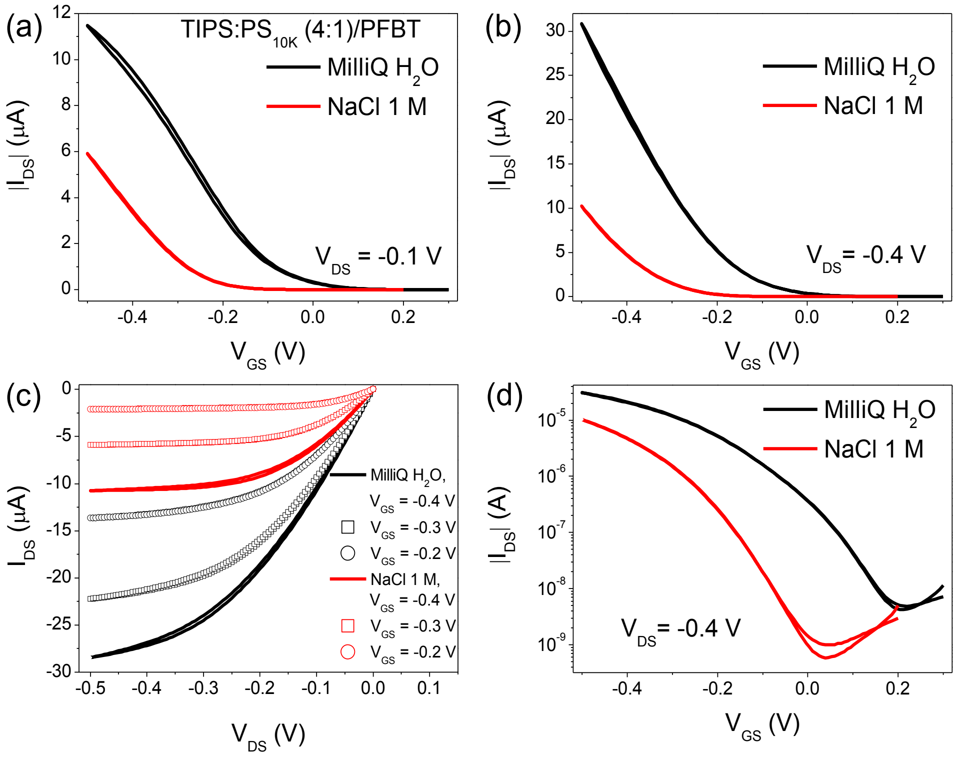

Figure 2.12: *T*ransfer characteristics of TIPS:PS$_{10K}$(4:1)/PFBT-based EGOFET device in (a) linear and (b) saturation regime in MilliQ H_2O and NaCl 1 M. (c) Output characteristics of the same device with three different V_{GS} values. (d) Log-lin plot of the *I-V* characteristics shown in (b).

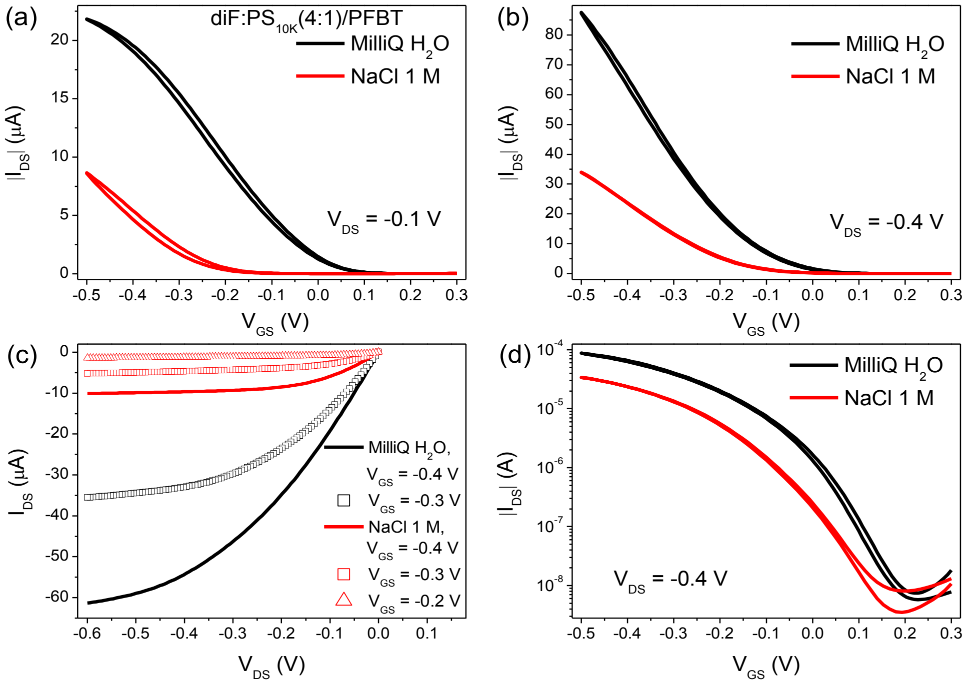

Figure 2.13: *I-V* transfer characteristics of diF:PS$_{10K}$(4:1)/PFBT-based EGOFET device in (a) linear and (b) saturation regime with MilliQ H_2O and NaCl 1 M. (c) Output characteristics of the same device with three different V_{GS} values. (d) The corresponding Log-lin plot shown in (b).

In order to get deeper insights on the role of PFBT and PS on the electrical performance of the EGOFETs, we have performed a crosscheck by comparing again our best OSC formulations with the following 6 cases: TIPS:PS$_{10K}$ (4:1), TIPS/PFBT, TIPS, diF:PS$_{10K}$(4:1), diF/PFBT and diF. In the TIPS-pentacene case, the I_{DS} current of TIPS:PS$_{10K}$ (4:1)/PFBT-based device (extracted at V_{GS}= -0.4 V, V_{DS}= -0.4 V) is three times higher than the PFBT-free device (TIPS:PS$_{10K}$ (4:1), see **Figure 2.14 (a)-(c)**), and two orders of magnitude higher than the PS-free device (TIPS/PFBT and TIPS-based device, see **Figure 2.14 (d-f)** and **Figure 2.14 (g-i)**, respectively). However, a smaller difference can be observed in the diF-TES-ADT case. A comparable I_{DS} was obtained in diF:PS$_{10K}$(4:1)/PFBT and diF:PS$_{10K}$(4:1)-based EGOFETs (see **Figure 2.15 (a-c)**), while the current drops one order of magnitude in the case of diF/PFBT and diF (see **Figure 2.15 (d-f)** and **Figure 2.15 (g-i)**, respectively). All the above results demonstrate that the beneficial effect of PFBT functionalization is not strong as the one derived from the addition of the binder polymer.

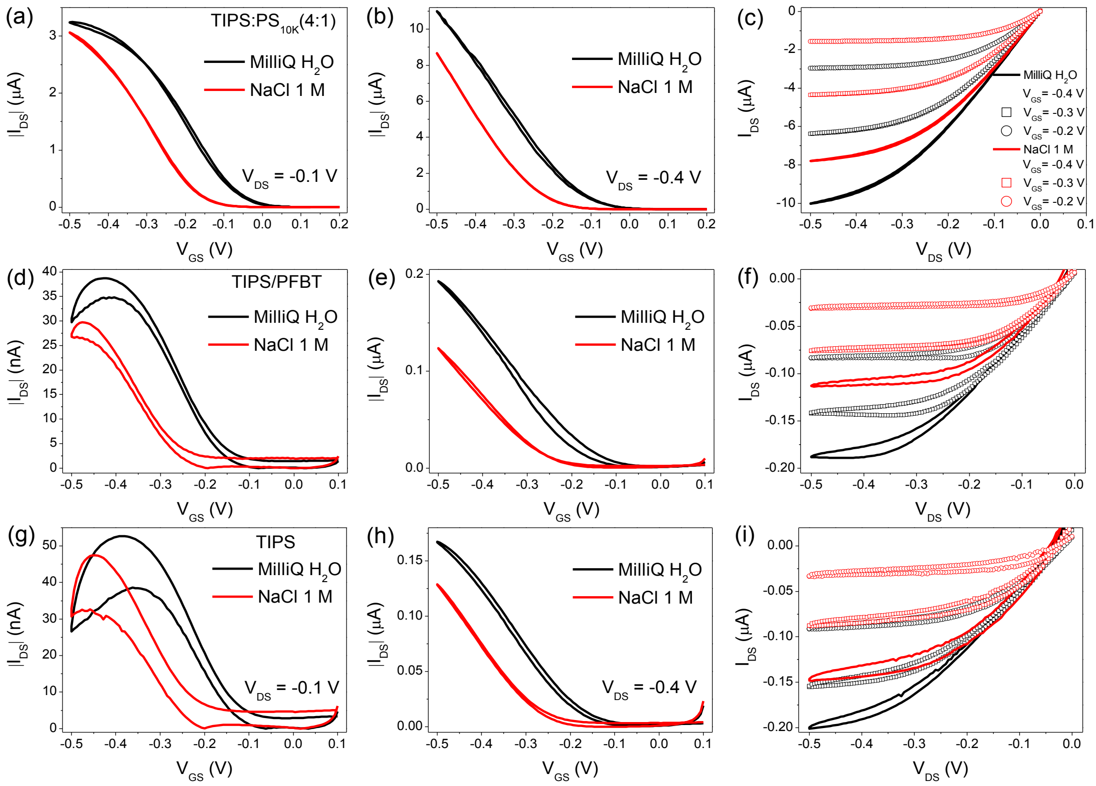

Figure 2.14: Transfer (linear and saturation regime) and output characteristics with MilliQ H_2O and NaCl 1 M as media recorded in (a-c) TIPS:PS$_{10K}$(4:1), (d-f) TIPS/PFBT and (g-i) TIPS based EGOFETs.

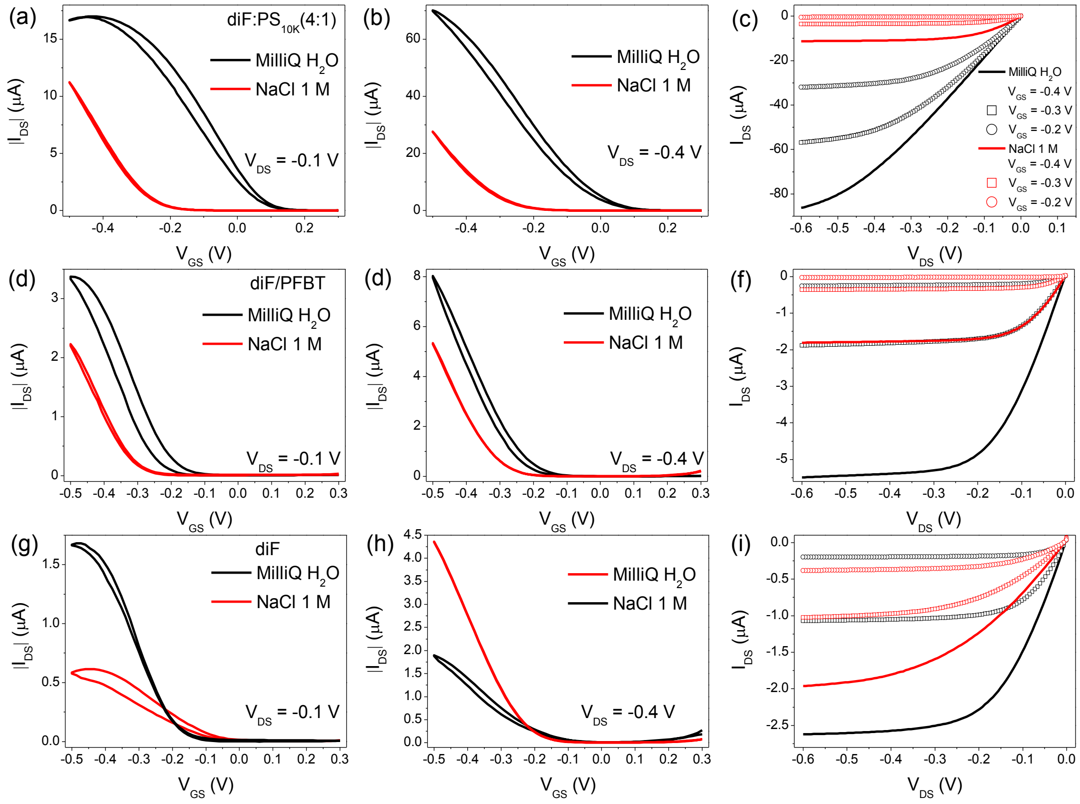

Figure 2.15: Transfer (linear and saturation regime) and output characteristics with MilliQ H_2O and NaCl 1 M as media recorded in (a-c) diF:PS$_{10K}$(4:1), (d-f) diF/PFBT and (g-i) diF based EGOFETs.

Aiming to the accurate calculation of μ and V_{th}, we firstly characterized the capacitance of the electrical double layer (C_{dl}) by carrying out two well-accepted tests: (i) electrochemical impedance spectroscopy (EIS)[38] and (ii) displacement current measurement (DCM).[39] The TIPS:PS$_{10K}$(4:1)/PFBT and diF:PS$_{10K}$(4:1)/PFBT thin films were selected for the above two tests. These experiments exploit the same device architecture and the only difference relies on the short-circuited *S*/*D* electrodes. The EIS measurement is capable to provide the capacitance response as a function of the voltage applied and frequency (see **Figure 2.16**).

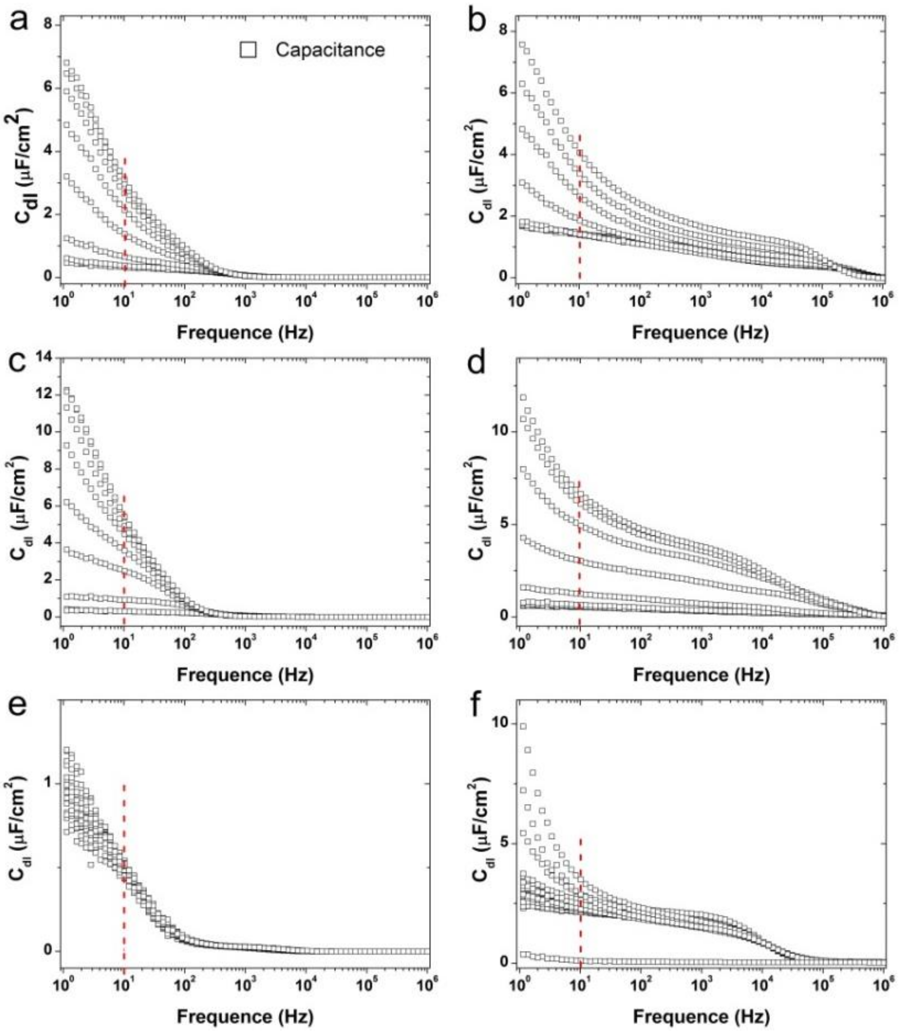

Figure 2.16: EIS measurements of TIPS:PS$_{10K}$(4:1)/PFBT-based device recorded at different DC voltages (from 0.1 V to -0.5 V with a pace of -0.1 V) under (a) MilliQ H_2O and (b) NaCl 1 M. EIS measurements of diF:PS$_{10K}$(4:1)/PFBT-based device in (c) MilliQ H_2O and (d) NaCl 1 M. EIS measurements of the uncoated device in (e) MilliQ H_2O and (f) NaCl 1 M.

Capacitance has been extracted from C_{dl}-V_G graphs at a fixed frequency equal to 10 Hz (see **Figure 2.17 (a)** and **(b)**), as already used in similar studies.[38,40] As reference, the same experiments were performed with the bare Au free of any thin-film (see **Figure 2.16 (e-f)**). According to EIS results, the C_{dl} values are 2.9 µF cm^{-2} (3.3 µF cm^{-2}) for TIPS:PS$_{10K}$(4:1)/PFBT and 5.3 µF cm^{-2} (6.1 µF cm^{-2}) for diF:PS$_{10K}$(4:1)/PFBT in MilliQ water (and in NaCl 1M) at V_{GS} = - 0.4 V. On the other hand, as a crosscheck, DCM was employed to confirm the C_{dl} extracted from EIS. The DCM experiments allowed us to monitor the peak current (i_p) caused by the accumulation/withdrawal of the charge carriers in the OSC thin film (see **Figure 2.18**). According to the analysis described in Chapter 5, the C_{dl} was extracted from the i_p *vs.* v plots (**Figure 2.17 (c)** and **(d)**).[35] As a result, the C_{dl} is 2.6 µF cm^{-2} (3.4 µF cm^{-2}) for TIPS:PS$_{10K}$(4:1)/PFBT and 4.5 µF cm^{-2} (7 µF cm^{-2}) for diF:PS$_{10K}$(4:1)/PFBT in MilliQ water (and in NaCl 1M). The two techniques gave coherent capacitance results (**Table 2.1**), therefore, we used the results extracted from the EIS measurements to calculate the field-effect mobility. For the sake of simplicity, the same C_{dl} values were employed for the other devices with the same type of OSC.

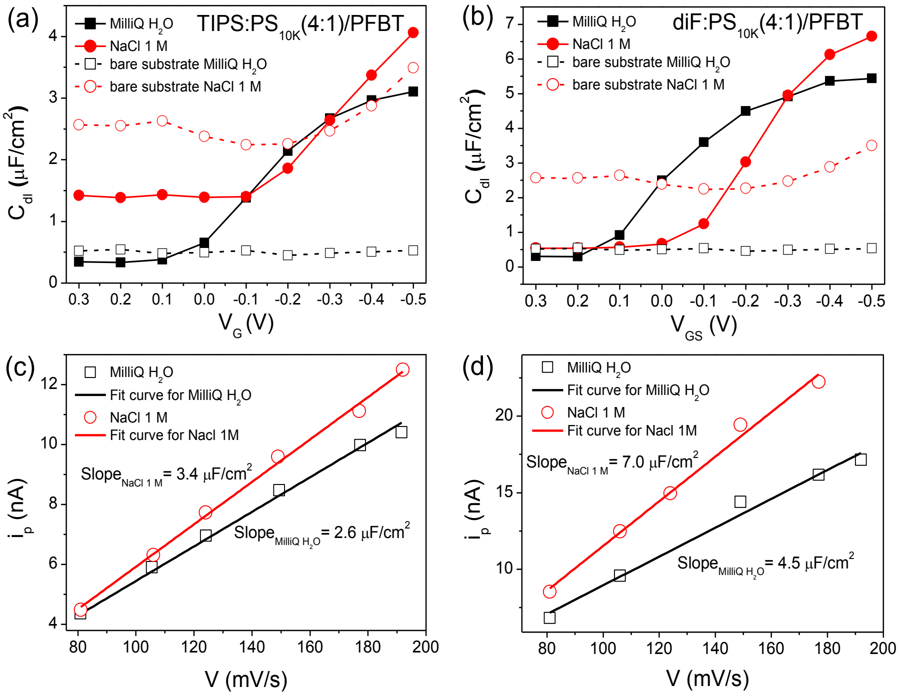

Figure 2.17: C_{dl} vs V_{GS} plots for (a) TIPS:PS$_{10K}$(4:1)/PFBT and (b) diF:PS$_{10K}$(4:1)/PFBT-based devices. Dashed black line (unfilled squares) is for MilliQ water and dashed red line (unfilled circles) stand for NaCl 1M related to bare Au. Solid lines (filled symbols) are the corresponding coated devices. Current peak (i_p) versus scan rate (v) plots are shown for (c) TIPS:PS$_{10K}$(4:1)/PFBT and (d) diF:PS$_{10K}$(4:1)/PFBT-based devices. Black line and empty squares correspond to the linear fit in MilliQ water; red lines and empty circles are linear fit in NaCl 1M solution.

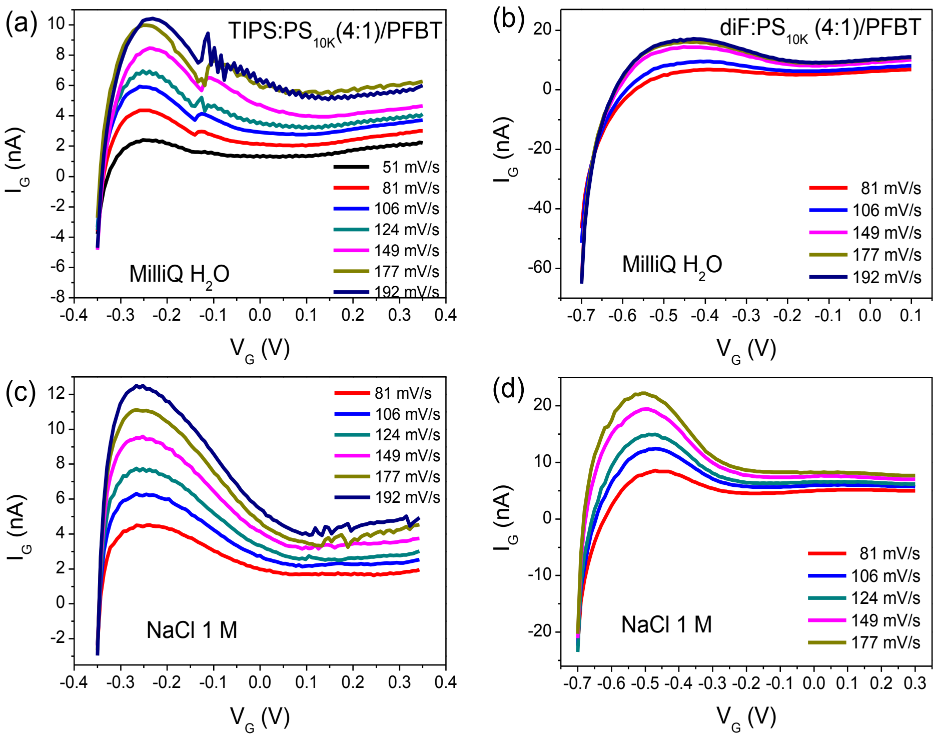

Figure 2.18: Overlay of DCM measurements at different scan rates of the TIPS:PS$_{10K}$(4:1)/PFBT-based device in (a) MilliQ H_2O and (c) NaCl 1 M solution. The same results of DCM for diF:PS$_{10K}$(4:1)/PFBT devices recorded in (b) MilliQ H_2O and (d) NaCl 1 M solution.

Table 2.1: Values of C_{dl} extracted by DCM and EIS techniques.

	Capacitance (μF/cm^2) (Method: EIS)		Capacitance (μF/cm^2) (Method: DCM)	
	MillQ H_2O	NaCl 1 M	MillQ H_2O	NaCl 1 M
TIPS:PS$_{10K}$(4:1)/PFBT	2.9	3.3	2.6	3.4
diF:PS$_{10K}$(4:1)/PFBT	5.3	6.1	4.5	7

According to the methodology reported in Chapter 5, the μ, V_{th}, I_{on}/I_{off} ratio and SS of all the devices have been extracted and their results are listed in **Table A.1** and **A.2**. The parameters from the eight devices studied more in-depth are summarized in **Table 2.2**. The data shown in **Table 2.2** include the average values together with the standard deviations extracted for at least 10 devices of each type. It is clear that the presence of both PS and PFBT are fundamental for achieving the top performance. Concerning the mobility, TIPS:PS$_{10K}$(4:1)/PFBT devices reach a μ equal to 0.12 ±0.01 cm^2 V^{-1} s^{-1} and 0.18 ±0.01 cm^2 V^{-1} s^{-1} for diF:PS$_{10K}$(4:1)/PFBT ones both extracted in MilliQ water. The device mobility has a 45-60% drop where the S/D electrodes have not been modified with PFBT. Furthermore, when PS is not present in the active material, the mobility dramatically decreases down to one or two orders of magnitude elucidating the major role that the polymer is playing. It is clear that the presence of both binder and PFBT are fundamental for achieving the best performances.[35] For all these reasons, we can safely state that the best EGOFET configurations are the TIPS:PS$_{10K}$(4:1)/PFBT and diF:PS$_{10K}$(4:1)/PFBT. Hence, our investigations have been further carried out only on these two types of devices.

Table 2.2: Field effect mobility (μ), threshold voltage (V_{th}), on/off ratio (I_{on}/I_{off}), and subthreshold swing (*SS*) extracted in saturation regime for the TIPS-pentacene and diF-TES-ADT based EGOFETs.

Device type	Media	μ (cm^2 V^{-1} s^{-1})*	V_{th} (mV)	I_{on}/I_{off}	SS (mV/dec)
TIPS:PS$_{10K}$(4:1)/PFBT	MilliQ H_2O	0.12	12(±2)	7.3×10^3	87(±3)
TIPS:PS$_{10K}$(4:1)		0.05	-112(±3)	6.1×10^3	80(±2)
TIPS/PFBT		0.002	-79(±1)	1.1×10^2	184(±1)
TIPS		0.001	-51(±1)	8.3×10^1	211(±7)
TIPS:PS$_{10K}$(4:1)/PFBT	NaCl 1 M	0.07	-166(±5)	1.0×10^4	77(±6)
TIPS:PS$_{10K}$(4:1)		0.02	-194(±5)	3.7×10^3	87(±9)
TIPS/PFBT		0.001	-156(±3)	1.8×10^2	100(±5)
TIPS		0.001	-129(±1)	4.1×10^1	208(±7)
DIF:PS$_{10K}$(4:1)/PFBT	MilliQ H_2O	0.18	49(±1)	1.5×10^4	82(±2)
DIF:PS$_{10K}$(4:1)		0.10	125(±1)	4.3×10^3	87(±7)
DIF/PFBT		0.04	-145(±3)	1.2×10^3	97(±5)
DIF		0.004	-28(±4)	1.6×10^2	121(±1)
DIF:PS$_{10K}$(4:1)/PFBT	NaCl 1 M	0.08	-19(±1)	9.7×10^3	86(±7)
DIF:PS$_{10K}$(4:1)		0.07	-152(±4)	8.6×10^3	86(±7)
DIF/PFBT		0.02	-200(±4)	1.6×10^3	87(±5)
DIF		0.02	-120(±2)	5.5×10^2	90(±4)

* All these values are affected by an error ranging from 2% to 20%.

2.2.3 Potentiometric Sensitivity and Switching Speed

Such promising results prompted us to perform a deeper investigation on the TIPS:PS$_{10K}$(4:1)/PFBT and diF:PS$_{10K}$(4:1)/PFBT EGOFETs by studying two important figure of merits, the potentiometric sensitivity and switching speed.[9,15,35,41] Details regarding the experimental setup and data analysis are described in Chapter 5. In general, the first test provides information about the lowest detectable voltage change, while the second measurement defines the temporal scale of the signal detected and the limit of the EGOFET in detecting short pulses.[35] Since MilliQ water represents our benchmark to assess the field-effect operation, we verified both TIPS:PS_{10K}(4:1)/PFBT and diF:PS_{10K}(4:1)/PFBT EGOFETs by means of different gate-source pulses (*viz.* ΔV_{GS}) ranging from 50 mV to 100 µV as voltage amplitudes, as shown in **Figure 2.19 (a)** and **(b)**. The potentiometric sensitivity of TIPS:PS_{10K}(4:1)/PFBT device turned out to be equal to 100 µV, whereas the diF:PS_{10K}(4:1)/PFBT one was capable to detect ΔV_{GS} equal to 200 µV. In both cases, the signal to noise ratio was equal to 50. The increase of the ionic strength, namely moving from MilliQ water to NaCl 1 M solution, did not affect the potentiometric sensitivity, although a worse signal to noise ratio was observed likely due to the negative V_{on} shift, as evidenced in **Figure 2.19 (c)** and **(d)**. The extracted potentiometric sensitivity values are listed in **Table 2.3.**

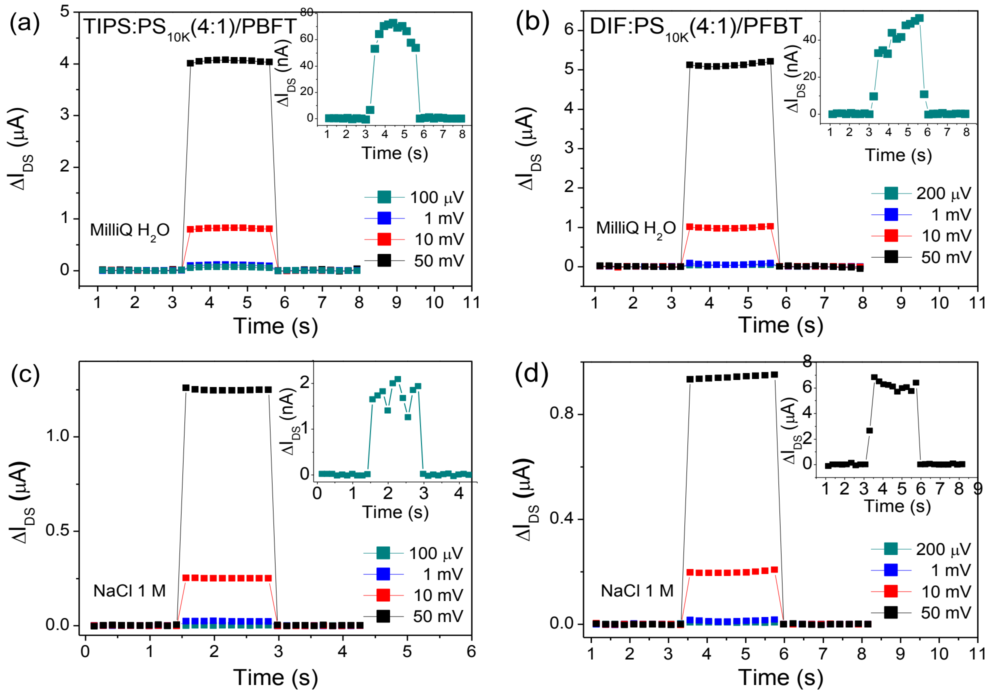

Figure 2.19: *I-t* plots recorded corresponding to different step potentials (ΔV_{GS}) with different amplitudes for TIPS:PS_{10K}(4:1)/PFBT-based EGOFET device in (a) MilliQ H_2O and (c) NaCl 1 M solution and for diF:PS_{10K}(4:1)/PBFT-based device in (b) MilliQ H_2O and (d) NaCl 1 M solution.

Regarding the switching speed, fixing V_{DS} and applying a square pulse at the V_{GS} yielded the current profile shown in **Figure 2.20.** When the V_{GS} switches from 0 V (OFF state) to -0.5 V (ON state), the I_{DS} increases sharply and then follows a saturation behavior over a short time. In contrast, the I_{DS} current recovers its initial value once the V_{GS} switches from -0.5 V (ON state) to 0 V (OFF state). The I_{DS} *vs* *t* plot shows a slight asymmetry between the switch-on (τ_{on}) and switch-off (τ_{off}) behaviors. The extracted τ values are also listed in **Table 2.3.** Importantly, our devices are at least one order of magnitude faster than EGOFETs previously reported, in which τ was equal to 4.6 ms and 50 ms for a pentacene evaporated film and a rubrene single crystal, respectively.[1,9] All the reported τ values here are lower than 1 ms, supporting the fact that no electrochemical doping is occurring and that the devices can work at frequencies higher than 1000 Hz.[12] The increase of the ionic strength induces an additional switch-on acceleration, which pushes τ values even beyond our instrumental I_{DS} recording (*i.e.* < 250 µs), as shown in **Figure 2.20 (c)** and **(d)**. This indicates that our system is mainly governed by the capacitance of TIPS:PS$_{10K}$/PFBT and diF:PS$_{10K}$(4:1)/PFBT films together with the electrolyte resistance,[42] hence the increase of the ionic strength lowers the electrolyte resistance and, consequently, τ.

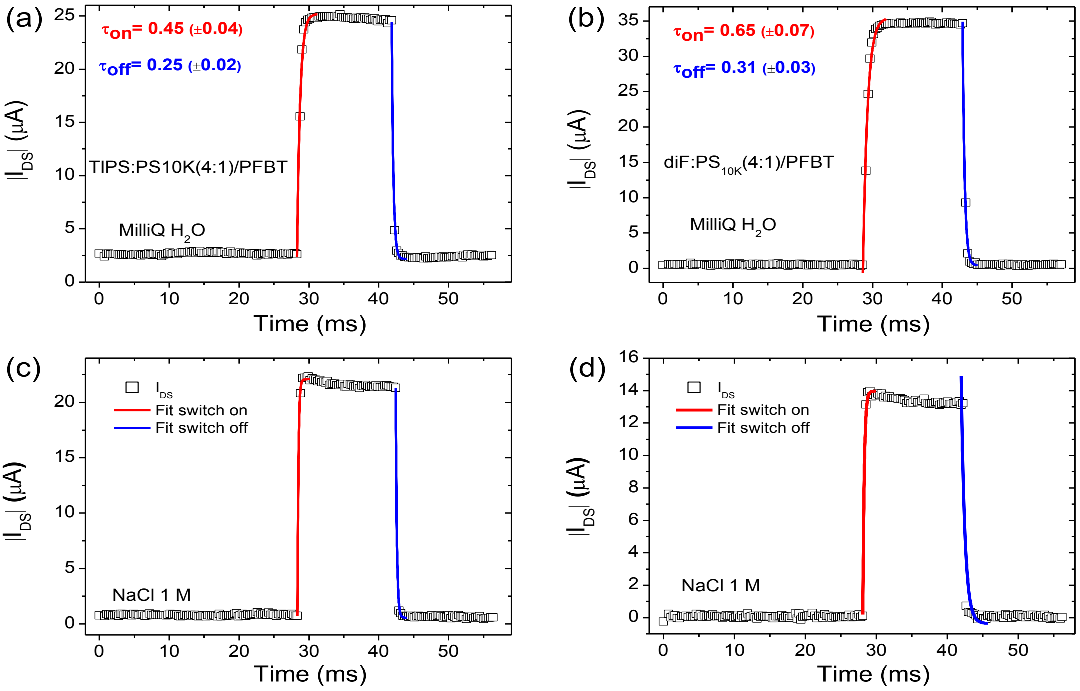

Figure 2.20: *I-t* plot of a step potential with amplitude equal to 0.5 V for TIPS:PS$_{10K}$(4:1)/PFBT-based EGOFET device in (a) MilliQ H_2O and (c) NaCl 1 M solution and for diF:PS$_{10K}$(4:1)/PBFT-based device in (b) MilliQ H_2O and (d) NaCl 1 M solution. All the measurements were recorded at V_{DS} = -0.4 V. Red and blue lines stand for the exponential fit related to the switch on and off of the device.

Table 2.3: Potentiometric sensitivity, switching speed and degradation speed in MilliQ H_2O and NaCl 1 M solution in the TIPS:PS_{10K}(4:1)/PFBT and diF:PS_{10K}(4:1)/PFBT EGOFET devices.

		TIPS:PS_{10K}(4:1)/PFBT		diF:PS_{10K}(4:1)/PFBT	
		MilliQ H_2O	NaCl 1 M	MilliQ H_2O	NaCl 1 M
Potentiometric sensitivity (μV)		100	100	200	200
Switching speed	τ_{on} (ms)	0.45±0.04	<0.25	0.65±0.07	<0.25
	τ_{off} (ms)	0.25±0.02	<0.25	0.31±0.03	<0.25
Degradation speed	Current monitoring (%/hour)	3.4	30.9	3.9	21.6
	Shelf stability (%/day)	11.6	12.3	6.9	9.1

2.2.4 Stability Measurements

Electrical stability is a great challenge in the field of organic electronics operated in aqueous media.[10,11] The majority of EGOFET devices provide reliable data for standard experiments demanding only single-spot measurements within a time-scale of a few hours. This limited water stability restricts the number of organic semiconductors that can be applied in EGOFETs and it is surely the main bottleneck that hampers the real application of these devices. According to our electrical characterization, no signs of electrochemical doping have been observed.[10] For all these reasons, we undertook a manifold approach in order to investigate in depth the stability of the TIPS:PS_{10K} (4:1)/PFBT and diF:PS_{10K}(4:1)/PFBT-based EGOFETs. *In-situ* real-time monitoring, bias stress and shelf stability are three different tests employed to evaluate the long time operation of the EGOFETs (see Chapter 5 for the detailed description of the experimental setup).

In the first test, the I_{DS} current is monitored *versus* time at a fixed V_{GS} and V_{DS} (*i.e.* V_{GS} = -0.4 V and V_{DS}= -0.4 V). The responses of two EGOFETs are displayed in **Figure 2.21**. In MilliQ water, both EGOFETs show a similar behavior, where I_{DS} undergoes a first transient increase (namely, within 30 min) and a consequent slow decrease with a total current loss of 35 ~ 40% within 11 hours (see **Figure 2.21 (a)** and **(b)**). In NaCl 1 M solution (**Figure 2.21 (c)** and **(d)**), the two active materials differ in I_{DS} lowering, being the effective loss 31 %/hour and 25 %/hour for TIPS:PS_{10K}/PFBT and diF:PS_{10K}(4:1)/PFBT, respectively (see **Table 2.3**). This clearly shows that the second device is more stable than the first one, even though both EGOFETs are still effectively working with weaker performances. This difference in stability between both materials could be attributed to a more favorable OSC/electrolyte interface in diF-TES-ADT-based devices probably due the larger crystallites present in these thin films. In addition, the increased ionic strength of the aqueous media does not allow us to observe the transient I_{DS} increase, which is present when we were using MilliQ water. This is likely due to the slower polarization process in MilliQ water compared to saline solutions. It should be emphasized that despite the devices are significantly diminishing their performance upon continuous operation, to our knowledge, there are no precedents of EGOFETs device working for such a long time in these conditions.[11]

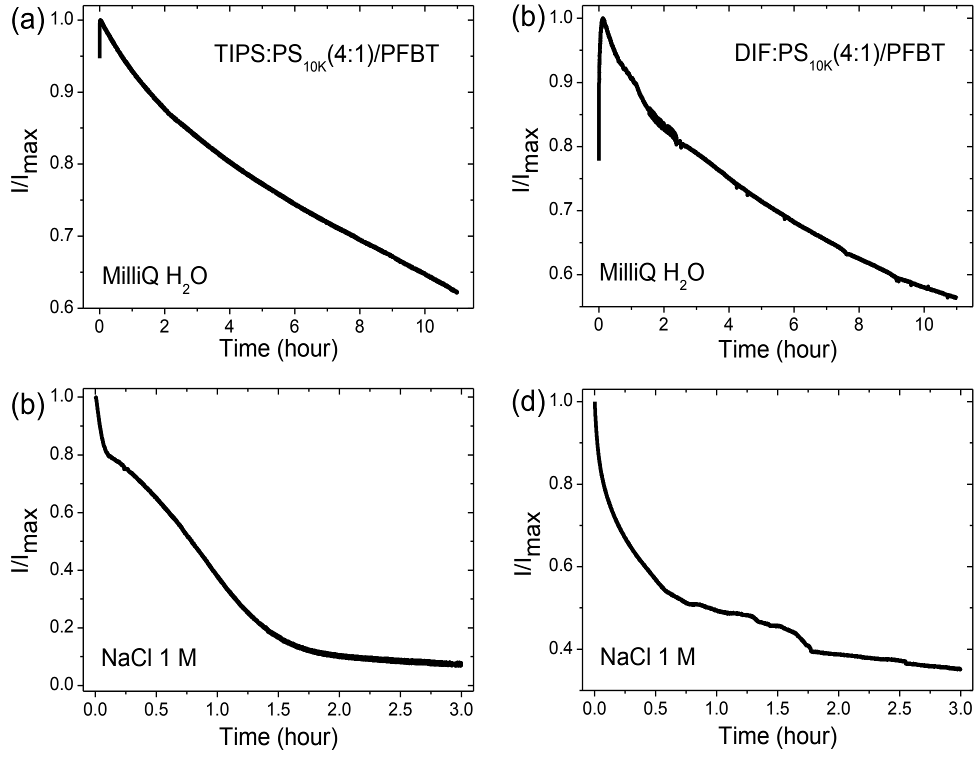

Figure 2.21: *I-t* plot of TIPS:PS_{10K}(4:1)/PFBT-based EGOFET devices operated in (a) MilliQ water and (c) NaCl 1M solution. The same *I-t* plot of diF:PS_{10K}(4:1)/PFBT-based EGOFET devices operated in (b) MilliQ water and d) NaCl 1M solution. All measurements were carried out in saturation regime (V_{DS} = -0.4 V, V_{GS} = -0.4 V).

Bias stress measurements were also carried out in MilliQ water and NaCl 1 M solution, as reported in **Figure 2.22**. This is a common characterization test in standard OFET devices, but has not been performed in water gated transistors.[43] Our results recorded in EGOFET configuration are completely coherent with the previous stability tests. It has been not only observed the electrical polarization occurring at the beginning of the experiment in MilliQ water case, but also the higher stability of diF:PS$_{10K}$(4:1)/PFBT with respect to TIPS:PS$_{10K}$(4:1)/PFBT (see **Figure 2.22 (a)** and **(b)**). As a result, the former shows a small V_{on} shift during 2 hours of stress, whereas the latter undergoes a worsening in mobility after 30 minutes of bias-stress. In addition, a more pronounced decrease is observed by working with NaCl 1 M solution, which is consistent with the results presented up to now (see **Figure 2.22 (c)** and **(d)**).

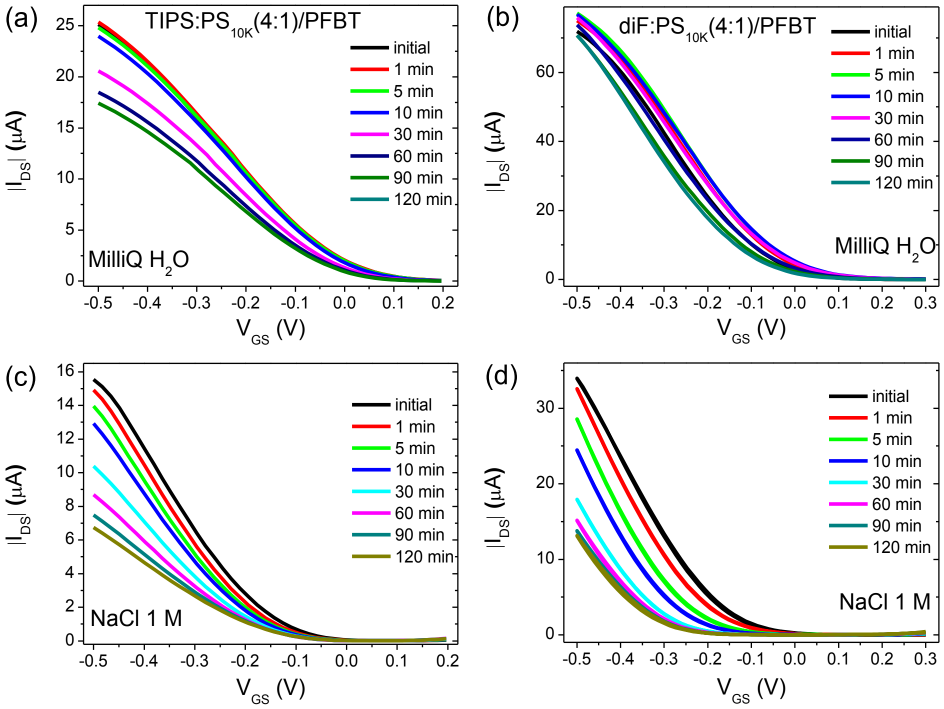

Figure 2.22: *I-V* transfer characteristics during the bias-stress experiment for TIPS:PS$_{10K}$(4:1)/PFBT-based EGOFET device in (a) MilliQ H_2O and (c) NaCl 1 M solution and for diF:PS$_{10K}$(4:1)/PBFT-based device in (b) MilliQ H_2O and (d) NaCl 1 M solution. For sake of clarity, only some measurements have been shown. All the *I-V* transfer characteristics were automatically recorded after 1 minute of electrical stress (V_{GS} = -0.4 V, V_{DS} = -0.4 V).

Some specific electronic applications might need few single-spot measurements within a long period of time. Aiming at this particular usage, the so-called shelf-stability has been devised. Clearly, the devices still work within a period of 7 days as displayed in **Figure 2.23**, even in the harsher aqueous medium. Again, diF:PS10K(4:1)/PFBT-based EGOFET is mostly affected by a negative V_{on} shift, whereas the TIPS:PS$_{10K}$(4:1)/PFBT-based device is additionally affected by a mobility worsening. However, both devices still work within this period, even in the harsher aqueous media. All these tests not only prove the good electrical performances of these two EGOFET devices but also point towards their potential applicability in saline aqueous media.

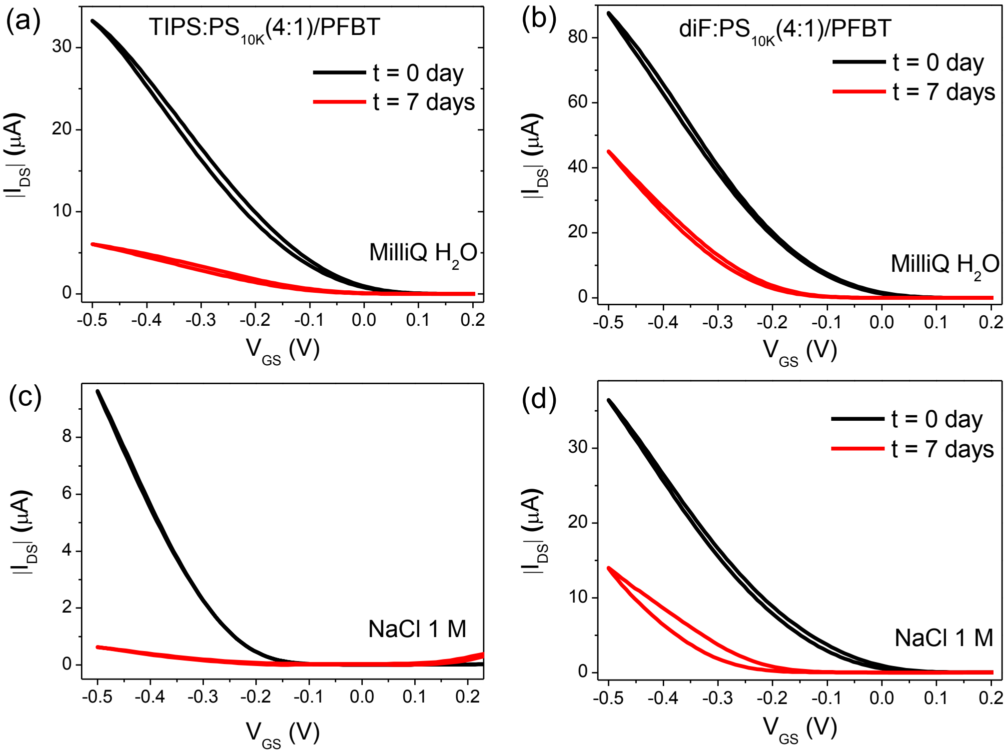

Figure 2.23: *I-V* transfer characteristics at the beginning (black line) and after one week (red line) of TIPS:PS$_{10K}$(4:1)/PFBT-based EGOFET device in (a) MilliQ water and (c) NaCl 1 M solution and for diF:PS$_{10K}$(4:1)/PBFT-based device in (b) MilliQ H_2O and (d) NaCl 1 M solution.

2.3 DPTTA:PS Blend

The *p*-type semiconductor meso-diphenyltetrathia[22]annulene[2,1,2,1] (DPTTA) is a circular annulene having the chemical structure shown in **Figure 2.28**. The charge transport properties were firstly documented by Singh *et al.* in 2011,[25] where they reported a fairly good OFET field-effect mobility of 0.7 cm^2 V^{-1} s^{-1} in a single-crystal and 0.29 cm^2 V^{-1} s^{-1} in an evaporated thin film.[25] Lately, DPTTA was exploited as active material in organic electronics by different research groups.[29,30] For instance, it has been exploited as the donor component in donor/acceptor co-crystals exhibiting ambipolar characteristics with high hole- and electron-mobilities.[30]

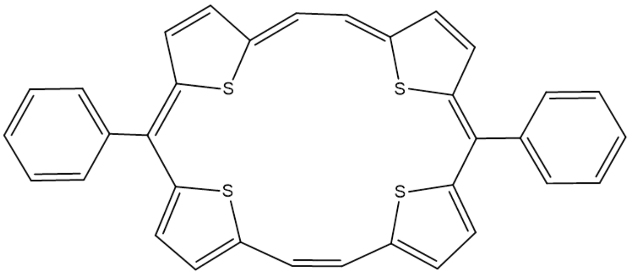

Figure 2.28: Chemical structure of DPTTA.

Despite the high potential of this material as active component in OFETs, up to date, it had not been processed yet in thin-film by any solution processing method, leaving the door open for further improvement in terms of both performance and processability. Our fabrication approach, that has achieved excellent results with the two previous OSCs, has been adapted to this material for the fabrication of OFETs and EGOFETs.

Our preliminary experiments aimed to obtain a homogeneous DPTTA-based thin film on Si/SiO$_2$ substrate by varying different fabrication parameters, like ink formulation (*i.e.* the OSC:PS blend ratio, the Mw of PS binder polymer), and coating conditions (*i.e.* the functionalization of the *S*/*D* electrode with PFBT and deposition speed, *etc.*). As a result the optimized formulations have the following parameters:

For OFET fabrication:

- Formulation: DPTTA:PS$_{10K}$ mixed in a 1:2 ratio, 22.6 mg/mL
- Solvent: Chlorobenzene

- S/D coating: 2,3,4,5,6-Pentafluorothiophenol (PFBT)
- Coating parameters: 1 cm/s at 105 °C.

For EGOFET fabrication:

- Formulation: DPTTA:PS_{10K} mixed in a 1:3 ratio, 20 mg/mL
- Solvent: Chlorobenzene
- S/D coating: 2,3,4,5,6-Pentafluorothiophenol (PFBT)
- Coating parameters: 1 cm/s at 105 °C.

In this case the two measuring configurations, *i.e.* OFET and EGOFET, have their own optimized formulation contrarily to the OSCs reported in the previous sections where a unique formulation was found optimal for both types of devices. In addition, following the same labelling protocol used in the previous cases, the two formulations are defined as DP:PS_{10K}(1:2)/PFBT and DP:PS_{10K}(1:3)/PFBT, respectively. The additional data related to DPTTA can be found in **Appendix A.3**[*], and a complete resume of the preliminary screening tests performed on DPTTA can be found in **Table A.3**.

2.3.1 Morphological Characterization of the Blend Thin-film[&]

As mentioned before, DPTTA is a quite unexplored OSCs and this work represents the first attempt to prepare solution-processed thin films by using this material in combination with an insulating polymer (*i.e.* PS). The single component solution, free of any insulating binder, resulted in a none homogenous thin film due to the low solubility of this material and the low viscosity of the solution. Hence, blending solutions of DPTTA in a concentration not exceeding 7.5 mg/ml, with PS has revealed to be essential for the formation of continuous thin films.

In general, BAMS is performed by means of a metallic bar which, unfortunately, was not suitable for the deposition of DPTTA:PS due to the preferred interaction of this solution with the metallic surface compared to the target substrate,[44] as evidenced in

---

[*] The characterization data of the samples prepared during the optimization process (optical microscopy, OFET electrical performance and EGOFET configuration with MilliQ water and NaCl 1 M solution as media) can be found in Appendix A.3.

[&] This work was carried out in collaboration with Dr. Antonio Campos Garcia.

Figure 2.29 (a) and **(b),** where an amorphous and more continuous film is shown. Interestingly, the problem was overcome by employing a polytetrafluoroethylene (PTFE) bar (see **Figure 2.29 (c)** and **(d)**) which promote a more favorable meniscus shape due to its hydrophobicity. A similar observation has been reported by Giri *et al.*, who have employed an octadecyltrichlorosilane (OTS)-modified plate during the shearing deposition of an OSC to enhance the OFET performance.[23] Furthermore, a pre-heating of the blend solution was required for achieving a high reproducibility coating and to reduce device-to-device variation.

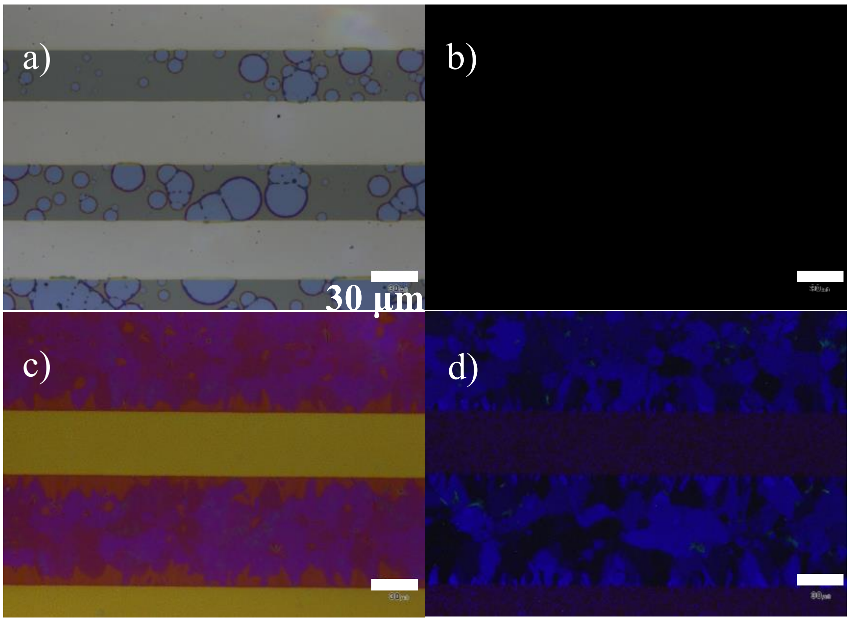

Figure 2.29: Optical microscope images of films deposited (a) (b) with a metal bar and (c) (d) with a PTFE bar. On the left, polarizer/analyzer = 0°. On the right, polarizer/analyzer = 90°.

The optical microscopy images of the optimized films, *i.e.* DP:PS$_{10K}$(1:2)/PFBT and DP:PS$_{10K}$(1:3)/PFBT, are shown in **Figure 2.30**. The two thin films exhibit a different crystallinity with bigger grains located on the channel area and smaller domains on the Au/PFBT regions. Moreover, wave-like microstructures can be noticed in the channel region, especially in the DP:PS$_{10K}$ (1:3)/PFBT case which is further confirmed by the AFM images of **Figure 2.31.** Such texture increases the roughness σ_{rms} of the thin films up to 16.8 nm and 15.4 nm for DP:PS$_{10K}$(1:2)/PFBT and DP:PS$_{10K}$(1:3)/PFBT, respectively. Furthermore, the phase contrast shows a negligible change in the surface energy between the two regions of the transistor (see **Figure 2.32**), suggesting that the active layer is everywhere covered by a PS encapsulating layer.[44]

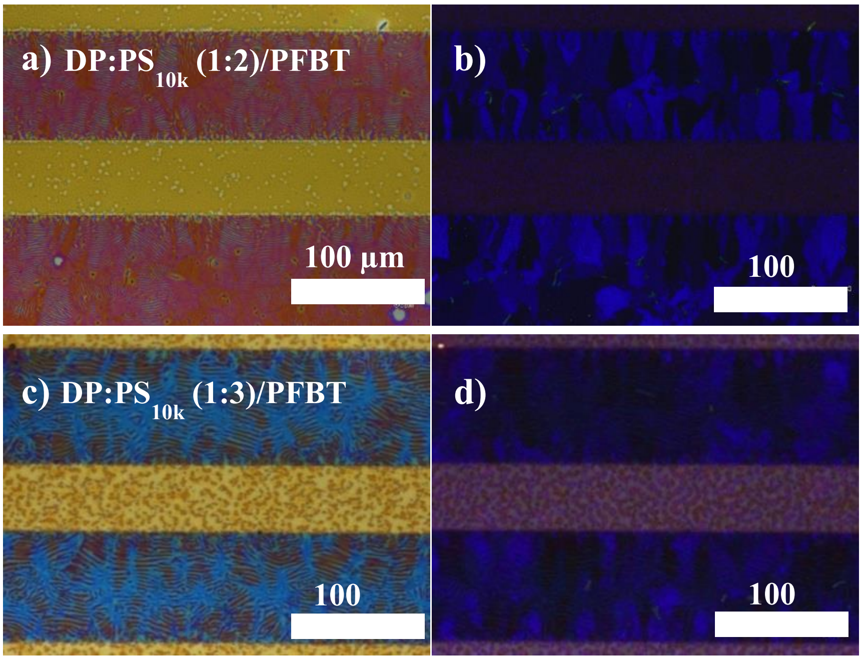

Figure 2.30: Optical microscope of (a) (b) DP:PS$_{10K}$(1:2)/PFBT and (c) (d) DP:PS$_{10K}$(1:3)/PFBT thin film. On the left, polarizer/analyzer = 0°. On the right, polarizer/analyzer = 90°.

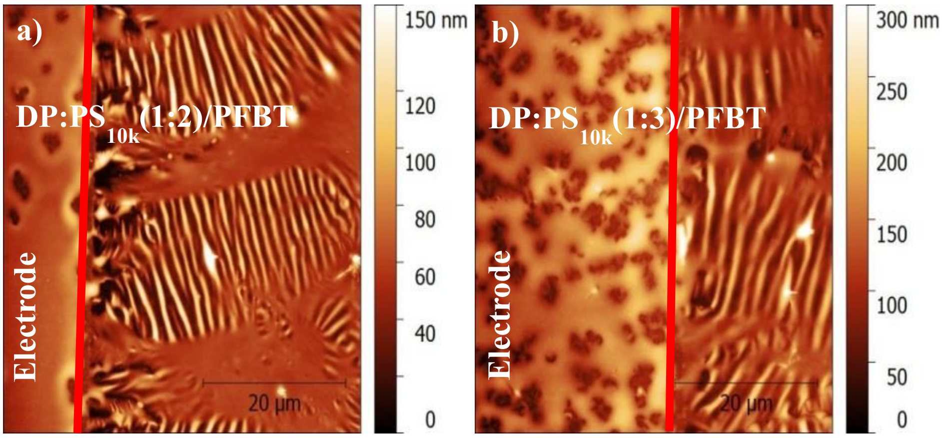

Figure 2.31: AFM images of (a) DP:PS$_{10K}$(1:2)/PFBT and (b) DP:PS$_{10K}$(1:3)/PFBT thin film.

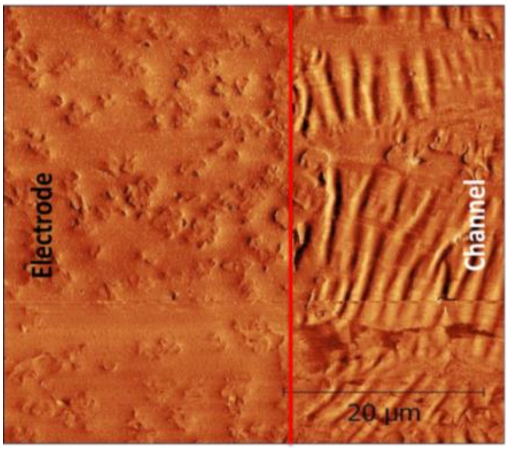

Figure 2.32: Phase AFM image of DP:PS$_{10K}$(1:3)/PFBT thin film.

Furthermore, X-ray powder diffraction (XRPD) analysis of the films confirmed that all the films belong to the same crystalline phase, as shown in **Figure 2.33**. Additionally, the crystalline phase observed in the films does not seem to correspond to the reported one for the single crystal (SC).[45] The reflections cannot be associated to any (0 0 n) crystallographic plane due to the lack of periodicity in the peaks spacing in the diffractogram. This indicates that the crystals are not oriented with respect to the substrate, which could be expected because of the wave-like microstructure of the film. This different polymorph of DPTTA may be associated to a surface promoted growth as it has been commonly observed in other OSCs such as in tetrathiafulvalene derivatives.[46,47]

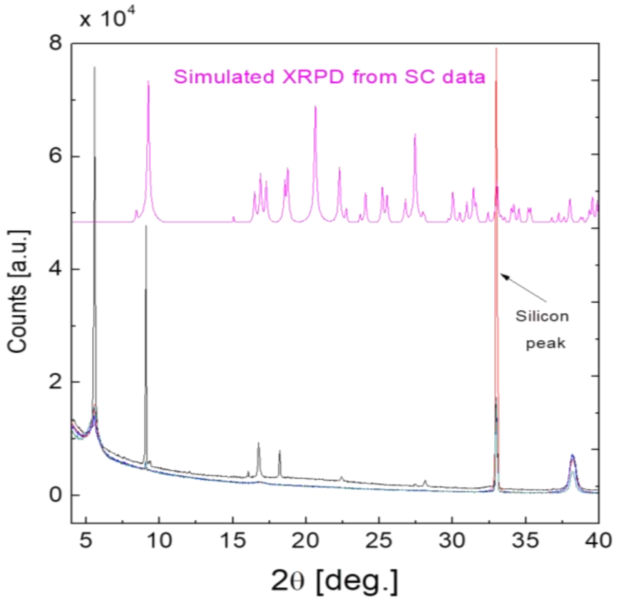

Figure 2.33: X-ray powder diffraction of the films fabricated.

2.3.2 Electrical Performance

BG/BC architecture with Si/SiO_2 serving as gate electrode/dielectric was employed to evaluate the OFET electrical characteristics of the two DP:PS formulations. As reported in **Figure 2.34**, the transfer and output characteristics show a clear *p*-type behavior with no hysteresis in both cases. The corresponding parameters of the two formulations are summarized in **Table A.3**. Among them, the V_{th} close to 0 V and the sharp switch on represented by a small sub-threshold swing are indicators of the good quality of the films. Furthermore, the two devices exhibited a fairly high, over 0.5 cm^2 V^{-1} s^{-1}, average field effect mobility. Remarkably, the OFETs based on DP:PS$_{10K}$(1:2)/PFBT thin films show an average mobility of 1 cm^2 V^{-1} s^{-1}. This value is larger than the one reported for the single crystal (0.7 cm^2 V^{-1} s^{-1}) suggesting that probably this new polymorph possesses better electronic transport properties than the previously reported single crystal polymorph.

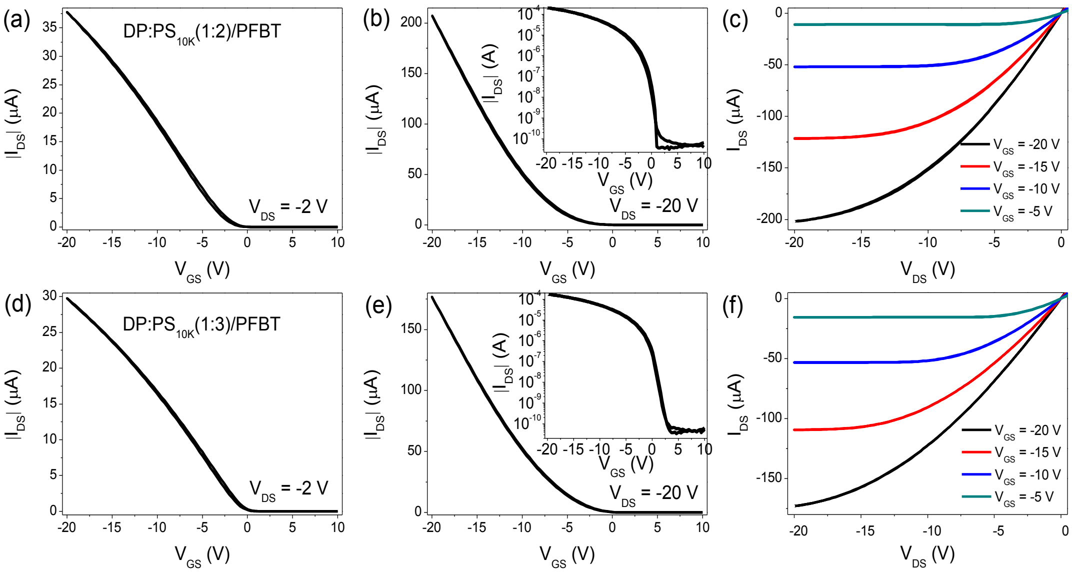

Figure 2.34: Transfer characteristics in (a) linear and (b) saturation regime, and (c) output characteristics in a DP:PS$_{10K}$(1:2)/PFBT-based device with W/L = 100. The inset in (b) is the corresponding Log-Lin plot. Transfer in (d) linear and (e) saturation regime, and (f) output characteristics of a DP:PS$_{10K}$(1:3)/PFBT-based OFET device with W/L = 100.

Moving from OFET to EGOFET configuration, the optimized formulation DP:PS$_{10K}$(1:3)/PFBT has been employed for the characterization in MilliQ H_2O and NaCl 0.5 M solution. As expected, the EGOFET transfer and output characteristics exhibit clearly *p*-type behavior in both media with anti-clockwise hysteresis (**Figure 2.35**). This evidence suggests the presence of some traps on the thin film surface probably caused by the high surface roughness (σ_{rms} ~ 15.4 nm). Furthermore, it is worth noting that no negative V_{th} shifting is observed when the device is measured in NaCl 0.5 M solution, which is common due to the "ionic screening" effect.[50] Unfortunately, the reason behind this behavior is unclear and further study is required.

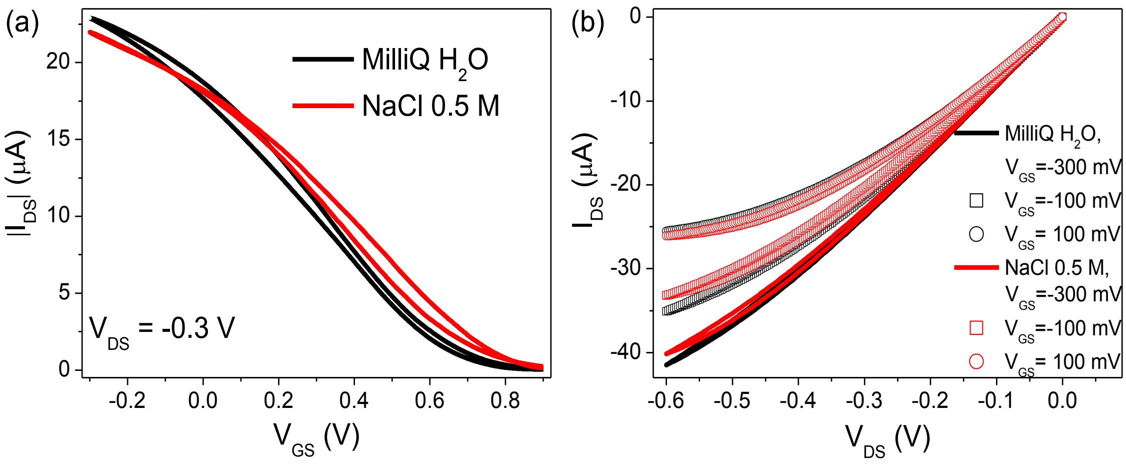

Figure 2.35: (a) Transfer and (b) output characteristics of a DP:PS$_{10K}$(1:3)/PFBT-based EGOFET device in MilliQ water and in NaCl 0.5 M solution.

In order to calculate the EGOFET mobility, EIS measurements were carried out to extract the electrical double layer capacitance (C_{dl}). Capacitance responses in MilliQ water and NaCl 0.5 M solution were recorded at different DC voltages, as shown in **Figure 2.36 (a)** and **(b)**. The corresponding C_{dl}-V_G plots, extracted at a frequency of 10 Hz, are displayed in **Figure 2.36 (c)** and **(d)**. The C_{dl} trend shows the transition from OFF to ON state in the DP:PS$_{10K}$(1:3)/PFBT-coated thin film, whereas no similar behavior is observed in OSC coating-free substrates. The C_{dl} was equal to 1.2 μF cm^{-2} and 3.4 μF cm^{-2} in MilliQ water and NaCl 0.5 M, respectively. These values are comparable to our previous investigation on OSC:PS blends thin films (*i.e.* TIPS:PS and DIF:PS).[35] The corresponding mobility (μ) and V_{th} in EGOFET configuration are listed in **Table A.3**. Charge carrier mobility is impressively high (0.12±0.03 cm^2 V^{-1} s^{-1} for MilliQ water and 0.03±0.01 cm^2 V^{-1} s^{-1} for NaCl 0.5 M solution, respectively) but, as expected, the EGOFET displays a lower value compared to the OFET due to the high dielectric constant of the aqueous media.[48] Notably, this drop of mobility is not even one order of magnitude lower compared to the back-gated OFET, as it was previously observed in the case of TIPS-pentacene and diF-TES-ADT.[35]

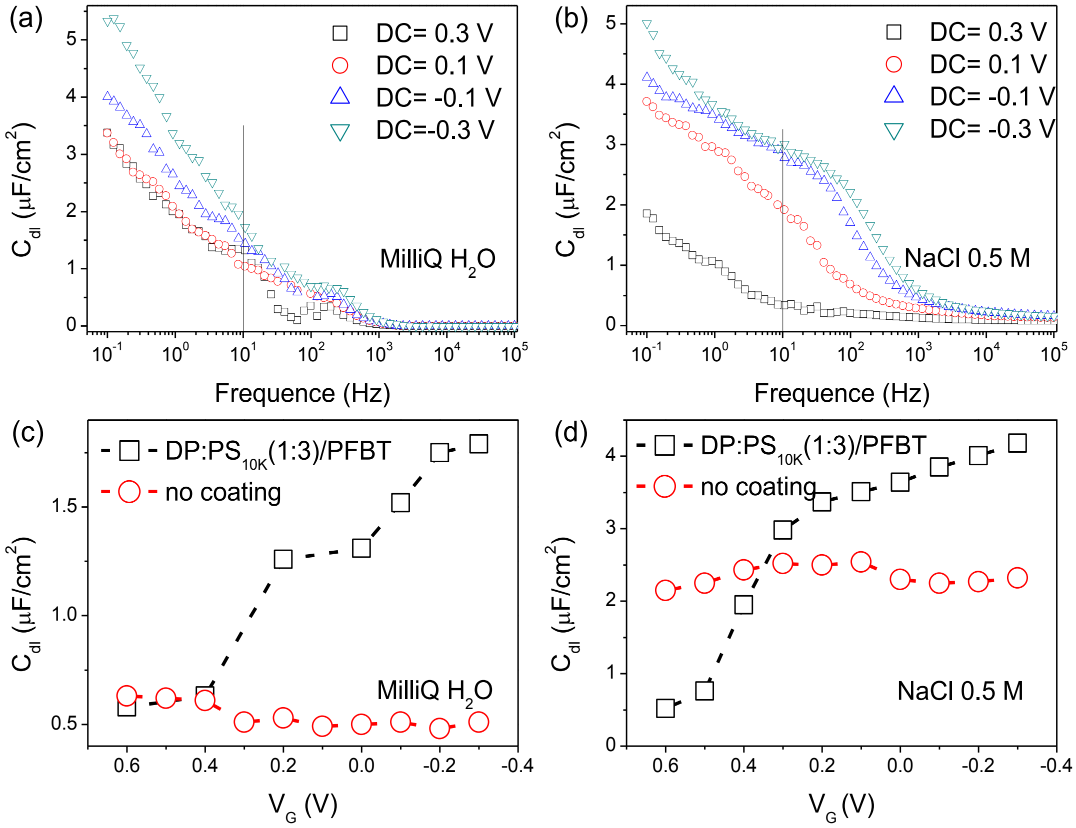

Figure 2.36: EIS measurements of the DP:PS$_{10K}$(1:3)/PFBT-based device recorded at different DC gate voltages (from 0.3V to -0.3 V with a pace of -0.2V) under (a) MilliQ H_2O and (b) NaCl 0.5 M solution. C_{dl} versus V_G plot of the same blend under (c) MilliQ H_2O and (d) NaCl 0.5 M solution. The red trace represents the OSC free-coating reference device.

2.3.3 Potentiometric Sensitivity and Switching Speed

As mentioned before, EGOFETs are promising candidates for sensor platforms due to their ability to easily transduce a chemical or biological signal into a measurable electric current.[7,9,10] Therefore, the potentiometric sensitivity and switching speed measurements are two figures of merits which have been extracted for the EGOFET based on DP:PS$_{10K}$(1:3)/PFBT. As shown in **Figure 2.37 (a)**, DP:PS$_{10K}$(1:3)/PFBT is able to detect a gate voltage step as low as 200 μV in MilliQ water while, the lowest detectable value was 500 μV in NaCl 0.5 M media due to the higher electrical noise (see **Figure 2.37 (b)**). The switching speed test recorded in the two electrolytic media was defined by a square pulse of V_{GS} (1.2 V for OFF and 0 V for ON), as displayed in **Figure 2.37 (c)** and **(d)**. The τ_{ON} and τ_{OFF} values were extracted according to the methods described in Chapter 5 and summarized in **Table 2.7**. However, the values are one order of magnitude lower than those observed for TIPS-pentacene and diF-TES-ADT blends.

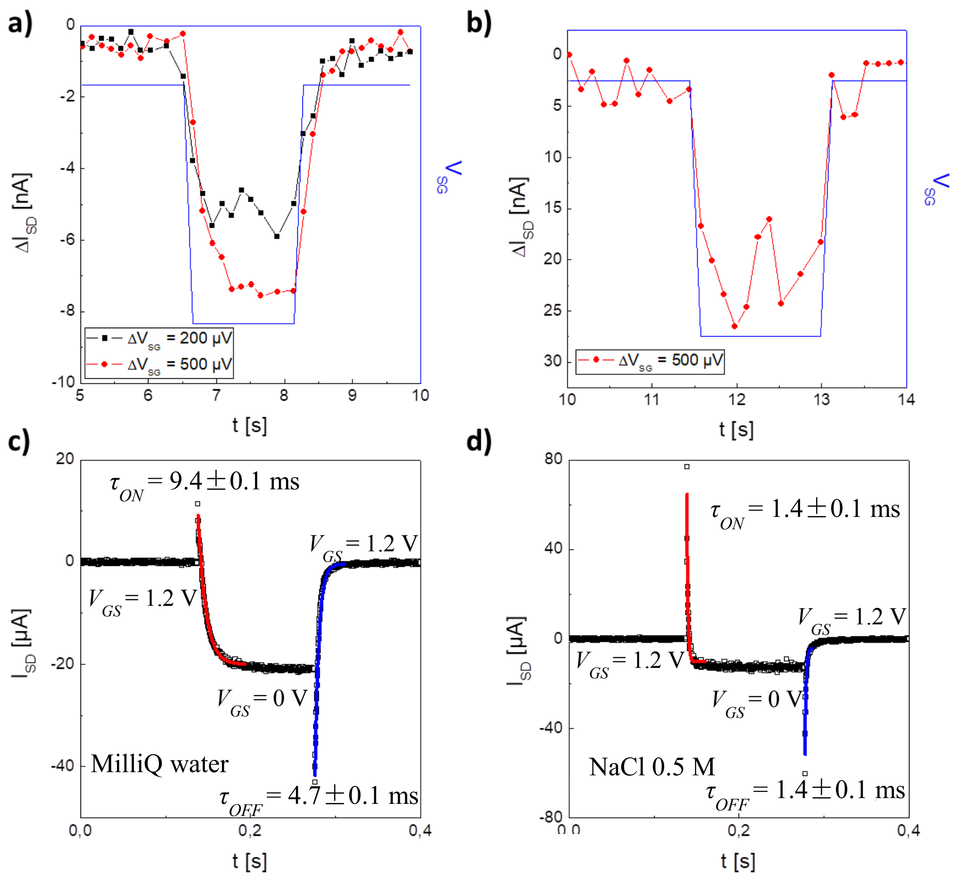

Figure 2.37: Potentiometric sensitivity of EGOFETs measured when (a) MilliQ water and (b) NaCl 0.5 M is used as dielectric. Switching speed measurement with the exponential fit used to obtain the turn on and off time using (c) MilliQ water and (d) NaCl 0.5 M. In all measurements the V_{DS} was 300 mV.

Table 2.7: Potentiometric sensitivity, switching speed and degradation speed found in DP:PS$_{10K}$(1:3)/PFBT-based EGOFETs.

Media	Potentiometric sensitivity (µV)	τ_{on} (ms)	τ_{off} (ms)	Max. *P.S.* (µV)	Degradation speed (%/h)
MilliQ H_2O	200	9.4	4.7	200	3.5
NaCl 0.5 M	500	1.3	1.4	500	19.5

2.3.4 Stability Measurements

Stability measurements represent the last figure of merit for depicting the quality of an EGOFET device. **Figure 2.38** displays the *in-situ* real-time recording of an

EGOFET based on DP:PS$_{10K}$(1:3)/PFBT at V_{DS} = 300 mV and V_{GS} = 0 mV in MilliQ water and NaCl 0.5 M. This kind of electrical tests are usually desirable if the platform is envisioned for monitoring the presence of a certain analyte, *i.e.* a water pollutant, a specific biomolecule, *etc.*[49] As displayed in **Figure 2.38 (a)**, the I_{DS} current drops quickly during the first 2 hours and then it continues to decrease displaying a total current loss of 30% at the end of the test. The degradation speeds in both media are summarized in **Table 2.7**. In addition, transfer characteristics were recorded before and after the stability experiment (insert of **Figure 2.38 (a)**), and a small negative shift of V_{th} was observed which is a normal consequence of the prolonged electrical test. As expected, in NaCl 0.5 M the current degradation is faster and it occurred within just 3 hours of electrical monitoring (**Figure 2.38 (b)**).

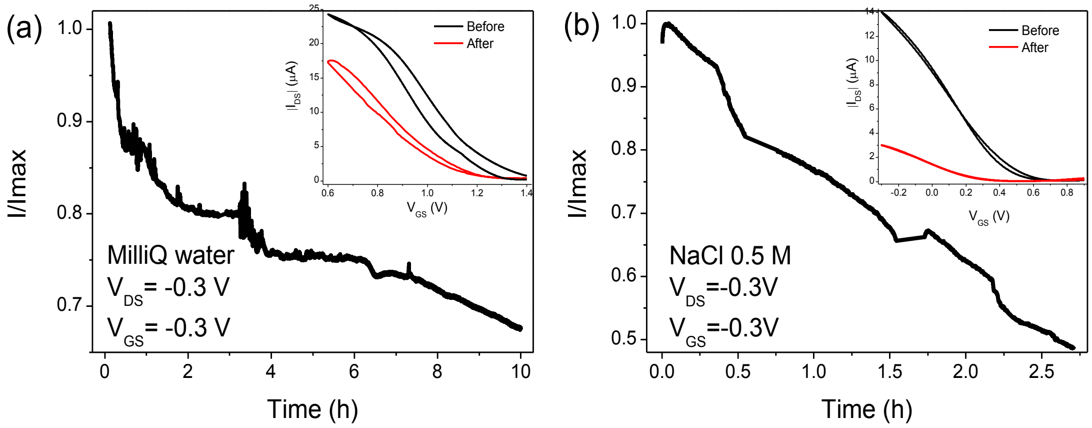

Figure 2.38: Real-time current monitoring of DP:PS$_{10K}$(1:3)/PFBT-based EGOFET device with (a) MilliQ water and (b) NaCl 500 mM solution as media. The insert of each figure was the transfer characteristic measured before and after the current monitoring.

2.4 PDPP-TT(1)-SVS(9):PS Blend

The organic semiconductor poly[2,5-bis(7-decylnonadecyl)pyrrolo[3,4-c]pyrrole-1,4(2H,5H)-dione-2,2'-bithieno[3,2-b]thiophene]-co-[2,5-bis(7-decylnonadecyl)pyrrolo[3,4-c]pyrrole-1,4(2H,5H)-dione-(E)-(1,2-bis(5-(thiophen-2-yl)selenophen-2-yl)ethene)] (PDPP-BTT-SVS) is a donor-acceptor random co-polymer which belongs to the class of polymer semiconductors, contrarily to the three OSCs previously presented. The chemical structure of this polymer is shown in **Figure 2.39**. This polymer OSC exhibits good solubility in various non-chlorinated and chlorinated solvents because the random copolymerization strategy is helpful to increase the solubility of the donor-acceptor copolymers.[27]

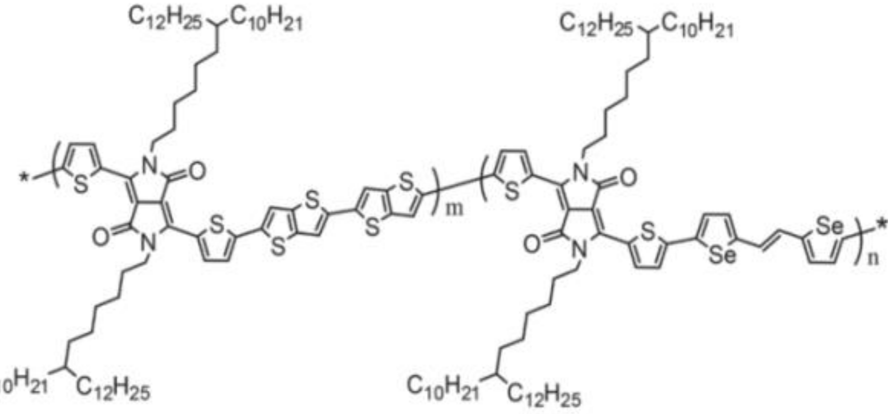

n = 9, m = 1, PDPP-BTT (1)-SVS (9)

Figure 2.39: Chemical structure of the PDPP-BTT(1)-SVS(9)

The outstanding performance of this material has already been reported by Kim *et al.* which have studied how the co-polymer composition affects the electrical behavior once this material is employed in OFETs.[26] However, this OSC was solely processed *via* spin coating and measured under controlled atmosphere thus, its exploitation with roll-to-roll compatible techniques or the electrical response recorded under ambient atmosphere were still unexplored.

In this section, PDPP-BTT-SVS, having a DPP-TT/DPP-SVS monomer ratio equal to 1:9, has been processed following the same methodology as already demonstrated previously with other benchmark small molecule OSCs. A blend composed of PDPP-BTT(1)-SVS(9) and polystyrene (PS) was processed as thin film by BAMS under ambient conditions. Noticeably, the process has been performed by means of a non-chlorinated solvent (*i.e.* tetralin) in order to realize an environmental friendly fabrication process. As reported previously for the other OSCs, an optimization procedure was first carried out for the fabrication of OFETs and EGOFETs based on PDPP-BTT(1)-SVS(9):PS blends, which were prepared on *n*-doped Si/SiO_2 substrates. The details of the optimization process can be found in **Appendix A. 4.**[*]

After the optimization, the two blend formulations with the following characteristics were selected:

- Ink formulation: a) PDPP-BTT(1)-SVS(9):PS_{3K} mixed in a 1:2 ratio, 1 wt%;
  b) PDPP-BTT(1)-SVS(9):PS_{100K} mixed in a 1:2 ratio, 1 wt%
- Solvent: Tetralin
- *S*/*D* electrode functionalization: 2,3,4,5,6-Pentafluorothiophenol (PFBT)
- Coating parameters: 1 cm/s at 150 °C.

The devices based on this formulation have been labelled as follows: SVS:PS_{3K}(1:2)/PFBT and SVS:PS_{100K}(1:2)/PFBT while the other acronyms from the screening formulation tests and their corresponding electrical results are listed in **Table A. 4**.

2.4.1 Morphological Characterization of the Blend Thin-film

PDPP-BTT(1)-SVS(9) is an random polymeric semiconductor which does not display any crystallinity under polarized optical microscopy, as evidenced from **Figure 2.40**. The thin film morphology was evaluated by atomic force microscopy. **Figure 2.41 (a)** shows the AFM of the SVS:PS_{3K}(1:2)/PFBT thin film having a thickness of ~ 31±5 nm , which is similar to the one of SVS:PS_{100K}(1:2)/PFBT thin film (~ 26±5 nm, **Figure 2.42 (a)**). Despite the different molecular weight of the insulating binders and thus, the different solution viscosity, surprisingly the two films show a comparable thickness, in

---

[*] The OFET and EGOFET electrical performance with MilliQ water can be found in **Appendix A.4**.

addition, a top surface characterized by a high roughness ($\sigma_{rms} \sim 6$ nm). The smooth morphology of these two thin films (**Figure 2.41 (b) and Figure 2.42 (b)**) suggest the presence of a PS top layer. In the case of SVS:PS_{100K}(1:2)/PFBT the top layer is highly porous. For the SVS:PS_{3K}(1:2)/PFBT films, a clear view of the bottom layer was provided by the phase contrast of **Figure 2.41 (c)** which, in fact, has evidenced a complex microstructure which can be characteristic of the OSC layer. In the case of SVS:PS_{100K}(1:2)/PFBT film, the scenario is markedly different (**Figure 2.42 (c)**). The top PS layer seems thicker compared to the previous case likely caused by the higher viscosity of the ink. Thus, the phase image cannot reveal any detail of the bottom OSC. However, the porosity of the film (porous depth = 17.1 ± 1.2 nm) allows a glimpse of the OSC layer lying below a PS top cover (**Figure 2.42 (b)**). Time of Flight Secondary Ions Mass Spectrometer (ToF-SIMS) performed on a SVS:PS_{3K}(1:2)/PFBT thin film confirmed the presence of the OSC in the bottom part of the film, where strong S and Se signals, characteristic of PDPP-BTT(1)-SVS(9), are dominant (see **Figure 2.43**).

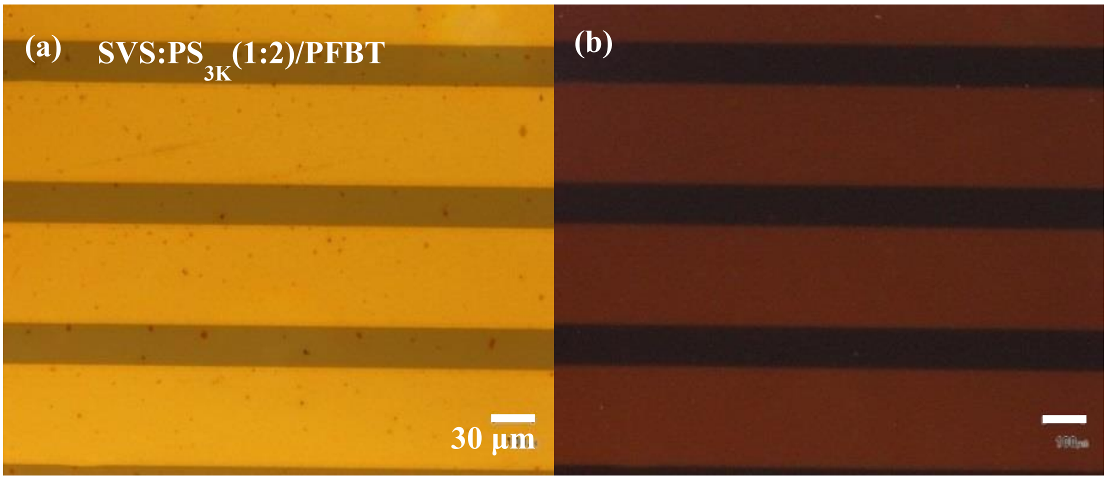

Figure 2.40: Optical microscope images of SVS:PS_{3K}(1:2)/PFBT-based thin film. On the left, polarizer/analyzer = 0°. On the right, polarizer/analyzer = 90°.

Unfortunately, our investigations have just evidenced a bi-layer structure and currently, we cannot ensure the presence of a third PS layer located below the OSC, which could act as passivating layer for the SiO_2 dielectric.

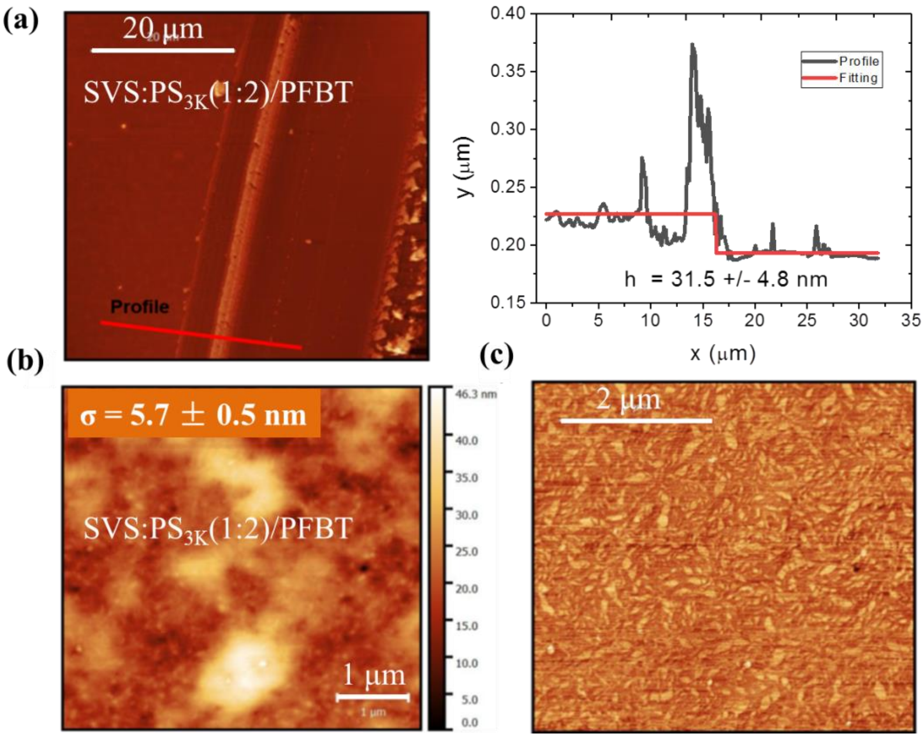

Figure 2.41: (a) AFM profile and their corresponding 2D fitting of a SVS:PS$_{3K}$(1:2)/PFBT-based thin film. (b) AFM images (5×5 μm^2) and (c) phase image of the same thin film were acquired on the channel region.

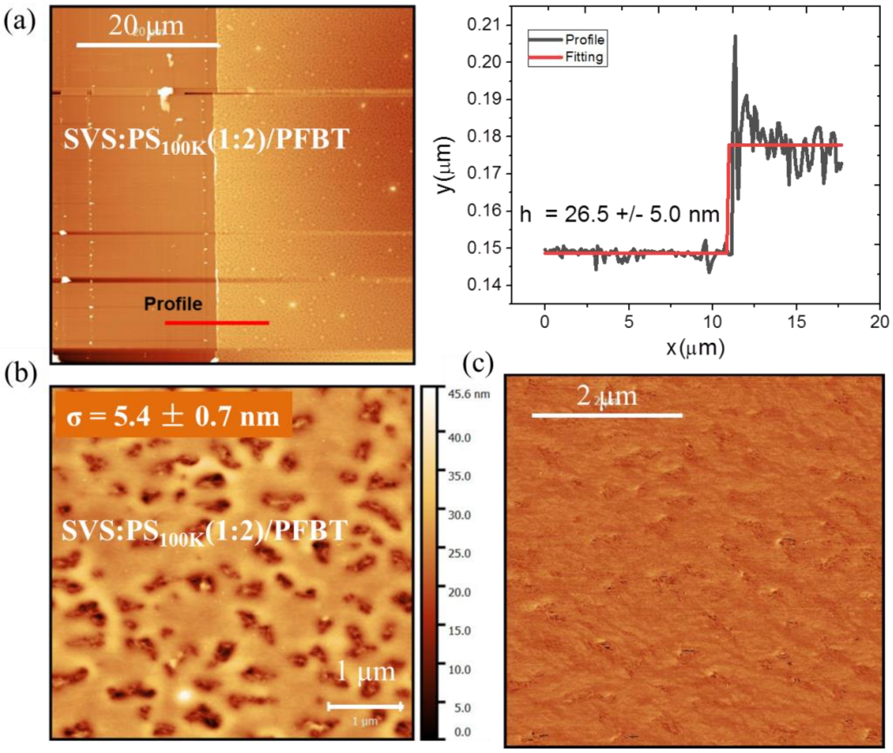

Figure 2.42: (a) AFM profile and their corresponding 2D fitting of a SVS:PS$_{100K}$(1:2)/PFBT-based thin film. (b) AFM images (5×5 μm^2) and (c) phase image of the same thin film were acquired on the channel region.

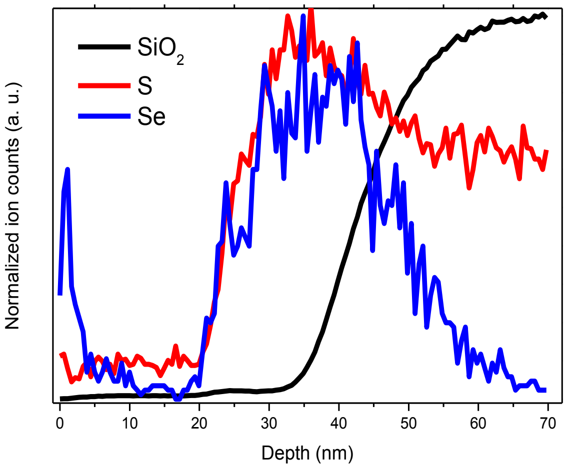

Figure 2.43: ToF-SIMS depth profile of SiO_2, S, and Se of a typical of SVS:PS_{3K}(1:2)/PFBT-based thin film starting from the surface and reaching the SiO_2/organic blend interface.

During the EGOFET operation, the blend is kept in direct contact with water thus the numerous holes present on the top layer can be crucial if electrolyte penetration occurs. In order to understand the role of the holes on top of the blend thin films, EIS measurements were performed on a stacked architecture comprising of Pt/water/ SVS:PS/Au. The EIS response was studied in a frequency range from 10^5 to 10^{-1} Hz by applying two DC voltages (0 V, -0.6 V) superposed to a sinusoidal AC signal of 10 mV. The two DC voltages selected correspond to the gate voltage window of the EGOFET, where the charge transport channel is mostly emptied or the device is accumulating (see next section). **Figure 2.44** shows the Bode plots recorded in MilliQ water for both SVS:PS_{3K}(1:2)/PFBT and SVS:PS_{100K}(1:2)/PFBT thin films. At 0 V the thin films prepared with PS_{3K} and PS_{100K} display a similar phase (θ) response, however, PS_{100K} displayed higher impedance as depicted in **Figure 2.44 (a)** and **(c)**. At high frequency (HF, $f > 100$ Hz) the two systems display a conductive behavior, which is probably due to the polarization of water. However, the blend-coated samples evidenced θ values closer to 30° at $f > 10^4$ Hz deviating from the pure conducting behavior observed in the uncoated sample (**Figure A.32**). As reported by Cotrone *et al.*,[50] this θ response could be ascribed to the migration of water ions through the thin film. In the low frequency regime (LF, $f < 100$ Hz), the system responds as a capacitor due to the formation of a Helmholtz double layer. By switching the DC voltage to -0.6 V, the impedance of the two films decrease and the phase response remains unchanged except at LF regime where a predominantly more conductive response is observed (0 < θ < 45°). A similar DC dependence was already reported by other authors[1,13] and it is probably due to the onset of water electrolysis or to a charge transfer process related to the presence of the organic semiconductor.[51]

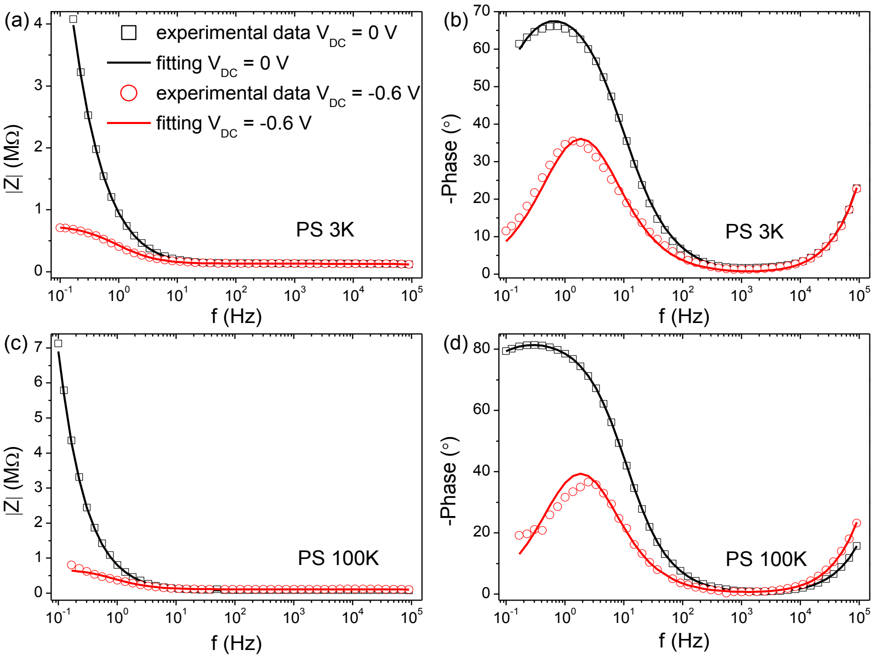

Figure 2.44: (a and c) Impedance and (b and d) phase angle response of the SVS:PS_{3K}(1:2)/PFBT and SVS:PS_{100K}(1:2)/PFBT-based blend films at two selected DC voltages. The open symbols represent the experimental data while the solid lines correspond to the fitting results.

2.4.2 Electrical Performance

As mentioned in the introduction of this section, PDPP-BTT(1)-SVS(9) has already displayed excellent performance as active materials in OFET configuration under controlled environment. However, our current work deals with a technique compatible with up-scaling and with a fabrication process entirely performed under environmental conditions. The role of PS is pivotal for the formation of a compact and homogeneous thin film and the molecular weight of the PS has demonstrated to be fundamental in determining the thin film morphology which can, in turn, affect the final device performance.

As evidenced in **Figure 2.45 (a-c)**, the SVS:PS_{3K}(1:2)/PFBT-based OFET displays a clear *p*-type behavior, whose electrical performance surpasses the electrical results obtained from the SVS:PS$_{100K}$(1:2)/PFBT-based device (**Figure 2.45 (d-f)**). The V_{th} and hysteresis are remarkably more ideal in the case of SVS:PS$_{3K}$(1:2)/PFBT-based device compared to the SVS:PS$_{100K}$(1:2)/PFBT-based one, which probably indicates a lower trap density at the OSC/SiO$_2$ interface in the first case. The parameters (μ, V_{th}, I_{on}/I_{off} and SS) extracted at saturation regime are summarized in **Table A.4**. The overall charge-carrier mobility remains lower compared to the one previously reported by Kim *et al.*,[26] which is an expected consequence considering that our thin film processing and electrical measurements are performed under ambient conditions and, no temperature post-annealing step was performed to achieve thin film crystallinity. However, remarkable mobilities are still achieved, especially considering that the as-prepared films are amorphous, being the average μ of SVS:PS$_{3K}$(1:2)/PFBT and SVS:PS$_{100K}$(1:2)/PFBT-based device equal to 0.22 and 0.10 cm^{2}V^{-1}s^{-1}, respectively.

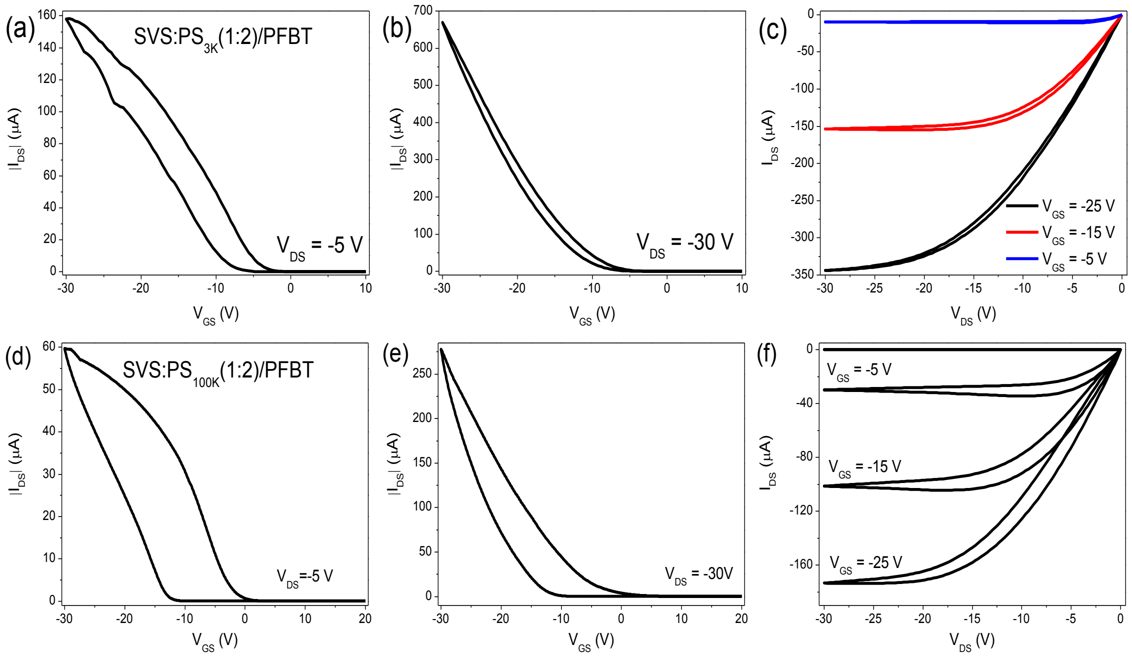

Figure 2.45: Transfer characteristics of SVS:PS$_{3K}$(1:2)/PFBT-based OFETs in (a) linear regime, (b) saturation regime and (c) *I-V* output characteristics of the same device. Transfer characteristics of SVS:PS$_{100K}$(1:2)/PFBT-based OFETs in (d) linear regime, (e) saturation regime and (f) *I-V* output characteristics of the same device.

It should be highlighted that thin films prepared following the same methodology but using solely PDPP-BTT(1)-SVS(9) exhibit poor electrical performance, as reported in **Figure A.33** and **34.** Low I_{DS} and a huge hysteresis were observed. This can be ascribed to the poor film formation due to the lower viscosity of the solution used.

Indeed, this parameter is fundamental when solution shearing techniques are employed, particularly at high coating speeds.[16] Further, the use of PS has previously been shown to be useful for passivating the hydroxyl groups present in the SiO_2 dielectric that act as charge traps, which results in devices with less hysteresis and steeper switch on.[44,52]

Regarding to EGOFET configuration, the results show once again the superior performance in the SVS:PS_{3K}(1:2)/PFBT-based device with MilliQ water and NaCl 0.1 M solution as media. As shown in **Figure 2.46**, the representative *I-V* transfer and output curves of the EGOFET based on this formulation exhibit small hysteresis and possess a I_{on}/I_{off} ratio of ~10^4 in MilliQ water. However, a negative V_{th} shift and an obvious hysteresis are observed in NaCl 0.1 M. For comparison, the electrical performance of SVS:PS_{100K}(1:2)/PFBT-based EGOFET device are reported in **Figure 2.47**. Although in this case a small hysteresis is observed, the device exhibited a lower electrical performance, *i.e.*, lower I_{DS} current and smaller I_{on}/I_{off} ratio.

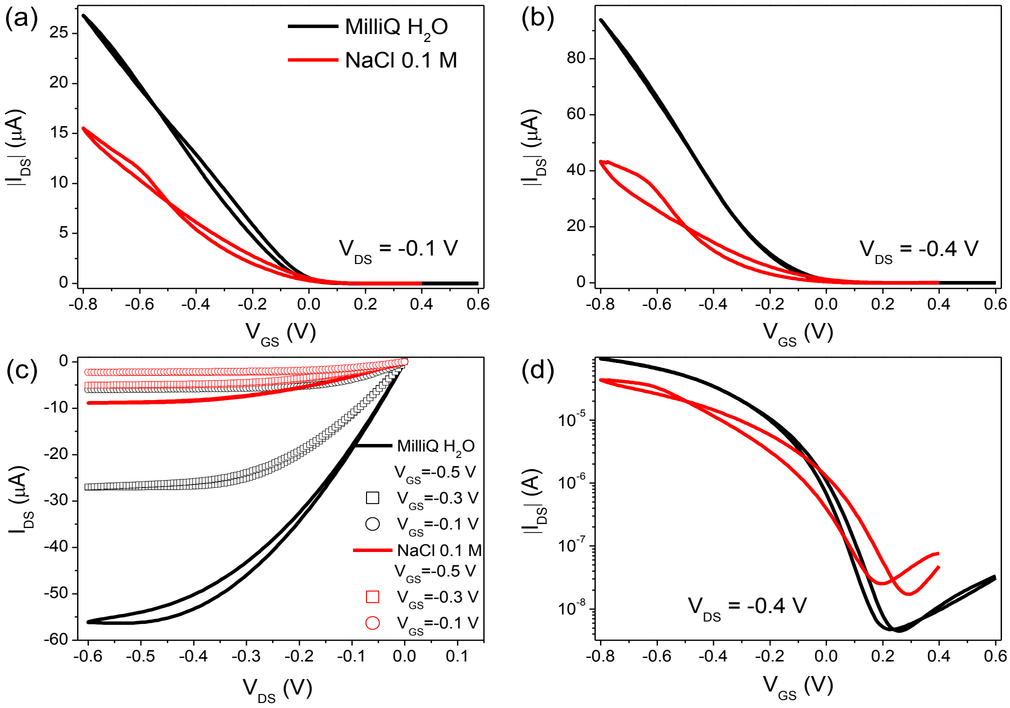

Figure 2.46: *I-V* transfer characteristics of SVS:PS_{3K}(1:2)/PFBT-based EGOFET device in (a) linear and (b) saturation regime. (c) Output characteristics of the same device with three different V_{GS} values. (d) Log-lin plot of the transfer characteristics in saturation regime.

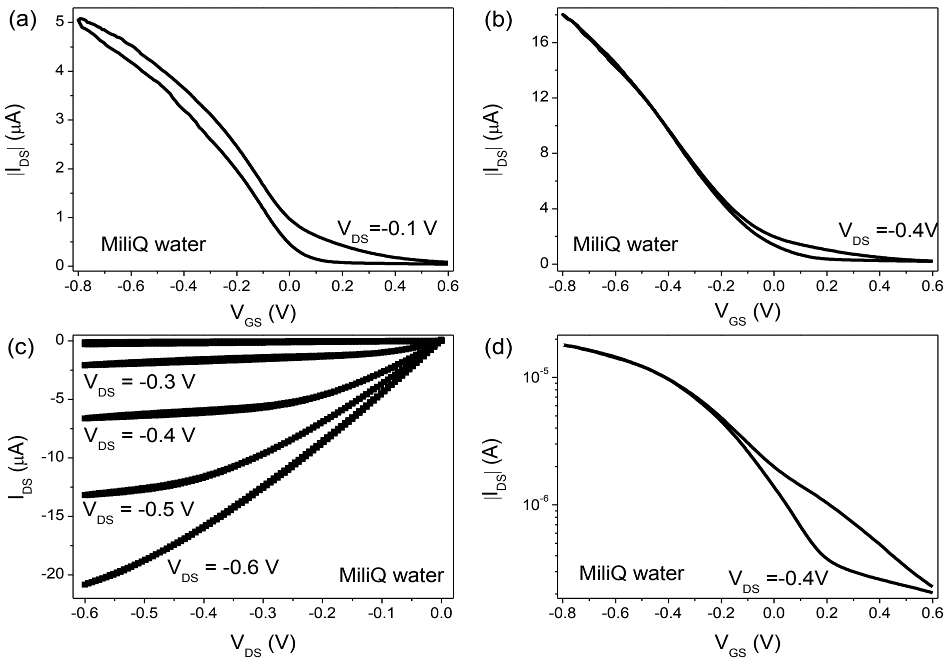

Figure 2.47: *I-V* transfer characteristics of SVS:PS$_{100K}$(1:2)/PFBT-based EGOFET device in (a) linear and (b) saturation regime. (c) Output characteristics of the same device with three different V_{GS} values. (d) Log-lin plot of the transfer characteristics in saturation regime.

In order to extract the mobility, EIS measurements were repeated to obtain the C_{dl}, as shown in **Figure 2.48**. The C_{dl} at a frequency of 10 Hz is equal to 6.4 μF cm^{-2} (8.5 μF cm^{-2}) for SVS:PS$_{3K}$(1:2)/PFBT and 7.6 μF cm^{-2} (7.9 μF cm^{-2}) for SVS:PS$_{100K}$/PFBT in MilliQ water (NaCl 0.1 M). The μ, V_{th} and I_{on}/I_{off} values extracted in saturation regimes are summarized in **Table A.4**. In addition, the devices prepared without PS revealed a much lower performance (**Figure A. 33 - 34**), with μ values of one order of magnitude lower (0.002 cm^2 V^{-1} s^{-1}), proving again that the insulating binder plays a key role for achieving high electrical performance as already demonstrated with the previous OSCs.

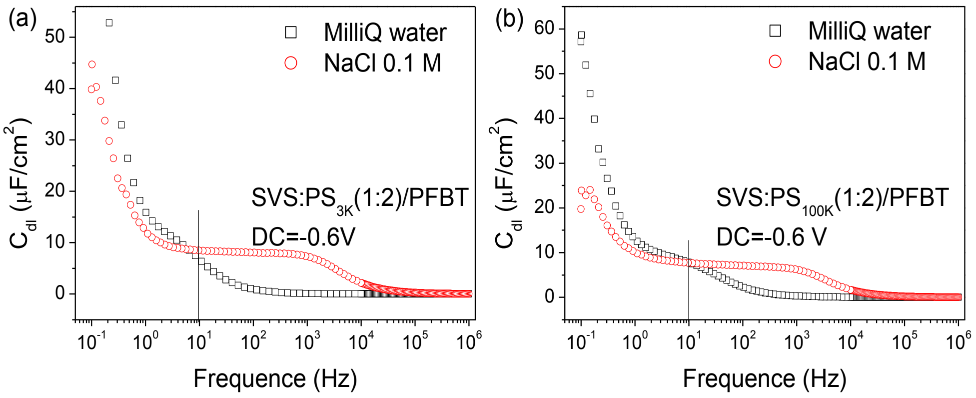

Figure 2.48: EIS measurements of (a) SVS:PS$_{3K}$(1:2)/PFBT and (b) SVS:PS$_{100K}$(1:2)/PFBT blend films in MilliQ H_2O and NaCl 0.1 M solution.

2.4.3 Stability Measurements

Stability study was performed on EGOFET based on SVS:PS_{3K}(1:2)/PFBT in order to understand the behavior of the device in MilliQ water and NaCl 0.1 M solutions. Also, the stability test was repeated in the case of SVS:PS_{100K}(1:2)/PFBT, however, the results are not shown here since their properties are much lower. As shown in **Figure 2.49 (a)** and **(b)**, the devices exhibited a similar behavior both in MilliQ water and NaCl 0.1 M: a fast decrease of the I_{DS} current during the first hour which slows down in the following three hours. The degradation rate is 16 %/h in MilliQ water and 14%/h in NaCl 0.1 M solution, respectively (**Table 2.8**). The current decay is faster compared to the one observed for EGOFETs based on TIPS-pentacene and diF-TES-ADT blends.

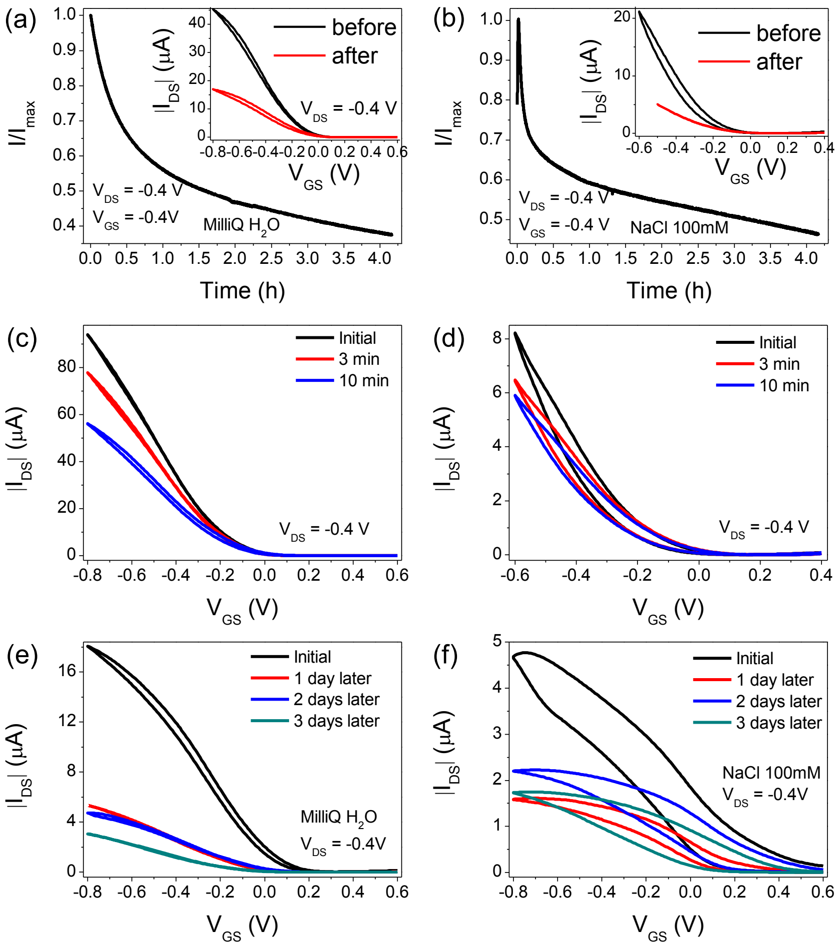

Figure 2.49: *I-t* plot of SVS:PS_{3K}(1:2)-based EGOFET devices operated in (a) MilliQ water and (b) NaCl 0.1 M solution at the saturation regime (V_{DS} = -0.4 V, V_{GS} = -0.4 V). Overlay of *I-V* transfer characteristics in the same type of device for the bias-stress experiment in (c) MilliQ water and (d) NaCl 0.1 M solution. *I-V* transfer characteristics in the same kind of device of the shelf-stability at beginning (black line) and the next three days in (e) MilliQ water and (f) NaCl 0.1 M solution.

The faster degradation is also confirmed by bias stress measurements, as shown in **Figure 2.49 (c)** and (**d**). SVS:PS_{3K}(1:2)/PFBT-based devices exhibit ~ 30 % (~ 25 %) loss of the current in MilliQ water (NaCl 0.1 M) during the first 10 minutes of the bias stress test. Furthermore, the shelf stability reported in **Figure 2.49 (e)** and **(f)**, further confirms the fast degradation of the thin film once operated in water media (**Table 2.8**). Such fast deterioration can be justified if we consider the numerous porous on the top layer that could facilitate the penetration of the electrolyte into the OSC.

Table 2.8: Degradation speeds for *in-situ* current monitoring and shelf-stability in MilliQ H_2O and NaCl 0.1 M solution for an SVS:PS_{3K}(1:2)/PFBT-based EGOFET device.

	Current monitoring (%/hour)		Shelf stability(%/day)	
	MilliQ H_2O	NaCl 0.1 M	MilliQ H_2O	NaCl 0.1 M
SVS:PS_{3K}(1:2)/PFBT	15	13	28	22

2.5 Summary

The aim of this chapter has been to demonstrate the high performance and robustness of EGOFETs based on three small molecule OSCs (*i.e.* TIPS-pentacene, diF-TES-ADT and DPTTA) and one polymer OSC (*i.e.* PDPP-BTT(1)-SVS(9)) blended with an insulating polymer (*i.e.* PS) by using the BAMS as deposition technique. For each OSC:PS blend, a careful optimization process (*i.e.* varying the ink formulations and deposition parameters) was carried out to obtain high quality this film and, in turn, excellent OFET and EGOFET electrical performance. Thanks to this process, the optimal ink formulation of each OSC:PS blend were addressed by comparing the morphology and electrical performance of all the formulations tested. EGOFETs based on the four OSC:PS blend films were systematically studied by evaluating their transfer and output characteristics, potentiometric sensitivity, switching speed and their electrical stability properties using MilliQ water and a NaCl solution as electrolyte media. Two pivotal parameters, the presence of PS in the ink solution and the *S/D* coating with a SAM of PFBT, have revealed to be fundamental for guaranteeing well-defined and densely connected crystals in the film, which are crucial for obtaining high electrical performance and high stability of the EGOFET platform. Among the four OSC:PS blends, the EGOFET based on diF:PS$_{10K}$(4:1)/PFBT appears to be highest performing device due to the superior electrical performance (*i.e.* μ > 0.1 cm^{2}V^{-1}s^{-1}, I_{on}/I_{off} ratio ~10^3, switch on time ~ 1 ms) accompanied with a high operation stability. Moreover, in the next chapters, two different EGOFET applications for sensing are described in detail and due to its superior performance, diF:PS$_{10K}$(4:1)/PFBT has been selected as the active material for the development of these EGOFET sensors. In conclusion, all the work reported in this chapter not only confirms the potential of our experimental approach but also widens the library of OSCs suitable for EGOFETs.

Bibliography

1. Kergoat, L. *et al.* A water-gate organic field-effect transistor. *Adv. Mater.* **22,** 2565–2569 (2010).
2. Manoli, K. *et al.* Printable bioelectronics to investigate functional biological interfaces. *Angew. Chemie Int. Ed.* **54,** 12562–12576 (2015).
3. Wang, D., Noël, V. & Piro, B. Electrolytic Gated Organic Field-Effect Transistors for Application in Biosensors—A Review. *Electronics* **5,** 9 (2016).
4. Cramer, T. *et al.* Water-gated organic field effect transistors-opportunities for biochemical sensing and extracellular signal transduction. *J. Mater. Chem. B* **1,** 3728–3741 (2013).
5. Casalini, S., Bortolotti, C. A., Leonardi, F. & Biscarini, F. Self-assembled monolayers in organic electronics. *Chem. Soc. Rev.* **46,** 40–71 (2017).
6. Casalini, S., Leonardi, F., Cramer, T. & Biscarini, F. Organic field-effect transistor for label-free dopamine sensing. *Org. Electron.* **14,** 156–163 (2013).
7. Casalini, S. *et al.* Multiscale Sensing of Antibody-Antigen Interactions by Organic Transistors and Single-Molecule Force Spectroscopy. *ACS Nano* **9,** 5051–5062 (2015).
8. Kergoat, L. *et al.* Use of poly(3-hexylthiophene)/poly(methyl methacrylate) (P3HT/PMMA) blends to improve the performance of water-gated organic field-effect transistors. *Org. Electron.* **12,** 1253–1257 (2011).
9. Cramer, T. *et al.* Double layer capacitance measured by organic field effect transistor operated in water. *Appl. Phys. Lett.* **100,** (2012).
10. Knopfmacher, O. *et al.* Highly stable organic polymer field-effect transistor sensor for selective detection in the marine environment. *Nat. Commun.* **5,** 2954 (2014).
11. Yun, M. *et al.* Stable organic field-effect transistors for continuous and nondestructive sensing of chemical and biologically relevant molecules in aqueous environment. *ACS Appl. Mater. Interfaces* **6,** 1616–1622 (2014).
12. Larsson, O., Laiho, A., Schmickler, W., Berggren, M. & Crispin, X. Controlling

the dimensionality of charge transport in an organic electrochemical transistor by capacitive coupling. *Adv. Mater.* **23,** 4764–4769 (2011).

13. Porrazzo, R. *et al.* Improving mobility and electrochemical stability of a water-gated polymer field-effect transistor. *Org. Electron.* **15,** 2126–2134 (2014).
14. Buth, F., Kumar, D., Stutzmann, M. & Garrido, J. A. Electrolyte-gated organic field-effect transistors for sensing applications. *Appl. Phys. Lett.* **98,** 153302 (2011).
15. De Oliveira, R. F., Merces, L., Vello, T. P. & Bof Bufon, C. C. Water-gated phthalocyanine transistors: Operation and transduction of the peptide-enzyme interaction. *Org. Electron.* **31,** 217–226 (2016).
16. Niazi, M. R. *et al.* Solution-printed organic semiconductor blends exhibiting transport properties on par with single crystals. *Nat. Commun.* **6,** 8598 (2015).
17. Kumar, A., Baklar, M. A., Scott, K., Kreouzis, T. & Stingelin-Stutzmann, N. Efficient, stable bulk charge transport in crystalline/crystalline semiconductor-insulator blends. *Adv. Mater.* **21,** 4447–4451 (2009).
18. Yu, L. *et al.* Wire-bar coating of semiconducting polythiophene/insulating polyethylene blend thin films for organic transistors. *J. Appl. Phys.* **110,** 093523 (2011).
19. Del Pozo, F. G. *et al.* Single crystal-like performance in solution-coated thin-film organic field-effect transistors. *Adv. Funct. Mater.* **26,** 2379–2386 (2015).
20. Temiño, I. *et al.* A Rapid, Low-Cost, and Scalable Technique for Printing State-of-the-Art Organic Field-Effect Transistors. *Adv. Mater. Technol.* **1,** 1600090 (2016).
21. Niazi, M. R. *et al.* Contact-induced nucleation in high-performance bottom-contact organic thin film transistors manufactured by large-area compatible solution processing. *Adv. Funct. Mater.* **26,** 2371–2378 (2016).
22. Georgakopoulos, S., Del Pozo, F. G. & Mas-Torrent, M. Flexible organic transistors based on a solution-sheared PVDF insulator. *J. Mater. Chem. C* **3,** 12199–12202 (2015).
23. Giri, G., Park, S., Vosgueritchian, M., Shulaker, M. M. & Bao, Z. High-Mobility,

Aligned Crystalline Domains of TIPS-Pentacene with Metastable Polymorphs Through Lateral Confinement of Crystal Growth. *Adv. Mater.* **26,** 487–493 (2014).

24. Subramanian, S. *et al.* Organic Single-Crystal Field-Effect Transistors of a Soluble Anthradithiophene. *Chem. Mater.* **20,** 6733–6737 (2008).
25. Singh, K., Sharma, A., Zhang, J., Xu, W. & Zhu, D. New sulfur bridged neutral annulenes. Structure, physical properties and applications in organic field-effect transistors. *Chem. Commun.* **47,** 905–907 (2011).
26. Yun, H.-J., Lee, G. B., Chung, D. S., Kim, Y.-H. & Kwon, S.-K. Novel Diketopyrroloppyrrole Random Copolymers: High Charge-Carrier Mobility From Environmentally Benign Processing. *Adv. Mater.* **26,** 6612–6616 (2014).
27. Yun, H. J., Cho, J., Chung, D. S., Kim, Y. H. & Kwon, S. K. Comparative studies on the relations between composition ratio and charge transport of diketopyrrolopyrrole-based random copolymers. *Macromolecules* **47,** 7030–7035 (2014).
28. Malandraki, A. *et al.* Enhanced reproducibility of inkjet printed organic thin film transistors based on solution processable polymer-small molecule blends. *J. Mater. Chem.* **20,** 9155 (2010).
29. Qin, Y. *et al.* Charge-transfer complex crystal based on extended-π-conjugated acceptor and sulfur-bridged annulene: Charge-transfer interaction and remarkable high ambipolar transport characteristics. *Adv. Mater.* **26,** 4093–4099 (2014).
30. Qin, Y. *et al.* Efficient ambipolar transport properties in alternate stacking donor-acceptor complexes: From experiment to theory. *Phys. Chem. Chem. Phys.* **18,** 14094–14103 (2016).
31. Whitesides, G. M. Self-Assembly at All Scales. *Science.* **295,** 2418–2421 (2002).
32. Poirier, G. E., Tarlov, M. J. & Rushmeier, H. E. Two-Dimensional Liquid Phase and the $p \times \sqrt{3}$ Phase of Alkanethiol Self-Assembled Monolayers on Au(111). *Langmuir* **10,** 3383–3386 (1994).
33. Onclin, S., Ravoo, B. J. & Reinhoudt, D. N. Engineering silicon oxide surfaces using self-assembled monolayers. *Angew. Chemie - Int. Ed.* **44,** 6282–6304

(2005).

34. Gundlach, D. J. *et al.* Contact-induced crystallinity for high-performance soluble acene-based transistors and circuits. *Nat. Mater.* **7,** 216–221 (2008).

35. Zhang, Q., Leonardi, F., Casalini, S., Temiño, I. & Mas-Torrent, M. High performing solution-coated electrolyte-gated organic field-effect transistors for aqueous media operation. *Sci. Rep.* **6,** 39623 (2016).

36. Schamoni, H., Noever, S., Nickel, B., Stutzmann, M. & Garrido, J. A. A,Ω -Dihexyl-Sexithiophene Thin Films for Solution-Gated Organic Field-Effect Transistors. *Appl. Phys. Lett.* **108,** 073301 (2016).

37. Mailly-Giacchetti, B. *et al.* PH sensing properties of graphene solution-gated field-effect transistors. *J. Appl. Phys.* **114,** (2013).

38. Kim, S. H. *et al.* Electrolyte-gated transistors for organic and printed electronics. *Adv. Mater.* **25,** 1822–1846 (2013).

39. Panzer, M. J. & Frisbie, C. D. Polymer electrolyte-gated organic field-effect transistors: Low-voltage, high-current switches for organic electronics and testbeds for probing electrical transport at high charge carrier density. *J. Am. Chem. Soc.* **129,** 6599–6607 (2007).

40. Lee, J., Panzer, M. J., He, Y., Lodge, T. P. & Frisbie, C. D. Ion gel gated polymer thin-film transistors. *J. Am. Chem. Soc.* **129,** 4532–4533 (2007).

41. Leonardi, F. *et al.* Electrolyte-Gated Organic Field-Effect Transistor Based on a Solution Sheared Organic Semiconductor Blend. *Adv. Mater.* **28,** 10311–10316 (2016).

42. Han, Z. J., Morrow, R., Tay, B. K. & McKenzie, D. Time-dependent electrical double layer with blocking electrode. *Appl. Phys. Lett.* **94,** 4–7 (2009).

43. Bobbert, P. A., Sharma, A., Mathijssen, S. G. J., Kemerink, M. & De Leeuw, D. M. Operational stability of organic field-effect transistors. *Adv. Mater.* **24,** 1146–11458 (2012).

44. Campos, A., Zhang, Q., Ajayakumar, M. R., Leonardi, F. & Mas-Torrent, M. High Performance Organic Field-Effect Transistor with a Solid and Aqueous Dielectric Based on a Solution Sheared Sulfur-Bridged Annulene Derivative. *Adv.*

Electron. Mater. 1700349 (2017).

45. Singh, K., Sharma, A., Zhang, J., Xu, W. & Zhu, D. New sulfur bridged neutral annulenes. Structure, physical properties and applications in organic field-effect transistors. *Chem. Commun.* **47,** 905–907 (2011).
46. Pfattner, R. *et al.* High-performance single crystal organic field-effect transistors based on two dithiophene-tetrathiafulvalene (DT-TTF) polymorphs. *Adv. Mater.* **22,** 4198–4203 (2010).
47. Mas-Torrent, M. & Rovira, C. Role of Molecular Order and Solid-State Structure in Organic Field-Effect Transistors. *Chem. Rev.* **111,** 4833–4856 (2011).
48. Veres, J., Ogier, S. D., Leeming, S. W., Cupertino, D. C. & Khaffaf, S. M. Low-k insulators as the choice of dielectrics in organic field-effect transistors. *Adv. Funct. Mater.* **13,** 199–204 (2003).
49. Campana, A., Cramer, T., Simon, D. T., Berggren, M. & Biscarini, F. Electrocardiographic recording with conformable organic electrochemical transistor fabricated on resorbable bioscaffold. *Adv. Mater.* **26,** 3874–3878 (2014).
50. Cotrone, S. *et al.* Phospholipid film in electrolyte-gated organic field-effect transistors. *Org. Electron.* **13,** 638–644 (2012).
51. Tullii, G. *et al.* Bimodal functioning of a mesoporous, light sensitive polymer/electrolyte interface. *Org. Electron.* **46,** 88–98 (2017).
52. Campos, A., Riera-Galindo, S., Puigdollers, J. & Mas-Torrent, M. Reduction of Charge Traps and Stability Enhancement in Solution-Processed Organic Field-Effect Transistors Based on a Blended n-Type Semiconductor. *ACS Appl. Mater. Interfaces* **10,** 15952–15961 (2018).

Chapter 3. EGOFETs as Mercury Ions Sensors: a Surface Doping Approach[iv]

Abstract: Controlling surface doping in organic transistors represents a key challenge since charge transport in transistors only takes place at near-surface regime close to the dielectric layer. Up to now, surface doping is normally accomplished through the deposition of an extra ultrathin solid adsorbates layer on top or below the host material. However, this aspect is still challenging due to the fabrication restrictions that OFET architecture imparts. In this chapter, we report the control of the doping level at the top surface of *p*-type OSC:PS blend film by means of mercury cations (Hg^{2+}) that selectively act on the conducting channel. Our approach exploits electrolyte-gated field-effect transistors (EGOFETs) as organic device, which possess a transport channel at the top surface of the organic thin film. The exposure of the EGOFET to an aqueous solution of Hg^{2+} ions induces a positive shift of the threshold voltage (V_{th}). The system exhibits a wide linear response in the range (1 nM ~ 1 mM) with a detection limit of 1 nM towards Hg^{2+}. Considering the harmful effects of Hg^{2+}, this EGOFET could be exploited to sense this ion reaching the maximum allowable limit set by U. S. Environmental Protection Agency (EPA) for drinking water. In particular, this interaction has been demonstrated to be limited to the Hg^{2+} cations when compared to other divalent cations (*i.e.* Zn^{2+}, Cu^{2+}, Ca^{2+}, Mg^{2+}…). The highly selective and sensitive response is attributed to the redox reaction between the *p*-type organic semiconductor and Hg^{2+} ions, which has been further supported by KPFM and EIS measurements. Therefore, these results not only provide a new approach for controlling the surface doping of OSCs by means of an EGOFET architecture, but also extend the potential application of EGOFETs as novel label-free sensors for the detection of an extremely harmful water pollutant.

[iv] Q. M. Zhang, F. Leonardi, S. Casalini, and M. Mas-Torrent, *Adv. Funct. Mater.* 2017, 27, 1703899

3.1 Introduction

- **Surface doping**

In inorganic semiconductor processing, doping is defined as introduction of impurities (dopants) into the host lattice of the intrinsic semiconductor to control or modulate its electrical property.[1–3] By the introduction of dopants, additional energy states are created near the conduction band or valence band depending on the dopant type. In other terms, electron donor dopants create states near the conduction band to create excess of electrons, which is called *n*-type doping, while the electron acceptor impurities create energy states near the valence band of the semiconductor to generate holes, also known as *p*-type doping.[1] Although there are some significant differences between organic and inorganic semiconductors (*i.e.* chemical structure, transport mechanisms, *etc.*), the fundamental doping mechanism is analogous in an organic semiconductor (OSC), *i.e.* an impurity is added to the host material, donating or accepting electrons.[1,4–6] *P*-type doping of an OSC results in the extraction of electrons from the highest occupied molecular orbital (HOMO) creating vacancies, while in the case of *n*-type doping, the dopant donates electrons to the lowest unoccupied molecular orbital (LUMO),[4–6] as shown in **Figure 3.1**. The main advantages of doping OSCs are: i) the increase of the electrical conductivity of the bulk OSC matrix with the consequent decrease of the bulk Ohmic loss, and ii) the reduction of the energy barrier between the OSC and the metal electrodes which, due to the creation of a thin space charge layer at the OSC/electrode contact interface, an efficient charge carriers injection is impeded in organic electronic devices.[4,5] Doping of OSCs is normally achieved through different techniques which result in the incorporation of a dopant into the bulk of the material. Three main approaches exist for achieving a homogeneous doping of an OSC layer: i) the co-evaporation of the host and dopant organic materials in vacuum conditions, ii) the addition of a dopant into the host semiconductor solution followed by a wet-deposition process (*e.g.* spin coating, blade coating, zone casting, spray coating, and dip coating), and iii) the exposure of the organic semiconductor film to an oxidizing gas of dopant.[4–6] Up to now, doping is currently applied in organic optoelectronics for the fabrication of several commercial products, such as high efficient white organic light-emitting diodes or organic solar cells.[5–8]

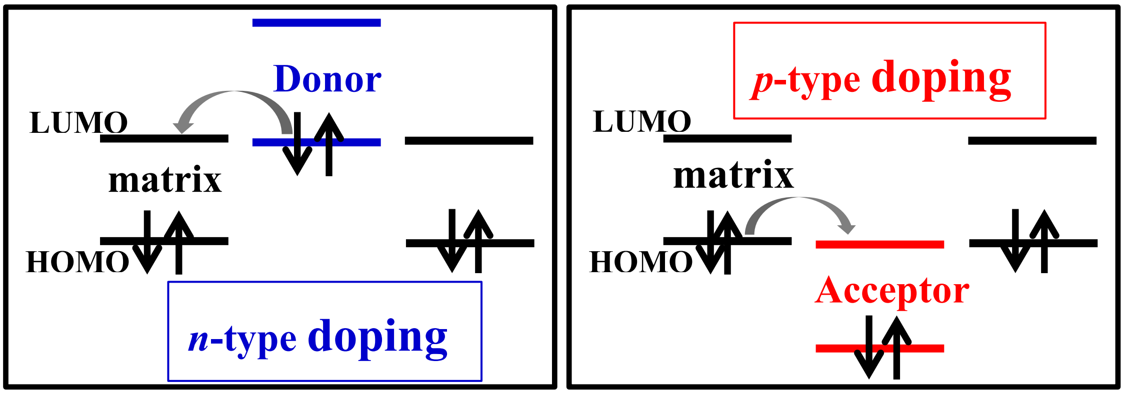

Figure 3.1: A simplified scheme of the doping process of OSCs.[4–6]

Doping of organic semiconductors has also been exploited in organic field-effect transistors (OFETs).[6,9,10] However, since charge transport in conventional Bottom Gate/Bottom Contact (BG/BC) OFETs takes place only at the first monolayers close to the dielectric surface,[11] the conventional doping techniques, in some case, results in a poor enhancement of the electrical properties or even on a reduction of charge carrier mobility due to the increase of the disorder in the conduction channel.[5,12] Therefore, it is desirable to control the doping in the active layer of OFETs but not the doping in all the bulk material. Surface doping is an alternative technique to avoid the direct addition of dopants into the OSC matrix,[5] which aims to modify directly the intrinsic charge transport channel resulting in the controlled modulation of the electrical properties of the organic semiconductor.[4,5] Up to now, surface doping has been successfully achieved by means of 1) depositing or grafting an extra ultrathin solid dopant layer on the active layer near the charge transport channel and 2) growing self-assembled monolayers (SAMs) on the dielectric surface.[4,15-17] The first route has shown to be successful to fine-tune the transistor characteristics and to control the threshold voltage. For example, Hählen *et al*. deposited a thin layer of F4-TCNQ on top of a pentacene bottom-gate transistor in vacuum conditions and the performance of the device increased with increasing F4-TCNQ coverage.[16] Considering the second case, adding a SAM on top of the gate insulator exhibits a strong influence on the OFET electrical performance due to the molecular dipole introduced at the insulator/organic interface. The group of Zojer *et al.* reported a strong shifting of the threshold voltage in OFETs where the dielectric had been functionalized with SAMs with acidic end groups to create a local doped channel.[14]

An unusual approach was previously reported for the surface doping of graphene and diamond based on the use of solvated dopants in aqueous solutions.[1,17,18] The mechanism of this process is based on the electrochemical redox reaction between the semiconductor and the solvated dopant. In 2000, Maier *et al.* reported the doping of a diamond surface by using solvated ions (*i.e.* H_3O^+/H_2 red/ox couple) within a thin wetting layer on hydrogenated diamond as surface acceptors.[19] A similar behavior was also reported by using other solvated ionic species, such as a higher O_2 concentration dissolved in the adsorbed water layer on graphene and carbon nanotube.[1,20] However, this approach still remained unexplored in the field of organic semiconductor thin films due to the difficult control on the porosity of the film itself preventing the selective doping of the OSC surface.

- **Hazardous properties of Hg^{2+}-ions**

Mercury is one of the highest toxic environment pollutants and atmosphere as well as water systems suffer from this contamination.[21–27] Due to human activities (*i.e.* burning of fossil fuels, mining of silver and coal, and industrial process),[26] the increase of mercury contamination has boosted the research at the academic and industrial levels for novel detection approaches to fabricate cheap and disposal sensors. In general, mercury is normally present in three different forms: metallic (Hg^0), as inorganic salt (Hg^+, Hg^{2+}), and as organic compound, which is formed at high interconversion rates.[26,27] In fact, metallic mercury is prone to oxidize to its divalent salt, which can easily convert to an organic mercury compound.[25–28] The harmful nature of Hg^{2+} ions can cause permanent damage of different organs such as brain, kidneys, liver and the central nervous system.[22,25,26] According to the regulation of U.S. Environmental Protection Agency (EPA), the maximum allowable concentration of Hg^{2+} ions in drinking water is 10 nM, which sets a limit for its detection.[29] To date, various methods based on spectrometry,[30,31] fluorometry[32,33] and electrochemical[34] techniques have been developed to detect Hg^{2+}. Although highly sensitive and selective device characteristics have been achieved using the above mentioned techniques, they still require expensive apparatus and complicated analysis procedures. Therefore, the development of low-cost, low-power, and point-of-need Hg^{2+} ions sensors is highly desirable.

Organic electronics offers great potential to address this issue. A few OFETs to sense Hg^{2+} ions have been recently reported by, for instance, DNA-functionalized gold nanoparticles arrays on the semiconductor surface[21] or by utilizing an extended-gate functionalized with a self-assembled monolayer (SAM) of dipicolylame[25] or *L*-cysteine[35]. The detection mechanism in the first case was based on the change of the negative charge density due to the conformational modification of the DNA probe once is binding the Hg^{2+} ions, while the mechanism of the second case can be explained by surface potential shifts at the extended-gate electrode/solution interface because of the capture of the positively charged Hg^{2+} ions on the SAMs.[25,35] However, the direct grafting of a recognition moiety on the OSC or the gate is an additional fabrication step that could also damage the platform itself and then reduce the electrical performance. In 2009, Kim *et al.* reported a Hg^{2+} ions sensor based on single-walled carbon nanotubes (swCNTs) field-effect transistor.[36] In this work, the sensing mechanism was based on the redox reaction between the swCNTs and Hg^{2+} ions, which exhibited a unique sensitivity and selectivity towards Hg^{2+} ions.

- **The objective of this chapter**

As mentioned before, the EGOFETs, whose conducting channel is at the top surface of the semiconductor, offer a unique, but completely unexplored, opportunity to be subjected to surface doping by adding the appropriate dopant in the aqueous medium. Therefore, the objective of this chapter is two-fold:[37] (i) providing a new approach for surface doping of a *p*-type OSC by using of the EGOFET configuration and Hg^{2+} as dopant, and (ii) developing a simple and novel organic sensing platform to detect harmful Hg^{2+} pollutant without the need of using complex device architectures or specific receptors grafted on the gate electrode or the semiconductor surface. To do so, the diF-TES-ADT:PS blend films was firstly fabricated on a Si/SiO$_2$ substrate which is advantageous for the cross-checking of both the EGOFET response and bottom gate characteristics, as shown in **Figure 3.2**. Then, the EGOFET device was systematically exposed to Hg^{2+} ions and a series of common environmental divalent metal cations (*i.e.* Zn^{2+}, Mg^{2+}, Ca^{2+}, Fe^{2+}, Cu^{2+} and Pb^{2+}) to test the sensitivity and selectivity of the platform. Finally, we proceeded to explore the detection mechanism by means of Kelvin probe force microscopy (KPFM) and electrochemical impedance spectroscopy (EIS) techniques.

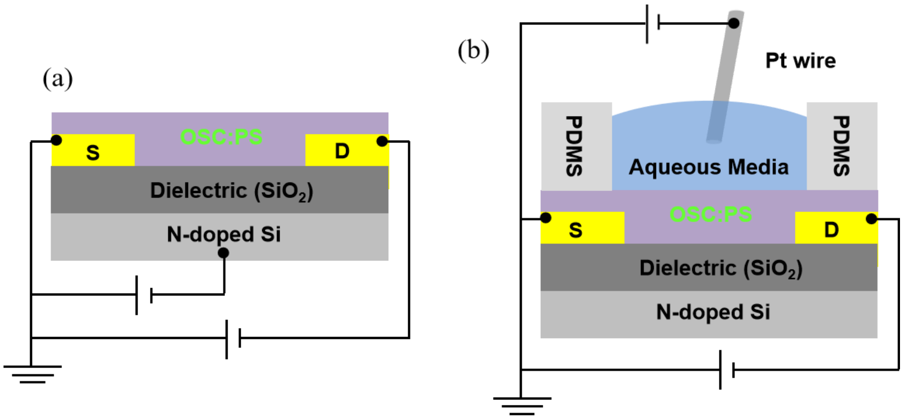

Figure 3.2: (a) Bottom-gate bottom-contact OFET and (b) top-gate bottom-contact EGOFET configurations used in this work.

3.2 Electrical Characteristics

As discussed in Chapter 2, the use of OSCs blended with polystyrene (PS) deposited by BAMS results in highly crystalline and homogenous thin-films that exhibit excellent EGOFET performance with high mobility and fast switching speed.[38,39] One additional advantage of this strategy is represented by the thin PS protecting layer which acts as a barrier for the underlying OSC and confers to the devices high operational stability.[40–42] In this work, we selected 2,8-difluoro-5,11-bis(triethylsilylethynyl)anthradithiophene (diF-TES-ADT) as the active organic semiconductor material, which was blended with PS (M_w~10,000 g mol^{-1}) in a ratio (4:1) and dissolved in chlorobenzene (2 wt %). Films were prepared by BAMS at 105 ºC and 1 cm/s as previously reported in Chapter 2.[38] The EGOFET configuration (**Figure 3.2 (b) and 3.4 (a)**) consisted in a polydimethylsiloxane (PDMS) pool mounted on top of the device with a Pt wire acting as gate electrode.

3.2.1 EGOFET Response to Hg^{2+}

Prior to exposing the device to the Hg^{2+} aqueous solution, a stability check of the EGOFETs in MilliQ water (*i.e.* few *I-V* transfer characteristics) was always performed in order to be sure that we had a reproducible electrical response. As displayed in **Figure 3.3**, the perfect overlapping of the transfer curves ensures that the EGOFETs response is stable and no electrical deterioration is occurring during the experimental time-scale. Transfer characteristics exhibit a typical *p*-type behavior in a V_{GS} windows ranging from +700 to -300 mV. These results are similar to those observed in Chapter 2.

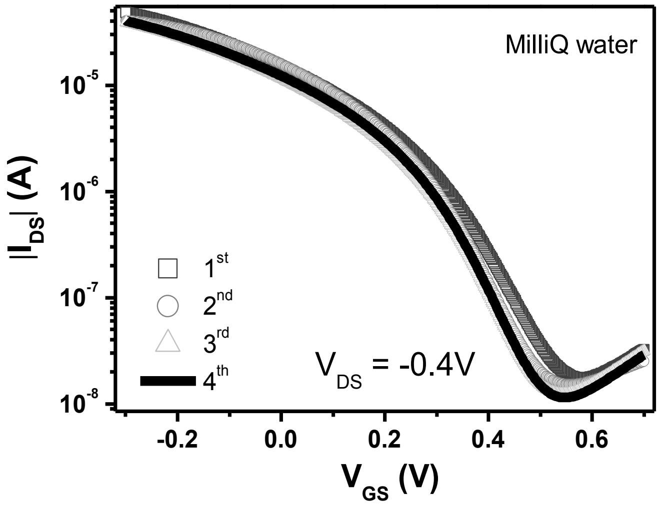

Figure 3.3: The bias stress procedure followed to verify the stability of the device before exposure to Hg^{2+} ion solution (1 mM).

Once assessed the electrical stability, the OSC:PS blend film was exposed to different concentrations of $HgCl_2$ and their EGOFET electrical responses were recorded. The sensitivity has been assessed by exposing the blend thin film to increasingly concentrations of $HgCl_2$ by spanning 6 orders of magnitude, namely from nanomolar to millimolar levels (*i.e.* 1 nM, 50 nM, 1 μM, 50 μM and 1 mM). The detection procedure followed is sketched in **Figure 3.4 (a-c)**. A droplet of the solution containing $HgCl_2$ was casted on the interdigitated area for three minutes followed by an abundant washing of the surface with MilliQ water in order to remove traces of this salt solution that could interfere with the water-gated measurements.

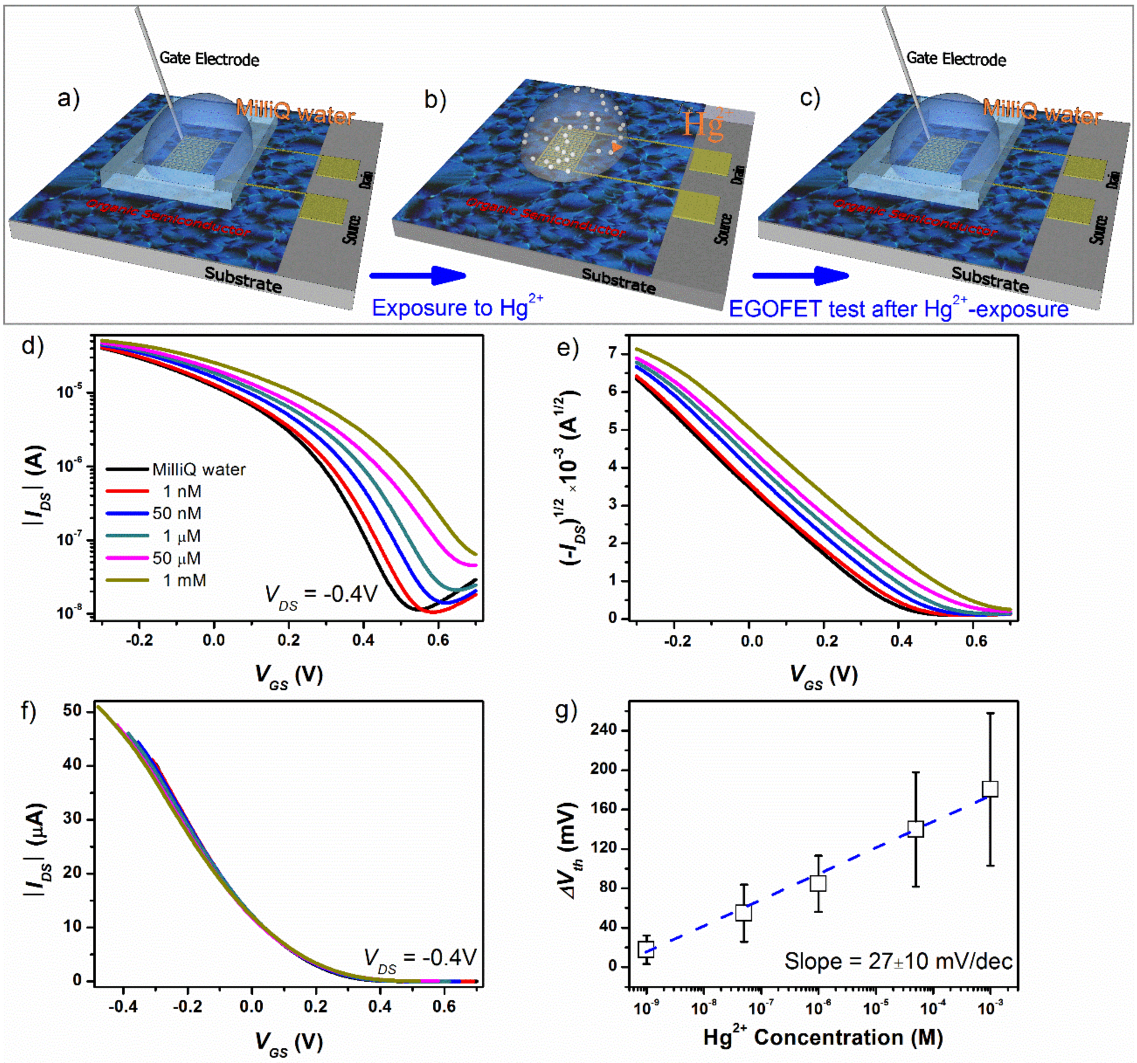

Figure 3.4: (a-c) Schematic diagram of EGOFET platform and Hg^{2+}-mediated surface doping procedure. Measurement protocol: (a) first the devices were measured in MilliQ water, afterwards, (b) they were exposed to the aqueous Hg^{2+} solutions, and (c) they were measured in MilliQ water again. (d) *I-V* transfer characteristics (log-lin scale) and (e) the square root scale of dif-TES-ADT:PS blends prior to and after Hg^{2+} exposure with different concentrations. (f) The transfer curves after exposure to different Hg^{2+} concentrations shifted along the V_{GS} axis for the best overlap with MilliQ water results. (g) Average threshold voltage shifting ΔV_{th}plotted against different concentrations of Hg^{2+} ion solutions. The samples were exposed to Hg^{2+} from 1 nM to 1 mM in ascending order.

After mercury exposure, an additional stability check in MilliQ water was employed again in order to ensure the stability and reproducibility of the data (see **Figure 3.5 (a)**). After being exposed to the analyte, the EGOFET performance is clearly affected by the presence of Hg^{2+} (see **Figure 3.5 (b)**) and a marked threshold voltage (V_{th}) shift is observed.

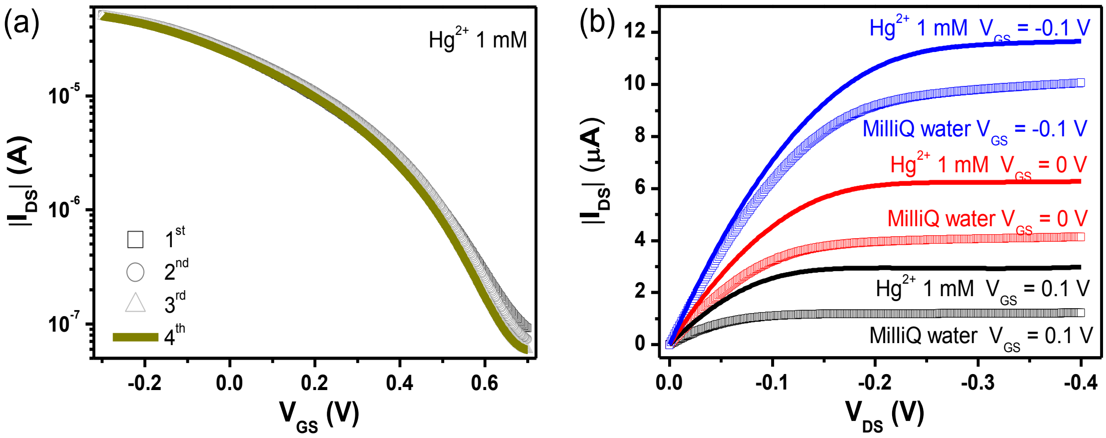

Figure 3.5: (a) Bias stress procedure followed to verify the stability of the device after exposure to Hg^{2+} ion solution (1 mM). (b) Output characteristics before and after exposure to Hg^{2+} ion (1 mM).

As evidenced in **Figure 3.4 (d)**, the gradual positive V_{th} shift seems to be caused by increasing the concentration of Hg^{2+}. Furthermore, this gradual shift is accompanied by an increase in the off-current (I_{off}) and on-current (I_{on}) (see **Figure 3.4 (e)**). These trends are characteristic of a *p*-doping process of the organic semiconductor.[15] In order to rationalize the effect of the analyte on the electrical response of the device, we have shifted the curves along the V_{GS} axis according to:

$$V_{GS}^{eff} = V_{GS} - V_{shift} \qquad (3.1)$$

Figure 3.4 (f) shows the universal curve of the device where all transfer curves corresponding to the Hg^{2+}-exposed devices are compared to the reference one (*i.e.* MilliQ water). The excellent overlap of all these transfer curves suggests that the EGOFET response to Hg^{2+} is mainly potentiometric and the V_{shift} represents the main evidence.

In order to quantify the V_{th} dependence with respect to Hg^{2+} concentration, we have extracted this parameter according to the classical MOSFET equation in saturation regime:

$$I_{DS} = \frac{W}{2L} C_{dl} \mu_{FET} (V_{GS} - V_{th})^2 \qquad (3.2)$$

where μ_{FET} is the charge-carriers mobility, W is the channel width, L is the channel length, V_{th} is the threshold voltage, V_{GS} is the gate-source voltage and C_{dl} is the capacitance of the electrical double layer.[38] The constant slopes of $\sqrt{I_{DS}}$ *vs.* V_{GS}

(-0.00889$\pm$0.00027, **Figure 3.4 (e)** and **Table 3.1**) indicate that the following product, $\mu_{FET} \cdot C_{dl}$ (in accumulation regime), are not significantly affected by Hg^{2+} exposure.[43]

We define the shift of V_{th} (ΔV_{th}) as:

$$\Delta V_{th} = V_{th}^{Hg^{2+}} - V_{th}^{MilliQ\ water} \tag{3.3}$$

where $V_{th}^{Hg^{2+}}$ is the V_{th} after Hg^{2+}-exposure, and $V_{th}^{MilliQ\ water}$ is the V_{th} before Hg^{2+}-exposure. **Figure 3.4 (g)** shows that a linear relationship (in the range: 1 nM - 1 mM) exists between ΔV_{th} and the log [Hg^{2+}], such linear dependence suggests that the sensitivity of the device is 27 ± 10 mV/dec. These data were extracted from 10 devices (**Table 3.2**). All the positive ΔV_{th} indicates that a higher gate voltage is required to switch the channel off due to the p-doping effect of Hg^{2+}.[44]

Table 3.1: Calculation of the device parameters from Figure 3.4 (d) extracted from the fitting before and after exposure to different $HgCl_2$ concentrations. The electrical double layer capacitance used here (5.3 μF/cm^2) is extracted by impedance spectroscopy measurements (Figure 3.16 (b)) at 10 Hz before and after exposure to 1 mM $HgCl_2$ solution.

Hg^{2+} concentration	slope ($\times10^{-3}$)	intercept ($\times10^{-3}$)	V_{th} *(mV)*	C_{dl} (μF/cm^2)	μ_{FET} ($\times10^{-2}$ cm^{2}V^{-1}s^{-1})	μ_{FET}* C_{dl} ($\times10^{-2}$ μF V^{-1}s^{-1})
MilliQ	-8.9	3.5	392	5.3	4.3	2.3
1 nM	-8.8	3.6	407	5.3	4.3	2.3
50 nM	-9.1	4.0	440	5.3	4.5	2.3
1 μM	-9.1	4.3	473	5.3	4.4	2.3
50μM	-8.7	4.5	517	5.3	4.2	2.2
1 mM	-8.6	5.1	585	5.3	4.2	2.2

Table 3.2: ΔV_{th} after exposure to Hg^{2+} extracted from 10 devices.

ΔV_{th} / Device number	1 nM (mV)	50 nM (mV)	1 μM (mV)	50 μM (mV)	1 mM (mV)
$1^{\#}$	23	55	87	164	201
$2^{\#}$	12	56	56	122	174
$3^{\#}$	6	26	73	120	210
$4^{\#}$	42	88	112	199	237
$5^{\#}$	5	55	100	164	180
$6^{\#}$	24	68	87	129	132
$7^{\#}$	37	76	119	181	256
$8^{\#}$	3	38	43	83	101
$9^{\#}$	9	33	84	108	115
$10^{\#}$	15	48	82	124	193

3.2.2 Calculation of Charge Carrier Density due to the Doping Effect

The comparison of charge carriers (holes in this case) concentration prior to and after Hg^{2+}-exposure can provide the first evidence to support the above mentioned *p*-type doping effect. The hole density (n) induced by the gate voltage V_{GS} can be estimated using the formula below:[15]

$$n = -\frac{C_{dl}(V_{GS}-V_{th})}{e} \tag{3.4}$$

where e is the elementary charge, C_{dl} is the double layer capacitance and V_{th} is the threshold voltage. Considering the EGOFET transfer characteristics in the linear regime shown in **Figure 3.6 (a),** the concentration of the doping-induced holes (Δn_{doping}) was calculated at V_{GS} = -0.1 V in accumulation regime based on the following equation:

$$\Delta n_{doping} = n^{Hg^{2+}} - n^{initial} \tag{3.5}$$

where $n^{Hg^{2+}}$ is the hole concentration after Hg^{2+}-exposure, and $n^{initial}$ is the hole concentration before Hg^{2+}-exposure. The Δn_{doping} with respect to different Hg^{2+} concentrations is plotted in **Figure 3.6 (b)**. A gradual increase of the charge carriers density from 0.47×10^{12} to 4.88×10^{12} cm^{-2} (V_{GS} = -0.1 V) is observed, in agreement with the fact that the exposure of the organic thin film to Hg^{2+} raises progressively the number of mobile holes in the OSC channel. In other terms, the surface doping raises up to one order of magnitude the charge carrier density.

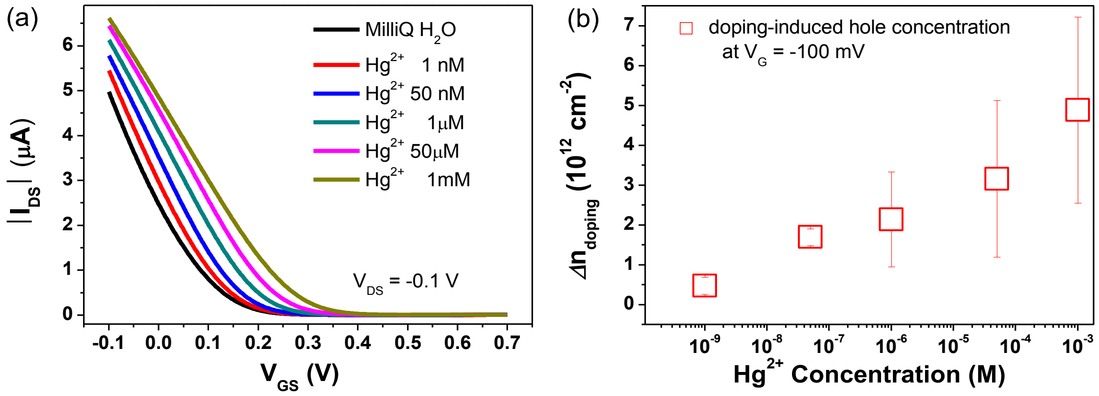

Figure 3.6: (a) *I-V* transfer characteristics recorded in linear regime (V_{DS} = -0.1 V) prior to and after exposure to different Hg^{2+} concentrations. (b) Surface charge carriers induced by mercury exposure (values extracted in linear regime V_{DS} = -0.1V).

3.2.3 Selectivity

In order to demonstrate that this peculiar response solely occurs between the organic semiconductor and Hg^{2+}, we have systematically tested our organic platform with a series of common environmental contaminant divalent metal cations (*e.g.* Zn^{2+}, Mg^{2+}, Mn^{2+}, Ca^{2+}, Fe^{2+}, Cu^{2+}, and Pb^{2+}) with the same concentration (1 mM) and even mixed ion solutions. Firstly, the EGOFET platforms were exposed to various single reference metal ions following the same detection procedure. As shown in **Figure 3.7 (a)** and **Figure 3.8**, all the transfer characteristics only exhibit a small negative shift of V_{th} after exposing the OSC to reference metal cation solutions, which is normally observed within the experimental error. This first evidence suggests the absence of the above mentioned *p*-type doping effect between the semiconductor and the possible interfering cations. To further prove the selectivity of this interaction, mixed metal cation solutions were prepared by keeping the same final concentration (*i.e.* 1 mM) in order to test the EGOFET response in a more complex media. As shown in **Figure 3.7 (b)-(d)** and **Figure 3.9**, the positive V_{th} shifts occurs only when Hg^{2+} is added into the mixture cation solution while no change or a slightly negative shift is observed when Hg^{2+}

cations are absent. All the above mentioned results confirm that the OSC (*i.e.* diF-TES-ADT) and Hg^{2+} cations interact in a selective manner.

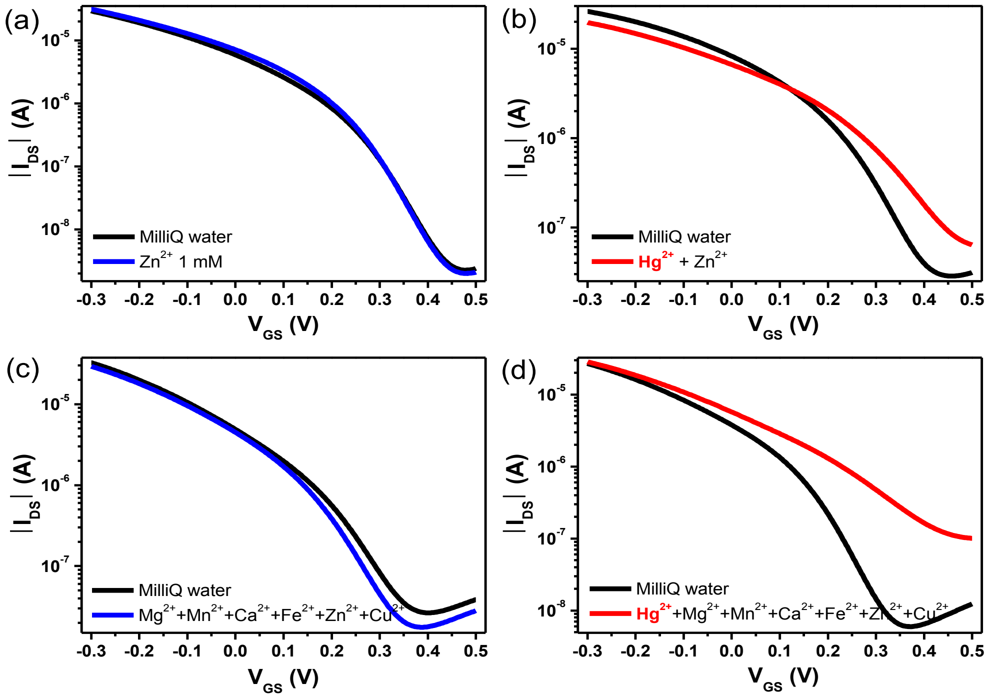

Figure 3.7: The *I-V* transfer characteristics recorded at saturation regime (V_{DS}= -0.4V) prior to and after exposure to (a) single metal ion (Zn^{2+}), (b) mixture metal ion solution (Zn^{2+} + Hg^{2+}), (c) 6-mixed metal ion solution and (d) 6-mixed metal ion plus Hg^{2+} solution. All the black curves are from the devices before exposure to metal ions, the blue curves come from the devices exposed to reference ions without Hg^{2+} and the red ones after adding Hg^{2+} in the solutions. In all the experiments, the total concentrations of the exposure ion solutions were 1 mM.

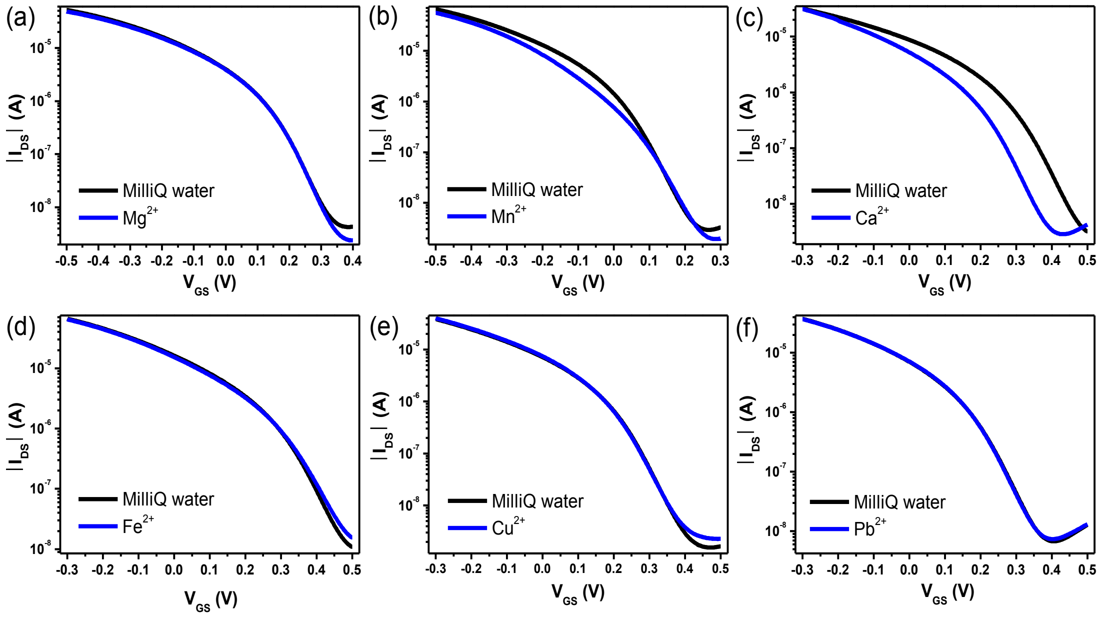

Figure 3.8: *I-V* transfer characteristics prior to and after exposure to single reference metal ions with the same concentration (1 mM). All the black (blue) curves represent the transfer characteristics before (after) exposure to reference metal ion solutions. All the curves were recorded at V_{DS} = -0.4V.

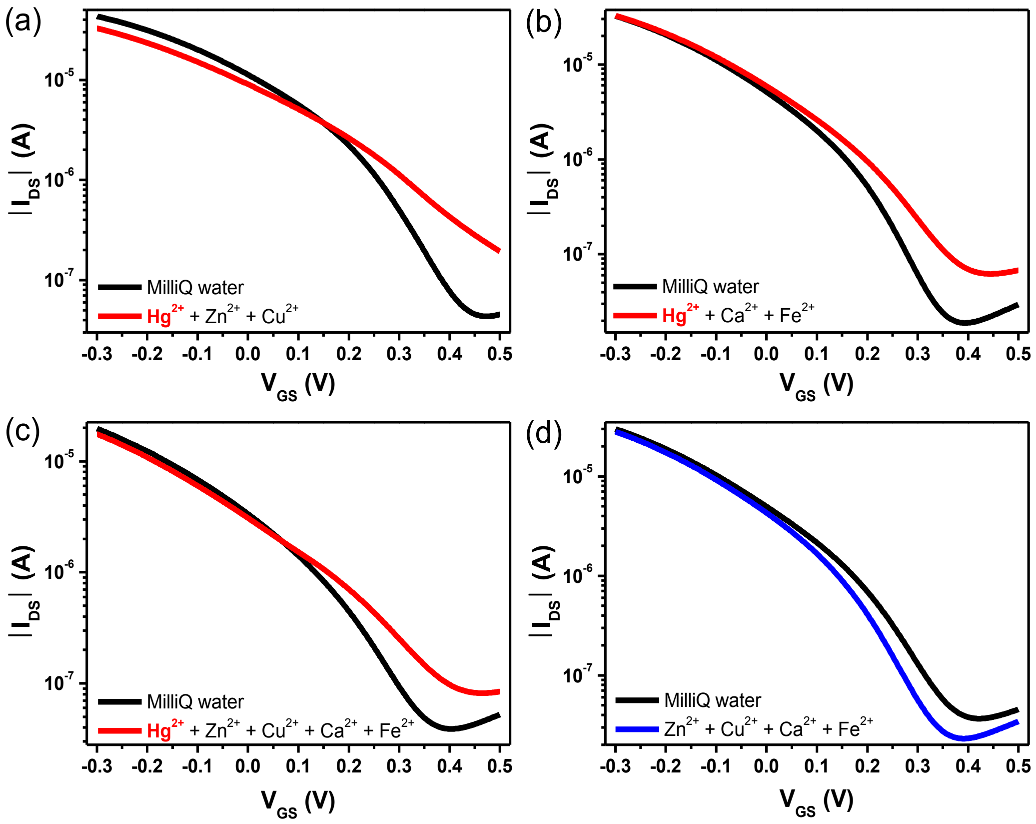

Figure 3.9: *I-V* transfer characteristics prior to and after exposure to mixed metal ion solutions. The mixed solutions were prepared by mixing the individual ions with the same final concentration (1 mM). All the black curves are before exposure to metal ions, the red curves are from the devices exposed to aqueous ion solutions containing Hg^{2+} and the blue curves come from devices exposed to ions solutions where Hg^{2+} was not present. All the curves were recorded at V_{DS} = -0.4V.

3.3 Rationale of Doping Mechanism

3.3.1 Cross-check Experiments

In order to get deeper insight into the interaction mechanism and to understand how Hg^{2+} affects the organic semiconductor, we performed a series of cross-check experiments. First, to rule out the possible interaction between Hg^{2+} and the underlying Au contacts (*viz.* *S* and *D* electrodes) caused by Hg^{2+} percolation, we performed back gate measurements using the Si/SiO_2 as gate/dielectric in dry state before and after treating the thin-film with the Hg^{2+} solution. **Figure 3.10** clearly indicates that the device response in this configuration is unaffected by Hg^{2+}-exposure. Thus, it seems clear that only the semiconductor top surface is altered by Hg^{2+}.

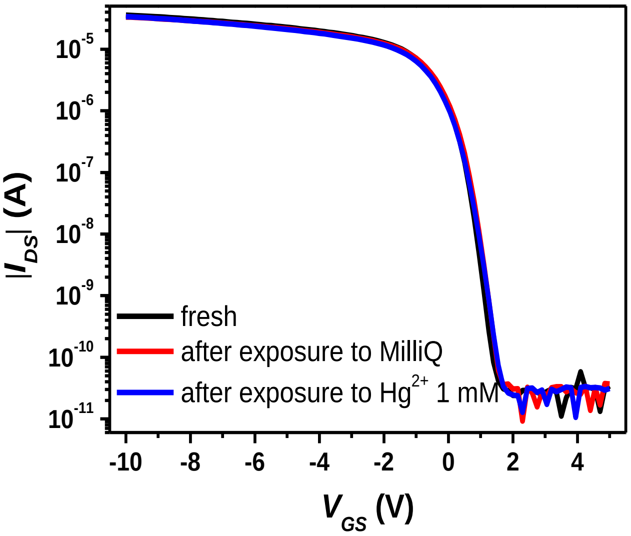

Figure 3.10: *I–V* transfer characteristics of the diF-TES-ADT:PS blend-based device (dry state) before and after exposure to MilliQ H_2O and the Hg^{2+} solution using the bottom gate configuration.

The PS presence could play a pivotal role in preventing the permeation of metal ions across the thin film leaving the back gate transport channel unaffected. Therefore, the same experiments were repeated with films prepared only with diF-TES-ADT without PS to understand the role of the insulating polymer in the blend film. As shown in **Figure 3.11 (a)**, bare diF-TES-ADT-based EGOFET displays a similar but much more pronounced positive shift of the V_{th} after being exposed to Hg^{2+} compared to the EGOFET with the blended OSC. Remarkably, the exposure of bare diF-TES-ADT-based device to a higher concentration of Hg^{2+} solution (c= 10 µM), affects the electrical characteristics in a much larger extent. Furthermore, as shown in **Figure 3.11 (b)**, when the bare diF-TES-ADT film was measured with the back gate, we observed that the doping effect results in a drastic current increase and a lowering of the modulation capability of the device. A similar behavior was also observed by Bao *et al.* on a DDFTTF-based OFET (where DDFTTF stands for 5,5'-bis-(7-dodecyl-9*H*-fluoren-2-yl)-2,2'-bithiophene) and was tentatively attributed by the authors to the doping effect of Hg^{2+} to the OSC layer or to the formation of a charge transfer complex between Hg^{2+} and the semiconductor.[21] Considering these results, it can be stated that the PS encapsulation layer has revealed to be crucial for impeding the percolation of Hg^{2+} ions into the bulk of the OSC film preventing the interaction of this species with the bottom conducting channel of the device.

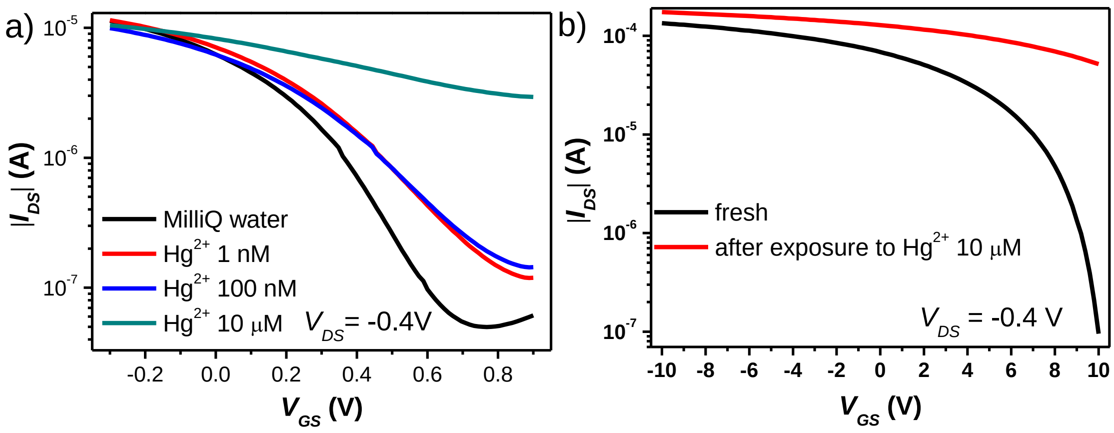

Figure 3.11: (a) *I-V* transfer characteristics of diF-TES-ADT device free of PS before and after exposure to Hg^{2+} ion solution in electrolyte gating. (b) The OFET characteristics of the same device recorded in bottom gate configuration.

3.3.2 Redox Reaction Between Hg^{2+} ions and the *p*-type OSC (diF-TES-ADT)

A possible explanation of the response of the EGOFET device to the presence of Hg^{2+} can be attributed to the redox reaction between Hg^{2+} and semiconductor molecules. **Figure 3.12** sketches the process at the first surface layers where charge accumulation takes place in the EGOFET configuration. Kim and co-workers have also shown that single-walled carbon nanotube-based FETs respond in a similar manner to Hg^{2+} proving the preferential chemical interaction of a sensor based on carbon nanotubes to this divalent ions.[36] Such behavior can be justified if we consider the standard oxidation potential of Hg^{2+} (0.8535 V *vs* normal hydrogen electrode, (NHE)) that is significantly larger compared to the other reference divalent metal ions (**Table 3.3**).[36,45]

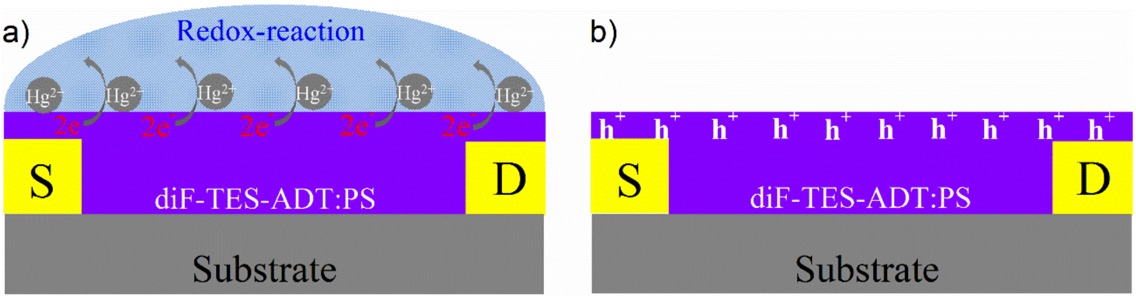

Figure 3.12: (a) Schematic representation of the redox reaction between diF-TES-ADT and the Hg^{2+} ions in solution. (b) Schematic of *p*-type surface transfer doping on the top of semiconductor thin film induced by the redox reaction.

Table 3.3: Standard reduction potentials of different cations at 25℃. [45]

Half-reaction			Standard potential (V)
Oxidant	⇌	Reductant	
$Ca^{2+}+2e^-$	⇌	Ca(s)	-2.924
$Mg^{2+}+2e^-$	⇌	Mg(s)	-2.372
$Mn^{2+}+2e^-$	⇌	Mn(s)	-1.185
$Zn^{2+}+2e^-$	⇌	Zn(s)	-0.763
$Fe^{2+}+2e^-$	⇌	Fe(s)	-0.44
$Pb^{2+}+2e^-$	⇌	Pb(s)	-0.126
$Cu^{2+}+2e^-$	⇌	Cu(s)	+0.159
$Fe^{3+}+e^-$	⇌	Fe^{2+}	+0.77
$Hg^{2+}+2e^-$	⇌	Hg(l)	+0.854

In order to confirm our assumptions, the experiments were repeated by moving to another OSC with similar HOMO level, *i.e.* bis(triisopropylsilylethynyl)pentacene (TIPS-pentacene). This OSC has been also blended with PS as in the previous case and prepared in an analogous experimental manner. As depicted in **Figure 3.13**, the electrical response of TIPS-pentacene based EGOFETs remains practically identical to the one found with diF-TES-ADT. In other terms, a positive shift of the V_{th} together with an increase of I_{on} and I_{off} were observed once the thin films were exposed to Hg^{2+} solutions in the same concentration range (1 nM - 1 mM). Moreover, unlike diF-TES-ADT, the chemical structure of TIPS-pentacene is free of sulphur atoms which chemical affinity for Hg^{2+} is quite recognized. Our experimental cross-check excludes any possible interaction mechanism between this element and the mercury cations.

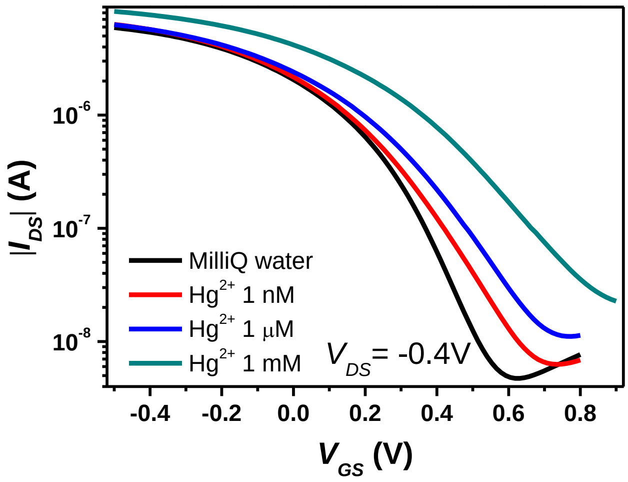

Figure 3.13: *I-V* transfer characteristics of TIPS-pentacene:PS films prior to and after exposure to different concentrations of Hg^{2+} ion solutions.

In order to further support the redox mechanism behind the electrical response of the EGOFET, another metal cation (Fe^{3+}) possessing a slightly less oxidation capability (0.77 V *vs* NHE, **Table 3.3**) has been used.[45] *I-V* characteristics did not show any shift after being exposed to 1 mM solution of Fe^{3+} ions (see **Figure 3.14 (a)**). However, the same doping effect is observable only when the Fe^{3+} concentration is increased to 50 mM (see **Figure 3.14 (b)**). Such evidence supports the fact that a less oxidizing agent induces a similar effect only at higher concentrations. However, in the presented concentration range (1 nM - 1 mM), our EGOFET platform presents a high selectivity towards Hg^{2+} and considering its harmful nature as pollutant,[25] our device represents a promising sensing platform to detect this ion.

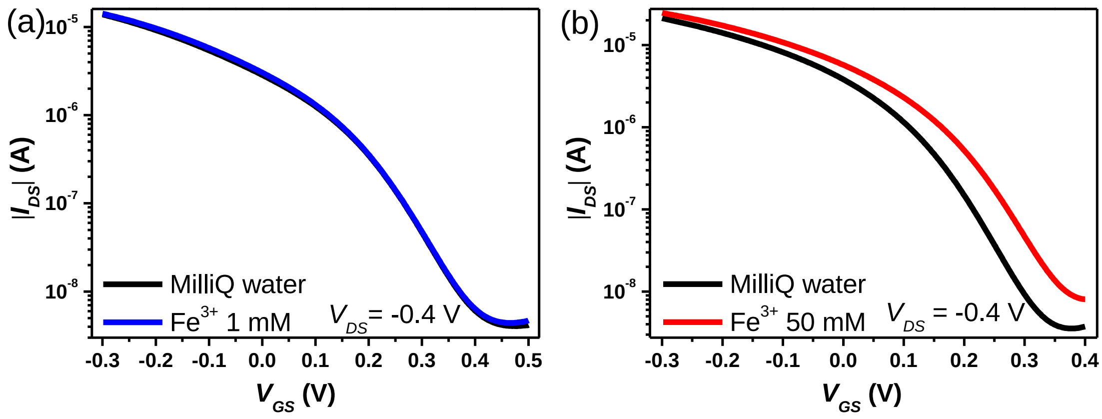

Figure 3.14: *I-V* transfer characteristics prior to and after exposure to a Fe^{3+} metal ion solution with (a) 1 mM and (b) 50 mM concentration.

3.3.3 Kelvin Probe Force Microscopy[v]

As previously mentioned, an electron transfer process between the OSC and Hg^{2+} is expected to be taking place. This process results in the creation of additional charge carriers in the semiconductor which can be defined as doping-induced holes. Such rationale is in agreement with the modulation of the EGOFET response according to the Hg^{2+} concentration due to extra charge carriers in the top charge transport channel. To further support the above mentioned mechanism, we have performed a series of experiments aiming to study the top surface of the thin-film.

Kelvin probe force microscopy (KPFM) is a valuable technique to measure the work function or electrical surface potential of the semiconductor at nanometer-scale.[46] Such kind of measurement is able to measure the contact potential difference (CPD) between the tip and the semiconductor prior to and after exposure to Hg^{2+} solution. Here, the CPD is defined as:

$$V_{CPD} = \frac{\emptyset_{tip} - \emptyset_{sample}}{-e}, \tag{3.6}$$

where e is the electronic charge and $\emptyset_{tip}$ and $\emptyset_{sample}$ are the work function of the tip and the semiconductor, respectively. For a semiconductor thin film, the measured V_{CPD} is related to the surface potential ($\emptyset_{surface}$), which differs from the work function of semiconductor materials due to the surface-charge limit near the semiconductor surface.[46,47] The equation used to measure the V_{CPD} is:

$$F_{\omega} = -\frac{\partial C(z)}{\partial z}(V_{DC} \pm V_{CPD})V_{AC}\sin(\omega t), \tag{3.7}$$

where the ± sign depends whether the bias (V_{DC}) is applied to the sample (+) or to the tip (-).[46] In our case, we applied the DC bias to the sample, which indicates that the sign is + in the equation 3.6 to extract the V_{CPD} value. Therefore, when the F_{ω} drops to zero from the equation 3.6, the V_{CPD} can be extracted as $V_{CPD} = -V_{DC}$. Regarding the calculation of V_{CPD} change (ΔV_{CPD}) in the OSC thin film, it is firstly needed to calculate the V_{CPD} prior to and after Hg^{2+}-exposure ($V_{CPD}^{fresh} = -V_{DC}^{fresh}$ and $V_{CPD}^{Hg^{2+}} = -V_{DC}^{Hg^{2+}}$), respectively. In our case, each OSC:PS blend film contained two interest regions: the

---

[v] I would like to thank Dr. Esther Barrena (ICMAB-CSIC) for useful discussions about the KPFM results.

first one is the metal ions-exposed region prepared according to the protocol reported in the Experimental section (chapter 5), while the second region is the non-exposed zones which were kept unaltered and it represented a reference zone for the KPFM measurements. The CPD tests were performed on the electrode area (Au) and on the channel area (SiO_2). The V_{AC} bias generates oscillating electrical forces between the cantilever tip (Au) and the sample surface, which is compensated by a second bias (V_{DC}) until the CPD is extracted. During the KPFM test, we used the same Au tip acting as the reference before and after Hg^{2+}-exposure. Therefore, the surface potential change (ΔV_{CPD}) of the sample can be obtained by the following equation:

$$\Delta V_{CPD} = V_{CPD}^{Hg^{2+}} - V_{CPD}^{initial} = -\Delta V_{DC} \tag{3.8}$$

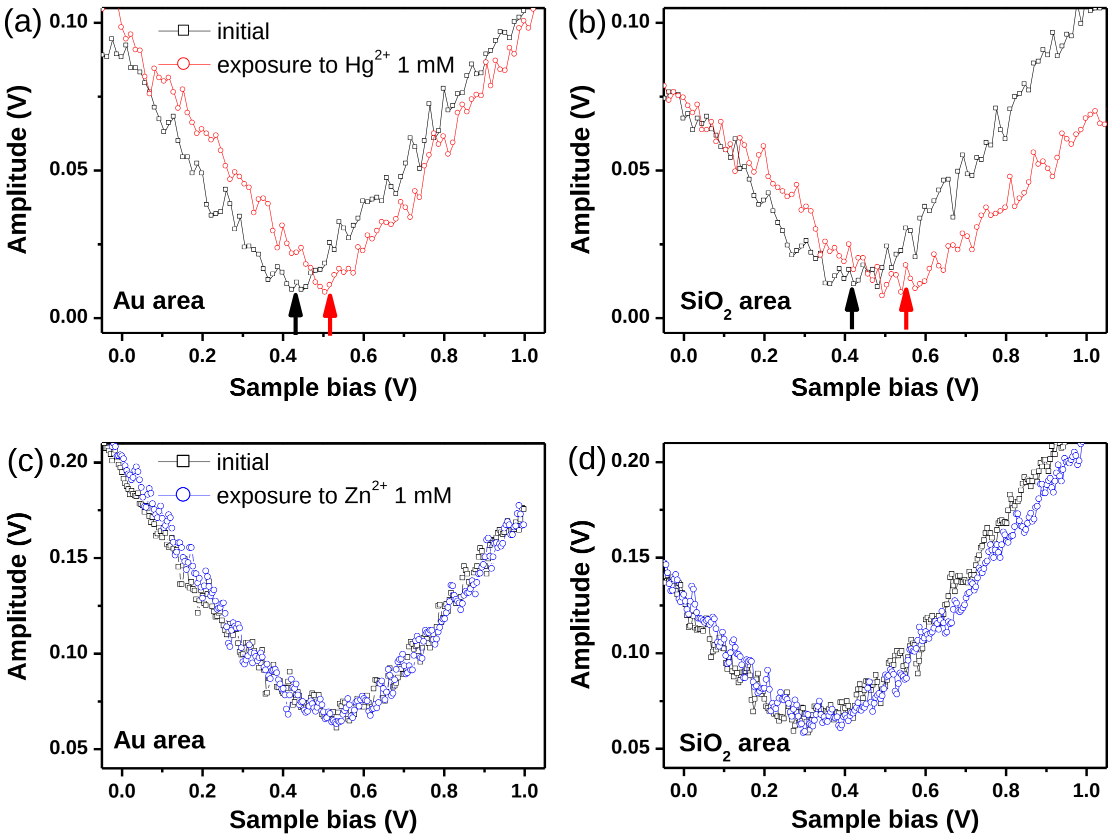

Figure 3.15: CPD measurements recorded prior to (black square) and after Hg^{2+} treatment (red circle) and Zn^{2+} treatment (blue circle) of the blend thin-film deposited on the EGOFET device. CPD scans on (a) Au electrode and on (b) SiO_2 area in the interdigitated region before and after exposure to Hg^{2+} (1 mM). CPD scans on (c) Au electrode and on (d) SiO_2 area in the interdigitated region before and after exposure to Zn^{2+} solution (1 mM).

As shown in **Figure 3.15 (a)** and **(b)**, the DC voltage applied to the sample shifts to positive values after Hg^{2+}-exposure on both Au electrode and SiO_2 regions. The extracted average DC voltages before and after Hg^{2+}-exposure are summarized in **Table 3.4**, where - 68.6 mV and - 99.7 mV are the ΔV_{CPD} corresponding to the OSC blend thin film coated on the Au electrode and SiO_2 regions, respectively. The decreasing of the surface potential in both two areas confirms that a *p*-type surface doping is reasonable due to the transfer of electrons from the top surface of the OSC to the Hg^{2+} cations during the exposure process. For comparison, the ΔV_{CPD} values did not show any apparent change when the thin film was exposed to a Zn^{2+} solution on both the Au electrode and SiO_2 regions (**Figure 3.15 (c)** and **(d)**), which further confirms that the high oxidation potential of Hg^{2+}-ions is responsible for the doping mechanism.

Table 3.4. Average V_{CPD} values extracted before and after exposure to Hg^{2+} and Zn^{2+} solutions with the same concentration (1 mM).

Type of ions	Area	intercept	slope	V_{Bias} (V)	$V_{Bias,average}$ (V)	Average V_{CPD} (V)
$HgCl_2$ 1 mM	Au area initial	-0.041	0.091	0.451	0.443	-0.443
		-0.04	0.091	0.439		
		-0.04	0.091	0.441		
	Au area Hg^{2+} exposure	-0.047	0.093	0.506	0.512	-0.512
		-0.048	0.093	0.516		
		-0.048	0.093	0.514		
	SiO_2 area initial	-0.035	0.082	0.433	0.432	-0.432
		-0.035	0.081	0.432		
		-0.035	0.081	0.432		
	SiO_2 area Hg^{2+} exposure	-0.034	0.066	0.519	0.532	-0.532
		-0.035	0.065	0.538		
		-0.035	0.065	0.538		
$ZnCl_2$ 1 mM	Gold area initial	0.158	-0.322	0.489	0.494	-0.494
		0.157	-0.321	0.488		
		0.164	-0.323	0.505		
	Gold area Zn^{2+} exposure	0.168	-0.332	0.505	0.497	-0.497
		0.164	-0.329	0.497		
		0.173	-0.351	0.490		
	SiO_2 area initial	0.082	-0.301	0.275	0.282	-0.282
		0.085	-0.299	0.284		
		0.085	-0.295	0.287		
	SiO_2 area Zn^{2+} exposure	0.091	-0.299	0.303	0.287	-0.287
		0.074	-0.278	0.266		
		0.088	-0.299	0.293		

3.3.4 Electrochemical Impedance Spectroscopy

A more clear view of the process occurring at the semiconductor/water interface could be provided by electrochemical impedance spectroscopy (EIS). This technique can be extremely useful to further understand how the double layer capacitance is influenced by the doping process.[39] In an EGOFET, the total electrical double layer capacitance C_{dl} is the result of two capacitances in series, *i.e.* gate/water capacitance (C_1) and semiconductor/water capacitance (C_2), $\frac{1}{C_{dl}} = \frac{1}{C_1} + \frac{1}{C_2}$. In general, the gate/water capacitance (C_1 ~ tens of μF/cm^2) is larger than the semiconductor/water capacitance (C_2 is a few μF/cm^2).[43] Therefore, C_2 dominates when the channel is depleted, whereas the two capacitances can be assumed to be roughly comparable in the accumulation regime. After exposing the OSC to Hg^{2+}, the C_{dl} increases compared to the pristine device in the off-state (V_{DC} = 0.3V, **Figure 3.16 (a)**) while no marked differences can be observed in the on-state (V_{DC} = -0.3V, **Figure 3.16 (b)**). The response between the untreated and the Hg^{2+}-treated device (1 mM) suggests that the doping-induced holes are detectable only when the channel is completely depleted. In fact, C_{dl} measured on a device in the on-state, remains practically unchanged (5.3 μF/cm^2 at 10 Hz, as shown in **Figure 3.16 (b)**) due to the high charge carrier density present in the channel that dominates the effective interface capacitance. In other terms, the contribution of the surface doping-induced holes becomes less relevant when the device is in the on-state.

In addition, the constant capacitance response in the accumulation regime (**Figure 3.16 (b)**) further agrees with the fact that the product $\mu_{FET} \bullet C_{dl}$ is not altered after Hg^{2+}-exposure and only a potentiometric shift in the transfer curves is effectively observed (**Figure 3.4 (d)-(f)**). Again for comparison, the same experiments were repeated by treating the devices with a Zn^{2+} solution (1 mM) and no detectable changes were observed (**Figure 3.16 (c)** and **(d)**). In other words, the total double layer capacitance remains unaltered in both operating conditions. Thus, all these data confirms that the redox reaction taking place between Hg^{2+} cations and the OSC (diF-TES-ADT) induces a surface *p*-type doping, which is the effective cause of the positive V_{th} shift and, the I_{on} and I_{off} increase after exposing the OSC to an aqueous Hg^{2+} solution.

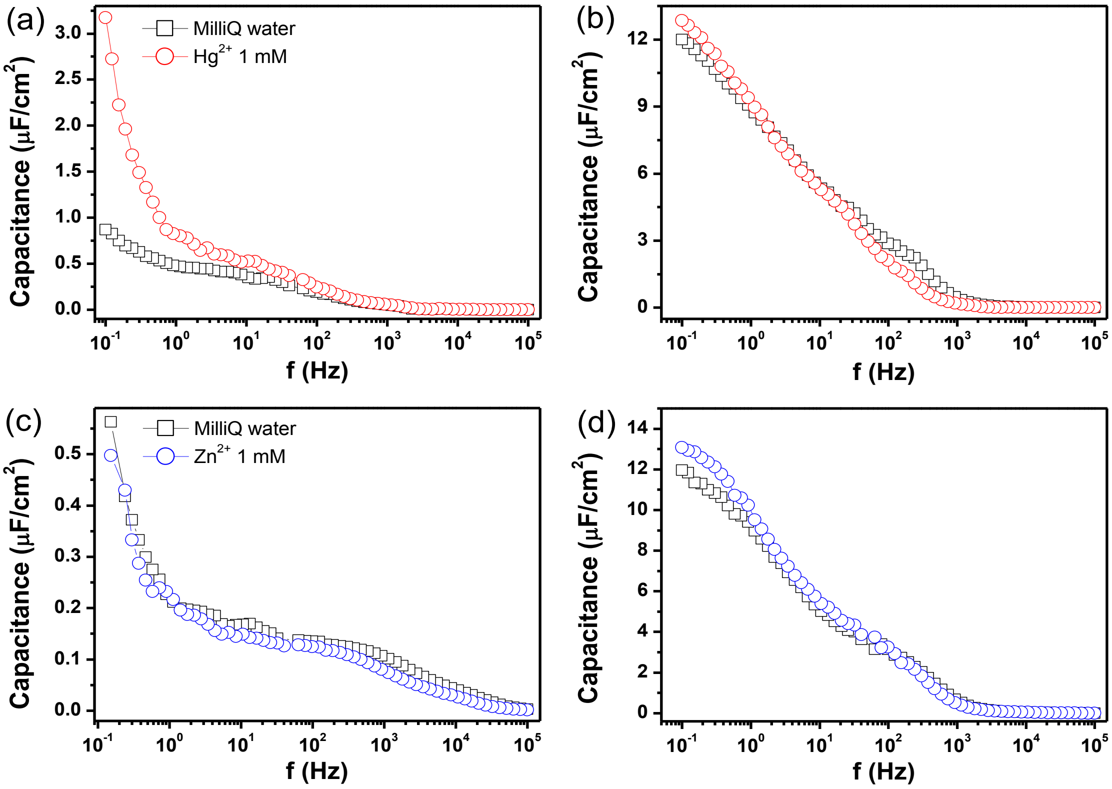

Figure 3.16: Capacitance measurements before (black square) and after Hg^{2+} treatment (red circle) and Zn^{2+} treatment (blue circle) of the same EGOFET platform. The capacitance recorded at (a) $V_{DC} = 0.3$ V (channel OFF) and (b) on-state, $V_{DC} = - 0.3$ V (channel ON) of the device treated with Hg^{2+}. The same measurement at (c) $V_{DC} = 0.3$ V (channel OFF) and (d) on-state, $V_{DC} = - 0.3$ V (channel ON) of the device treated with Zn^{2+}.

3.4 Summary

In conclusion, we have fabricated an electrolyte-gated field-effect transistor based on the organic semiconductor diF-TES-ADT blended with polystyrene. By exposing the OSC blend thin film to aqueous Hg^{2+} ions solutions at various concentrations, *p*-type surface doping on the top accumulating channel of the EGOFET is occurring. This effect is caused by the redox reaction taking place between Hg^{2+} and the semiconductor surface, as supported by KPFM and EIS measurements. Exposure of the OSC blended film to Hg^{2+}-ions has the main effect of shifting positively the V_{th} of the EGOFET, which exhibits a linear response towards this harmful agent in a concentration range spanning from nanomolar to millimolar. Furthermore, this peculiar interaction of the organic semiconductor with Hg^{2+} seems to be limited to this cation in a concentration range up to 1 mM and no effects have been observed in the presence of other divalent cations. It should be highlighted that the detection limit of 1 nM towards Hg^{2+} cation is comparable to other fluorescence sensors and biosensors reported in literature and satisfies the requirement of the U. S. Environmental Protection Agency standards in terms of Hg^{2+} contamination of drinking water.[48] Therefore, this work further elucidates the potential applications of OSC: polymer blend-based EGOFETs as efficient transduction platforms to develop simple and portable electronic devices for Hg^{2+} detection.

Bibliography

1. Chen, W., Qi, D., Gao, X. & Wee, A. T. S. Surface transfer doping of semiconductors. *Prog. Surf. Sci.* **84,** 279–321 (2009).
2. Liu, H., Liu, Y. & Zhu, D. Chemical doping of graphene. *J. Mater. Chem.* **21,** 3335 (2011).
3. Ley, L., Ristein, J., Meier, F., Riedel, M. & Strobel, P. Surface conductivity of the diamond: A novel transfer doping mechanism. *Phys. B Condens. Matter* **376–377,** 262–267 (2006).
4. Lüssem, B., Riede, M. & Leo, K. *Doping of organic semiconductors*. *Physica Status Solidi A* **210,** (2013).
5. Lüssem, B. *et al.* Doped Organic Transistors. *Chem. Rev.* **116,** 13714–13751 (2016).
6. Walzer, K., Maennig, B., Pfeiffer, M. & Leo, K. Highly efficient organic devices based on electrically doped transport layers. *Chem. Rev.* **107,** 1233–1271 (2007).
7. Reineke, S. *et al.* White organic light-emitting diodes with fluorescent tube efficiency. *Nature* **459,** 234–8 (2009).
8. Meerheim, R., Körner, C. & Leo, K. Highly efficient organic multi-junction solar cells with a thiophene based donor material. *Appl. Phys. Lett.* **105,** 063306 (2014).
9. Khim, D. *et al.* Control of ambipolar and unipolar transport in organic transistors by selective inkjet-printed chemical doping for high performance complementary circuits. *Adv. Funct. Mater.* **24,** 6252–6261 (2014).
10. Minari, T. *et al.* Highly enhanced charge injection in thienoacene-based organic field-effect transistors with chemically doped contact. *Appl. Phys. Lett.* **100,** 093303 (2012).
11. Dinelli, F. *et al.* Spatially Correlated Charge Transport in Organic Thin Film Transistors. *Phys. Rev. Lett.* **92,** 116802–1 (2004).
12. Kleemann, H. *et al.* Structural phase transition in pentacene caused by molecular doping and its effect on charge carrier mobility. *Org. Electron.* **13,** 58–65 (2012).

13. Marchl, M. *et al.* Tuning the threshold voltage in organic thin-film transistors by local channel doping using photoreactive interfacial layers. *Adv. Mater.* **22,** 5361–5365 (2010).

14. Pacher, P. *et al.* Chemical control of local doping in organic thin-film transistors: From depletion to enhancement. *Adv. Mater.* **20,** 3143–3148 (2008).

15. Xiang, D. *et al.* Surface transfer doping induced effective modulation on ambipolar characteristics of few-layer black phosphorus. *Nat. Commun.* **6,** 6485 (2015).

16. Hählen, T., Vanoni, C., Wäckerlin, C., Jung, T. A. & Tsujino, S. Surface doping in pentacene thin-film transistors with few monolayer thick channels. *Appl. Phys. Lett.* **101,** 033305 (2012).

17. Chakrapani, V. *et al.* Charge transfer equilibria between diamond and an aqueous oxygen electrochemical redox couple. *Science* **318,** 1424–1430 (2007).

18. Liu, W., Yan, X., Lang, J. & Xue, Q. Electrochemical behavior of graphene nanosheets in alkylimidazolium tetrafluoroborate ionic liquid electrolytes: Influences of organic solvents and the alkyl chains. *J. Mater. Chem.* **21,** 13205–13212 (2011).

19. Maier, F., Riedel, M., Mantel, B., Ristein, J. & Ley, L. Origin of surface conductivity in diamond. *Phys. Rev. Lett.* **85,** 3472–3475 (2000).

20. Pinto, H., Jones, R., Goss, J. P. & Briddon, P. R. Mechanisms of doping graphene. *Phys. Status Solidi* **207,** 2131–2136 (2010).

21. Hammock, M. L., Sokolov, A. N., Stoltenberg, R. M., Naab, B. D. & Bao, Z. Organic Transistors with Ordered Nanoparticle Arrays as a Tailorable Platform for Selective , In Situ Detection. *ACS Nano* **6,** 3100–3108 (2012).

22. Park, C. *et al.* A highly sensitive, direct and label-free technique for Hg 2+ detection using Kelvin probe force microscopy. *Nanotechnology* **26,** 305501 (2015).

23. Ramesh, M., Lin, H. & Chu, C. Biosensors and Bioelectronics Organic thin film transistors as selective sensing platforms for Hg 2 þ ions and the amino acid cysteine. *Biosens. Bioelectron.* **42,** 76–79 (2013).

24. Arbiol, J., Puntes, V. & Ojea-jime, I. Citrate-Coated Gold Nanoparticles As Smart Scavengers for Mercury (II) Removal from Polluted Waters. *ACS Nano* **6,** 2253–2260 (2012).

25. Tsuyoshi, M. *et al.* A mercury(II) ion sensor device based on an organic field effect transistor with an extended-gate modified by dipicolylamine. *Chem. Commun.* **51,** 17666–17668 (2015).

26. Selid, P. D., Xu, H., Collins, E. M., Face-Collins, M. S. & Zhao, J. X. Sensing mercury for biomedical and environmental monitoring. *Sensors* **9,** 5446–5459 (2009).

27. Zalups, R. K. Molecular interactions with mercury in the kidney. *Pharmacol. Rev.* **52,** 113–143 (2000).

28. Gu, B. *et al.* Mercury reduction and complexation by natural organic matter in anoxic environments. *Proc. Natl. Acad. Sci.* **108,** 1479–1483 (2011).

29. Chaudhary, A., Dwivedi, C., Chawla, M., Gupta, A. & Nandi, C. K. Lysine and dithiothreitol promoted ultrasensitive optical and colorimetric detection of mercury using anisotropic gold nanoparticles. *J. Mater. Chem. C* **3,** 6962–6965 (2015).

30. Puanngam, M., Dasgupta, P. K. & Unob, F. Automated on-line preconcentration of trace aqueous mercury with gold trap focusing for cold vapor atomic absorption spectrometry. *Talanta* **99,** 1040–1045 (2012).

31. Giakisikli, G., Miró, M. & Anthemidis, A. Integrated lab-in-syringe platform incorporating a membraneless gas-liquid separator for automatic cold vapor atomic absorption spectrometry. *Anal. Chem.* **85,** 8968–8972 (2013).

32. Beaudin, L., Johannessen, S. C. & Macdonald, R. W. Coupling Laser Ablation and Atomic Fluorescence Spectrophotometry : An Example Using Mercury Analysis of Small Sections of Fish Scales. *Anal. Chem.* **82,** 8785–8788 (2010).

33. Liu, Z., Zhu, Z., Zheng, H. & Hu, S. Plasma Jet Desorption Atomization-Atomic Fluorescence Spectrometry and Its Application to Mercury Speciation by Coupling with Thin Layer Chromatography. *Anal. Chem.* **84,** 10170–10174 (2012).

34. Cao, R., Zhu, B., Li, J. & Xu, D. Oligonucleotides-based biosensors with high sensitivity and selectivity for mercury using electrochemical impedance spectroscopy. *Electrochem. commun.* **11,** 1815–1818 (2009).

35. Lee, K., Weis, M. & Ou-yang, W. Detection of mercury (II) ion in water using an organic field-effect transistor with a cysteine- immobilized gold electrode electrode. *Jpn. J. Appl. Phys.* **55,** 04EL02 (2016).

36. Kim, T. H., Lee, J. & Hong, S. Highly Selective Environmental Nanosensors Based on Anomalous Response of Carbon Nanotube Conductance to Mercury Ions. *J. Phys. Chem. C* **113,** 19393–19396 (2009).

37. Zhang, Q., Leonardi, F., Casalini, S. & Mas-Torrent, M. Mercury-Mediated Organic Semiconductor Surface Doping Monitored by Electrolyte-Gated Field-Effect Transistors. *Adv. Funct. Mater.* **27**, 1703899 (2017).

38. Zhang, Q., Leonardi, F., Casalini, S., Temiño, I. & Mas-Torrent, M. High performing solution-coated electrolyte-gated organic field-effect transistors for aqueous media operation. *Sci. Rep.* **6,** 39623 (2016).

39. Leonardi, F. *et al.* Electrolyte-Gated Organic Field-Effect Transistor Based on a Solution Sheared Organic Semiconductor Blend. *Adv. Mater.* **28,** 10311–10316 (2016).

40. Del Pozo, F. G. *et al.* Single crystal-like performance in solution-coated thin-film organic field-effect transistors. *Adv. Funct. Mater.* **26,** 2379–2386 (2015).

41. Georgakopoulos, S., del Pozo, F. G. & Mas-Torrent, M. Flexible organic transistors based on a solution-sheared PVDF insulator. *J. Mater. Chem. C* **3,** 12199–12202 (2015).

42. Temiño, I. *et al.* A Rapid, Low-Cost, and Scalable Technique for Printing State-of-the-Art Organic Field-Effect Transistors. *Adv. Mater. Technol.* **1,** 1600090 (2016).

43. Manoli, K. *et al.* Printable bioelectronics to investigate functional biological interfaces. *Angew. Chemie Int. Ed.* **54,** 12562–12576 (2015).

44. Pernstich, K. P. *et al.* Threshold voltage shift in organic field effect transistors by dipole monolayers on the gate insulator. *J. Appl. Phys.* **96,** 6431–6438 (2004).

45. Patnaik, P. *Dean's Analytical Chemistry Handbook*. (McGraw-Hill, 2004).

46. Melitz, W., Shen, J., Kummel, A. C. & Lee, S. Kelvin probe force microscopy and its application. *Surf. Sci. Rep.* **66,** 1–27 (2011).

47. Ellison, D. J., Lee, B., Podzorov, V. & Frisbie, C. D. Surface Potential Mapping of SAM-Functionalized Organic Semiconductors by Kelvin Probe Force Microscopy. *Adv. Mater.* **23,** 502–507 (2011).

48. Liu, J. & Lu, Y. Rational Design of 'Turn-On' Allosteric DNAzyme Catalytic Beacons for Aqueous Mercury Ions with Ultrahigh Sensitivity and Selectivity. *Angew. Chemie Int. Ed.* **119,** 7731–7734 (2007).

Chapter 4. Hydrogel-Gated Organic Field-Effect Transistors as a Pressure Sensitive Platform[vi]

Abstract: Flexible electronics are increasingly impacting a wide variety of novel applications such as wearable health care sensor, *in-vivo* monitoring, and even artificial skin. As a fundamental component, electrolyte-gated organic field-effect transistors (EGOFETs) are an active research area due to their inherent advantages of miniaturization, low power consumption, direct transduction and label-free detection of aqueous media events. In this chapter, we present a novel EGOFET where the liquid electrolyte has been replaced by a water-based gel (*i.e.* hydrogel), named agarose gel. The fabrication strategy allows the fabrication of a flexible device that exhibits high electrical performance and long-term stability. Moreover, the hydrogel gated organic field-effect transistor (HYGOFET) exhibits an excellent response to pressure stimuli, whose mechanism is based on the water dipoles alignment within the OSC layer, disclosing new routes in this research branch.

[vi] Q. M. Zhang, F. Leonardi, R. Pfattner, M. Mas-Torrent, submitted, 2019

4.1 Introduction

As mentioned before in the previous chapters, electrolyte-gated organic field-effect transistors (EGOFETs) have already shown their potential as benchmark platform in many sensing applications taking advantage of their perfect integration with water-based media.[1–7] As previously stated, their layout consists in the direct exposure of the organic semiconductor (OSC) to the water electrolyte, which results in the formation of two capacitive coupled electrical double layers (EDLs) at the semiconductor/electrolyte and the electrolyte/gate electrode interface. The large capacitance (~ few μF cm^{-2}) allows low operation voltage (*i.e.* < 1 V) making EGOFETs suitable candidates for low power consumption electronic applications.[8] In addition, they can benefit from low cost processing techniques and flexible and light plastic supports (*i.e.* Kapton, PEN, PET).[2,9–11] These properties are mandatory requirements in the field of conformable electronics, like wearable health care devices where adhesion and the conformity to curvilinear surfaces like human skin are necessary.[12–14] However, in conventional EGOFETs, a PDMS pool or microfluidic channels are always required in order to confine the aqueous media,[5,7] which in turn hinders the development of prototypes and devices suitable for practical applications. Therefore, a soft solid water-based dielectric element is desirable to develop a novel flexible EGOFET architecture.

- **Hydrogels**

Within this context, hydrogels can be envisioned as ‘electrolytes in the form of a gel’, so they can overcome the limitations that liquid water-based media impact since they can be fabricated in the form of solid films. Hydrogels are complex 3D polymeric networks capable to swell a high amount of water due to the presence of the hydrophilic groups in the hydrogel (*i.e.* –COOH, -OH, -NH$_2$).[15–18] Hydrogels can be classified in many different ways based on their properties, such as the source of the hydrogel material, type of crosslinking, preparation method and network of the electrical charge inside the hydrogel (see **Figure 4.1**).[18,19] For example, according to the source of material, hydrogels can be divided into three classes: (i) natural-source hydrogel, (ii) synthetic-source hydrogel, and (iii) hybrid-source hydrogel.[19] In addition, depending on the type of crosslinking, hydrogels can be classified into two categories: (i) chemical cross-linked hydrogels, and (ii) physical cross-linked hydrogels.[18] Further, they can also be classified depending on how they are prepared or their ionic charge.

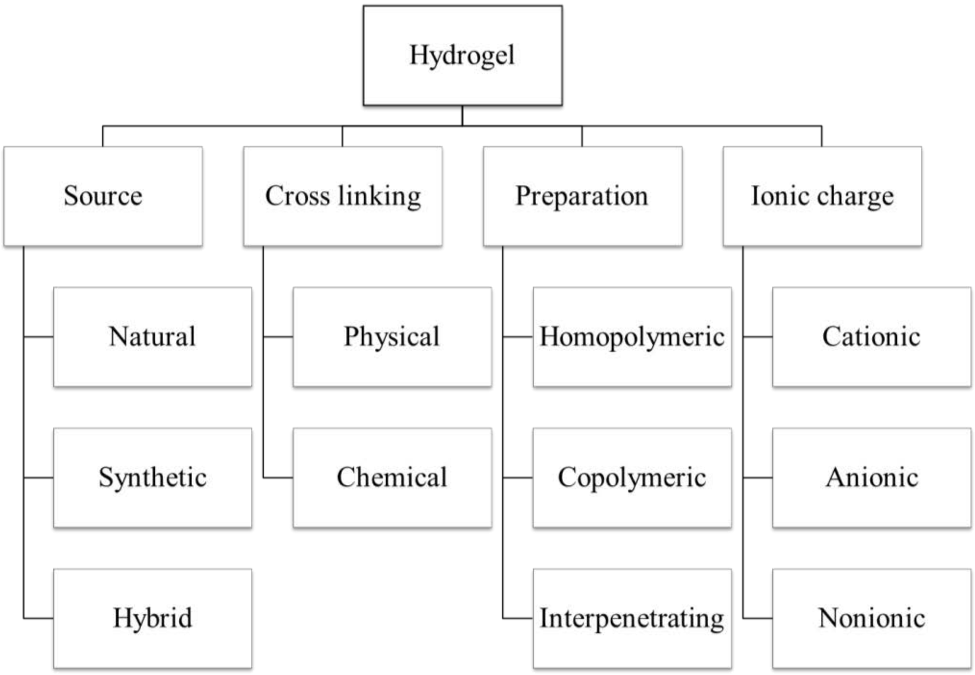

Figure 4.1: Classification of hydrogels based on different properties.[15] [Adapted from IntechOpen (2016)]

Over the last decade, hydrogels have gained considerable attention as valuable matrices for a wide range of applications, such as drug delivery, heavy metal ions removal, contact lenses and scaffolds in tissue engineering due to their good mechanical and optical properties, their capability to swell a large amount of water and their non-toxicity.[15,18,19] Hydrogels can also undergo a significant volume transition with releasing/absorbing different aqueous media in response to external stimuli, such as pressure, temperature, electric-field, pH and even specific chemical stimuli.[15,19] In most cases, these transitions are reversible and the hydrogel can return to its initial state once the external stimuli is removed.[15] Therefore, hydrogels are called “intelligent” or “smart” materials.[15,18,19] Furthermore, many hydrogels are excellent biocompatible materials because they offer a natural environment suitable for the immobilization of recognition agents, biomolecules and even for cell culture.[16,20–22] Considering all the above properties, the use of these materials as novel electrolytes for EGOFETs, which consequently can be named as hydrogel-gated organic field-effect transistors (HYGOFETs), opens new opportunities to expand their application as sensors and ultra-sensitive transducers. Up to now, the exploitation of hydrogels in EGOFET platforms has been very limited. For instance, in the work of Dumitru *et al.*[23] they exploited a gel of calcium alginate[23] to sense glucose-oxidase while Berto *et al.*[24] used bovine gelatinase[24] in an EGOFET capable to detect urea.

Agarose is a typical nature-source hydrogel, which is generally extracted from red seaweeds.[16] Agarose is a linear polymer with the repeating unit shown in **Figure 4.2** and can be classified as a natural hydrogel which jellifies due to intermolecular physical cross-linking. This natural compound is widely used in the food industry, electrophoresis, protein purification, separation technologies, and even for 3D cell culturing due to its biocompatibility and low production cost.[16,20,22] In general, agarose is insoluble in cold water, but hydrates in hot water. By cooling the agarose solution below 34 - 35℃, a firm and stable gel is obtained.[16]

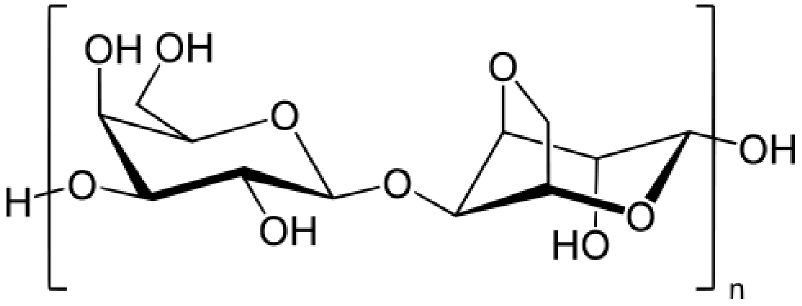

Figure 4.2: Structure of an agarose polymer.

- **Flexible pressure sensors**

In the past few years, flexible pressure sensors have been extensively investigated because of their potential use for many electronic applications, such as rollable touch screens, electronic skins and the next generation of portable (or wearable) health care products.[8,14,25–28] Most of these applications require low power consumption and high pressure sensitivity in the low-pressure regime (< 10 kPa, in the range of daily activities and intra-body pressures) and even in the subtle-pressure regime (1 Pa ~ 1 kPa, comparable to weak interactions such as touch screen) as well as low production costs.[8,28] Up to now, three main transduction mechanisms have been employed to convert pressure stimuli into electrical signals: piezoresistivity, capacitance and piezoelectricity.[8] Organic field-effect transistors (OFETs) are one of the attractive platforms for achieving flexibility, light weight and low cost pressure sensors due to the inherent merits of organic electronics.[8,14,29] In general, the transduction mechanism of a pressure sensor based on an OFET mainly relies on the capacitance change of the dielectric layer due to a pressure stimulus.[8,14,29] Bao *et al.* have reported a flexible capacitive pressure sensor with high sensitivity (0.55 kPa^{-1}) and fast response time (< 10 ms) by using a microstructured PDMS dielectric layer.[29] Recently, a similar ultra-sensitive OFET-based pressure sensor has been designed by Zhu and co-workers.[25] In this work, the authors exploit an air dielectric layer (several tens of micrometers) between the OSC and a flexible suspended gated electrode.[25] However the majority of the pressure sensors based on OFET technology operate at high voltage (> 60 V), which is not suitable for low power consumption applications.[8] The use of high *k* materials or the reduction of the dielectric thickness are two possible options for decreasing the operating voltage. The last option can be easily achieved by gating the transistor channel through liquid or solid electrolytes thanks to the large capacitance of the EDLs.

- **The objective of this chapter**

The objective of this chapter is two-folds: (1) developing a simple, low cost approach to achieve flexible hydrogel-gated OFETs (HYGOFETs) by using a homogeneous agarose gel film as dielectric component, and (2) employing the HYGOFETs as a pressure sensitive platform. To do so, the diF-TES-ADT:PS blend and an agarose gel thin layer were firstly deposited by BAMS on two separate Kapton substrates and then assembled to achieve the final HYGOFET. Then, the characteristics of the agarose film and the electrical performance of the HYGOFETs were carefully characterized in ambient conditions. Furthermore, we systematically tested the sensitivity of the pressure response of the HYGOFET platform addressing the pressure response mechanism behind it.

4.2 HYGOFET Prototype

The flexible HYGOFET prototype has been fabricated and assembled following the procedure described in Chapter 5. The two parts, namely diF-TES-ADT:PS-coated Kapton support and the agarose gel-coated Kapton support, have been fabricated separately and then assembled in a stacked configuration as sketched in **Figure 4.3.** Specifically, the diF-TES-ADT:PS_{10K}-coated support was mounted on top of the agarose-coated one in order to ensure top gate operation as a conventional EGOFET operating in liquid. The transparent agarose gel film was prepared by BAMS *via* fast pouring a hot agarose solution (in the range of 0.75 wt.% - 3 wt.%) on the metallic bar followed by the immediate shearing of the solution along the target substrate.[30]

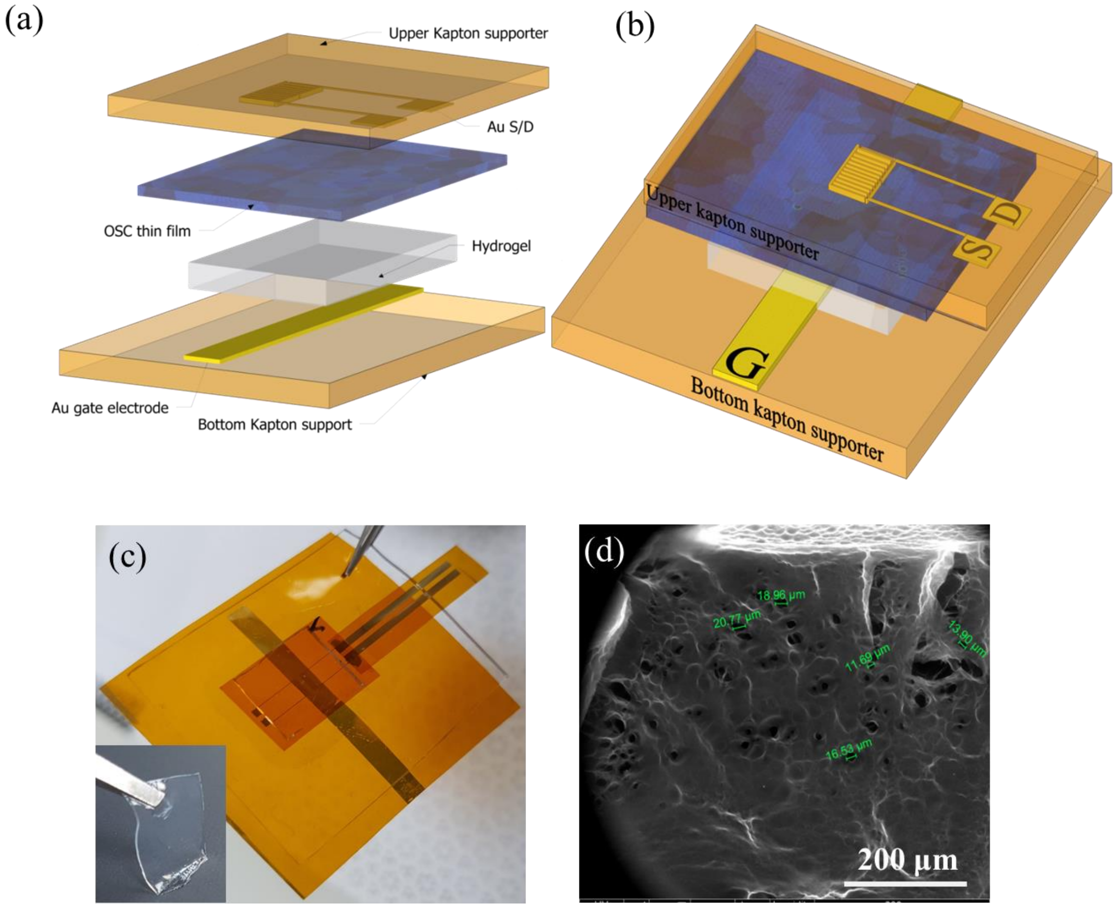

Figure 4.3: (a) and (b) Schematic diagram and (c) real photograph of the HYGOFET. The inset in (c) represents the photograph of the 1.5 wt.% agarose gel. (d) Cross-sectional view of the 1.5 wt.% agarose gel measured by SEM at 100Pa and RH% = 14%.

As shown in **Figure 4.4 (a)**, the thickness of the agarose layer is estimated to be in the range of 500-1000 μm as confirmed by scanning electron microscopy (SEM) measurements performed at 720 Pa and relative humidity RH% = 100 %. In addition, **Figure 4.4 (b)** displays a homogenous and smooth top agarose surface (recorded by SEM at 100 Pa and RH% = 14 %). Due to the nature of the gel, which is mainly composed by water, a shrinking of the film is expected under the SEM experimental conditions. The cross-sectional view of the film shows a complex network structure characterized by numerous pores with an average diameter of 20 μm (**Figure 4.3 (d)**).[16]

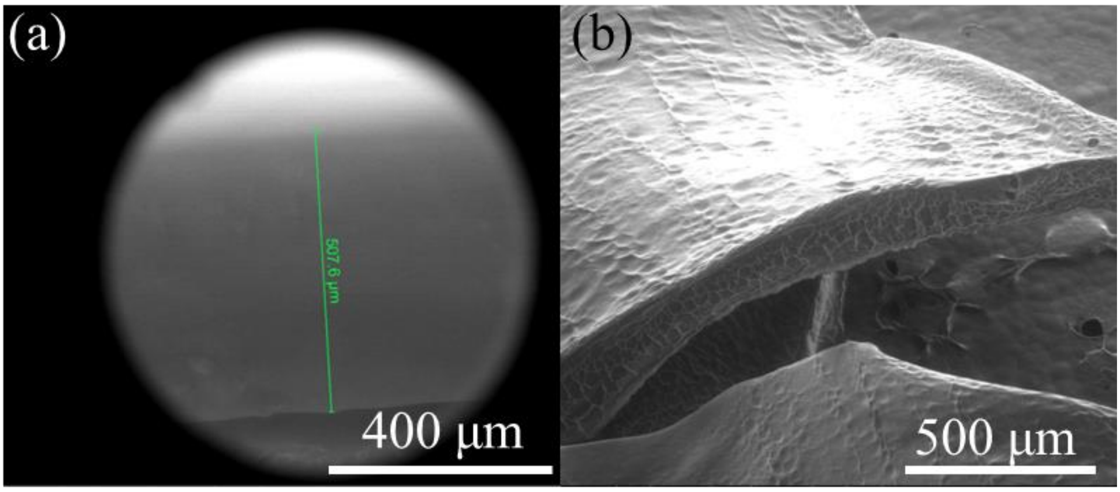

Figure 4.4: (a) SEM image of the profile of a 1.5 wt.% agarose gel film measured at 720 Pa and at RH of 100% in order to extract the thickness. (b) Top view of the same agarose gel film measured at 90 Pa and RH of 14%.

It is worth noting that the two coated thin films in the HYGOFET are totally different from each other in terms of chemical and physical properties: the diF-TES-ADT:PS_{10K} solution is a low viscosity ink soluble in organic solvent, whereas the agarose precursor solution has high viscosity and it is processed in water due to the hydrophilic nature of its backbone chains. Importantly, the successful deposition of both the organic semiconductor film and dielectric layer by BAMS is highly appealing considering that BAMS is a low-cost deposition technique.

4.3 Electrical Characterization of the HYGOFETs

HYGOFET devices based on different agarose concentrations were firstly tested in order to select the suitable concentration for further study. Three devices showing similar performance in a conventional EGOFET configuration with water as electrolyte (see **Figure 4.5 (a)**) were selected to be tested with agarose hydrogel employing three different concentrations, *i.e.*, 0.75 %, 1.5 % and 3 wt.%. As reported in **Figure 4.5 (b)** and **(c)**, a negative V_{th} shift is observed with increasing the gel concentration which is further accompanied by a decrease of the on-current (I_{on}) at V_{GS} = -0.5 V. This trend suggests that the more concentrated and stiffer the gel is, the less prone to accumulate charge carriers in the channel. This is probably due to the lower water content present in the high concentrated agarose film. However, the lower concentrated agarose gel was less robust and more difficult to manipulate. The opposite tendency was found in the 3 wt.% agarose devices. Taking all the results into account, the HYGOFET employing a 1.5 wt.% agarose gel film was selected as the best compromise to continue our studies.

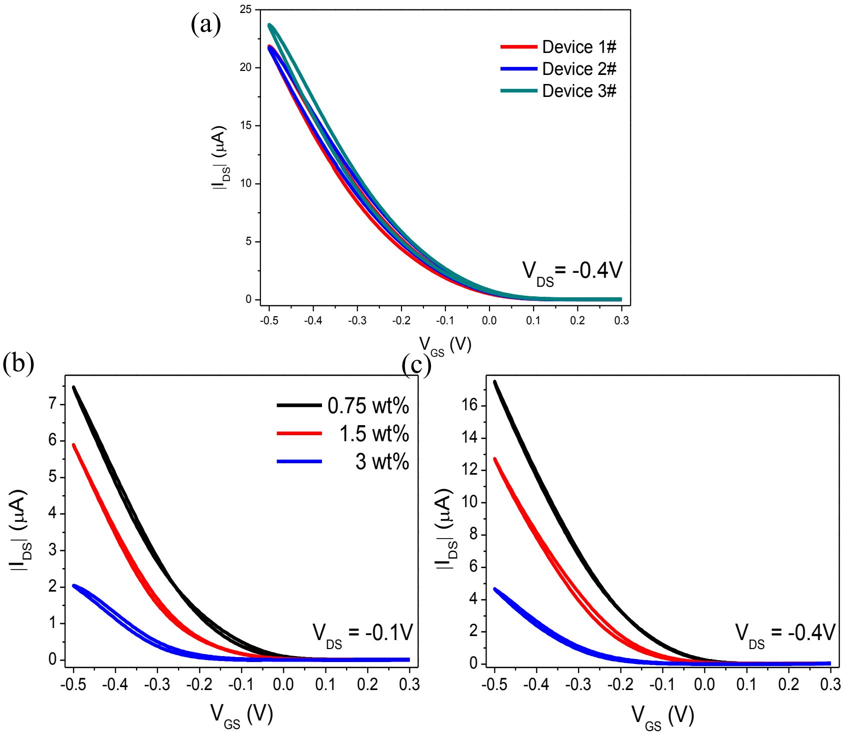

Figure 4.5: (a) Transfer characteristics of the three diF-TES-ADT:PS-based devices recorded in MilliQ water. Afterwards, the performance employing agarose gels of three different concentrations as dielectric were recorded at (b) low bias and (c) high bias regimes.

The evaluation of the HYGOFET electrical performance was performed by using 1.5 wt.% agarose gel as solid electrolyte. As shown in **Figure 4.6 (a)** and **(b)**, the transfer and output characteristics exhibit a typical *p*-type behavior in a V_{GS} window ranging from +0.3 V to -0.5 V with a negligible hysteresis. The electrical double layer capacitance (C_{dl}) of the agarose gel was evaluated through electrochemical impedance spectroscopy (EIS) by sandwiching a 1.5 wt.% agarose gel film between two gold electrodes. We estimated the capacitance of the electrical double layer (EDL) around 7.8 μF cm^{-2} at a frequency of 10 Hz (see **Figure 4.7 (a)**). This value is in good accordance with the ones already reported for high ionic strength electrolytes (*i.e.* NaCl 1M).[7] The conductivity of this gel was estimated around 0.4 mS/cm based on the EIS response in the high frequency region (see **Figure 4.7 (b)**). This result suggests that the conductivity of the agarose gel is far greater than that of MilliQ water (typical around 10^{-5} mS/cm).

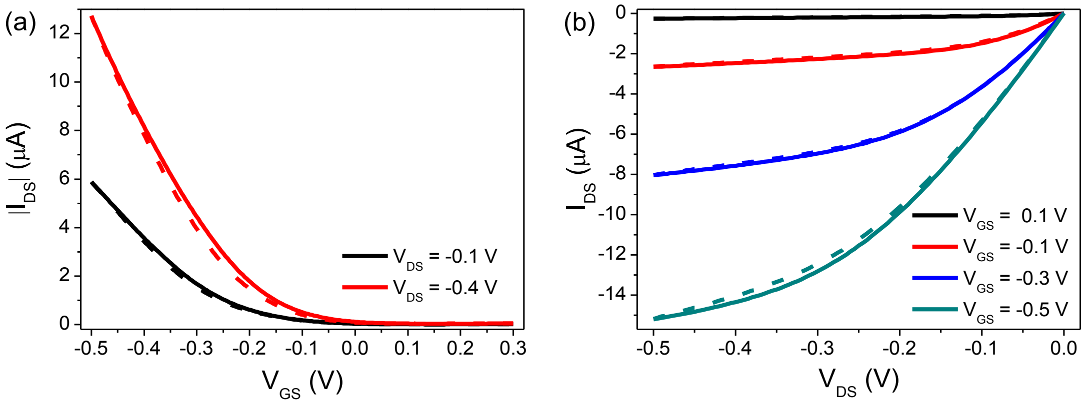

Figure 4.6: (a) Transfer curves of the HYGOFETs based on 1.5 wt.% agarose gel recorded at V_{DS} = -0.1 V and V_{DS} = -0.4 V. (b) Output curves recorded at different gate-source voltages. All the solid lines represent the forward sweep and the dashed lines are backward sweep.

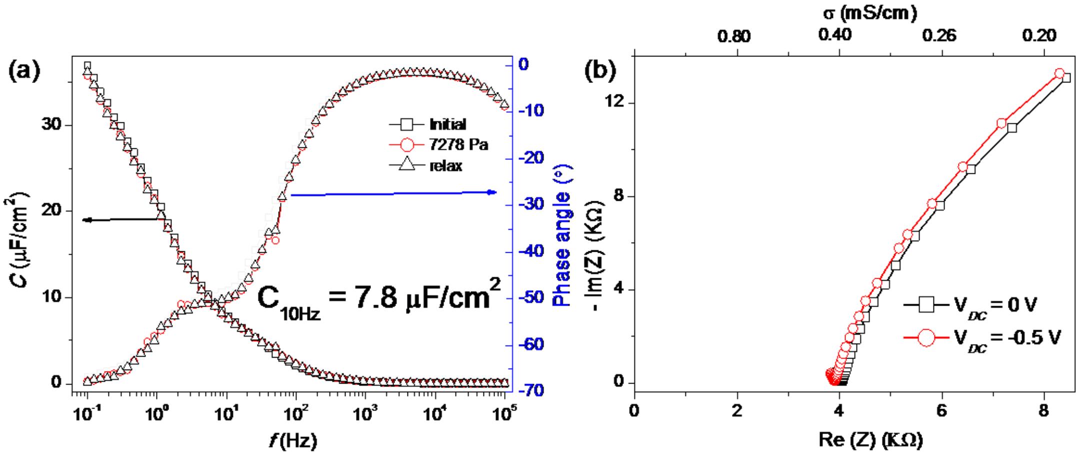

Figure 4.7: (a) Capacitance and (b) impedance response of a 1.5 wt% agarose gel film sandwiched between two gold electrodes.

The device parameters such as transconductance (g_m), switch-on voltage (V_{on}) and on/off ratio (I_{on}/I_{off}) have been extracted at the low bias (V_{DS} = -0.1 V) and high bias (V_{DS} = -0.4 V) regimes and they are summarized in **Table 4.1**. The transconductance, defined as $g_m = \Delta I_{DS}/\Delta V_{GS}$, was selected to describe the gate voltage ΔV_{GS} modulation of the HYGOFET current at the above-mentioned potentials.[31] One example of the transconductance plots at the low bias and high bias regimes are shown in **Figure 4.8 (a)**. The HYGOFET exhibited an average transconductance of 20 μS and 49 μS in the low bias and high bias regime, respectively.[32] To quantify the lowest detectable gate voltage change in the HYGOFET, we have performed the potentiometric sensitivity test by applying a gate-source pulse (ΔV_{GS}). The device exhibits sensitivity down to 100 μV, which is comparable to our previous results using water as media **(Figure 4.8 (b))**[32].

Table 4.1: HYGOFET parameters extracted at low bias and high bias regime from ten devices.

	V_{DS} = -0.1V			V_{DS} = -0.4V		
	I_{on}/I_{off}	V_{on} (mV)	g_m (μS)	I_{on}/I_{off}	V_{on} (mV)	g_m (μS)
1#	1.7×10^3	165	16	1.0×10^3	161	45
2#	6.2×10^2	176	10	4.4×10^2	180	27
3#	1.0×10^3	260	24	5.5×10^2	236	60
4#	8.9×10^2	148	28	5.5×10^2	198	75
5#	8.8×10^2	165	28	5.3×10^2	141	61
6#	8.1×10^2	145	25	3.7×10^2	125	50
7#	1.7×10^3	220	16	1.0×10^3	205	43
8#	2.5×10^3	129	20	8.9×10^2	168	48
9#	7.9×10^2	185	17	2.9×10^2	173	39
10#	6.5×10^2	110	18	4.6×10^2	117	40
Average			20			49

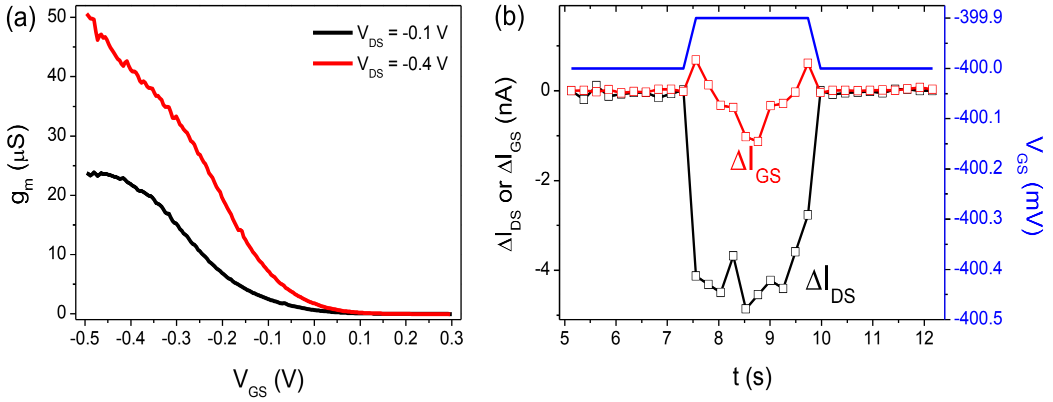

Figure 4.8: (a) Transconductance behavior corresponding to device of Figure 4.6 (a). (b) *I-t* plot corresponding to 100 μV step potential. The black curve represents the I_{DS} and the red one is I_{GS}.

Aiming at direct comparing this kind of architecture with a traditional EGOFET, we have carried out a more accurate electrical characterization. In particular, we evaluated the degree of hysteresis of the transfer curves at low bias and high bias regimes and we found that they did not show any dependence with the scan rate (136 mV/s, 72 mV/s and 31 mV/s), as shown in **Figure 4.9 (a)** and **(b)**. Electrical stability represents another important issue. The shelf stability has been monitored for two days. As shown in **Figure 4.9 (c)** and **(d)**, the device still works well after two days confirming again the high stability of our semiconductors. The decrease in I_{DS} current observed could be mainly ascribed to some water evaporation that cannot be totally excluded. Furthermore, the area of the gate dielectric layer seems not to affect the electrical performance, as evidenced by **Figure 4.10**.

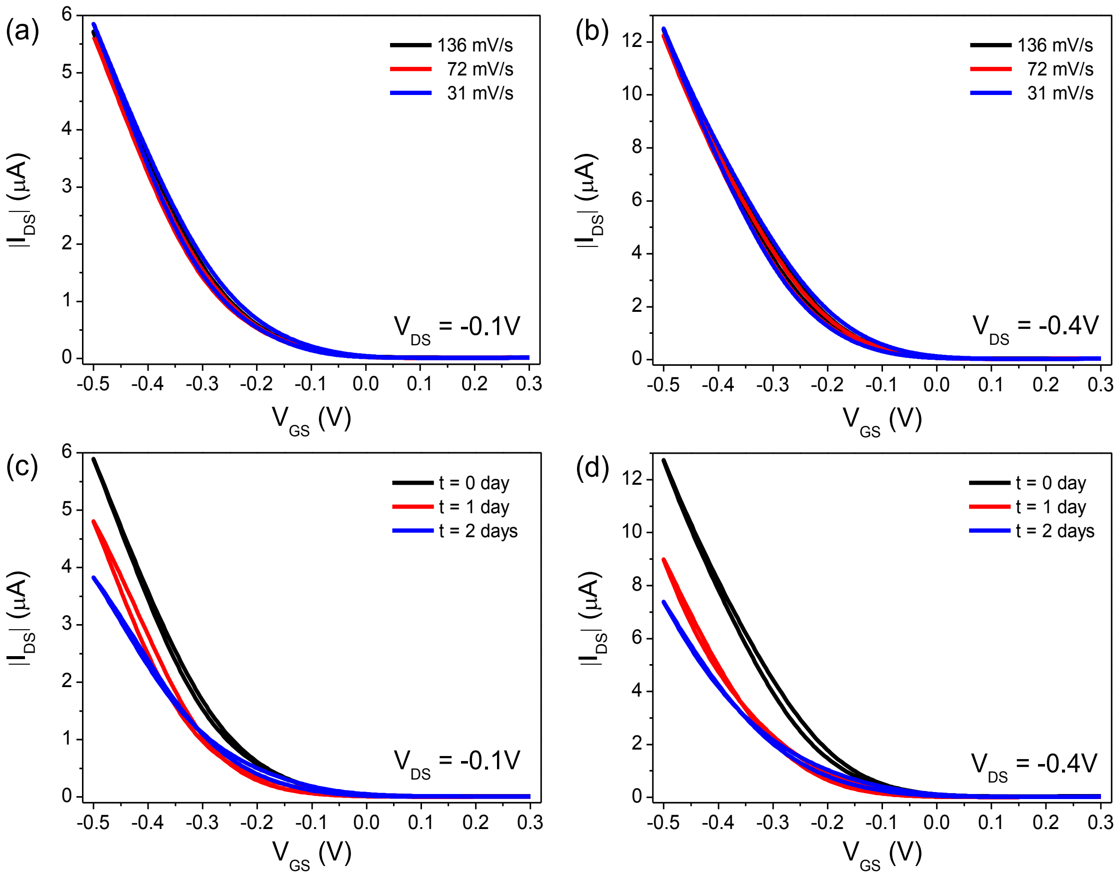

Figure 4.9: Transfer characteristics with three different scan rates recorded at (a) low bias regime (V_{DS} = -0.1 V) and (b) high bias regime (V_{DS} = -0.4 V). Shelf stability corresponding to the device of Figure 4.6 at (c) V_{DS} = -0.1V and (d) V_{DS} = -0.4V.

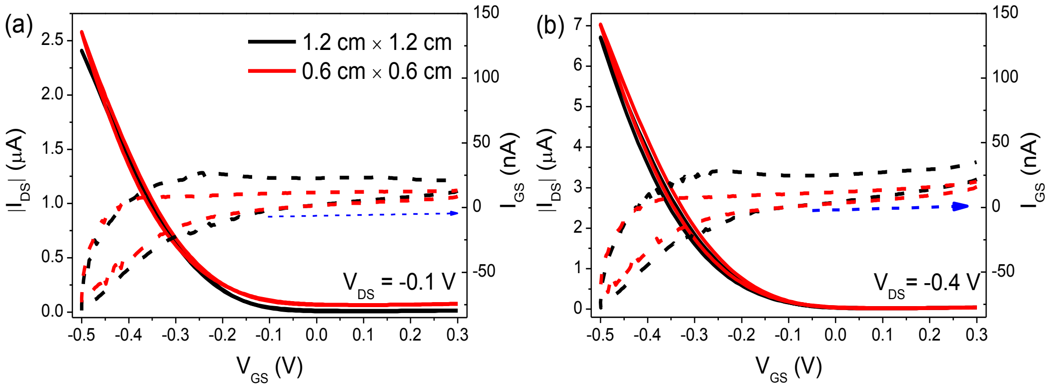

Figure 4.10: Influence of the agarose gel area on the HYGOFET electrical response recorded at (a) low bias and (b) high bias regime. The dashed lines are the corresponding leakage currents.

4.4 Pressure Response

Hydrogels are versatile materials that are prone to deformation. In the present case, such property could offer an interesting possibility due to its role as gate dielectric. Prior to the real pressure measurement, the electrical stability of the HYGOFETs was measured, as shown in **Figure 4.11**. After repetitive transfer recording, a negligible shift of V_{th} (less than 5 mV) and a perfect overlap of the transfer curves was observed in agreement with the high electrical stability of the HYGOFETs.

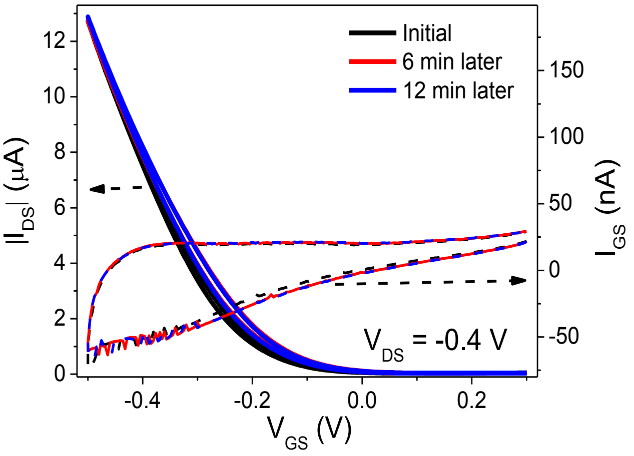

Figure 4.11: Electrical recording of a series of *I-V* transfer characteristics prior to the pressure test at high bias regime (V_{DC} = -0.4V). The dashed lines represent the I_{GS} current recorded at the same time.

Our approach consisted in the application of a controlled pressure on top of the HYGOFET by using a series of calibrated weights, as shown in **Figure 4.12 (a)**. The application of a pressure on the HYGOFET induces the response displayed in **Figure 4.12 (b)** (V_{DS} = -0.4 V) and **Figure 4.13 (a)** (V_{DS} = - 0.1 V). Once a pressure of 2.1 kPa was loaded on the channel area of the HYGOFETs device, a negative shift of V_{th} and a decrease of I_{on} were observed. Once the weight was removed, the I_{DS} current recovered its initial state. The high reproducibility of this behavior was confirmed even when the same experiment was repeated by applying an increasing pressure by means of a series of weights. **Figure 4.12 (c)** shows the HYGOFET response due to the application of an increasing pressure when the device operates at high bias regime. A gradual negative V_{th} shift is observed as the pressure increases. This gradual shift is accompanied by a decrease of both I_{on} and I_{off} (see **Figure 4.14 (a)**). The total recovery of the initial transfer characteristic after each pressure stimulus confirms again the recovery of our agarose dielectric and the absence of any damage to the OSC:PS active layer. A similar behavior was observed at low bias regime (see **Figure 4.13 (b) and (c)**).

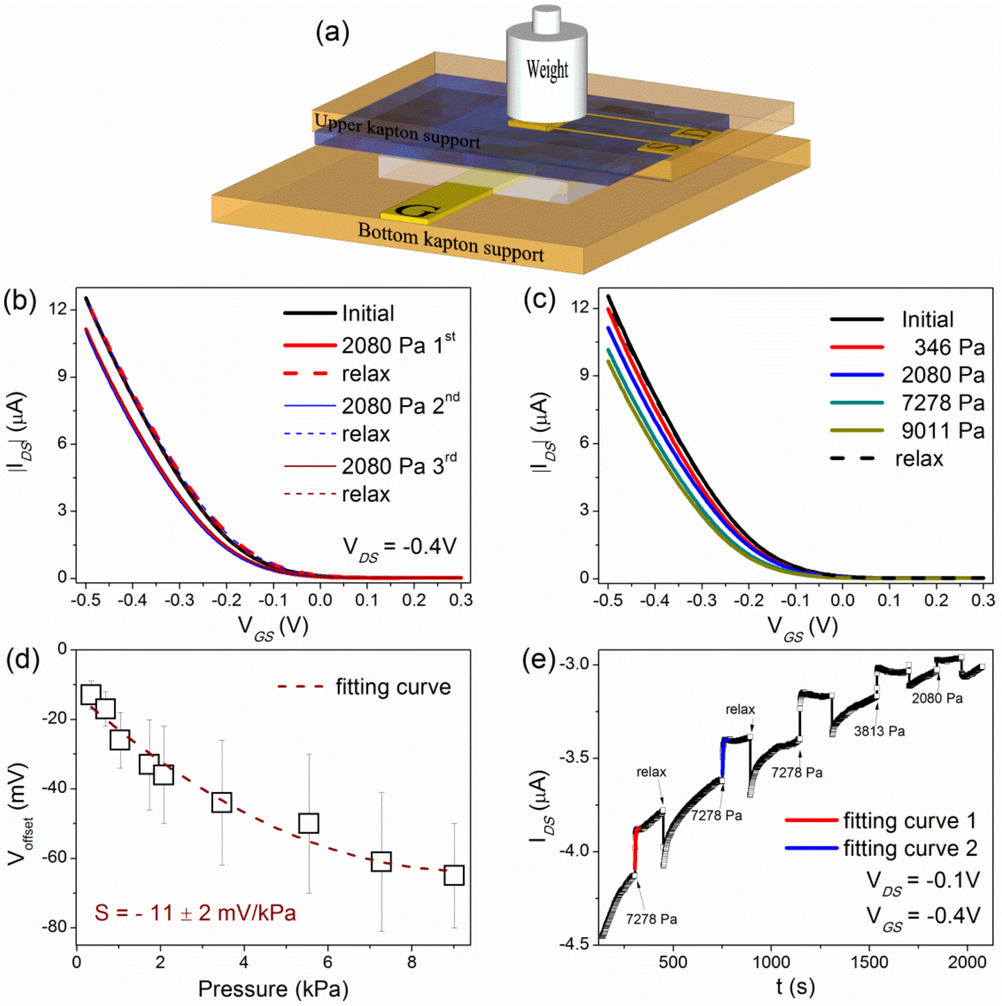

Figure 4.12: (a) Schematic diagram of the pressure test performed with the HYGOFET. Transfer characteristics recorded at (b) the same pressure value and (c) different pressures with a constant V_{DS} = -0.4 V. All the dashed lines represent the relax state once the weight has been removed. (d) Plot of V_{offset} *vs* pressure. The pressure was loaded from 300 Pa to 9 kPa in ascending order. (e) *I-t* plot of

the device operated with pressure loaded and relaxed at constant V_{GS} =-0.4 V and V_{DS}=-0.1 V. The red and blue lines stand for the exponential fit related to the response speed towards pressure.

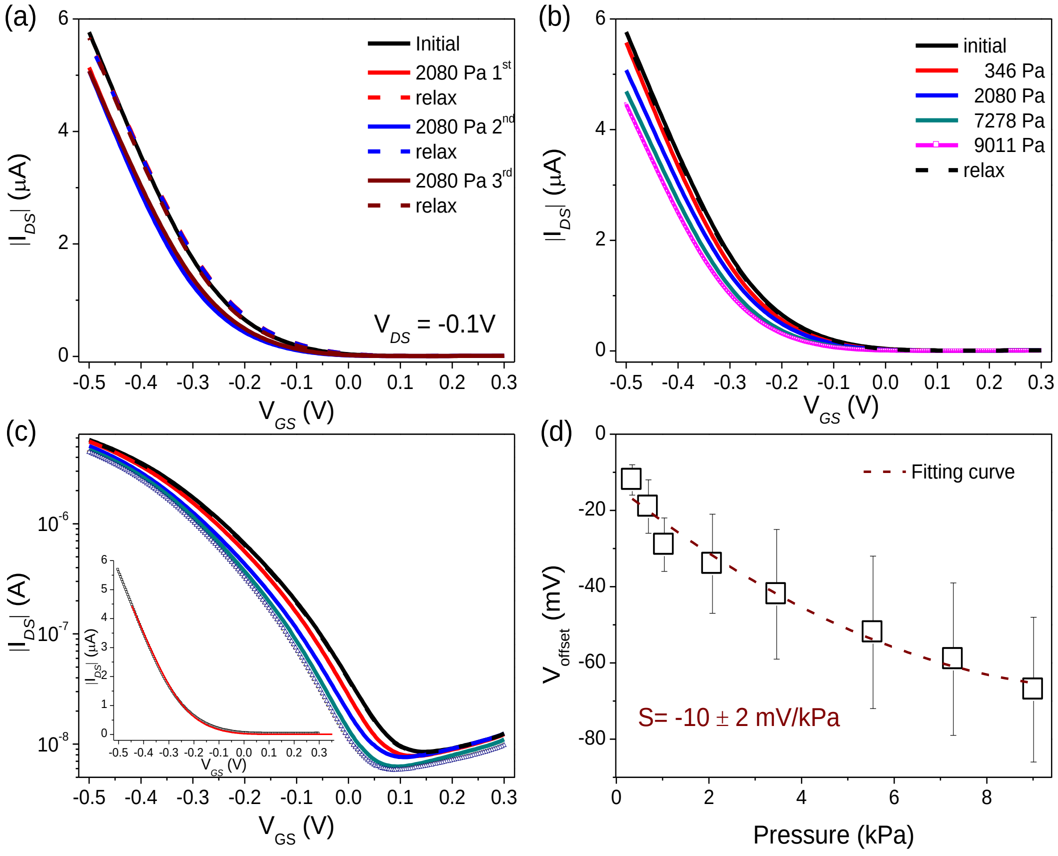

Figure 4.13: Pressure response in the low bias regime (V_{DS} = -0.1V) with the same device displayed in Figure 4.12. Transfer characteristics recorded with (a) the same pressure and (b) different pressure values. (c) the log-lin plot corresponding to (b) in the same figure. (d) Plot of V_{offset} versus pressure in the low bias regime.

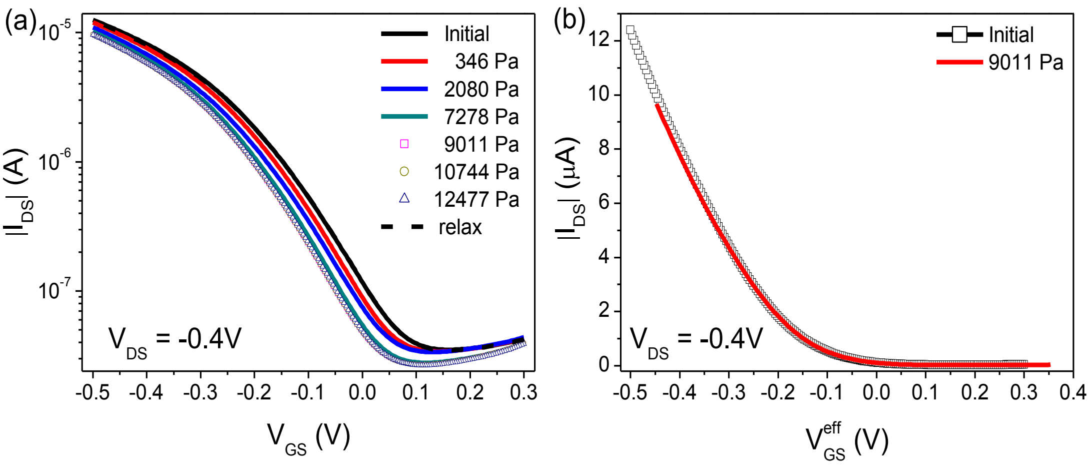

Figure 4.14: (a) Log-lin plot corresponding to the device of Figure 4.10. (b) Shifting of the transfer curves along the V_{GS} toward the initial transfer at high bias regime.

Moreover, it is interesting to observe how the slope of the transfer characteristic presented in **Figure 4.12 (b)** and **(c)** remains unaltered during the pressure test. This behavior suggests that the pressure stimulus is not significantly affecting the capacitance at the OSC/hydrogel interface. This fact was in agreement with the EIS measurements carried out with a vertical architecture (Au/1.5 wt%-agarose gel/Au) was employed (**Figure 4.7 (a)**). As shown in **Figure 4.14 (b)**, all the transfer characteristics can perfectly overlap by shifting the curves along the V_{GS} axis according to:

$$V_{GS}^{eff} = V_{GS} + V_{offset} \tag{4.1}$$

where V_{GS}^{eff} is the effective gate voltage and V_{offset} is an offset voltage that is dependent on the loading pressure. Such evidence indicates that pressure stimuli mainly shift the *I-V* characteristic along the horizontal axis by V_{offset}. The effect of pressure on HYGOFET electrical response is quantified in **Figure 4.12 (d)** by a quadratic fitting in a range of pressure spanning from 300 Pa to 9 kPa according to:

$$V_{offset}(\Delta P) = S' \cdot \Delta P^2 + S \cdot \Delta P + C_0 \tag{4.2}$$

Here ΔP denotes the loaded pressure. The sensitivity (S) of the device was approximated to the first order. A sensitivity of -11 ± 2 mV/kPa was estimated in high bias regime (**Figure 4.12 (d)**) and -10 ± 2 mV/kPa in low bias regime (**Figure 4.13 (d)**). These data were averaged between 6 devices, whose statistical results are listed in **Table 4.2**.

The HYGOFET was also tested under continuous operation as depicted in **Figure 4.12 (e)** (V_{DS} = -0.1 V and V_{GS} = -0.4 V). During the measurement three different pressures were applied that clearly induce a decrease of the absolute I_{DS}. Moreover, the current modulation was reproducible as evidenced by the first three tests that show no substantial differences and proportionality to the pressure applied. As depicted in **Figure 4.12 (e)**, the time response of the HYGOFET towards pressure was estimated to be ～2 s from the exponential fit of I_{DS} (*i.e.* $\Delta I_{DS}=e^{\pm(t/\tau)}$).[32]

Table 4.2: Extracted ΔV_{offset} values according to different pressure values.

	ΔV_{offset} (mV) in high bias regime (V_{DS} = -0.4V)							
	346 Pa	693 Pa	1039 Pa	2079 Pa	3466 Pa	5545 Pa	7278 Pa	9011 Pa
$1^{\#}$	-12	-18	/	-30	-31	-34	-45	-53
$2^{\#}$	-15	-21	-23	-29	-33	-40	-55	-63
$3^{\#}$	-13	/	-37	-50	-60	-70	-78	-80
$4^{\#}$	-9	-12	-27	-48	-62	-69	-81	/
$5^{\#}$	-15	/	/	-33	-35	-46	-57	/
$6^{\#}$	-13	-17	/	-26		-41	-49	/
Average	-13±4	-17±5	-26±8	-36±14	-44±18	-50±20	-61±20	-65±15
	ΔV_{offset} (mV) in low bias regime (V_{DS} = -0.1V)							
$1^{\#}$	-10	-17	/	-31	-32	-38	-41	-48
$2^{\#}$	-16	-26	-29	-36	-42	-48	-66	-71
$3^{\#}$	-11	/	-36	-47	-53	-60	-64	-66
$4^{\#}$	-11	-15	-23	-36	-55	-69	-70	-85
$5^{\#}$	-14	/	/	-33	-43	-64	-71	-87
$6^{\#}$	-11	-17	/	-21	-25	-32	-39	-48
Average	-12±4	-19±7	-29±7	-34±13	-42±17	-52±20	-59±20	-67±19

4.5 Mechanism of Pressure-Induced Response[vii]

Aiming at a complete understanding of the mechanism behind the HYGOFET towards pressure, we performed a series of experimental crosschecks. First of all, it is easy to assume that the changing of the electrical double layer capacitance is the origin of the pressure-induced response in the HYGOFET case due to a possible release/swelling of water inside the agarose gel when loading/removing the calibrated weight. However, the changing of capacitance is not the reason in our case based on two already addressed evidences: constant capacitance and constant slope of transfer curve between both pressure applied and pressure relaxed states (see **Figure 4.7 (a)** and **Figure 4.14 (b)**).

A possible reason behind the modulation of the current could be ascribed to the mechanical deformation of the semiconductor layer due to compression/tensile strain induced by the application of pressure. Such a behavior has already been studied by several groups that correlate the morphological change at the micro-scale to an

---

[vii] This work was carried out in collaboration with Dr. Raphael Pfattner (ICMAB-CSIC).

increase/decrease of I_{DS} current under compression/tensile condition.[33,34] Although this rationale was the most intuitive for our scenario, our experimental results showed clear discrepancies because the application of a tensile or compression deformation to the HYGOFET led the same effect on its electrical response. As evidenced in **Figure 4.12** and **Figure 4.15**, the two opposite mechanical stresses induce a similar electrical response, in contrast to what it has already been demonstrated in literature by several groups.[33,34] This pointed that the origin of the pressure response was not coming from the OSC deformation.

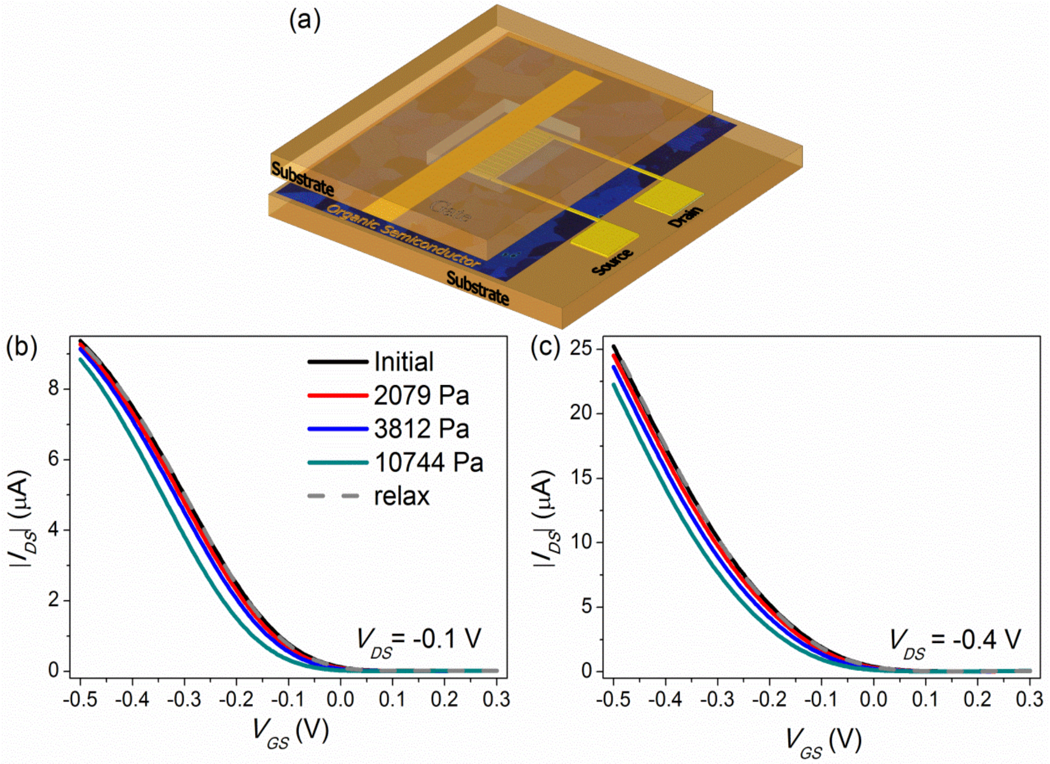

Figure 4.15: (a) Schematic diagram of the pressure test in inverse configuration of the HYGOFET. Transfer characteristics were recorded at (b) low bias (V_{DS} = -0.1 V) and (c) high bias (V_{DS} = -0.4 V) with different pressure stimulus.

In addition, to exclude any eventual role of the flexible support on the pressure response of our devices, we replaced the agarose-support Kapton substrate with a rigid Si/SiO_2 substrate, a typical gate electrode/dielectric support used in OFET technology. As shown in **Figure 4.16**, a similar behavior, *i.e.* the negative V_{offset} shift, was observed showing high reproducibility in both low bias and high bias regime. This indicated that the observed phenomenon was strictly correlated with the active thin layer. However, disentangling the role of the semiconducting blend and of the dielectric gel was pivotal.

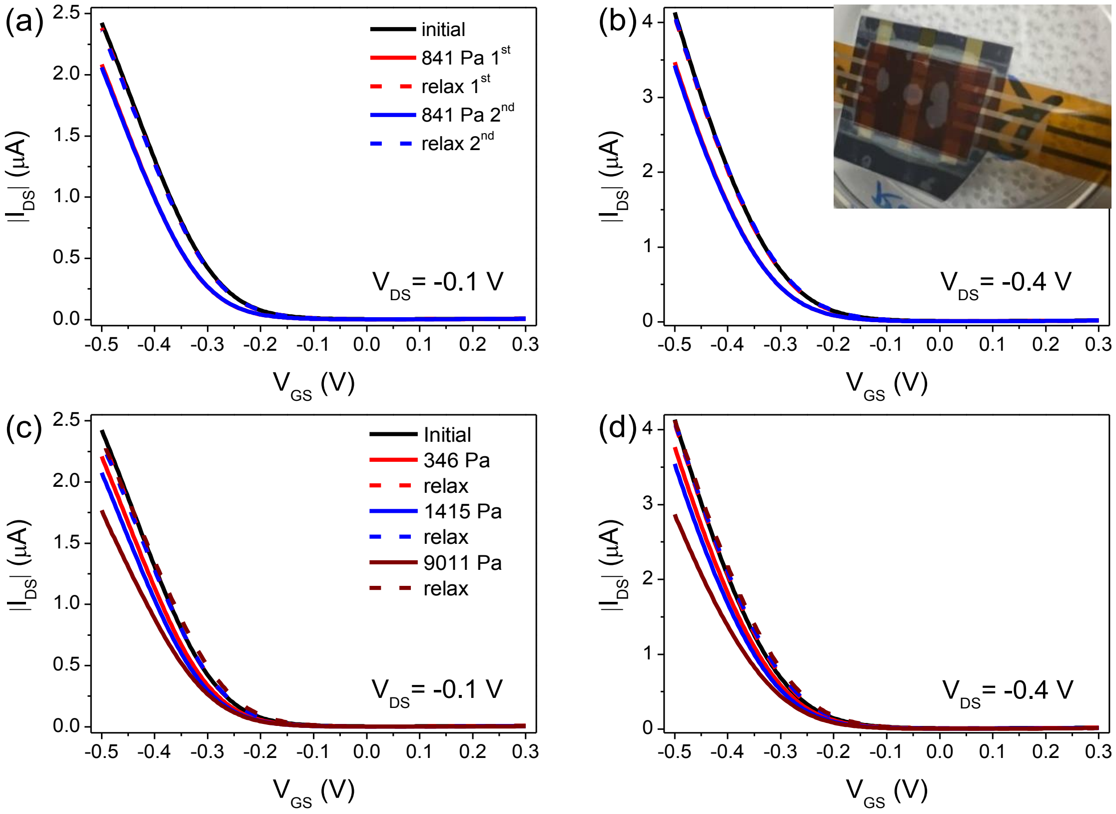

Figure 4.16: Pressure response of the Si/SiO$_2$-supported gated HYGOFETs at the same pressure value in (a) low and (b) high bias regime. The insert is the photo of the real device. Pressure response of the same device at different pressure values in the (c) low and (d) high bias regime.

So far, we have excluded two probable causes of the pressure-induced response in our HYGOFETs: capacitance and deformation of the OSC layer. These results prompted us to design another crosscheck by removing the hydrogel dielectric layer. To do so, Si/SiO$_2$-based OFETs bearing the same *S*/*D* geometry with BGBC configuration was fabricated using also the same OSC:polymer blend active layer, namely dif-TES-ADT:PS deposited by BAMS. A fast and preliminary pressure test was carried out by loading different calibrated weights on top of the channel region of the OFETs and recording their corresponding back-gate electrical performance, as illustrated in **Figure 4.17 (a)**. Surprisingly, once the pressure was loaded, a negative V_{th} shift and a consequent I_{DS} decrease was observed in this OFET device followed by a perfect recover of the initial transfer characteristics when the pressure was removed (see **Figure 4.17 (b)**). In other terms, the transfer characteristics in the OFET responded in a similar manner to what it was observed in the HYGOFET devices. Considering that the OSC active layer was deposited by a solution processing technique in ambient and the similar pressure-response behavior found in both cases, make us suspect that the water in the active OSC thin film could be playing an important role in the pressure-induced response. Furthermore, the pressure sensitivity of the OFET device was evaluated following the same calculation equation used for the HYGOFET. A comparable sensitivity (~ 30 mV/kPa) was obtained in the OFET device, which suggests that the agarose gel is not importantly influencing the pressure response.

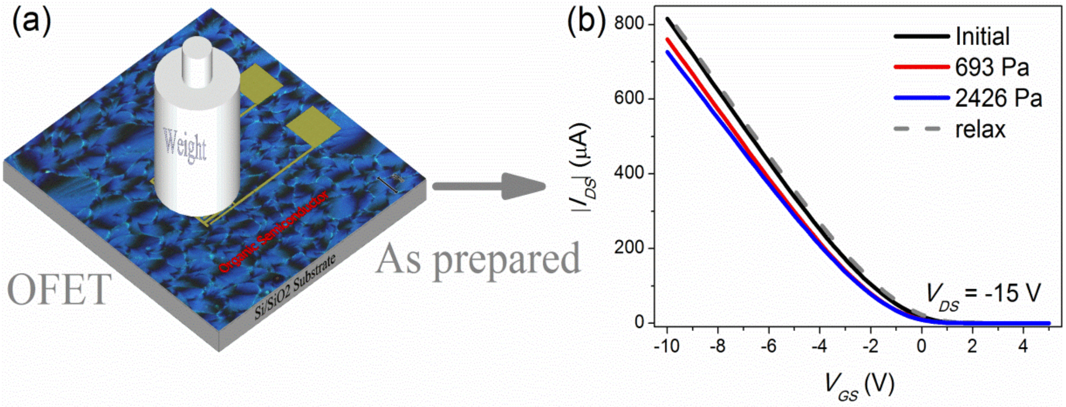

Figure 4.17: (a) Schematic diagram of the application of weights on OFETs. (b) *I-V* characteristics recorded in saturation regime of the as-prepared device measured in environment conditions.

The presence of traces of water in the active thin films, which is known that can affect the device performance,[35,36] cannot be completely avoided, especially in devices processed in ambient conditions. In the past years, many breakthrough studies have demonstrated how the water entrapped in the OSC layer affect the electrical response of the OFET causing threshold voltage instability[36] and serious hysteresis[37] due to the polar nature of water. In order to understand the role of the water present in the OSC and how it can affect the device response and even the pressure-induced response, a careful study has been performed by storing the OFET device in a high vacuum chamber to remove the entrapped water in the OSC thin film and, subsequently, storing the "dry" device again in ambient environment to achieve re-adsorption of water in the OSC thin film. During this procedure, the OFET electrical performances and pressure responses of each condition have been systematically measured and compared.

The same kind of OFET device has been fabricated again by BAMS as previously described on Si/SiO$_2$. The as-prepared devices measured in enviromental conditions exhibited a remarkable *p*-type field effect response in the saturatation and linear regime, as shown in **Figure 4.18 (a)** and **(b)**. However, the presence of water traces inside the active film is inevitable, which is translated in a visible hysteresis and a non-linear dependence of $I_{DS}^{1/2}$ *versus* V_{GS} in the transfer characteristics of the as-prepared device (**Figure 4.18 (a)**). A similar non-linear dependence of I_{DS} *versus* V_{GS} was also observed in the linear regime (**Figure 4.18 (b)**). In addition, the mobility profile exhibited a strong V_{GS}-dependent in the saturation and linear regime in the as-prepared devices, as shown in the inset of **Figure 4.18 (a)** and **(b)**.

In contrast, after storing the same device in a high vacuum chamber (~10^{-5} Pa) for more than 70 hours in order to "dry" it removing any trace of water, the OFET characteristics showed more ideal characteristics with non-appreciable hysteresis and a perfect linear dependences of $I_{DS}^{1/2}$ *versus* V_{GS} in the saturatuion regime (**Figure 4.18 (c)**) and a better linear dependences of I_{DS} *versus* V_{GS} in the linear regime (**Figure 4.18 (d)**). Here, the "dry" OFET was measured in glove box. It is worth noting that a V_{GS}-independent mobility profile was observed in the "dry" device (inset of **Figure 4.18 (c)**). Finally, the hysteresis and the non-linear dependence of $I_{DS}^{1/2}$ *versus* V_{GS} in the saturation regime (**Figure 4.18 (e)**) and non-linear dependence of I_{DS} *versus* V_{GS} in the linear regime (**Figure 4.18 (f)**) re-appeared by means of storing the "dry" sample again in the ambient conditions for 48 hours. Also, the mobility profile re-exhibited a strong V_{GS}-dependent behavior in saturation and linear regime (inset of **Figure 4.18 (e)** and **(f)**). These observations demonstrate that the water present in the OSC thin film clearly affect the device performance.

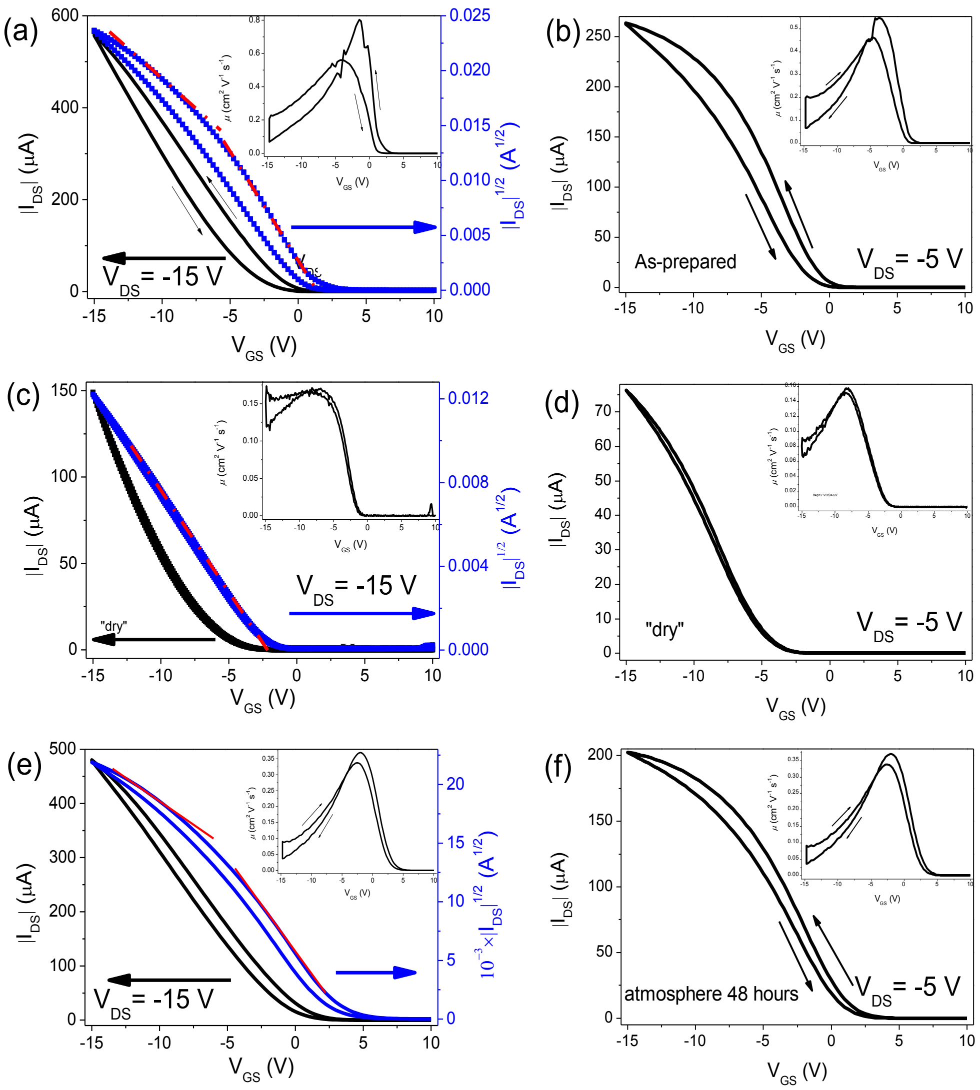

Figure 4.18: *I-V* characteristics of a as-prepared device recorded in (a) saturation and (b) linear rgime. *I-V* characterisitcs of the same device recorded in (c) saturation and (d) linear regime after storing the device in a high vacuum chamber (~10^{-5} Pa) for 70 hours to remove the traces of water. *I-V* characteristics of the same device recorded in (e) saturation and (f) linear regime after storing again the "dry" device in the atmosphere for 48 hours. The insets are their mobility profiles.

As already reported by several groups, water is known to orientate under the application of an electric field due to its dipolar nature and, further, such orientation can be affected by the application of pressure.[38–40] Subsequently, a controlled pressure was applied on top of the channel region of the Si/SiO_2 substrate-based OFET following the same procedure used before. Here, a PDMS layer was positioned on top of the active area to guarantee the uniform stimulation of the channel region with the calibrated weight (**Figure 4.19 (a)**). Also, the higher Young module of PDMS compared to the OSC film ensures that not deformation is occurring in the later. Again, in the as-prepared OFET device, a similar pressure-induced behavior was observed, as displayed in **Figure 4.19 (b)**. That is, a negative V_{th} shift and a consequent I_{DS} decrease was observed in "as-prepared" OFET device once the pressure was loaded, and a perfect recover of its initial transfer characteristics was noticed when the pressure was relaxed. In sharp contrast, the "dry" OFET (*i.e.* the device stored under high vacuum for 70 hours) did not respond to the loading of all the tested calibrated weights (**Figure 4.19 (c)**). In addition, the recovery of the pressure response was obtained after exposing the device again to ambient conditions for 48 hours, as evidenced in **Figure 4.19 (d)**. Furthermore, a similar pressure response was observed in the linear regime in the above three conditions (**Figure 4.20**). These results indicated that the changes in the water dipole orientation within the OSC film induced by the applied pressure affect the electrical device response in a reversible manner.

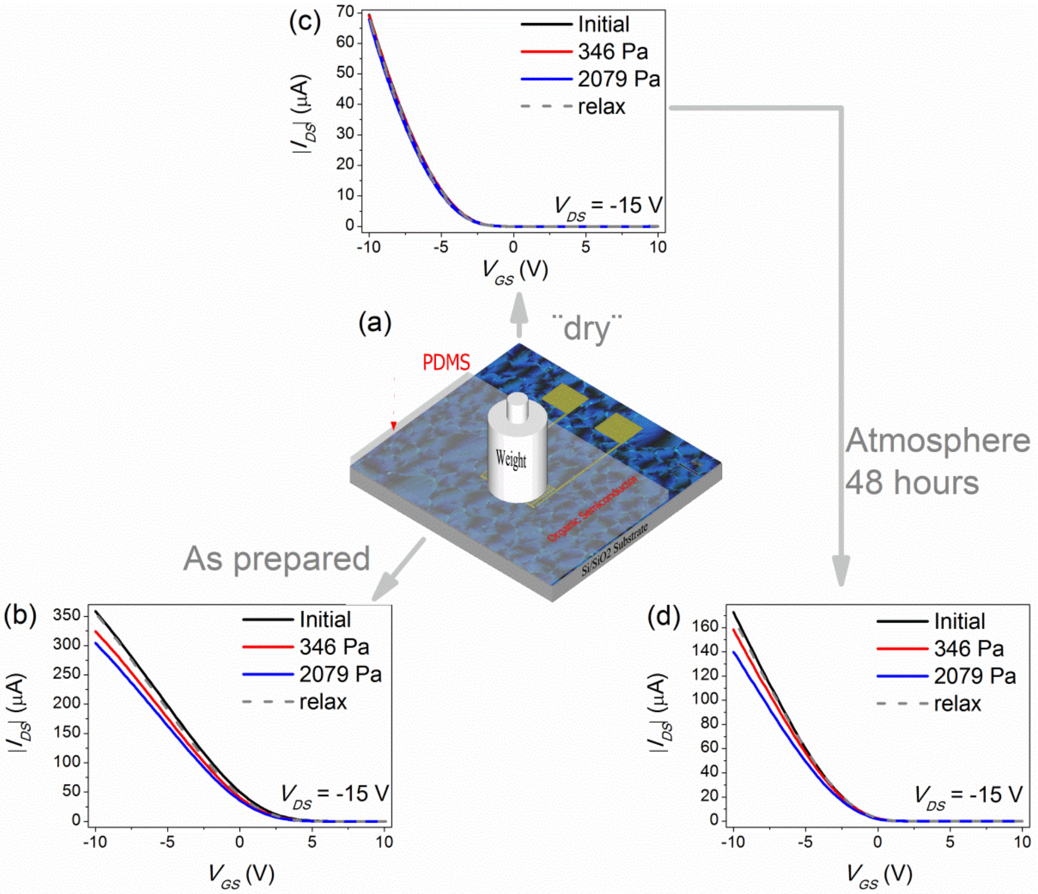

Figure 4.19: (a) Schematic diagram of the application of weights in OFETs. Transfer characteristics recorded in saturation regime for (b) the as-prepared device, (c) "dry" device and (d) again enviromentally exposed device in the presence and absence of the weights. The "dry" process was carried out by storing the OFET device in a high vacuum chamber (~10^{-5} Pa) for 70 hous. The atmosphere process recovery was realised by storing the "dry" device in atmosphere process for 48 hours.

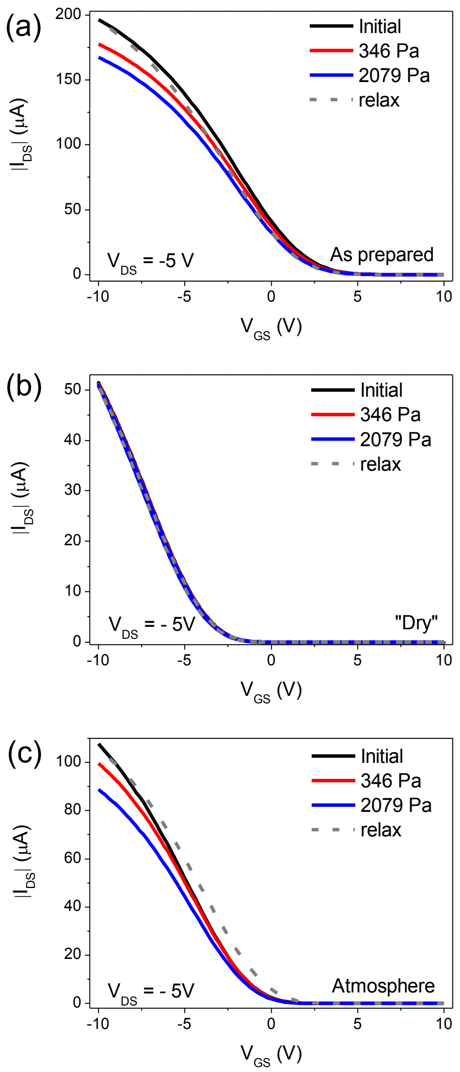

Figure 4.20: Electrical characteristics of the pressure-induced response of the Si/SiO$_2$-based OFET in the linear regime displayed in Figure 4.18. Transfer charactersitics recorded in the linear regime in the presence and absence of the weights for the (a) as-prepared, (b) “dry” device and (c) stored again in atmosphere conditions for 48 hours.

Effectively, the presence of water in OFET within the OSC thin film is pivotal for its pressure response. To further support the dominant role of water and connect to our HYGOFET result, the agarose gel film was assembled on top of a “dry” OSC thin film to achieve a top-gate bottom-contact configuration, as sketched in **Figure 4.21 (a)**. The same pressure stimulation protocol was repeated on the Si/SiO$_2$-based HYGOFET device. Interestingly, as shown in **Figure 4.21b**, the electrical response of the HYGOFET towards pressure resembles the trend observed for freshly prepared OFETs.

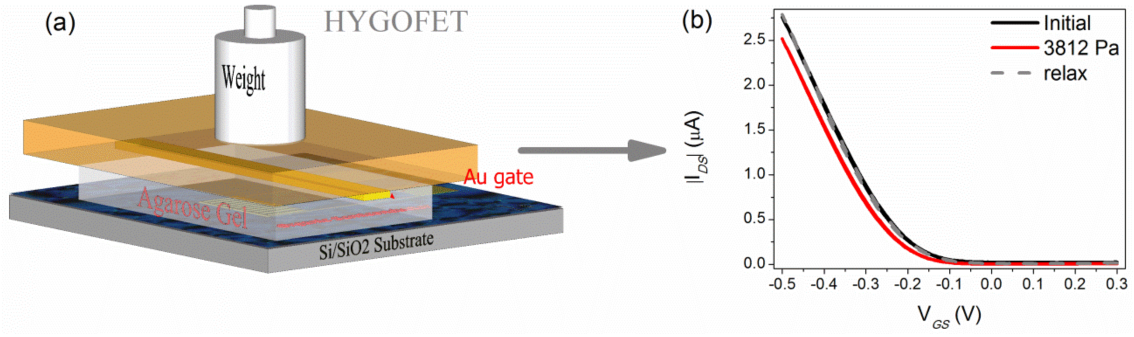

Figure 4.21: (a) Schematic diagram of the Si/SiO_2-based HYGOFET subjected to pressure. (b) Transfer characteristics of the HYGOFET recorded at high bias (V_{DS} = -0.4V) when a weight is applied and in the relaxed state.

Finally, the question that arises is: what is the role of the agarose gel in the HYGOFET related to the pressure response? As mentioned before, agarose is an attractive material due to its facile manipulation, easy availability and ability to swell a larger amount of water. Therefore, the first role of agarose gel in the HYGOFET device is the reduction of the operation voltage for realizing low-power consumption devices thanks to the high capacitance driven by the formation of EDLs. In addition, the agarose gel can provide a constant saturated water environment to the active OSC layer because it is difficult to control the amount of water present in the OSC active layers, which could be in turn dependent on the ambient humidity.

4.6 Summary

In conclusion, the bar-assisted meniscus shearing technique has revealed fundamental for the fabrication of different components of a hydrogel-gated field-effect transistor based on agarose. This water based gel has served as dielectric layer to achieve flexibility and a more compact solid state electrolyte-gated field-effect transitor, taking advantage of its high capacitance and constant saturated humidity environment. The HYGOFET exhibited high electrical performance and relative long-term stability due to a home-made encapsulation with a PDMS film. The electrical characteristics of this device respond to the application of low-pressures (in the range of several hundred Pa to 9 kPa) revealing a high reproducibility and sensitivity and, importantly, operating below 0.5 V. The origin of this pressure-induced response has been attributed to the changes in the orientation of the dipole of the water molecules which are entrapped in the OSC thin film. Thus, it has been elucidated that HYGOFETs offer an excellent platform to develop portable biocompatible, biodegradable and low-consumption pressure sensors taking advantage for the first time of the influence of the water dipoles alignment on the OSC electrical response. Such transduction mechanism differs from the well-known principles exploited up to now, which typically require of high operation voltages.

Bibliography

1. Buth, F., Donner, A., Sachsenhauser, M., Stutzmann, M. & Garrido, J. A. Biofunctional electrolyte-gated organic field-effect transistors. *Adv. Mater.* **24,** 4511–4517 (2012).
2. Magliulo, M. *et al.* Electrolyte-gated organic field-effect transistor sensors based on supported biotinylated phospholipid bilayer. *Adv. Mater.* **25,** 2090–2094 (2013).
3. Wang, D., Noël, V. & Piro, B. Electrolytic Gated Organic Field-Effect Transistors for Application in Biosensors—A Review. *Electronics* **5,** 9 (2016).
4. Kergoat, L. *et al.* A water-gate organic field-effect transistor. *Adv. Mater.* **22,** 2565–2569 (2010).
5. Cramer, T. *et al.* Water-gated organic field effect transistors-opportunities for biochemical sensing and extracellular signal transduction. *J. Mater. Chem. B* **1,** 3728–3741 (2013).
6. Zhang, Q., Leonardi, F., Casalini, S. & Mas-Torrent, M. Mercury-Mediated Organic Semiconductor Surface Doping Monitored by Electrolyte-Gated Field-Effect Transistors. *Adv. Funct. Mater.* **27**, 1703899 (2017).
7. Leonardi, F. *et al.* Electrolyte-Gated Organic Field-Effect Transistor Based on a Solution Sheared Organic Semiconductor Blend. *Adv. Mater.* **28,** 10311–10316 (2016).
8. Zang, Y., Zhang, F., Di, C. A. & Zhu, D. Advances of flexible pressure sensors toward artificial intelligence and health care applications. *Mater. Horizons* **2,** 140–156 (2015).
9. Mulla, M. Y. *et al.* Capacitance-modulated transistor detects odorant binding protein chiral interactions. *Nat. Commun.* **6,** 6010 (2015).
10. Kim, S. H. *et al.* Electrolyte-gated transistors for organic and printed electronics. *Adv. Mater.* **25,** 1822–1846 (2013).
11. Dumitru, L. M., Manoli, K., Magliulo, M., Palazzo, G. & Torsi, L. Low-voltage solid electrolyte-gated OFETs for gas sensing applications. *Microelectronics J.*

45, 1679–1683 (2014).

12. Liu, N. *et al.* Flexible Sensory Platform Based on Oxide-based Neuromorphic Transistors. *Sci. Rep.* **5,** 18082 (2015).
13. Zeng, W. *et al.* Fiber-based wearable electronics: A review of materials, fabrication, devices, and applications. *Adv. Mater.* **26,** 5310–5336 (2014).
14. Schwartz, G. *et al.* Flexible polymer transistors with high pressure sensitivity for application in electronic skin and health monitoring. *Nat. Commun.* **4,** 1859 (2013).
15. Ghanbarzadeh, B. & Almasi, H. *An Introduction to Hydrogels and Some Recent Applications*. *IntechOpen* (2016).
16. Zucca, P., Fernandez-Lafuente, R. & Sanjust, E. Agarose and Its Derivatives as Supports for Enzyme Immobilization. *Molecules* **21,** 1577 (2016).
17. Normand, V., Lootens, D. L., Amici, E., Plucknett, K. P. & Aymard, P. New insight into agarose gel mechanical properties. *Biomacromolecules* **1,** 730–738 (2000).
18. Buenger, D., Topuz, F. & Groll, J. Hydrogels in sensing applications. *Prog. Polym. Sci.* **37,** 1678–1719 (2012).
19. Ahmed, E. M. Hydrogel: Preparation, characterization, and applications: A review. *J. Adv. Res.* **6,** 105–121 (2015).
20. Selvalakshmi, S., Vijaya, N., Selvasekarapandian, S. & Premalatha, M. Biopolymer agar-agar doped with NH4SCN as solid polymer electrolyte for electrochemical cell application. *J. Appl. Polym. Sci.* **134,** 44702 (2017).
21. Lira, R. B., Steinkühler, J., Knorr, R. L., Dimova, R. & Riske, K. A. Posing for a picture: Vesicle immobilization in agarose gel. *Sci. Rep.* **6,** 25254 (2016).
22. Mercey, E. *et al.* The application of 3D micropatterning of agarose substrate for cell culture and in situ comet assays. *Biomaterials* **31,** 3156–3165 (2010).
23. Dumitru, L. M. *et al.* A hydrogel capsule as gate dielectric in flexible organic field-effect transistors. *APL Mater.* **3,** 014904 (2015).
24. Berto, M. *et al.* Label free urea biosensor based on organic electrochemical transistors. *Flex. Print. Electron.* **3,** 024001 (2018).

25. Zang, Y. *et al.* Flexible suspended gate organic thin-film transistors for ultra-sensitive pressure detection. *Nat. Commun.* **6,** 6269 (2015).

26. Kang, S. *et al.* Highly Sensitive Pressure Sensor Based on Bioinspired Porous Structure for Real-Time Tactile Sensing. *Adv. Electron. Mater.* **2,** 1600356 (2016).

27. Choong, C. L. *et al.* Highly stretchable resistive pressure sensors using a conductive elastomeric composite on a micropyramid array. *Adv. Mater.* **26,** 3451–3458 (2014).

28. Pan, L. *et al.* An ultra-sensitive resistive pressure sensor based on hollow-sphere microstructure induced elasticity in conducting polymer film. *Nat. Commun.* **5,** 3002 (2014).

29. Mannsfeld, S. C. B. *et al.* Highly sensitive flexible pressure sensors with microstructured rubber dielectric layers. *Nat. Mater.* **9,** 859–864 (2010).

30. Del Pozo, F. G. *et al.* Single crystal-like performance in solution-coated thin-film organic field-effect transistors. *Adv. Funct. Mater.* **26,** 2379–2386 (2016).

31. Berto, M. *et al.* EGOFET Peptide Aptasensor for Label-Free Detection of Inflammatory Cytokines in Complex Fluids. *Adv. Biosyst.* **2,** 1700072 (2018).

32. Zhang, Q., Leonardi, F., Casalini, S., Temiño, I. & Mas-Torrent, M. High performing solution-coated electrolyte-gated organic field-effect transistors for aqueous media operation. *Sci. Rep.* **6,** 39623 (2016).

33. Lai, S. *et al.* Morphology Influence on the Mechanical Stress Response in Bendable Organic Field-Effect Transistors with Solution-Processed Semiconductors. *Adv. Electron. Mater.* **4,** 1700271 (2017).

34. Manunza, I. & Bonfiglio, A. Pressure sensing using a completely flexible organic transistor. *Biosens. Bioelectron.* **22,** 2775–2779 (2007).

35. Chen, G. *et al.* Plasticizing Silk Protein for On-Skin Stretchable Electrodes. *Adv. Mater.* **30,** 1800129 (2018).

36. Bobbert, P. A., Sharma, A., Mathijssen, S. G. J., Kemerink, M. & De Leeuw, D. M. Operational stability of organic field-effect transistors. *Adv. Mater.* **24,** 1146–11458 (2012).

37. Kim, S. H. *et al.* Effect of water in ambient air on hysteresis in pentacene field-effect transistors containing gate dielectrics coated with polymers with different functional groups. *Org. Electron.* **9,** 673–677 (2008).
38. de Aquino, B. R. H., Ghorbanfekr-Kalashami, H., Neek-Amal, M. & Peeters, F. M. Electrostrictive behavior of confined water subjected to GPa pressure. *Phys. Rev. B* **97,** 144111 (2018).
39. Chopra, G. & Levitt, M. Remarkable patterns of surface water ordering around polarized buckminsterfullerene. *Proc. Natl. Acad. Sci.* **108,** 14455–14460 (2011).
40. He, Y., Sun, G., Koga, K. & Xu, L. Electrostatic field-exposed water in nanotube at constant axial pressure. *Sci. Rep.* **4,** 6596 (2014).
41. Zhang, C., Chen, P. & Hu, W. Organic field-effect transistor-based gas sensors. *Chem. Soc. Rev.* **44,** 2087–2107 (2015).

Chapter 5. Experimental Methods and Materials

5.1 Materials

- **Organic semiconductors and polymer semiconductors**

2,8-difluoro-5,11-bis(triethylsilylethynyl)anthradithiophene (diF-TES-ADT, purity > 99%**)** was purchased from *Lumtec*. and used as received.

6,13-Bis(triisopropylsilylethynyl)pentacene (TIPS-pentacene) was purchased from *Ossila* and used without further purification.

Dibenzo-tetrathiafulvalene (DB-TTF) was purchased from Sigma-Aldrich and used without further purification.

Meso-tetrathia[22]annulene[2,1,2,1] (DPTTA) was synthesized by Dr. M. R. Ajayakumar in the ICMAB as described in reference[1].

Poly[2,5-bis(7-decylnonadecyl)pyrrolo[3,4-c]pyrrole-1,4(2H,5H)-dione-2,2'-bithieno[3,2-b]thiophene]-co-[2,5-bis(7-decylnonadecyl)pyrrolo[3,4-c]pyrrole-1,4(2H,5H)-dione-(E)-(1,2-bis(5-(thiophen-2-yl)selenophen-2-yl)ethene)] (P-DPP-TT(1)-SVS(9)) was supplied by Prof. Yun-Hi Kim from the National University Jinju of Korea and synthesized according to their paper[2].

- **Polymers**

Polystyrene (M_w~3,000 g mol^{-1}, M_w~10,000 g mol^{-1} and M_w~100,000 g mol^{-1}) was purchased from Sigma-Aldrich and used without any further purification.

Polydimethilsiloxane (PDMS) (Sylgard® 184) was purchased from Dow Corning Corporation and prepared according to the standard protocol.[viii]

[viii] For more information about the protocol, please check the web-page: www.dowcorning.com

- **Solvents**

Chlorobenzene (CB) was purchased from Sigma-Aldrich and used as received.

1,2,3,4-Tetrahydronaphthalene (Tetralin) was purchased from Sigma-Aldrich and used as received.

Acetone (HPLC grade) was purchased from Chem-Lab NV and used for the “lift-off” step and for the cleaning of the substrates.

Propanol-2(iso-Propanol) (isopropanol, HPLC grade) was purchased from Chem-Lab NV and used for the “lift-off” step and for the cleaning of the substrates.

- **Self-Assembled Monolayers (SAMs)**

2,3,4,5,6-Pentafluorothiophenol (PFBT) was purchased from Sigma-Aldrich and used as received.

- **Metal Chloride salts**

All the **metal chloride salts**, including NaCl, $ZnCl_2$, $HgCl_2$, $MgCl_2$, $MnCl_2$, $CaCl_2$, $FeCl_2$, $CuCl_2$ and $FeCl_3$ were purchased from Sigma-Aldrich and used without any further purification. Due to the poor solubility of $PbCl_2$ in water, the corresponding nitrate salt ($Pb(NO_3)_2$) also from Sigma-Aldrich was used.

- **Hydrogel Material**

Agarose powder (Type I-B, low EEO) was obtained from Sigma-Aldrich.

- **Substrates and Top Gate Electrode**

Kapton$^{®}$ polyimide film (300 HN, 75 µm thick) was received from DuPont^{TM}.

Highly *n*-doped silicon wafers were purchased from SiMat with the following characteristics: Diameter: 100 mm; Type/Dopant: N/Sb; Orientation: <1-0-0>;

Resistivity: <0.05-0.02> Ω·cm; Thickness: 525±25 µm; Front Surface: Polished; Back Surface: Etched; Flats: SEMI Standard.

Platinum (Pt) wire (ø = 0.5 mm) was purchased from Sigma-Aldrich.

- **Other Materials**

Silver conductive paint (RS 186-3593) was purchased from RS Components Pty Ltd.

Gold (Au) and **Chromium (Cr)** for metal evaporation were 99.99% pure and were purchased from Kurt J. Lesker.

MilliQ water (resistivity: 18.2 MΩ•cm at 25°C) was obtained from Milli-Q® Integral Water Purification System.

Shipley Microposit S1813 photoresist were purchased from Shipley.

Shipley Microposit MF-319 Developer for use with S1800 series photoresists was purchased from Shipley.

5.2 Instrumentation

- **Optical microscopy.** Polarized optical microscopy images were recorded with the Olympus BX51 (Japan), by means of cross polarized filters which enable to study the crystalline nature of organic thin films.

- **Atomic force microscopy (AFM) and Kelvin probe force microscopy (KPFM).** The AFM and KPFM images were obtained by using a 5500LS SPM system from Agilent Technologies. The AFM images were performed in tapping mode, while the measurements from KPFM, which is a noncontact variant of AFM, were performed in amplitude mode by applying an AC voltage plus a DC voltage to the sample. All images were recorded in ambient conditions and analysed by Gwyddion 2.47 software.

- **X-Ray diffraction (XRD).** X-ray diffraction measurements were performed by a diffractometer equipped with a rotating anode source with a PANalytical X'Pert PRO diffractometer MRD for the test.

- **Scanning electron microscopy (SEM).** SEM images of agarose thin films were carried out under 100% humidity with a SEM FEI QUANTA 200 FEG-ESEM from Oxford Instruments, England.

- **Electrochemical impedance spectroscopy (EIS).** The EIS spectra were recorded with a Novocontrol Alpha-An impedance analyzer equipped with POT/GAL 30V/2A electrochemical interface in a frequency range of 10^5 – 10^{-1} Hz. The DC voltage spanned from 0.7 V to -0.3 V with a step of -0.1 V and was superimposed to an AC signal of 10 mV. For the EIS measurements, the *S*/*D* electrodes were short circuited and kept ground to serve as counter electrode, while Pt wire was immersed into the liquid electrolyte to act as working electrode.

- **Metal evaporators.** All metal coatings were deposited by an auto system 306 from Boc Edwards located in the clean room (10,000 class).

- **Laser micro-writer.** The photolithographic patterning of all the electrodes were performed by a MicroWriter MLTM from Durham Magneto Optics LTD located in the clean room (10,000 class).

- **Spin coater.** Spin coating of the photoresist (Shipley 1813) was carried out by means of a Laurell Technologies (WS-650SZ-6NPP/LITE) spin coater located in a 10,000 class clean room.

- **Bar coater.** All the BAMS deposition was performed with a custom-made automatic coater or with a RK101 applicator from RK, as shown in **Figure 5.1**. All the depositions were carried out in ambient conditions in a chemical hood.

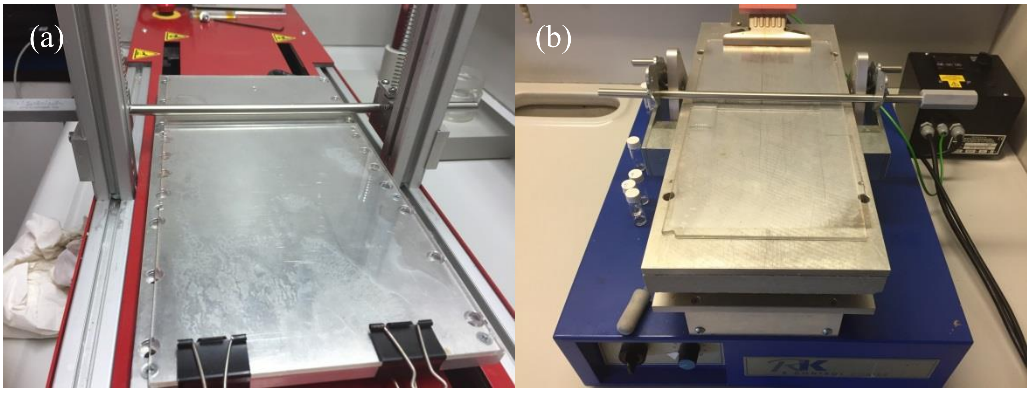

Figure 5.1: Photo of (a) the custom-made bar-coater and (b) the RK coater.

- **Semiconductor parameter analyser.** An Agilent B1500A semiconductor device analyzer (including the Easy expert software) was employed to record all the OFET and EGOFET results, the displacement current, and potentiometric sensitivity measurement unless otherwise specified (see experiments performed inside the glove box in chapter 4). The measurements were carried out in air with a Kärl SÜSS probe station, as displayed in **Figure 5.2**. Only some of the experiments from Chapter 4 were performed inside the glove box. Here, a Keithley 2612A Source Meter was used to perform the OFET characterization inside a glovebox to prevent the re-adsorption of water inside the thin film. A Keithley 2604B was employed to test the switching speed of EGOFETs, which was controlled by a software provided by the company (Chapter 2).

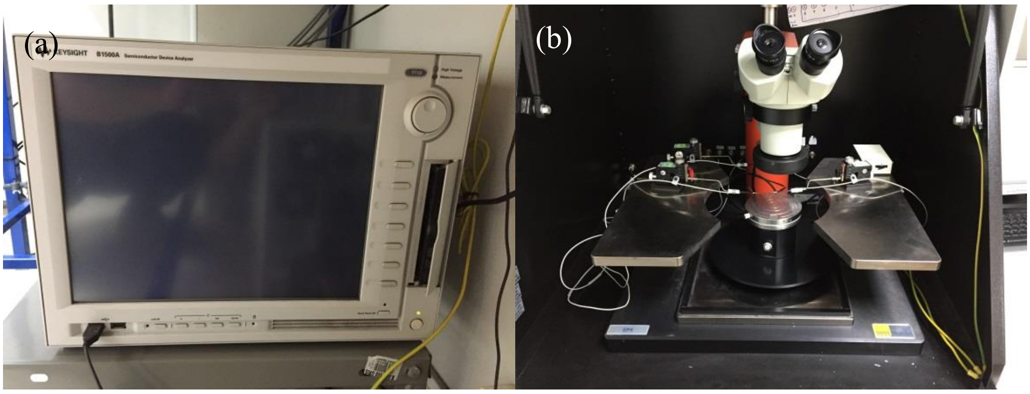

Figure 5.2: Images of (a) the Agilent B1500A semiconductor device analyzer and (b) the probe station.

5.3 Sample Fabrication

5.3.1 Photolithography

The source and drain gold electrodes for all samples were fabricated by photolithography on Si/SiO_2 wafer and Kapton® polyimide films. The fabrication process was carried out by using a Micro-writer from Durham Magneto Optics Ltd. The chromium and gold metal layers (Cr/Au) were deposited by thermal evaporation system (Evaporation System Auto 306 from Boc Edwards) under 2×10^{-4} Pa conditions. The process was performed as following:

1. The Si/SiO_2 wafers (Ø = 10 cm) or Kapton substrates (7×7 cm^2) were firstly cleaned with acetone and isopropanol and then dried with nitrogen gas. The Kapton substrate was then subsequently placed on top of a supporting substrate and flattered on a glycerol layer. Finally, the photoresist (Shipley Microposit S1813) was deposited on top of the sample by spin coating at 5000 rpm for 25 s.

2. The photoresist-coated Si/SiO_2 wafers (or Kapton substrates) were then transferred to a hotplate and kept at 70 °C for 1 minute.

3. The baked Si/SiO_2 wafers (or Kapton substrates) were subsequently mounted inside the Micro-writer system operating in Turbo mode (laser spot: 1 µm, laser wavelength: 405 nm, resolution: 5µm, writing speed: 375 mm^2/minute). The pattern used for photolithography was designed through the circuit design software CleWin4. The *S*/*D* fingers were previously designed according to the following geometrical parameters: channel width (W) = 20700 µm and channel length (L) = 30 µm, namely having a geometrical ratio W/L = 690. An illustration of the designed pattern is shown in **Figure 5.3**.

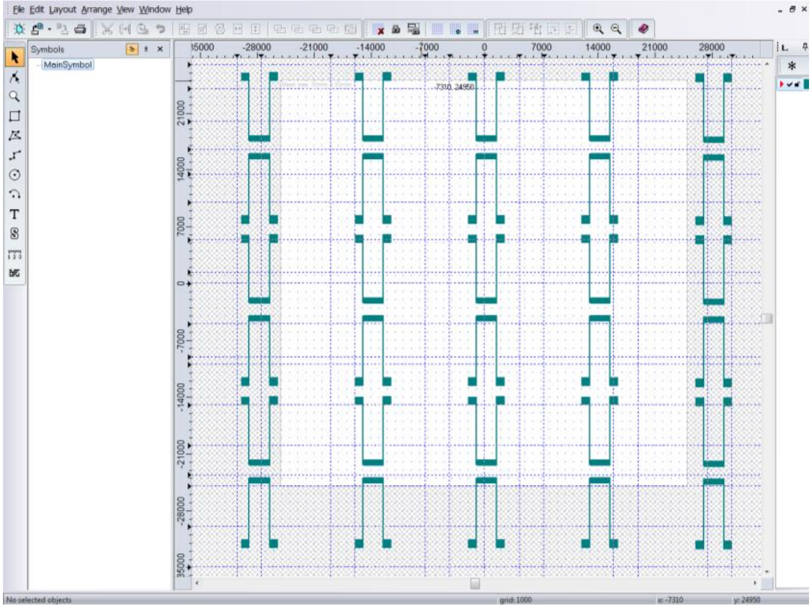

Figure 5.3: An example of the pattern designed by CleWin 4 software for a Kapton substrate.

4. The laser exposed portion of the photoresist was solubilized by the photoresist developer since the Shipley S1813 is a positive photoresist, whose solubility changes by the photo-generated acid. In contrast, the unexposed portion of the photoresist remained insoluble to the photoresist developer. After the laser-writing process, the Si/SiO_2 wafers (or Kapton substrates) were immersed into the developer solution (Shipley Microposit MF-319) for 1 minute to reveal the pattern. The substrates were then carefully cleaned by MilliQ water in order to remove any remaining developer traces from the surface and dried with a nitrogen gun.

5. The samples were subsequently fixed onto a sample holder inside the metal evaporator chamber. A metallic layer of Cr (5 nm) was firstly evaporated to serve as adhesive for the Au layer (40 nm).

6. The last step of the process consisted in the removal of the metal excess through the so called lift off process which uses acetone as solvent for solubilizing the remained photoresist leaving unaltered the metallic features that adhere directly on the substrate. Several cycles of acetone and isopropanol cleaning in an ultrasonic bath completed the cleaning of the sample surface.

5.3.2 Organic Semiconductor Ink Preparation and Deposition

- **Semiconductor ink.**

All the OSC:PS inks or pristine OSC inks used in this thesis were prepared according to a common protocol. In general, the OSC and polystyrene were mixed firstly in a fixed weight ratio and then dissolved in an organic solvent (CB or Tetralin) reaching the final concentration. The optimized OSC:PS ratios and the final concentrations of each ink are listed in **Table 5.1**. The OSC:PS inks and pristine OSC inks were then kept on a hotplate for 1 hour to ensure the complete dissolution of the components. Amber vials were always used in order to protect the organic semiconductor solution from light.

Table 5.1: Formulations of the main OSC:PS inks or pristine OSC inks and their corresponding coating parameters used in this thesis.

OSC:PS blend materials	OSC:PS ratio	Concentration (wt %)	Solvent	Coating Temperature (°C)	Coating speed (cm/s)
diF-TES-ADT:PS_{10K}	4:1	2	CB	105	1
diF-TES-ADT	/	3	CB	105	1
TIPS-Pentacene:PS_{10K}	4:1	2	CB	105	1
TIPS-Pentacene	/	3	CB	105	1
DB-TTF:PS_{3K}	1:2	4	CB	105	1
DPTTA:PS_{3K}	1:3	2	CB	105	1
DPTTA:PS_{10K}	1:3	2	CB	105	1
DPTTA:PS_{10K}	1:2	2	CB	105	1
DPTTA:PS_{100K}	1:2	2	CB	105	1
PDPP-TT(1)-SVS(9):PS_{3K}	1:2	1	Tetralin	150	1
PDPP-TT(1)-SVS(9):PS_{100K}	1:2	1	Tetralin	150	1

- **OSC deposition.**

Prior to the deposition of the OSC:PS blend solution, the substrates were cleaned in ultrasonic bath with acetone and isopropanol for 15 min each and afterwards ozone-treated for 25 min. The *S*/*D* electrodes were subsequently functionalized by immersing the substrates into a PFBT:isopropanol (2 µL : 1 mL) solution for 15 minutes. After PFBT-functionalization, the excess of PFBT molecules was removed by a further sonication step in fresh isopropanol for 5 minutes. For comparison, the devices without PFBT-functionalization were also immersed in isopropanol for 15 minutes.

All the OSC thin films reported in this thesis were prepared by the bar-assisted meniscus shearing (BAMS) technique.[3,4] As shown in **Figure 5.4**, the cleaned *S*/*D* substrates were placed between the supporting plate and the metal bar. The gap between the metal bar and the substrate was set approximately at 100 µm. Typically, a droplet (30 µL) of the OSC:PS blend solution (or pristine OSC solution) was injected at the gap by using a micropipette to form a liquid meniscus. Then, the bar horizontally moved on top of the substrate to achieve a uniform and homogeneous thin film.[3,4] In the case of DPTTA blend, the metal bar was replaced by a polytetrafluoroethylene (PTFE) bar to achieve a homogeneous polycrystalline film due to the different surface energy of the shearing component. The coating temperature was selected to be just below the boiling point temperature of the organic solvent. The details of the deposition parameters for each solution are listed in **Table 5.1**. It should be highlighted that all the OSC:PS blend solutions (or OSC solutions) must be dissolved very well to avoid the formation of holes or bubbles in the film caused by particles in suspension. Once achieved the thin film, the substrates were immediately removed from the hotplate to cool down.

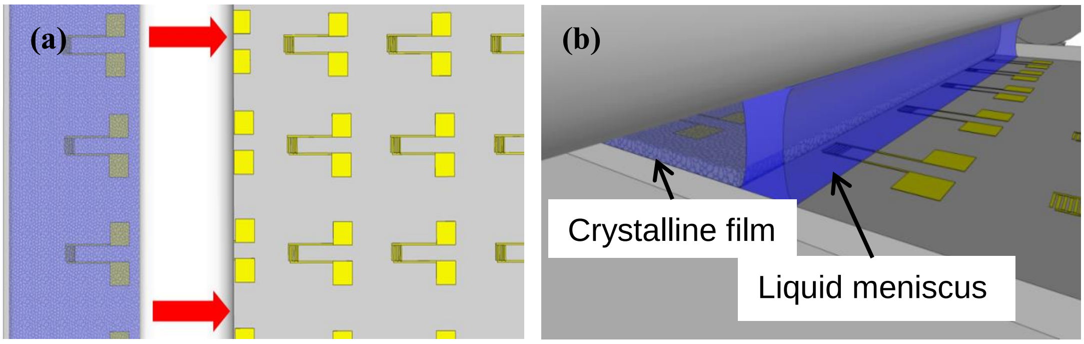

Figure 5.4: The schematic diagram of the BAMS technique. (a) Top view of bar shearing, (b) lateral zooming of the formed meniscus.

5.3.3 Hydrogel Gated Organic Field-Effect Transistor (HYGOFET) Device Assembly

- **Agarose solution:** The agarose solution was prepared following a similar methodology mentioned above. The agarose solutions used in chapter 4 were prepared at various concentrations (*i.e.* 0.75 wt%, 1.5 wt% and 3 wt%) by dissolving the agarose powder into MilliQ water (resistivity: 18.2 MΩ·cm at 25 °C) under continuous stirring (800 rpm) at 150 °C for 5-10 minutes. Once the agarose solution became transparent, it was immediately used for the film preparation.

- **Agarose gel deposition.** In the case of the agarose gel deposition, BAMS technique has been employed at a coating speed of 5 cm/s and keeping the plate temperature at 30 °C since the gelling temperature of normal agarose is around 35 °C.[5] Before gel deposition, the tip of the micropipette should be kept in the hot agarose solution (150 °C) for 30 s to avoid the solution gelling inside the plastic pipette. The resulting agarose film was subsequently cut into squares (0.6×0.6 cm^2) and immediately used for device measurements.

- **Device assembly.** Regarding HYGOFET fabrication (chapter 4), two kinds of Kapton substrates were employed. The first Kapton support (1.5×2 cm^2) bearing *S*/*D* electrodes (*W*/*L* = 690) was employed as substrate for the subsequent deposition of diF-TES-ADT:PS blend film. The second Kapton foil (3.5×3.5 cm^2) was patterned with a gold electrode strip (*W* = 0.25 cm, *L*=3 cm) which served as top gate electrode, and was also used as support for the agarose film deposition. The two Kapton substrates were then assembled together as depicted in **Figure 5.5**. Here, the OSC-coated substrate was laminated on top of the agarose-coated substrate and silver conductive paint was used to connect the *S/D* electrodes to external connections. The prepared HYGOFET was sandwiched in between two pieces of thin PDMS layers (～ 1 mm) to ensure the sealing of the device and to avoid the drying of the agarose gel. A hole in the center of the PDMS film allowed to maintain a fixed area (*A* = 0.36 cm^2) during the pressure stimulation of the device and the subsequent electrical tests.

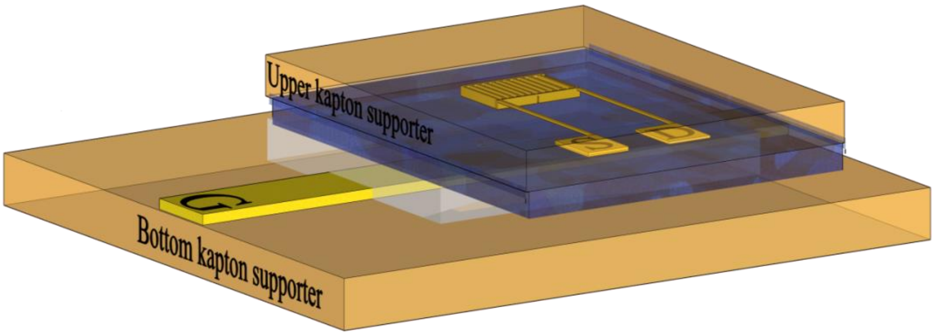

Figure 5.5: Schematic diagram of the assembled HYGOFET.

5.4 Electrical Characterization

The OFET measurements were performed using *n*-doped Si/SiO$_2$ stack as gate electrode and dielectric, respectively. Regarding the EGOFET measurements, a Pt wire acted as top gate electrode and the liquid electrolyte was confined on the interdigitated region by means of a PDMS pool (total volume was equal to 20 µL). The Pt wire was cleaned with sulphuric acid (0.1 M) and MilliQ water prior to be used.

- **Transfer and output characteristics.** All the transfer and output characteristics in OFET and EGOFET devices were recorded in ambient conditions using an Agilent 5100A equipped with the Easy Expert software connected to the samples through a Kärl SÜSS probe station. In this thesis, the scan rate of the transfer characteristics was around ~ 2.5 V/s in OFETs and ~ 70 mV/s in EGOFETs unless otherwise specified.

- ***In-suit I-t* monitoring.** For the current monitoring in the EGOFETs, V_{GS} and V_{DS} were fixed in the saturation regime (*i.e.* V_{GS} = -400 mV and V_{DS} = -400 mV) and I_{DS} was continuously recorded keeping a holding time of 1 s. In this case, a big PDMS pool (200 µL) sealed with parafilm was employed in order to minimize the solvent evaporation throughout the electrical test.

- **Bias stress measurements.** For the bias stress measurements in the EGOFETs, the recording of the transfer characteristics was alternated with a stressing cycle (V_{GS} = -400 mV, V_{DS} = -400 mV, t = 1 minute).

- **Shelf-stability measurements.** The shelf-stability characterization of the EGOFETs consisted of measuring, drying and storing the device every day. *I-V* transfer characteristics were recorded once per day up to one week.

- **Displacement current measurements (DCM).** The DCM tests of the EGOFETs were performed with the same equipment used for the standard electrical characterization. The source and drain electrodes were short-circuited and grounded. The gate current was recorded at different scan rates (v) with the same triangular potential ramp (as used for *I-V* transfer characteristics) and the resulting measurements were scaled according to a transistor area of 0.0208 cm^2.

- **Potentiometric sensitivity measurements.** The EGOFET potentiometric sensitivity tests were carried out with the same equipment used for the transfer and output characterization. For the potentiometric sensitivity measurements, a square pulse (ΔV_{GS}) of different amplitudes (from 50 mV to 100 μV) was applied with respect to a base V_{GS} equal to – 400 mV with an integration time of 20 ms.

- **Switching speed measurements.** The EGOFETs switching speed measurements were recorded by using a Keithley 2604B SMU controlled with a software provided by the company. In this case, the I_{DS} current was recorded by sweeping V_{GS} from 0 V to – 500 mV (with an integration time of ~ 270 μs) and vice versa with a fixed V_{DS} = -400 mV.

5.5 Metal-ion Solutions Preparation and Hg^{2+}-mediated Surface Doping Protocol

All the solutions containing metallic ions (1 mM) were prepared by dissolving the corresponding metal chloride salts in MilliQ water. Due to the poor solubility of $PbCl_2$ in water, the corresponding nitrate salt ($Pb(NO_3)_2$) was chosen in order to test Pb^{2+} as interfering agent. The electrical response of the OSC:polymer thin-film towards Hg^{2+}-ions, was monitored by exposing the devices to five different $HgCl_2$ solutions (1 nM, 50 nM, 1 μM, 50 μM, and 1 mM) in ascending order. A drop of $HgCl_2$ solution (30 μL) was placed on top of the active transistor area and kept for 3 min. Afterwards the samples were carefully rinsed three times with MilliQ water and dried under nitrogen gas. This procedure was repeated for all the solutions of the other metal cations. All the solutions were freshly prepared before each experiment, which was always carried out under ambient conditions.

5.6 Pressure Stimulation Tests

The electrical response of the HYGOFET device due to pressure stimulation was recorded by using different calibrated weights (reported in Chapter 4). In this case, transfer characteristics were recorded by gently placing increasing weights on the top of the device, as shown in **Figure 5.6**; the applied pressure was calculated according to the following relation: $P = \frac{m \times g}{A}$, where m is the mass of the calibrated weight, g is the gravity acceleration, and A is the area of the calibrated weight.

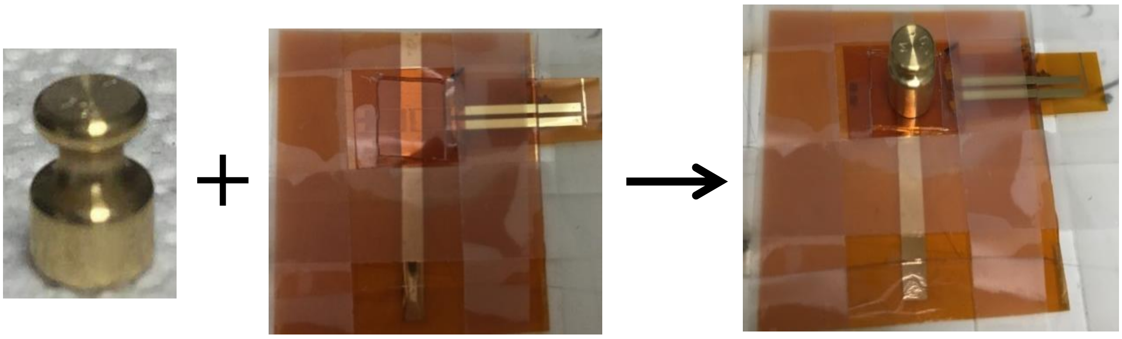

Figure 5.6: Pictures illustrating the pressure stimulation approach using calibrated weights.

5.7 Extraction of Device Parameters

Although a full and precise model to describe the properties of EGOFETs is still lacking, the classical MOSFET model has been employed to describe and understand the properties of this kind of device. The same model is used to characterize the OFETs. According to the MOSFET model, the I_{DS} in linear and saturation regime are approximately determined by the following equations:[6,7]

$$I_{DS} = \frac{W}{L} c_i \mu (V_{GS} - V_{th}) V_{DS} \qquad \text{(Linear)} \qquad (5.1)$$

$$I_{DS} = \frac{W}{2L} c_i \mu \, (V_{GS} - V_{th})^2 \qquad \text{(Saturation)} \qquad (5.2)$$

where W is the channel width, L is the channel length, c_i is the insulator capacitance per unit area, V_{th} is the threshold voltage and μ is the field-effect mobility. In the EGOFET and HYGOFET configuration, c_i represents the capacitance of the electrical double layer formed at the electrolyte/Pt interface and OSC/electrolyte interface, therefore, c_i can be replaced by c_{dl}.

- **Capacitance of electrical double layer (C_{dl}).** C_{dl} is frequency and gate voltage dependent thus it was extracted from DCM and EIS measurements.[8] In these two tests, the effective area was fixed to 0.0208 cm^2 according to the transistor interdigitated area.

For the DCM measurement (**Figure 5.7**), the I_G-V_G graphs were recorded at different scan rates (v) and, according to the method proposed by Frisbie et al.,[8] the C_{dl} was extracted through the following steps:

(1) Determination of the peak current (i_p) at each scan rate.

(2) Plot of the i_p - v curve and extraction of the slope.

(3) Normalization according to the effective transistor area.

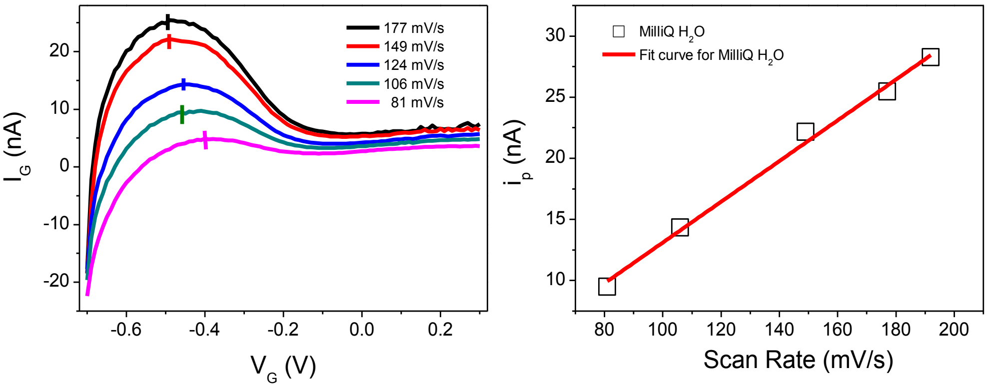

Figure 5.7: The typical DCM results recorded in the EGOFET device with MilliQ water as media.

Regarding to the EIS method, the C_{dl} – frequency (*f*) graphs were recorded at different DC voltages according to the operational window of the transistor; they was estimated at a frequency of 10 Hz. For calculating the mobility, the C_{dl} was extracted at a DC voltage corresponding to the ON state of the device.

- **Mobility (μ).** The mobility was extracted from the transfer curve using the slope of the linear fit of I_{DS} versus V_{GS} in linear regime and from the slope of $\sqrt{|I_{DS}|}$ versus V_{GS} in saturation regime, as described by the following equations:[6,7]

$$\mu_{lin} = \frac{L}{WC_iV_{DS}}\frac{\partial I_{DS,lin}}{\partial V_{GS}} \qquad (\text{if } |V_{GS} - V_{th}| \gg |V_{DS}|) \qquad (5.3)$$

$$\mu_{sat} = \frac{2L}{WC_i}\left(\frac{\partial\sqrt{I_{DS,sat}}}{\partial V_{GS}}\right)^2 \qquad (\text{if } |V_{GS} - V_{th}| < |V_{DS}|) \qquad (5.4)$$

- **Threshold voltage (V_{th}).** The threshold voltage was extracted from the linear fit of the mobility, by intercepting the x-axis with a straight line as described by the following formula:

$$V_{th} = -\frac{slope}{intercept} \qquad (5.5)$$

where *slope* is the slope of the linear fit of I_{DS} versus V_{GS} at linear regime and of $\sqrt{|I_{DS}|}$ versus V_{GS} at saturation regime, *intercept* is the y-intercept of the same linear fit.

- **Subthreshold swing (*SS*).** The subthreshold swing was extracted from the following formula:

$$\mathrm{SS} = \frac{d(V_{GS})}{d(logI_{DS})} \qquad (5.6)$$

- ***On*/*off* ratio (I_{on}/I_{off}).** The *on*/*off* ratio was simply extracted from the transfer curve by considering the saturation of the I_{DS} curve as ON current (I_{on}) and averaging the current relative to the off state of the device (I_{off}).

- **Transconductance (g_m).** In the HYGOFET device, the transconductance, g_m, was calculated according to the following formula at different V_{DS}:[6]

$$g_{m,lin} = \frac{\partial I_{DS}}{\partial V_{GS}} \qquad (5.7)$$

$$g_{m,sat} = \frac{\partial \sqrt{I_{DS}}}{\partial V_{GS}} \qquad (5.8)$$

- **Charge carriers concentration (*n*).** The charge carriers concentration in the EGOFET induced by the gate voltage in linear regime (in chapter 3) was extracted according to the following formula:[9]

$$n = -\frac{C_{dl}(V_{GS} - V_{th})}{e} \qquad (5.9)$$

where c_{dl} is the capacitance of the electrical double layer, V_{GS} is the gate-source voltage, V_{th} is the threshold voltage, and e is the elementary charge.

- **Switching speed (τ).** The switching speed, was extracted by fitting the two branches (τ_{on} and τ_{off}) of the square pulse according to the following formula:

$$\Delta I_{DS} = e^{\pm(t/\tau)} \qquad (5.10)$$

- **Potentiometric sensitivity.** The potentiometric sensitivity was performed by applying different V_{GS} pulses during I_{DS} recording (**Figure 5.8 (a)**). The square response was corrected through baseline subtraction as shown in **Figure 5.8 (b)** and **(c)** the minimum V_{GS} change (ΔV_{GS}) having a signal/noise ratio >5 was defined as the potentiometric sensitivity of the device.

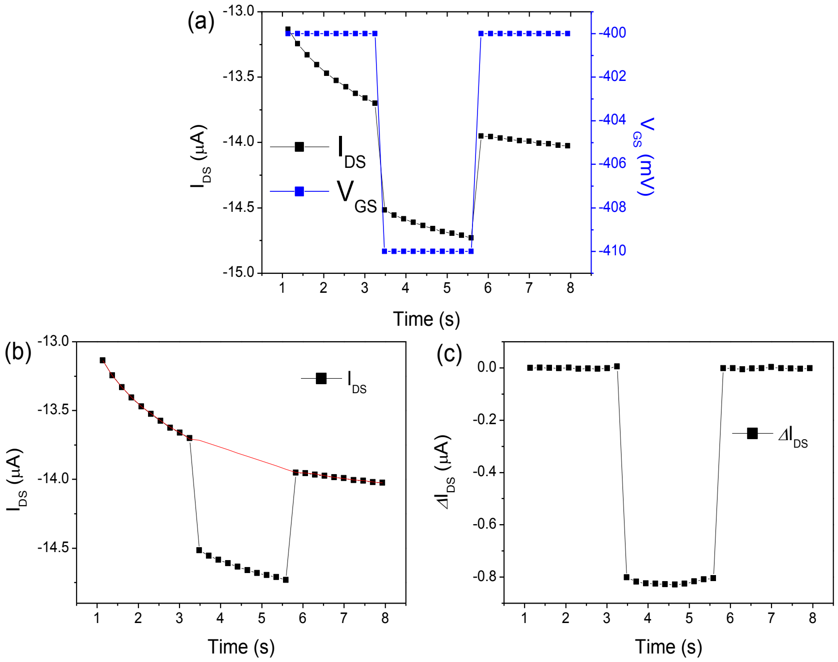

Figure 5.8: (a) The typical potentiometric sensitivity results recorded from the SMU and (b,c) the corresponding extraction process of the potentiometric sensitivity.

Bibliography

1. Singh, K., Sharma, A., Zhang, J., Xu, W. & Zhu, D. New sulfur bridged neutral annulenes. Structure, physical properties and applications in organic field-effect transistors. *Chem. Commun.* **47,** 905–907 (2011).
2. Yun, H.-J., Lee, G. B., Chung, D. S., Kim, Y.-H. & Kwon, S.-K. Novel Diketopyrroloppyrrole Random Copolymers: High Charge-Carrier Mobility From Environmentally Benign Processing. *Adv. Mater.* **26,** 6612–6616 (2014).
3. Del Pozo, F. G. *et al.* Single crystal-like performance in solution-coated thin-film organic field-effect transistors. *Adv. Funct. Mater.* **26,** 2379–2386 (2015).
4. Temiño, I. *et al.* A Rapid, Low-Cost, and Scalable Technique for Printing State-of-the-Art Organic Field-Effect Transistors. *Adv. Mater. Technol.* **1,** 1600090 (2016).
5. Normand, V., Lootens, D. L., Amici, E., Plucknett, K. P. & Aymard, P. New insight into agarose gel mechanical properties. *Biomacromolecules* **1,** 730–738 (2000).
6. Horowitz, B. G. Organic Field-Effect Transistors. *Adv. Mater.* 365–377 (1998).
7. Phan, H. *et al.* Electrical Double-Slope Nonideality in Organic Field-Effect Transistors. *Adv. Funct. Mater.* **28,** 1707221 (2018).
8. Panzer, M. J. & Frisbie, C. D. Polymer electrolyte-gated organic field-effect transistors: Low-voltage, high-current switches for organic electronics and testbeds for probing electrical transport at high charge carrier density. *J. Am. Chem. Soc.* **129,** 6599–6607 (2007).
9. Xiang, D. *et al.* Surface transfer doping induced effective modulation on ambipolar characteristics of few-layer black phosphorus. *Nat. Commun.* **6,** 6485 (2015).

Chapter 6. Conclusions

In this thesis, we have studied several aspects related to electrolyte-gated organic field-effect transistors (EGOFETs), including the fabrication, characterization and further applications. First of all, we have focused on obtaining a robust EGOFET device by systematically evaluating and comparing the electrical performance of four OSC:PS blends based devices. Then, a special attention has been paid to employ the EGOFET as a platform for detecting the Hg^{2+} ions in solution. Furthermore, by replacing the liquid electrolyte with a water-based hydrogel to serve as dielectric layer, we have presented a novel HYGOFET device with a high electrical performance, which further exhibits an excellent response to pressure stimuli due to the water dipoles alignment within the OSC layer. The key observations and results reported in this thesis are summarized as follows:

1) The combination of OSC: insulator polymer blend as the active material along with BAMS technique has been demonstrated as a powerful strategy to obtain high quality thin films and, in turn, excellent EGOFETs device with robustness performance. In this case, two pivotal parameters, the presence of PS in the precursor solution and the *S/D* coating with a SAM of PFBT, have revealed to be fundamental for guaranteeing well-defined and densely connected crystals in the film, which are crucial for obtaining high electrical performance and high stability of the EGOFET platform.
2) Aiming to obtain the best EGOFET platform, four OSC:PS blends based EGOFET devices have been systematically studied by evaluating and comparing their transfer and output characteristics, potentiometric sensitivity, switching speed and their electrical stability properties by using MilliQ water and a NaCl solution as electrolyte media. The EGOFET based on diF:PS_{10K}(4:1)/PFBT thin film was found to be the most performing device among the four OSC:PS blends due to their superior electrical performance (*i.e.* $\mu > 0.1$ $cm^2V^{-1}s^{-1}$, I_{on}/I_{off} ratio ~10^3, switch on

time < 1 ms) accompanied with a high operation stability.

3) The diF:PS_{10K}(4:1)/PFBT based EGOFETs have been demonstrated to constitute a simple and efficient transduction platform to detect Hg^{2+} ions in solution. In this case, by exposing the OSC blend thin film to aqueous Hg^{2+} ions solutions with different concentrations in ascending order, a gradual positive V_{th} shift of the EGOFET is observed with a linear response in a concentration range spanning from nanomolar to millimolar. This behavior is attributed to the *p*-type surface doping on the top accumulating channel of the EGOFET caused by the redox reaction between Hg^{2+} ion and the semiconductor surface. Furthermore, this peculiar interaction seems to be limited to this cation in a concentration range up to 1 mM since no effects have been observed in the presence of other divalent cations.
4) By replacing the liquid media with water-based gel (*i.e.* hydrogel) to serve as dielectric layer, a solid state EGOFET namely hydrogel-gated organic field-effect transistor (HYGOFET) has been fabricated with high electrical performance and long-term stability. During the device fabrication, the two components, including the OSC:PS blend film and the hydrogel film, have been successfully deposited by BAMS, which revealed again that BAMS is a powerful and low-cost deposition technique.
5) As a proof-of-concept, the flexible HYGOFETs exhibit a high reproducibility and sensitivity towards pressure stimuli in the low-pressure regime (several hundred Pa to 9 kPa) operating below 0.5 V. Its transduction mechanism is attributed to the water dipoles alignment in the OSC layer towards pressure application, which differs from the well-known principles based on piezoresistivity, capacitance and piezoelectricity.

Appendix A. Optimization process

A.1 Optimization Process of TIPS-pentacene based-EGOFETs

During the optimization process, EGOFETs and OFETs devices have been characterized through optical microscopy, atomic force microscopy and their electrical perfomances have been recorded. In order to select the better EGOFET the following parameters have been modified: (1) the PFBT functionalization of the *S*/*D* electrodes, (2) the PS, (3) the OSC:PS ratio, (4) the molecular weight of PS and (5) the coating speed.

A.1.1 The Influence of PFBT-functionalization

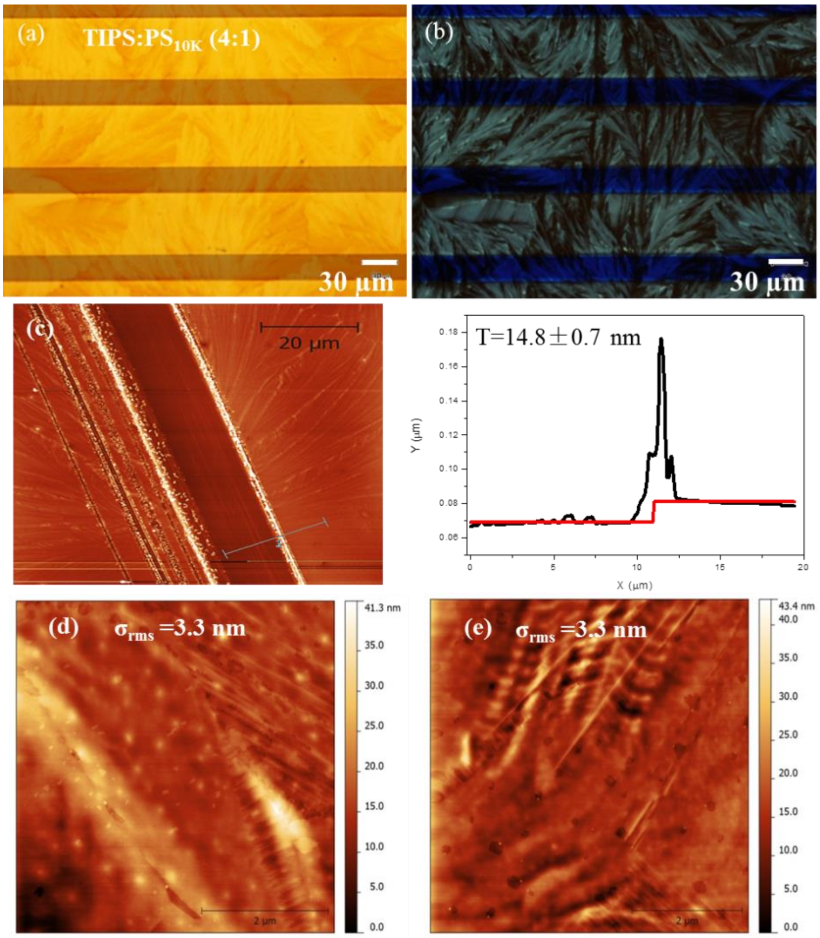

Figure A. 1: Polarized microscope images of TIPS:PS$_{10K}$(4:1)-based thin film at (a) polarizer/analyzer = 0° and (b) polarizer/analyzer = 90°. All thin films were coated by BAMS at 1 cm/s and 105 °C. (c) AFM profile and its corresponding 2D fitting of the same film. The AFM images (5×5 µm^2) of the same film were acquired on (d) the channel and (e) the electrodes region.

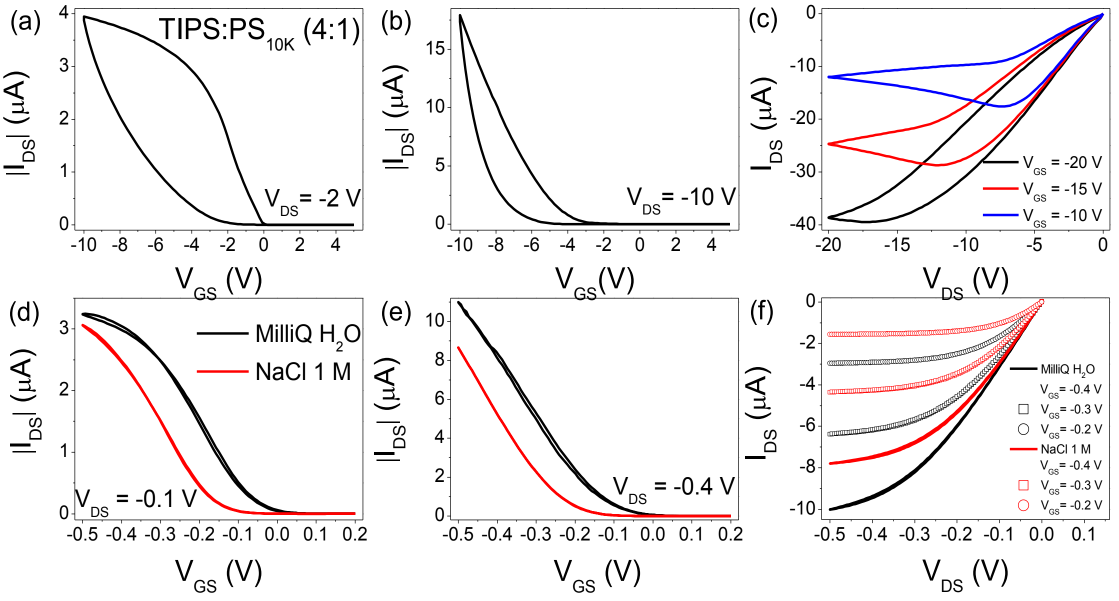

Figure A. 2: Typical *I/V* transfer recorded in linear and saturation regime and the corresponding output characteristic of the TIPS:PS$_{10K}$(4:1)-based OFETs (a, b, c) and EGOFETs (d, e, f). The coating speed and temperature are 1 cm/s and 105 °C.

A.1.2 The Influence of PS

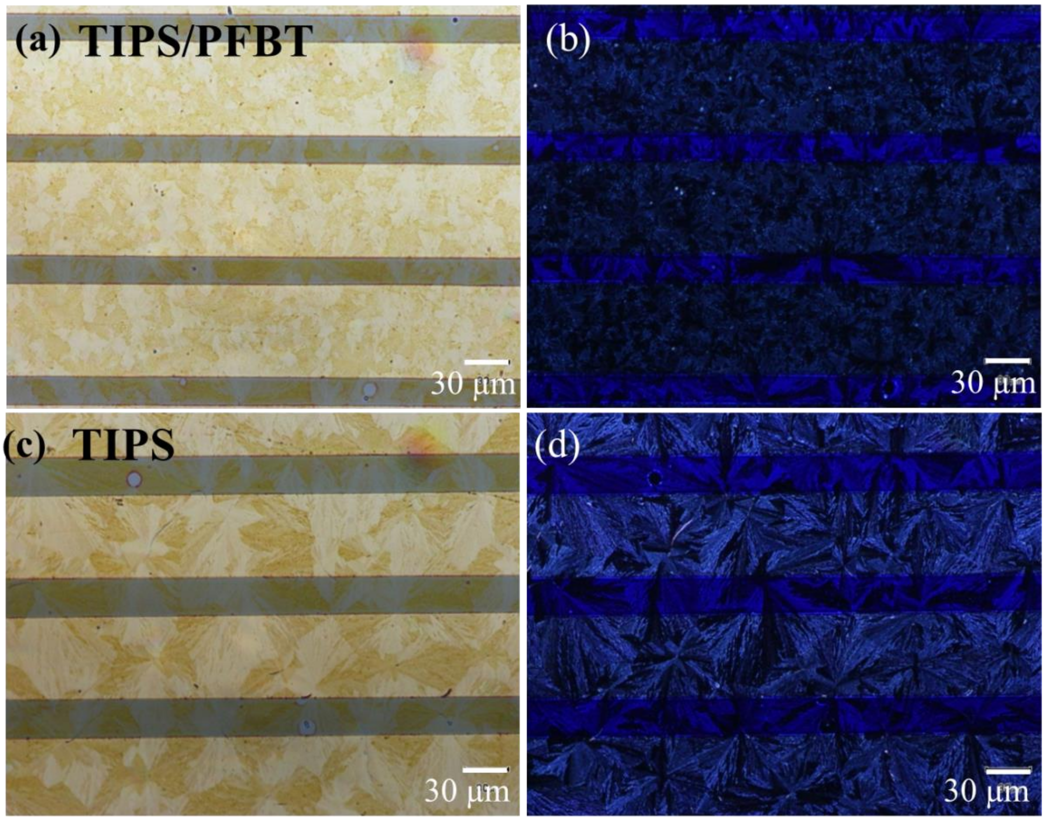

Figure A. 3: Polarized microscope images for PS-free device (a,b) with and (c,d) without PFBT-functionalization. On the left, polarizer/analyzer = 0°. On the right, polarizer/analyzer = 90°. All these thin films were coated by BAMS at 1 cm/s and 105 °C.

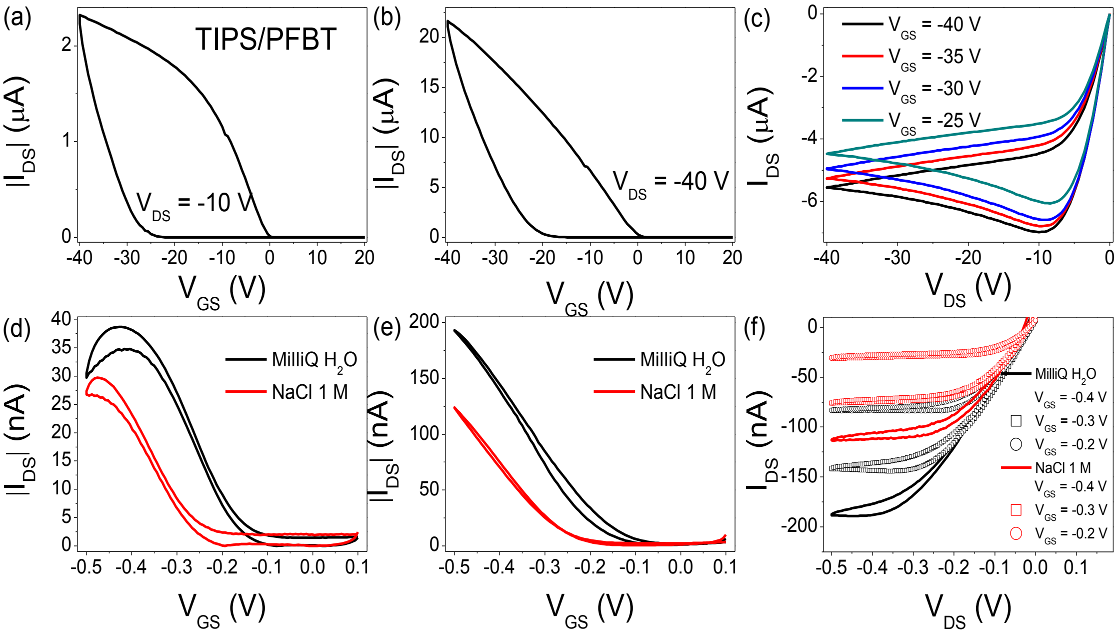

Figure A. 4: Typical *I/V* transfer recorded in linear and saturation regime and the corresponding output characteristic of the OFETs (a, b, c) and EGOFETs (d, e, f) based on TIPS/PFBT thin film. The coating speed is 1 cm/s and the coating temperature is 105 °C.

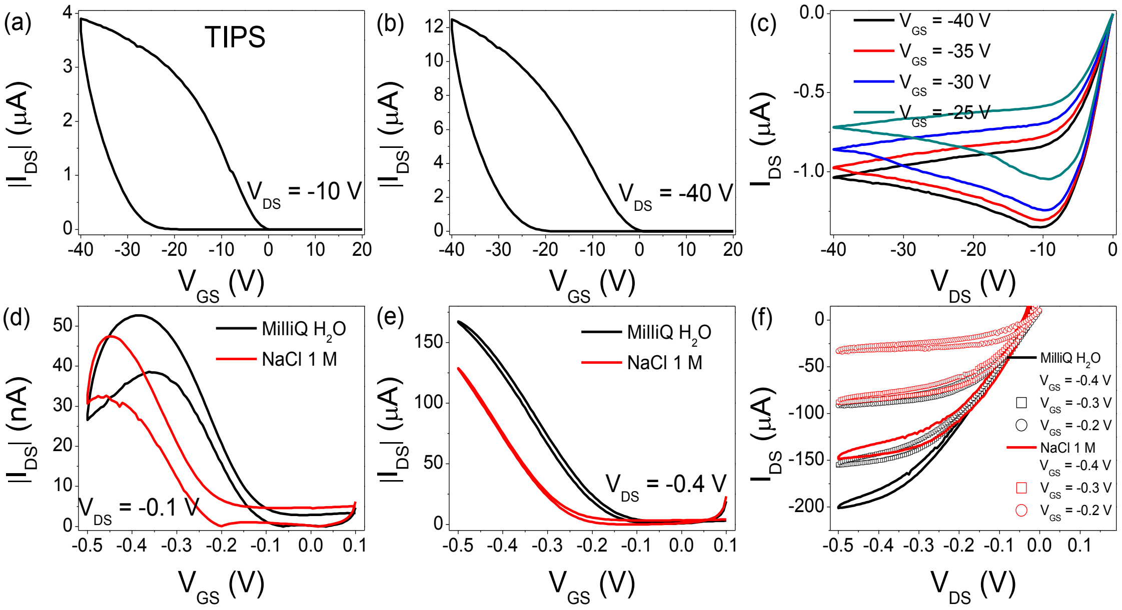

Figure A. 5: Typical *I/V* transfer recorded in linear and saturation regime and the corresponding output characteristic of the OFETs (a, b, c) and EGOFETs (d, e, f) based on TIPS-pentacene where S/D electrodes are PFBT-free. The coating speed is 1 cm/s and the coating temperature is 105 °C.

A.1.3 The Influence of OSC:PS Ratio

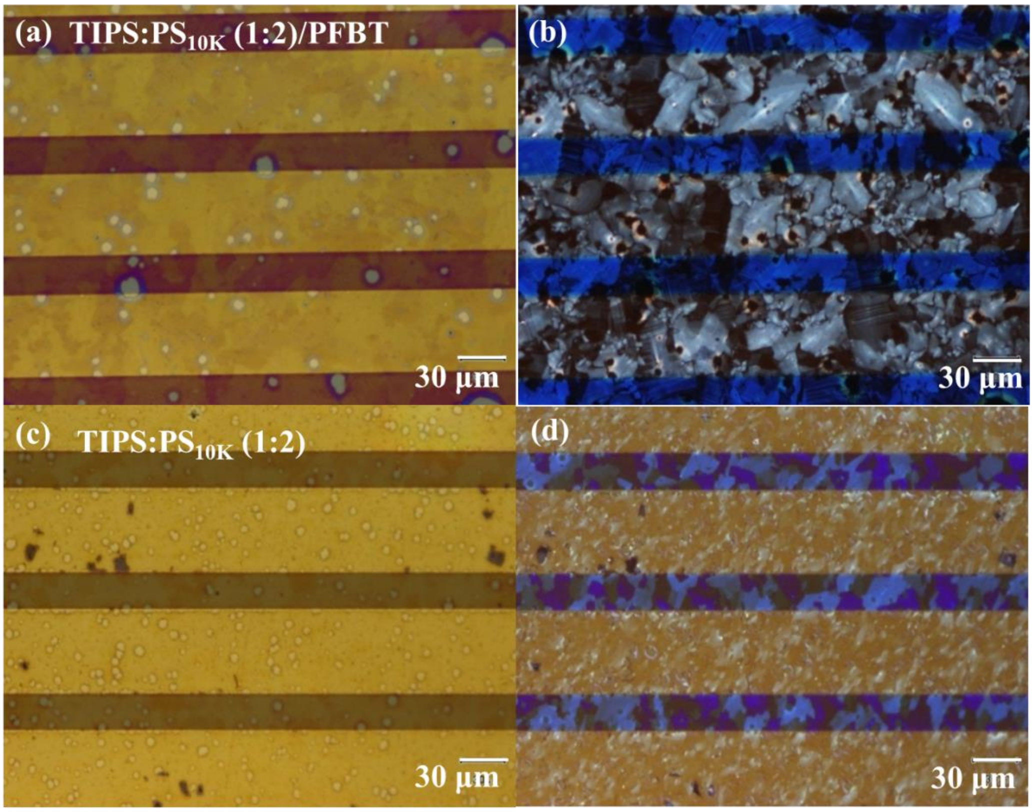

Figure A. 6: Polarized microscope images for TIPS:PS_{10K} (1:2) blend film with (a, b) and without (c, d) PFBT-functionalization. On the left, polarizer/analyzer = 0°. On the right, polarizer/analyzer = 90°. All these thin films were coated by BAMS at 1 cm/s and 105 °C.

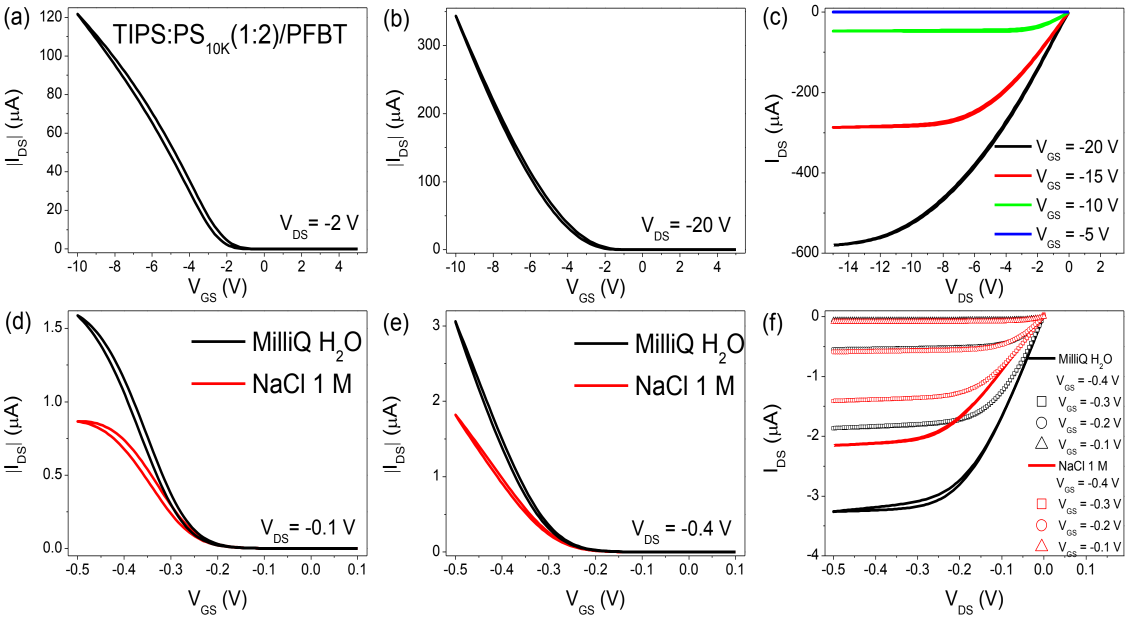

Figure A. 7: Typical *I/V* transfer recorded in linear and saturation regime and the corresponding output characteristic of the OFETs (a, b, c) and EGOFETs (d, e, f) based on TIPS:PS_{10K} (1:2)/PFBT thin film. The coating speed is 1 cm/s and the coating temperature is 105 °C.

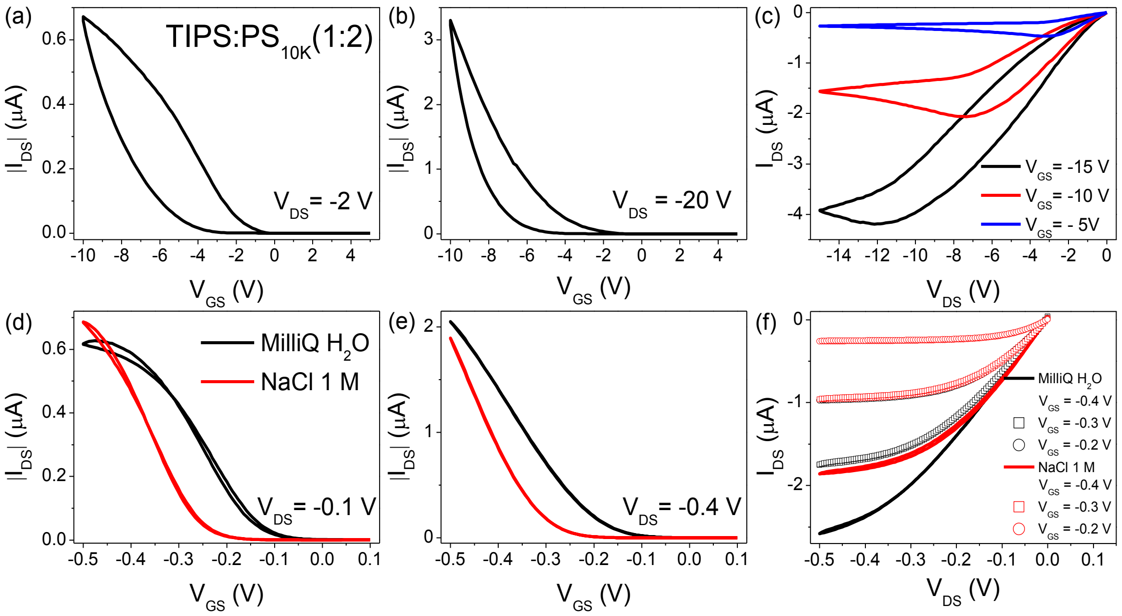

Figure A. 8: Typical *I/V* transfer recorded in linear and saturation regime and the corresponding output characteristics of the OFETs (a, b, c) and EGOFETs (d, e, f) based on TIPS:PS$_{10K}$ (1:2) thin film. The coating speed is 1 cm/s and the coating temperature is 105 °C.

A.1.4 The Influence of Coating Speed

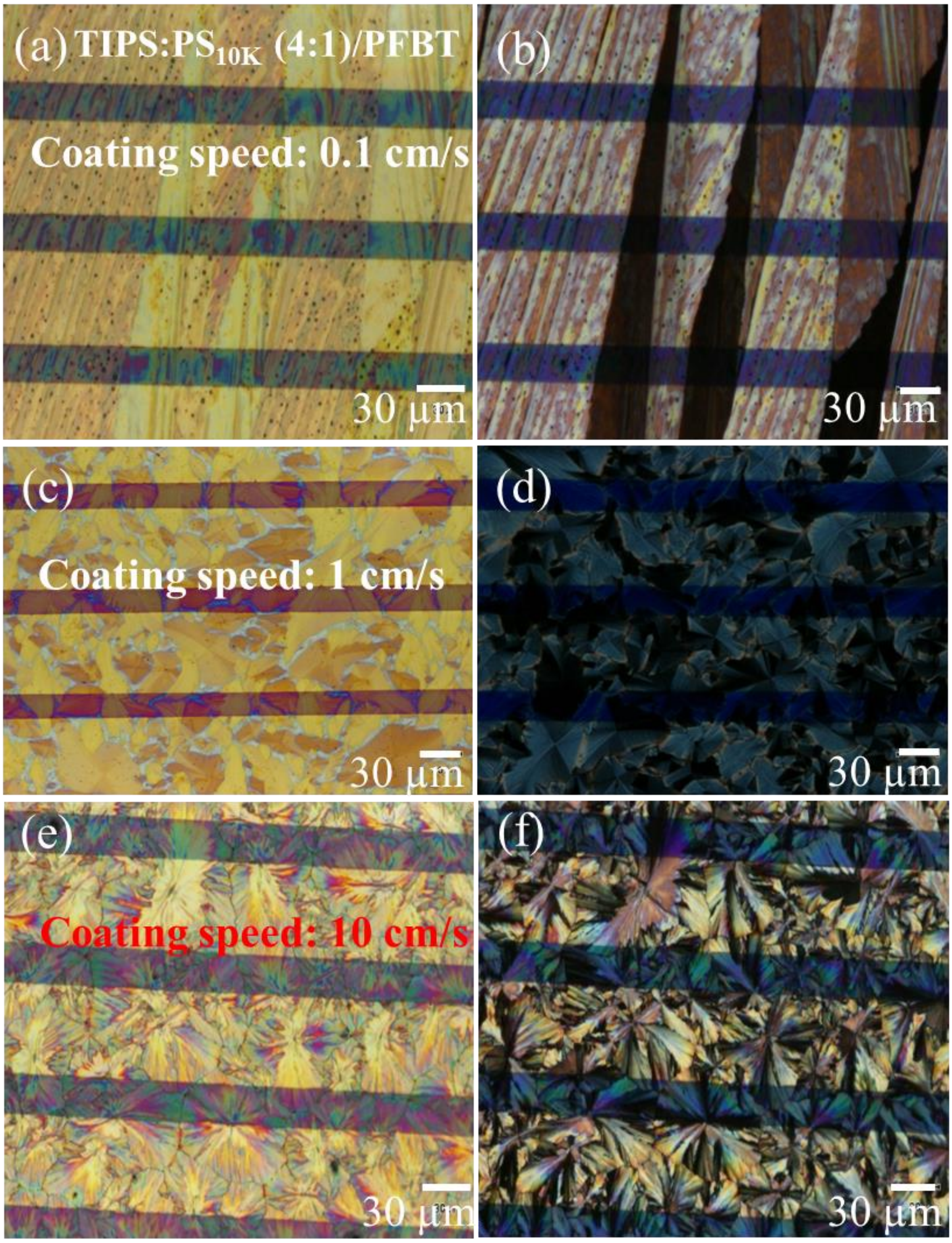

Figure A. 9: Polarized microscope images for TIPS:PS$_{10K}$(4:1)/PFBT thin film with different coating speeds (0.1 cm/s, 1 cm/s, and 10 cm/s). On the left, polarizer/analyzer = 0°. On the right, polarizer/analyzer = 90°. All these thin films were coated by BAMS at 105 °C.

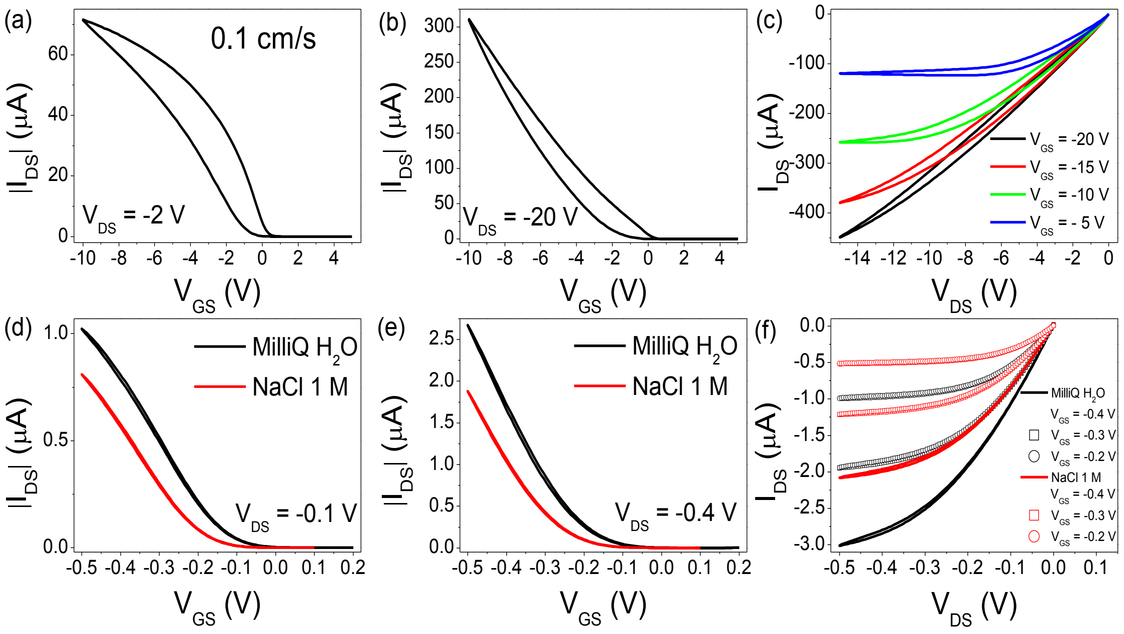

Figure A. 10: Typical *I/V* transfer recorded in linear and saturation regime and the corresponding output characteristics of the OFETs (a, b, c) and EGOFETs (d, e, f) based on TIPS:PS_{10K}(4:1)/PFBT thin film. The coating speed is 0.1 cm/s and the coating temperature is 105 °C.

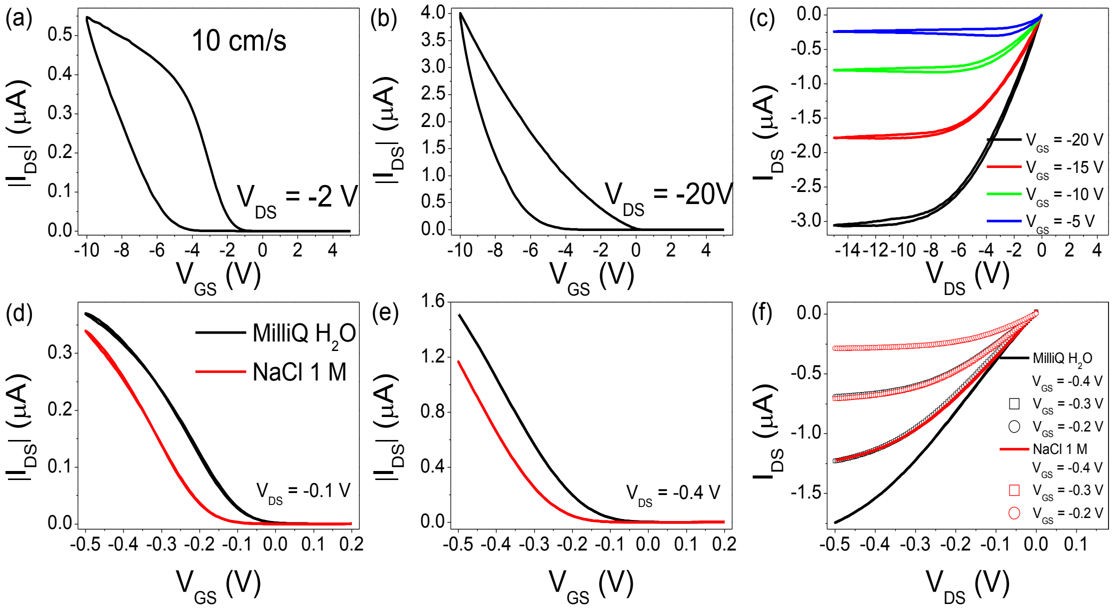

Figure A. 11: Typical *I/V* transfer recorded in linear and saturation regime and the corresponding output characteristics of the OFETs (a, b, c) and EGOFETs (d, e, f) based on TIPS:PS_{10K}(4:1)/PFBT thin film. The coating speed is 10 cm/s and the coating temperature is 105 °C.

A.1.5 The Influence of Molecular Weight of PS

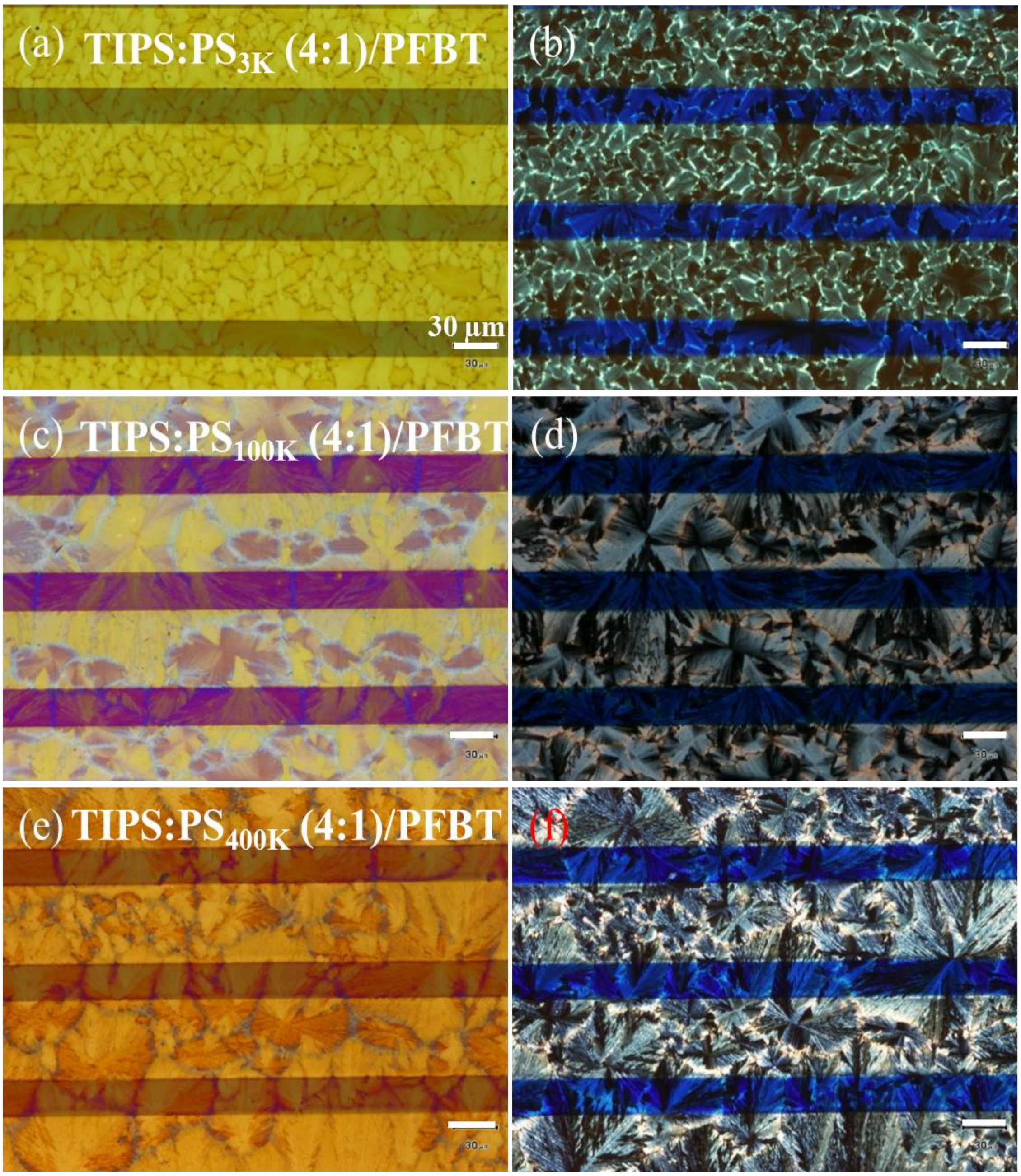

Figure A. 12: Polarized microscope images for TIPS:PS(4:1)/PFBT blend thin film with different molecular weight of PS (3 k, 100 k and 400 k g/mol). On the left, polarizer/analyzer = 0°. On the right, polarizer/analyzer = 90°. All these thin films were coated by BAMS at 105 °C.

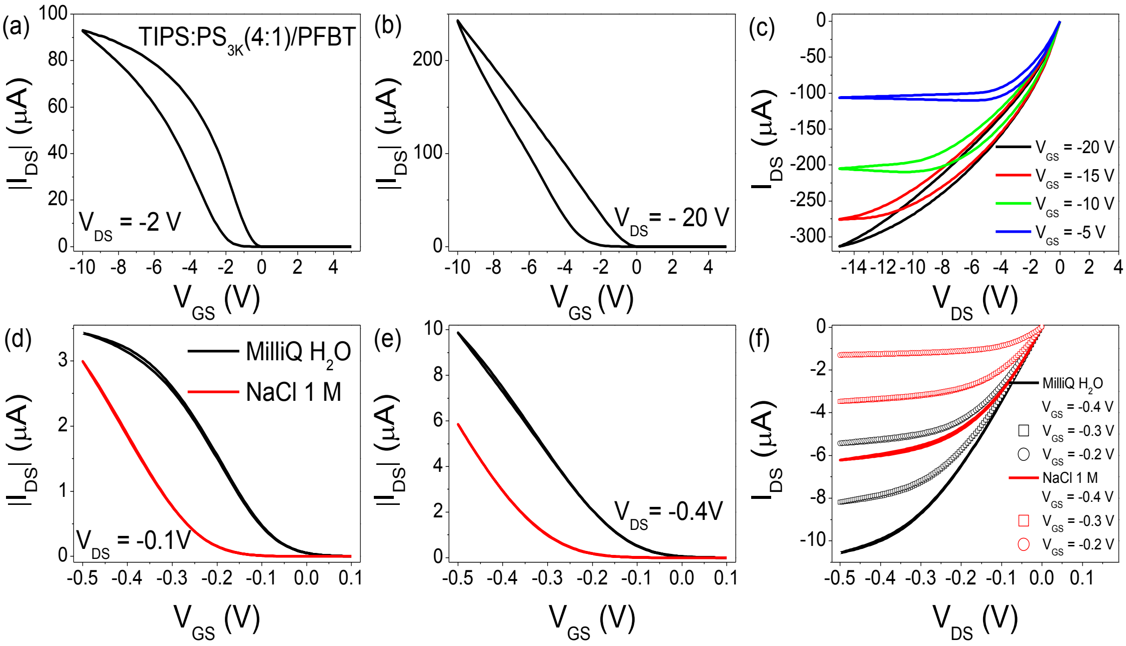

Figure A. 13: Typical *I/V* transfer recorded in linear and saturation regime and the corresponding output characteristics of the OFETs (a, b, c) and EGOFETs (d, e, f) based on TIPS:PS$_{3K}$ (4:1)/PFBT thin film. The coating speed is 1 cm/s and the coating temperature is 105 °C.

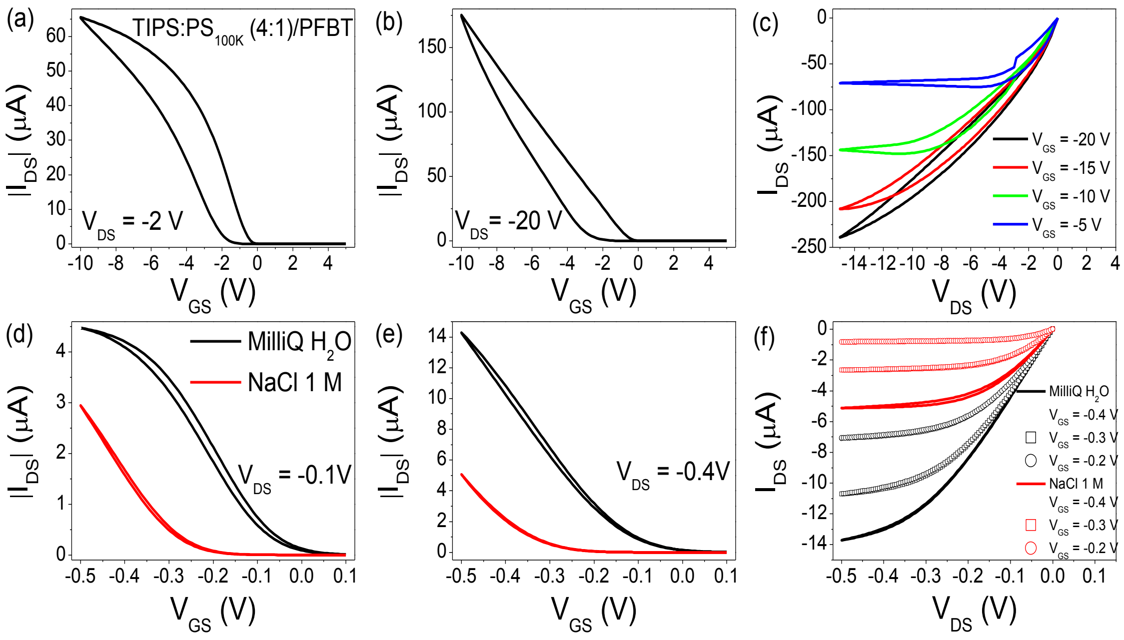

Figure A. 14: Typical *I/V* transfer recorded in linear and saturation regime and the corresponding output characteristics of the OFETs (a, b, c) and EGOFETs (d, e, f) based on TIPS:PS$_{100K}$ (4:1)/PFBT thin film. The coating speed is 1 cm/s and the coating temperature is 105 °C.

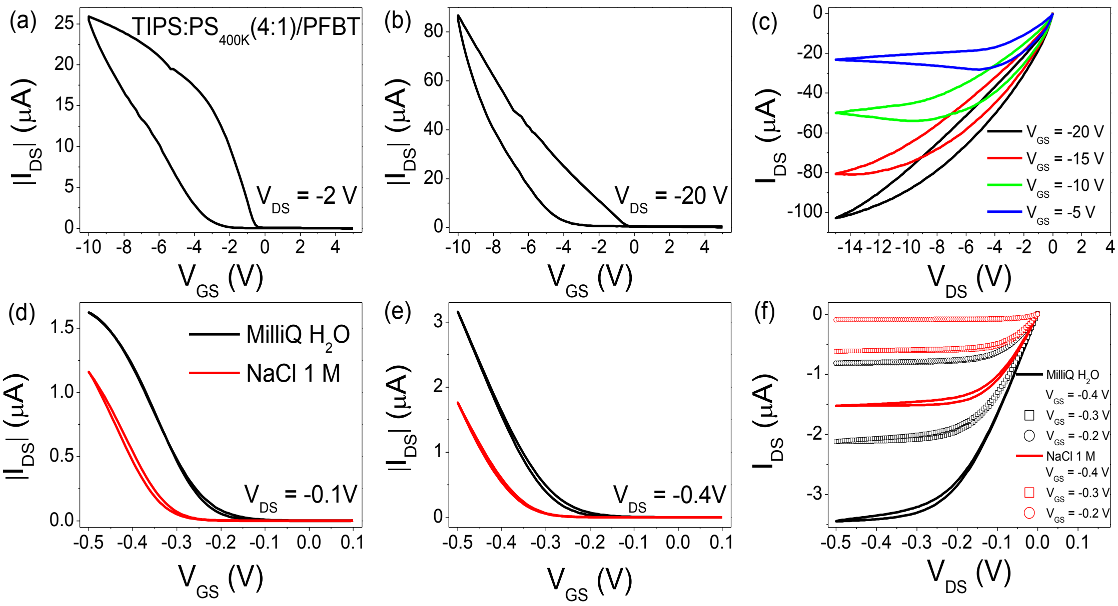

Figure A. 15: Typical *I/V* transfer recorded in linear and saturation regime and the corresponding output characteristics of the OFETs (a, b, c) and EGOFETs (d, e, f) based on TIPS:PS$_{400K}$ (4:1)/PFBT thin film. The coating speed is 1 cm/s and the coating temperature is 105 °C.

Table A. 1: The optimization process of TIPS-pentacene based device. All the inks were dissolved in chlorobenzene with a final concentration of 2 wt% and were deposited on SiO_2/Si substrates with the same *W*/*L* ratio (*W*/*L*=690) by BAMS at 105 °C

#	Polymer	Mw	ratio	SAM	*S* (cm/s)	Acronyms	OFET				EGOFET $_{\text{MilliQ}}$				EGOFET $_{\text{NaCl 1M}}$			
							μ_{sat} ($cm^2V^{-1}s^{-1}$)	V_{th} (V)	I_{on}/I_{off}	*SS* (V/dec)	$\mu_{MilliQ,sat}$ ($cm^2V^{-1}s^{-1}$)	V_{th} (mV)	I_{on}/I_{off}	*SS* (mV/dec)	$M_{NaCl,sat}$ ($cm^2V^{-1}s^{-1}$)	V_{th} (mV)	I_{on}/I_{off}	*SS* (mV/dec)
1	PS	10K	4:1	YES	1	TIPS:PS_{10K}(4:1)/PFBT	1.05±0.03	-0.27	2.8×10^7	0.25	0.12	12	7.3×10^3	87	0.07	-166	1.0×10^4	77
2	PS	10K	4:1	NO	1	TIPS:PS_{10K}(4:1)	0.06±0. 01	-2.47	2.3×10^5	1.65	0.05	-112	6.1×10^3	80	0.02	-194	3.7×10^3	87±9
3	/	/	/	YES	1	TIPS/PFBT	0.007±0. 001	-17.29	3.1×10^5	2.46	0.002	-79	1.1×10^2	184	0.001	-156	1.8×10^2	100
4	/	/	/	NO	1	TIPS	0.004±0. 001	-19.90	1.9×10^4	2.78	0.001	-51	8.3×10^1	211	0.001	-129	4.1×10^1	208
5	PS	10K	1:2	YES	1	TIPS:PS_{10K}(1:2)/PFBT	0.84±0. 03	-1.22	4.2×10^6	0.32	0.023	-194	7.4×10^3	89	0.034	-179	5.4×10^3	89
6	PS	10K	1:2	NO	1	TIPS:PS_{10K}(1:2)	0.01±0. 01	1.42	1.4×10^5	1.44	0.025	-83	6.0×10^3	87	0.021	-211	8.7×10^3	87
7	PS	10K	4:1	YES	0.1	/	0.36±0. 04	2.86	3.1×10^6	0.46	0.020	-7	4.9×10^3	97	0.012	-126	4.1×10^3	100
8	PS	10K	4:1	YES	10	/	0.007±0. 001	-0.15	6.8×10^4	0.93	0.007	24	1.6×10^3	99	0.007	-125	2.1×10^3	102
9	PS	3K	4:1	YES	1	TIPS:PS_{3K}(4:1)/PFBT	0.48±0. 02	1.49	5.4×10^5	0.45	0.053	-2	2.1×10^3	115	0.044	-159	5.0×10^3	97
10	PS	100K	4:1	YES	1	TIPS:PS_{100K}(4:1)/PFBT	0.27±0. 05	0.29	5.7×10^6	0.44	0.071	13	9.7×10^2	123	0.045	-2	3.5×10^3	75
12	PS	400K	4:1	YES	1	TIPS:PS_{400K}(4:1)/PFBT	0.04±0. 01	6.27	3.9×10^5	0.88	0.036	-195	6.8×10^2	125	0.029	-265	4.1×10^3	88

A.2 Optimization Process of diF-TES-ADT based Devices

During the optimization process, EGOFETs and OFETs devices have been characterized through optical microscopy, atomic force microscopy and their electrical performances have been recorded. In order to select the better EGOFET the following parameters have been modified: (1) the PFBT functionalization of the *S*/*D* electrodes, (2) the PS, (3) the OSC:PS ratio and (4) the binder polymer.

A.2.1 The Influence of PFBT-functionalization

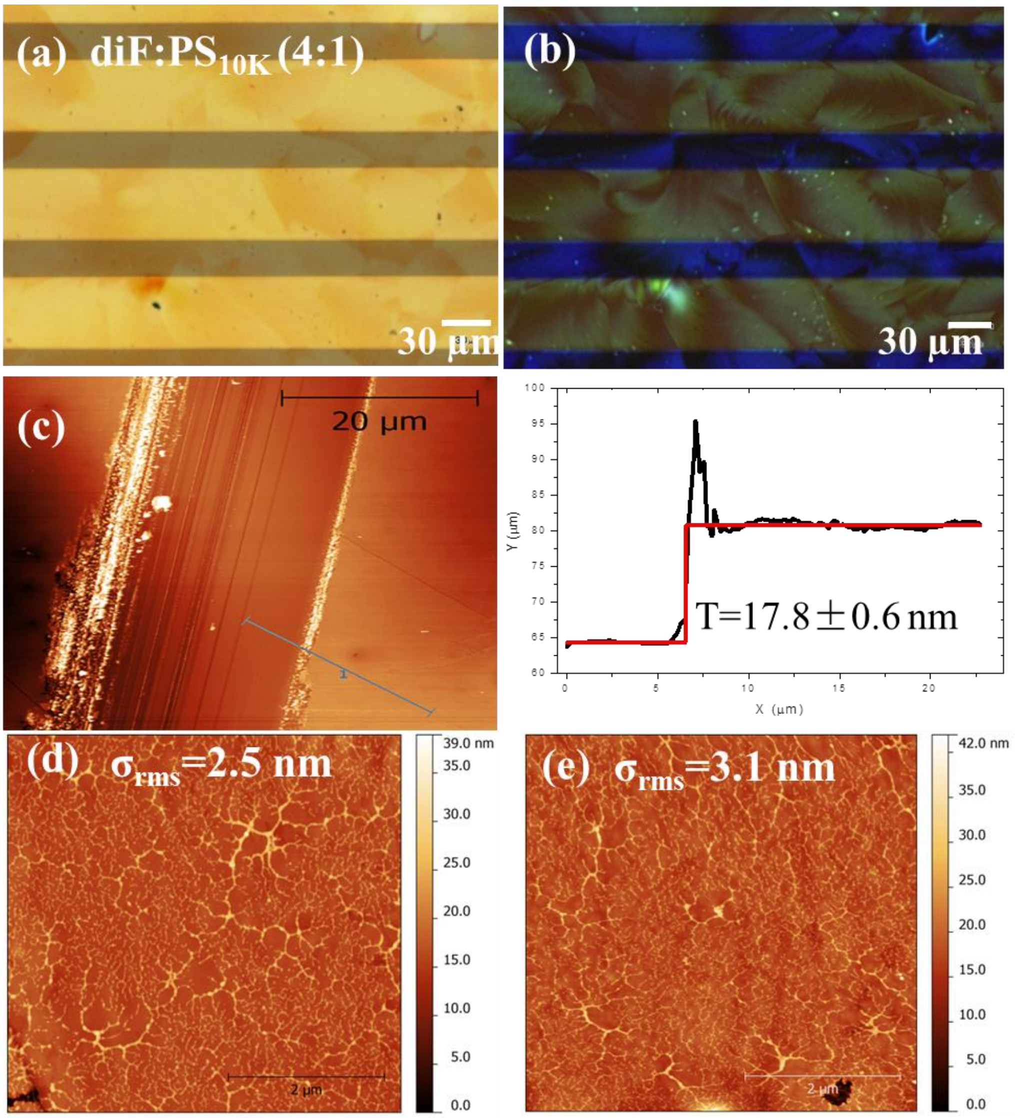

Figure A. 16: Optical microscopy images of diF:PS_{10K}(4:1)-based thin films acquired with cross polarizing filters: (a) polarizer/analyzer = 0°, and (b) polarizer/analyzer = 90°. (c) AFM profile and its corresponding 2D fitting of the same thin film. The AFM images (5×5 μm^2) of the same thin film were acquired on (d) the channel region and on (e) the electrodes region.

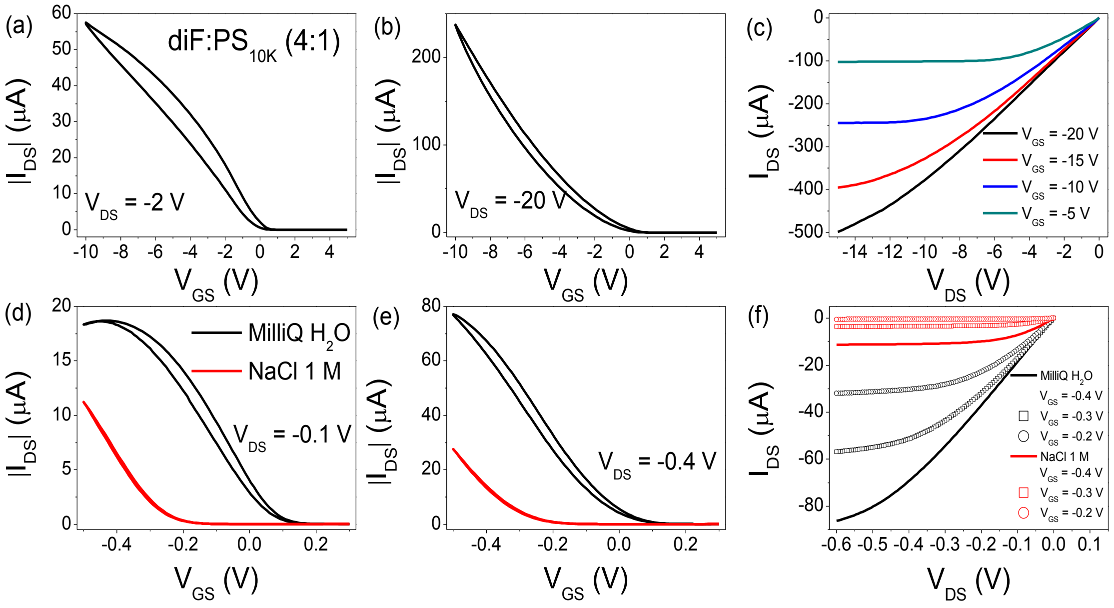

Figure A. 17: Typical *I/V* transfer recorded in linear and saturation regime and the corresponding output characteristics of the OFETs (a, b, c) and EGOFETs (d, e, f) based on diF:PS$_{10K}$(4:1) thin film. The coating speed is 1 cm/s and the coating temperature is 105 °C.

A.2.2 The Influence of PS

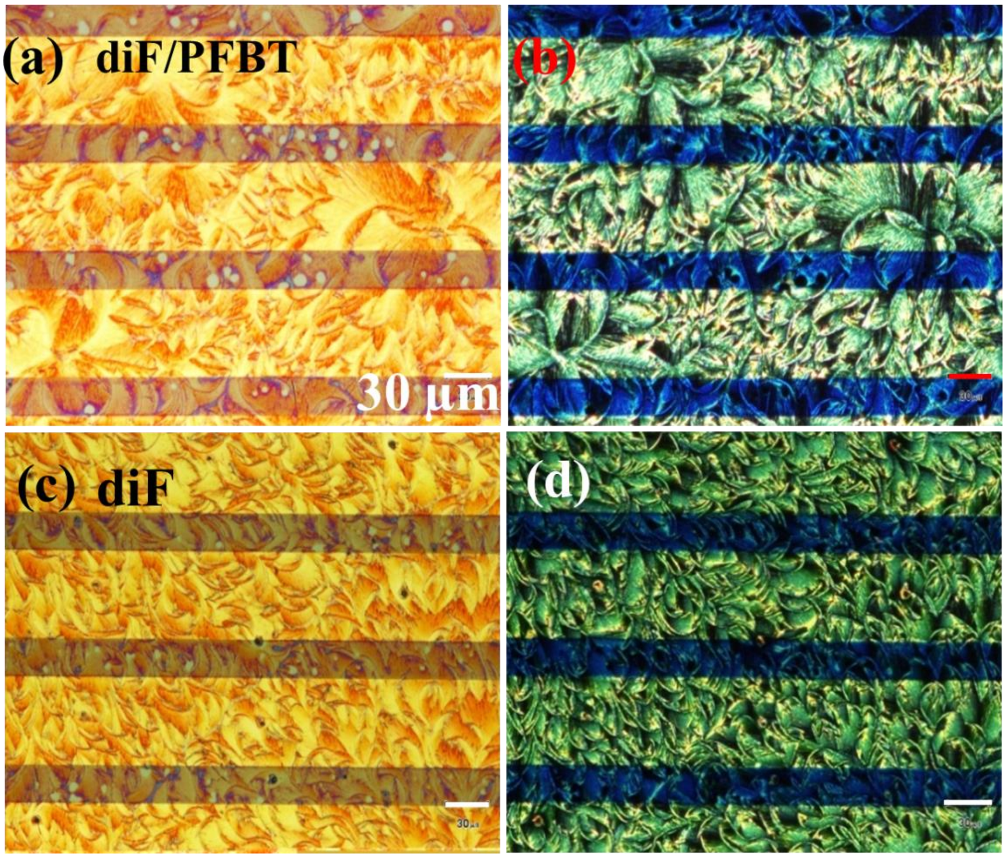

Figure A. 18: The optical microscopy images of PS-free thin films (a,b) with and (c,d) without PFBT-functionalization. On the left, polarizer/analyzer = 0°. On the right, polarizer/analyzer = 90°.

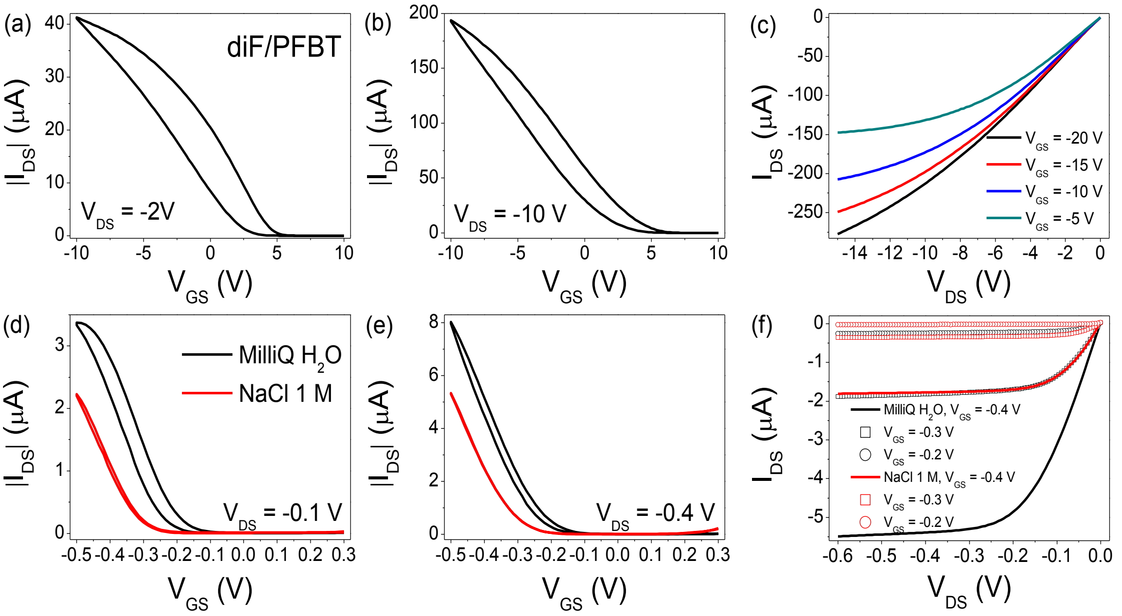

Figure A. 19: Typical *I/V* transfer recorded in linear and saturation regime and the corresponding output characteristics of the OFETs (a, b, c) and EGOFETs (d, e, f) based on diF/PFBT thin film. The coating speed is 1 cm/s and the coating temperature is 105 °C.

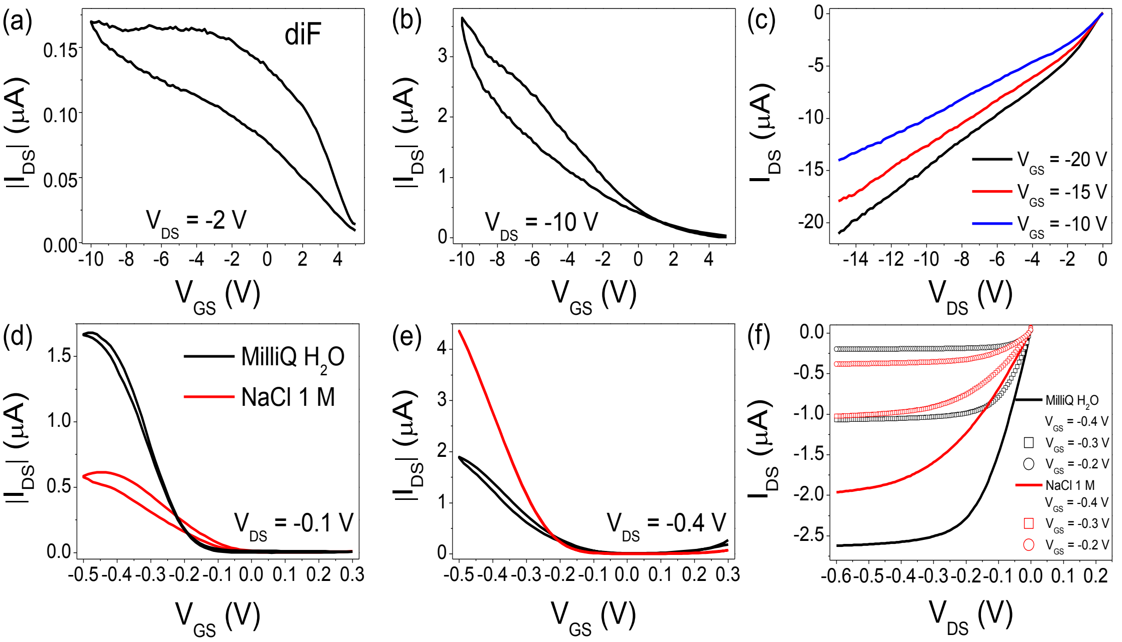

Figure A. 20: Typical *I/V* transfer recorded in linear and saturation regime and the corresponding output characteristics of the OFETs (a, b, c) and EGOFETs (d, e, f) based on diF thin film. The coating speed is 1 cm/s and the coating temperature is 105 °C.

A.2.3 The Influence of OSC:PS Ratio

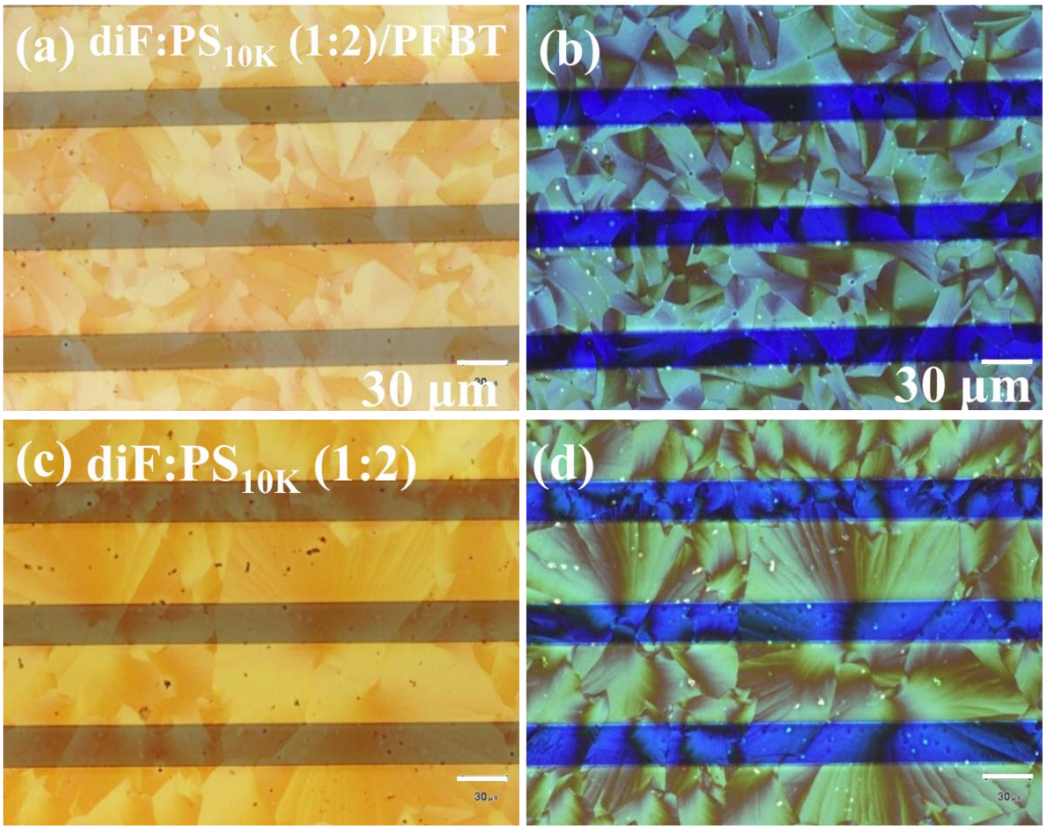

Figure A. 21: Microscope images for (a,b) diF:PS$_{10K}$(1:2)/PFBT-based and (c,d) diF:PS$_{10K}$(1:2)-based thin film. On the left, polarizer/analyzer = 0°. On the right, polarizer/analyzer = 90°. All these thin films were coated by BAMS at 1 cm/s and 105 °C.

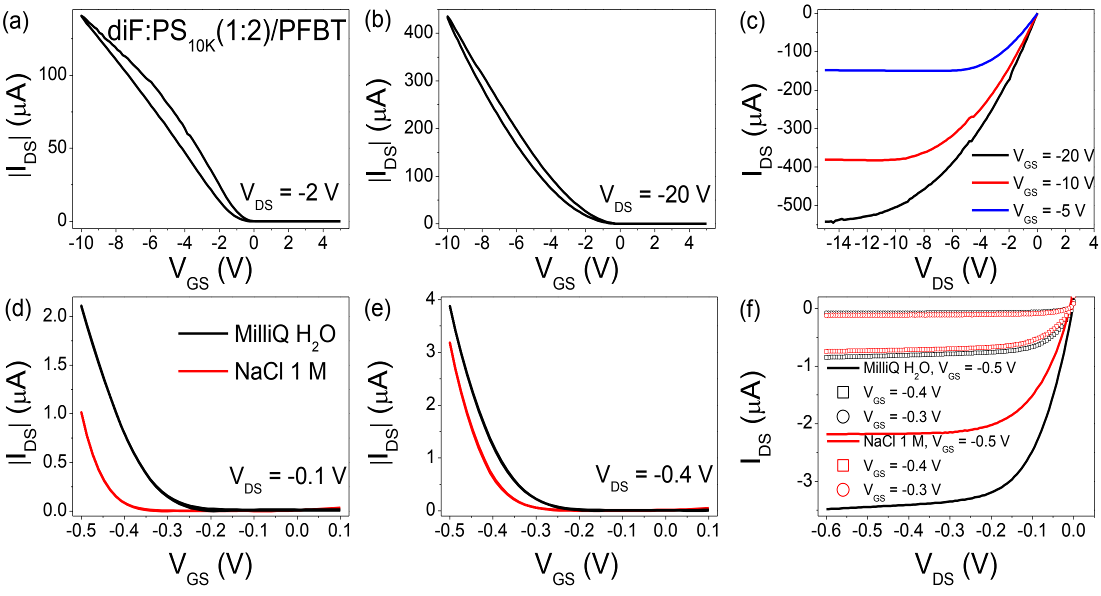

Figure A. 22: Typical *I/V* transfer recorded in linear and saturation regime and the corresponding output characteristics of the OFETs (a, b, c) and EGOFETs (d, e, f) based on diF:PS$_{10K}$ (1:2)/PFBT thin film. The coating speed is 1 cm/s and the coating temperature is 105 °C.

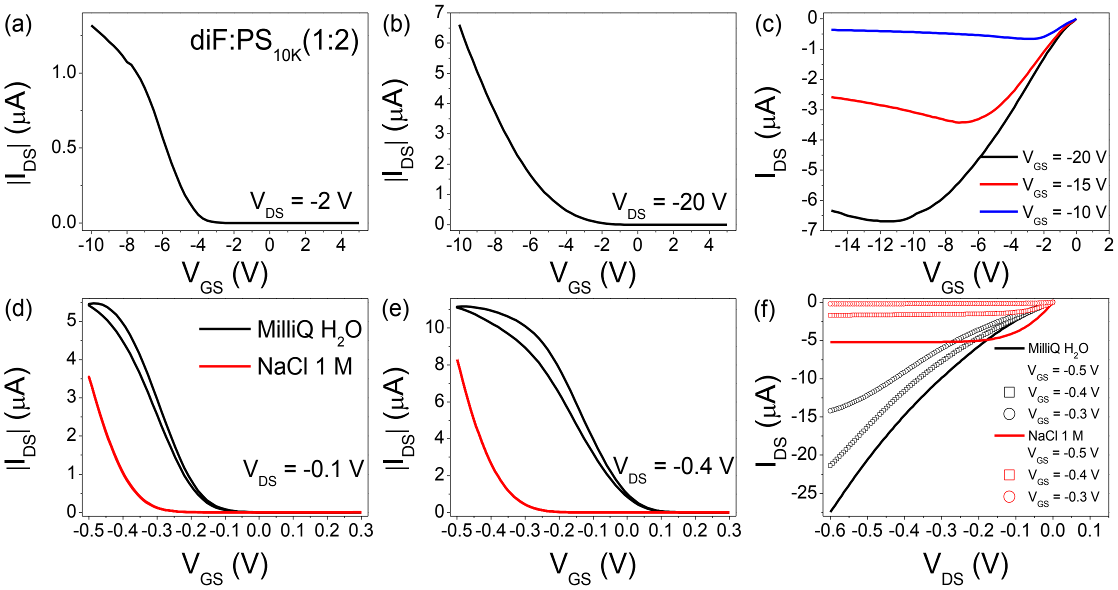

Figure A. 23: Typical *I/V* transfer recorded in linear and saturation regime and the corresponding output characteristics of the OFETs (a, b, c) and EGOFETs (d, e, f) based on diF:PS$_{10K}$ (1:2) thin film. The coating speed is 1 cm/s and the coating temperature is 105 °C.

A.2.4 The Influence of Different Binder Polymers

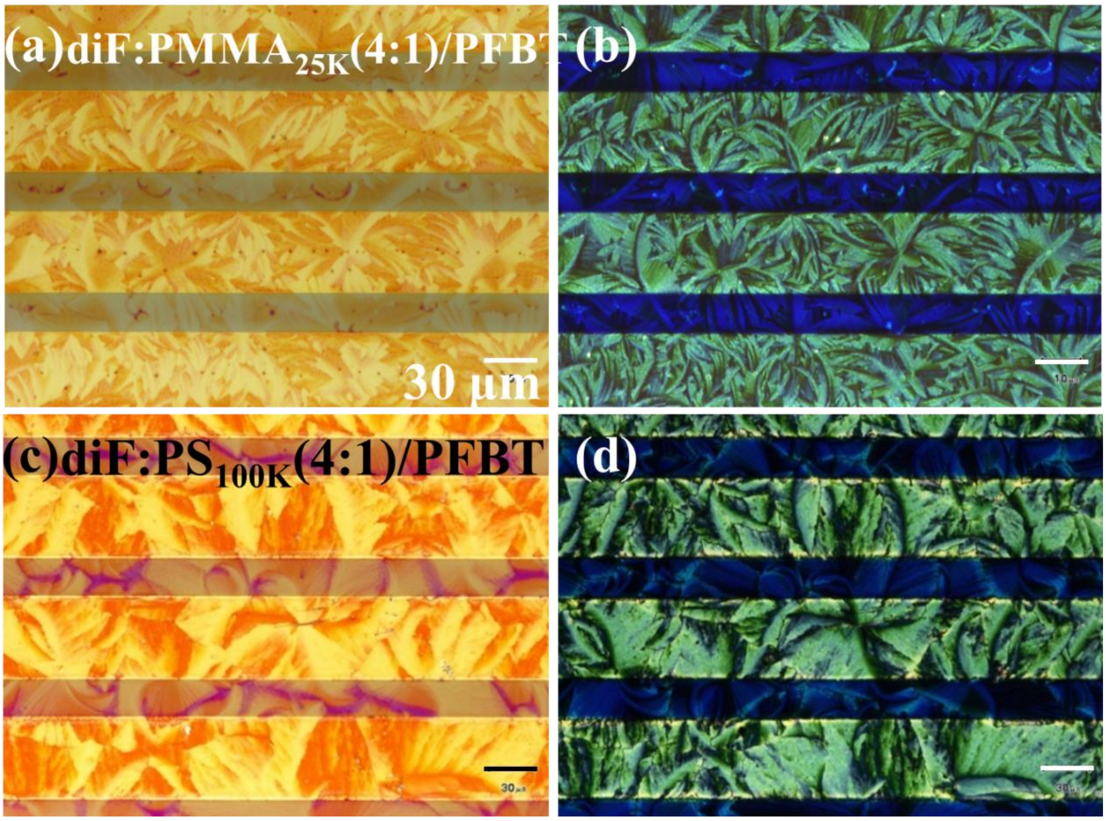

Figure A. 24: Microscope images for (a, b) diF:PMMA$_{25K}$(4:1)/PFBT blend and (c, d) diF:PS$_{100K}$ (4:1)/PFBT thin films. On the left, polarizer/analyzer = 0°. On the right, polarizer/analyzer = 90°. All these thin films were coated by BAMS at 1 cm/s and 105 °C.

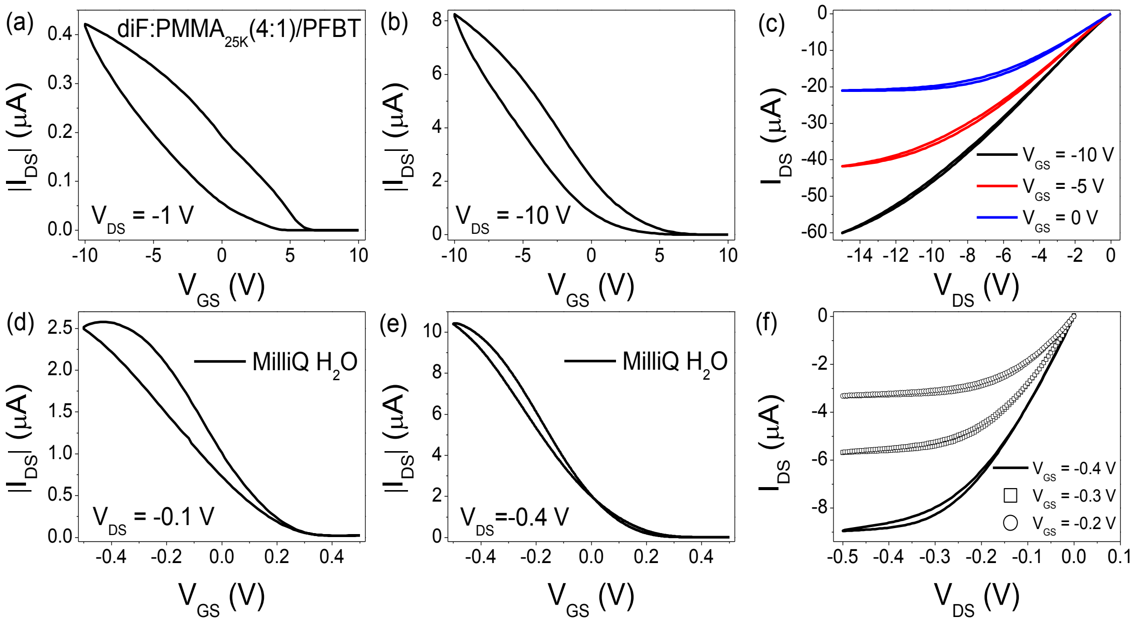

Figure A. 25: Typical *I/V* transfer recorded in linear and saturation regime and the corresponding output characteristics of the OFETs (a, b, c) and EGOFETs (d, e, f) based on diF:PMMA$_{25K}$(4:1)/PFBT thin film. The coating speed is 1 cm/s and the coating temperature is 105 °C.

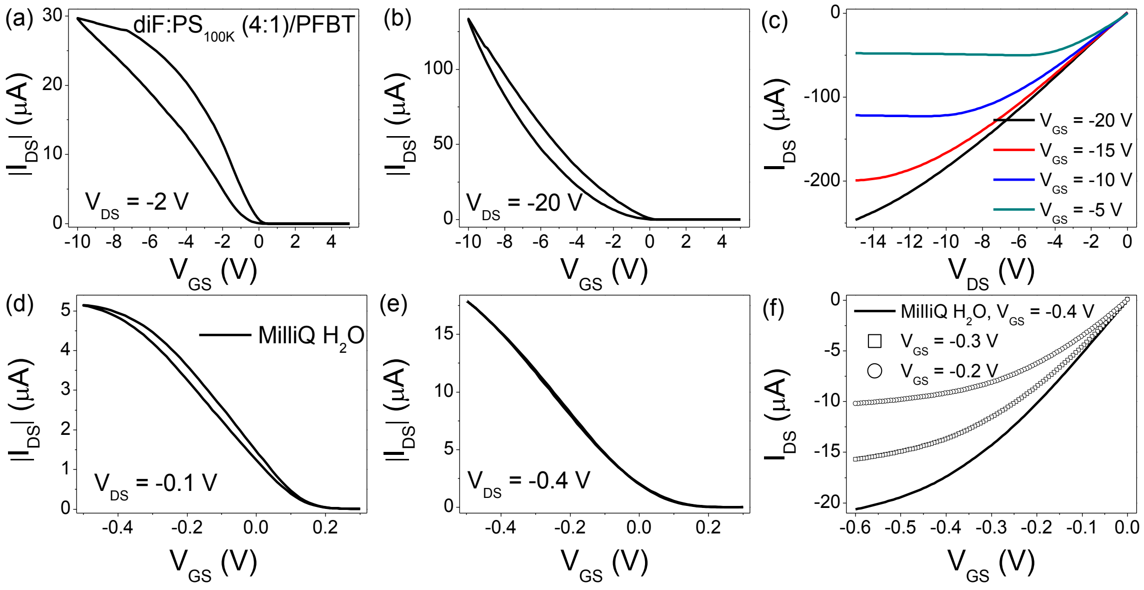

Figure A. 26: Typical *I/V* transfer recorded in linear and saturation regime and the corresponding output characteristics of the OFETs (a, b, c) and EGOFETs (d, e, f) based on diF:PS$_{100K}$ (4:1)/PFBT thin films. The coating speed is 1 cm/s and the coating temperature is 105 °C.

Table A.2: The optimization process of diF-TES-ADT based device. All the inks were dissolved in chlorobenzene with a final concentration of 2 wt% and were deposited on Si/SiO$_2$ substrates with the same *W*/*L* ratio (*W*/*L*=690) by BAMS at 1cm/s and 105 °C.

#	Polymer	Mw	ratio	SAM	Acronyms	OFET				EGOFET $_{\text{MilliQ}}$				EGOFET $_{\text{NaCl 1M}}$			
						μ_{sat} (cm^{2}V^{-1}s^{-1})	V_{th} (V)	I_{on}/I_{off}	*SS* (V/dec)	$\mu_{MilliQ,sat}$ (cm^{2}V^{-1}s^{-1})	V_{th} (mV)	I_{on}/I_{off}	*SS* (mV/dec)	$M_{NaCl,sat}$ (cm^{2}V^{-1}s^{-1})	V_{th} (mV)	I_{on}/I_{off}	*SS* (mV/dec)
1	PS	10K	4:1	YES	diF:PS$_{10K}$(4:1)/PFBT	1.11	-1.14	1.9×10^6	0.4418	0.18	49±1	1.5×10^4	82±2	0.08	-19±1	9.7×10^3	86±7
2	PS	10K	4:1	NO	diF:PS$_{10K}$(4:1)	0.63	-1.25	$.2.7\times10^5$	0.3901	0.10	125±1	4.3×10^3	87±7	0.07	-152±4	8.6×10^3	86±7
3	/	/	/	YES	diF/PFBT	0.17	7.70	$.2.4\times10^5$	1.2782	0.04	-145±3	1.2×10^3	97±5	0.02	-200±4	1.6×10^3	87±5
4	/	/	/	NO	diF	0.004	4.41	4.1×10^2	6.755	0.004	-28±4	1.6×10^2	121±1	0.002	-120±2	5.5×10^2	90±4
5	PS	10K	1:2	YES	diF:PS$_{10K}$(1:2)/PFBT	0.79	-0.06	1.5×10^6	0.3915	0.05	-313±5	2.6×10^2	98±2	0.015	-238±4	2.8×10^2	90±3
6	PS	10K	1:2	NO	diF:PS$_{10K}$(1:2)	0.017	2.00	5.5×10^5	2.611	0.039	109±4	3.5×10^3	94±2	0.068	-262±7	6.9×10^3	89±1
7	PMMA	25K	4:1	YES	diF:PMMA$_{25K}$(4:1)	0.007	7.03	4.8×10^4	0.959	0.01	327±6	6.9×10^2	182±5	/	/	/	/
8	PS	100K	4:1	YES	diF:PS$_{100K}$(4:1)/PFBT	0.195	0.38	1.9×10^6	0.329	0.02	269±6	8.1×10^2	116±2	/	/	/	/

A.3 Additional Data of DPTTA based Devices

The optimization process of DPPTTA has been used as organic semiconductor for the development of OFETs and EGOFETs. The optimization process related to the OFET device is reported in A. Campos, ‘Influence of organic semiconductors morphology, structure and processability on field-effect transistors performance’, thesis defense at 2018 and the best formulation has been further selected for EGOFET fabrication. The only optimization performed was related to the molecular weight of the binder. Finally, DP:PS$_{10K}$(1:3)/PFBT has revealed as the best formulation for the rest of the experimental work.

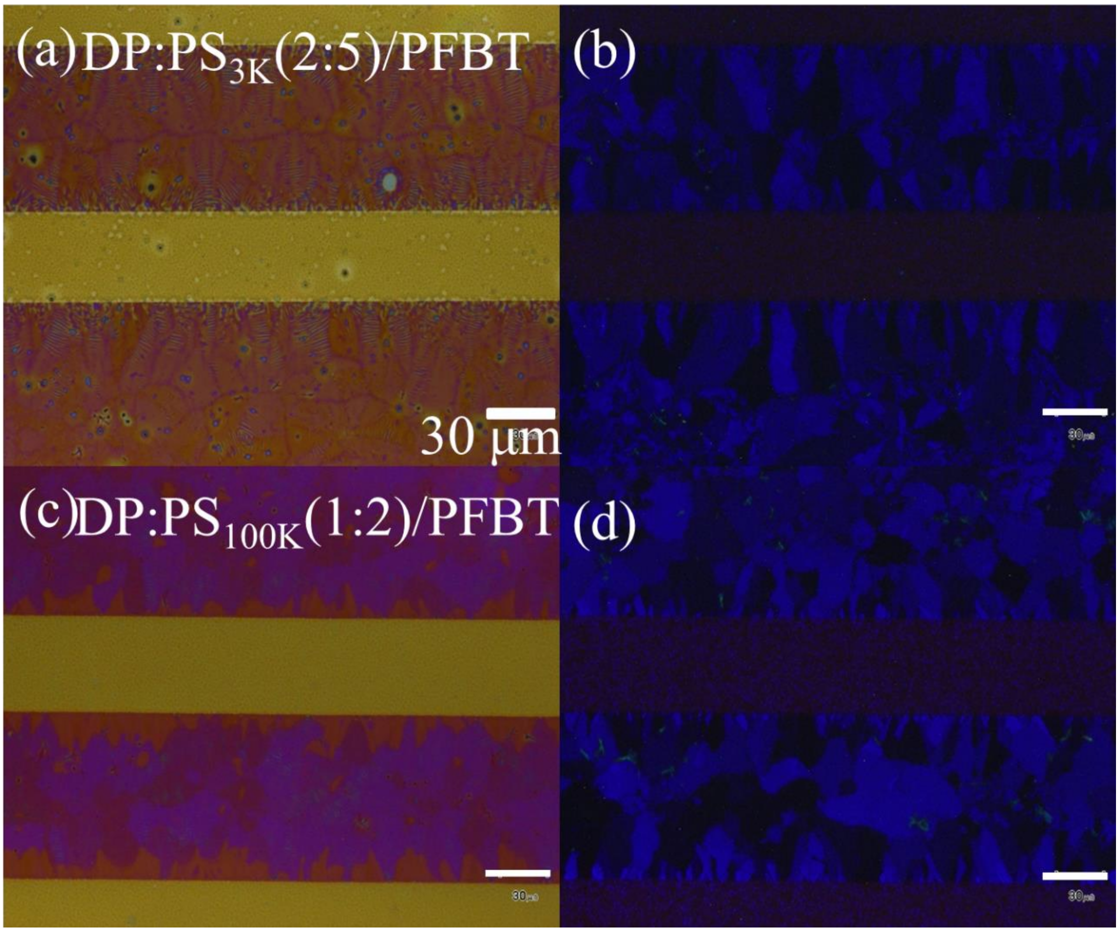

Figure A. 27: Microscope images for (a,b) DP:PS$_{3K}$ (2:5)/PFBT-based and (c,d) DP:PS$_{100K}$ (1:2)/PFBT-based thin film. On the left, polarizer/analyzer = 0°. On the right, polarizer/analyzer = 90°. All the thin films were coated by BAMS at 1 cm/s and 105 °C.

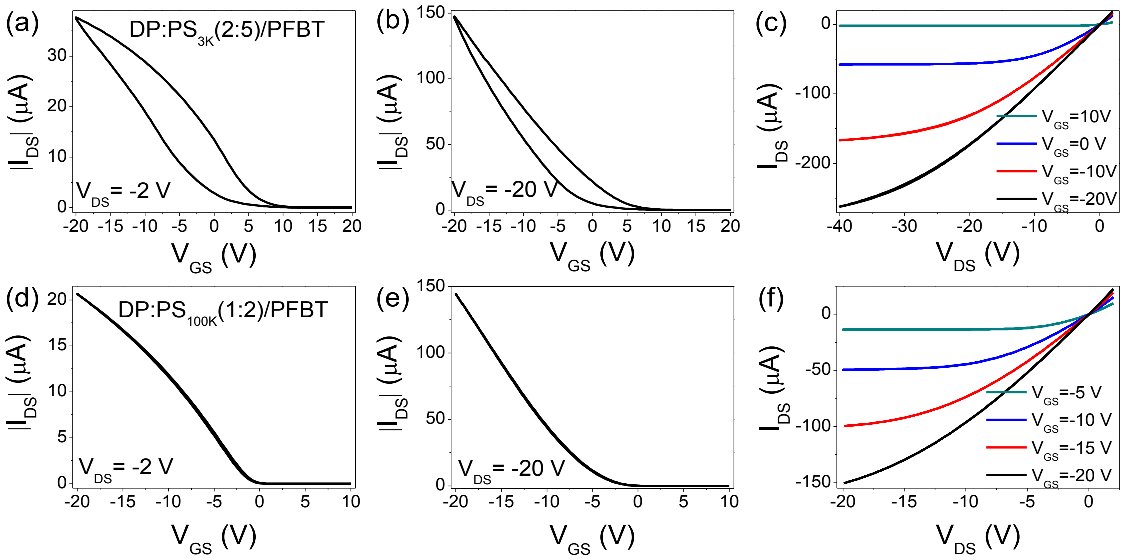

Figure A. 28: The typical transfer characteristics in linear and saturation regime, and output characteristics in BG/BC configuration of (a-c) DP:PS$_{3K}$(2:5)/PFBT-based and (d-f) DP:PS$_{100K}$(1:2)/PFBT-based OFET devices with *W*/*L* = 100.

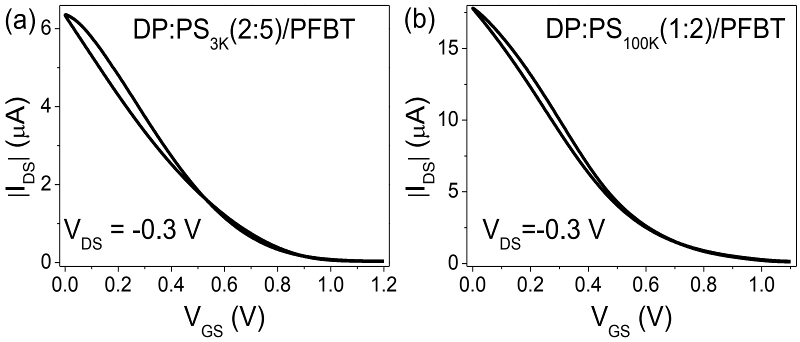

Figure A. 29: The typical transfer characteristics in saturation regime of (a) DP:PS$_{3K}$(2:5)/PFBT-based and (b) DP:PS$_{100K}$(1:2)/PFBT-based EGOFET device in MilliQ water.

Table A.3: The optimization process of DPTTA:PS blend based device. All the inks were dissolved in chlorobenzene and were deposited on SiO_2/Si substrates at 105 °C with W/L =100 for OFET and W/L = 690 for EGOFET. All the coating speed is fixed to1 cm/s.

#	Mw	ratio	SAM	C (mg/ml)	Acronyms	OFET				EGOFET $_{\text{MilliQ}}$				EGOFET $_{\text{NaCl 1M}}$			
						μ_{sat} ($cm^2V^{-1}s^{-1}$)	V_{th} (V)	I_{on}/I_{off}	SS (V/dec)	$\mu_{MilliQ,sat}$ ($cm^2V^{-1}s^{-1}$)	V_{th} (mV)	I_{on}/I_{off}	SS (mV/dec)	$M_{NaCl,sat}$ ($cm^2V^{-1}s^{-1}$)	V_{th} (mV)	I_{on}/I_{off}	SS (mV/dec)
1	3K	2:5	YES	26.0	DP:PS_{3K}(2:5)/PFBT	0.34	11.5	2.8×10^5	2.54	0.015	1.05	1.85×10^2	332	/	/	/	/
2	10K	1:2	YES	22.6	DP:PS_{10K}(1:2)/PFBT	1.03	-0.01	4.5×10^6	0.7	0.054	0.98	4.8×10^2	356	/	/	/	/
3	100K	1:2	YES	22.6	DP:PS_{100K}(1:2)/PFBT	0.55	0.34	1.1×10^5	0.26	0.022	1.11	1.46×10^2	502	/	/	/	/
4	10K	1:3	YES	20.0	DP:PS_{10K}(1:3)/PFBT	0.67	0.86	6.5×10^5	0.41	0.12	1.0	5.3×10^2	380	0.03	1.0±0.3	1.7×10^2	459±10

A.4 Additional Data of PDPP-TT(1)-SVS(9) Devices

A.4.1 AFM Images

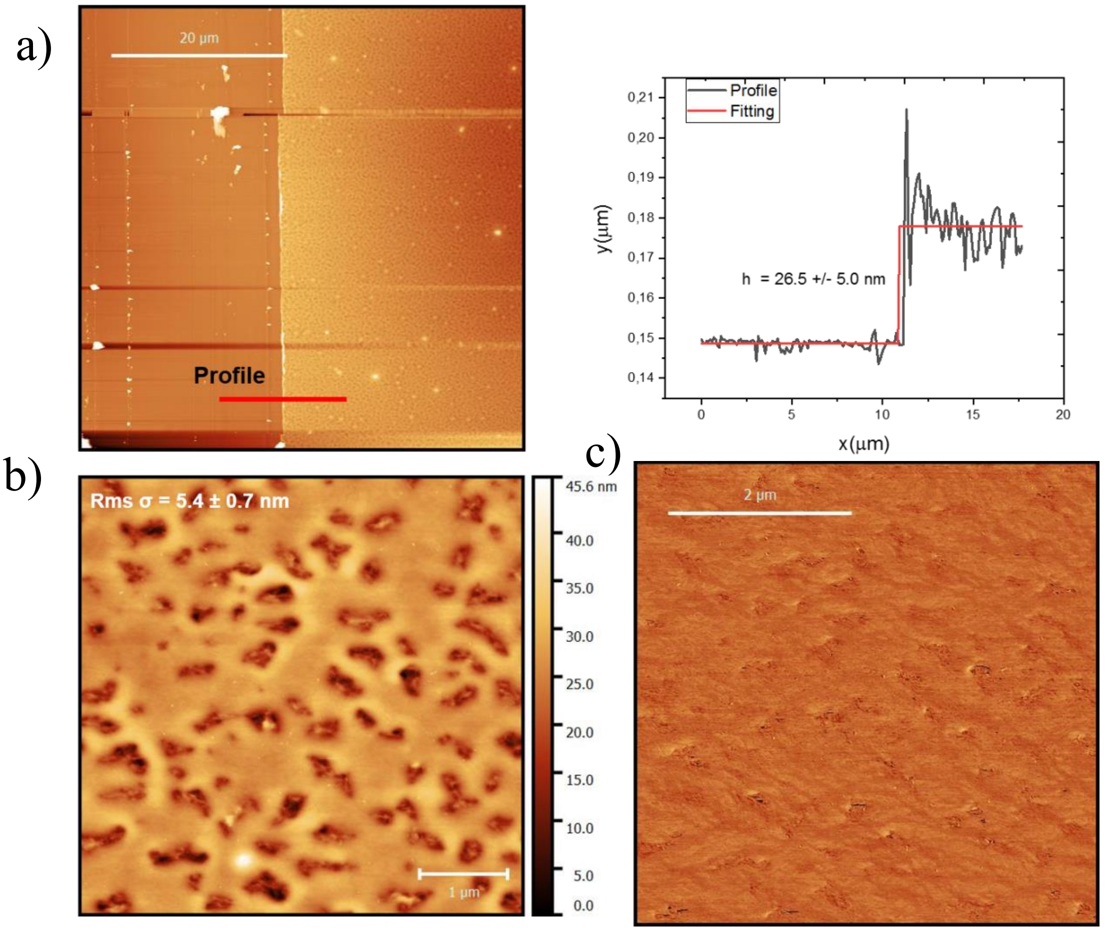

Figure A. 30: Height profiles extracted for (a) SVS:PS$_{100K}$(1:2)/PFBT based thin film. (b) The AFM images (5×5 µm^2) and (c) phase images of the same thin film were acquired on the channel region.

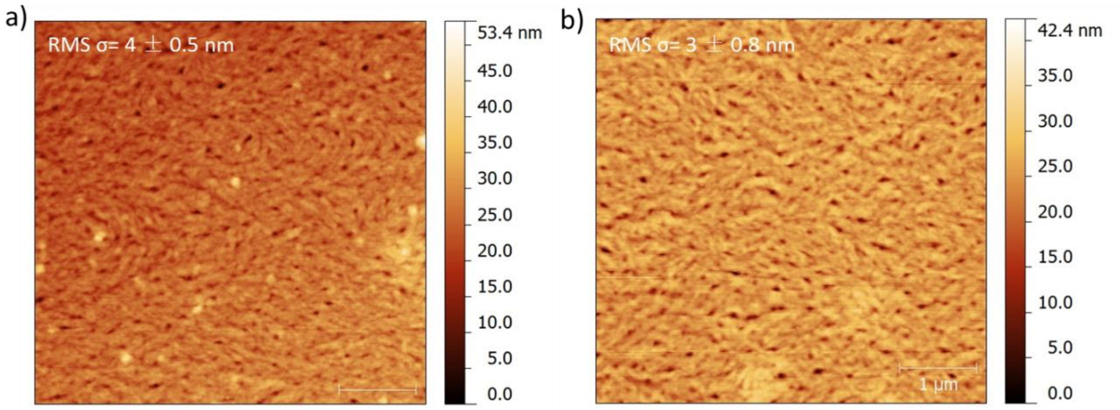

Figure A.31: AFM images (5×5 µm^2) of pristine PDPP-TT(1)-SVS(9) thin film on (a) Au electrode and (b) SiO$_2$ channel region. The rms values are averaged from 5 images.

A.4.2 The EIS Response of Bare Surface

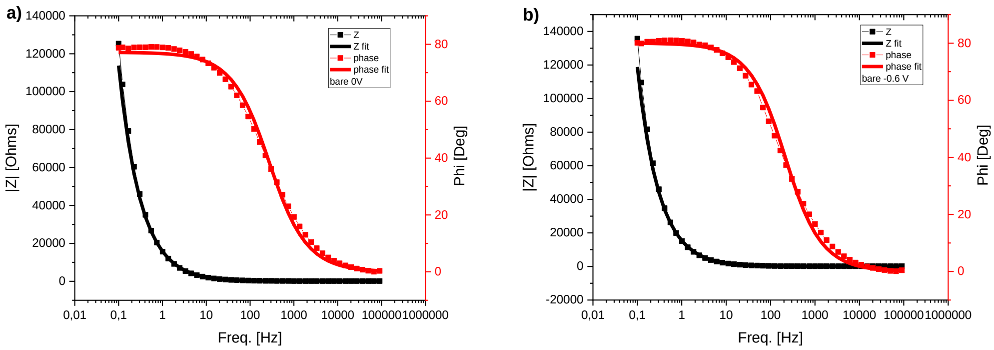

Figure A.32: Nyquist Plot of the bare surface employed for the electrochemical analysis of the two thin film. The impedance has been recorded at (a) V_{DC} = 0 V and (b) V_{DC} = -0.6 V.

A.4.3 The Influence of PS

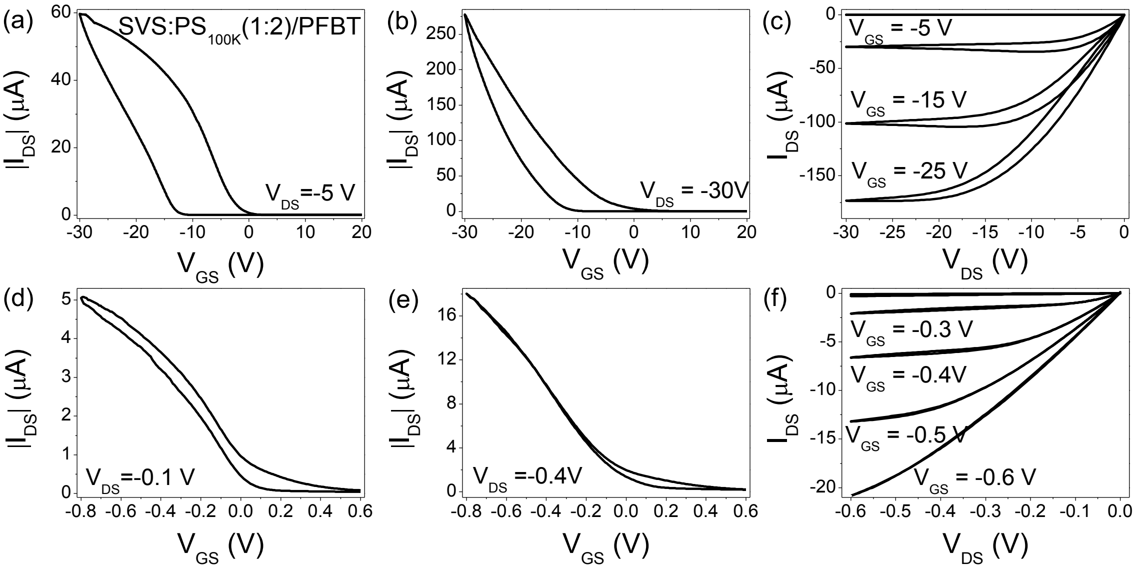

Figure A. 33: Typical *I/V* transfer recorded in linear and saturation regime and the corresponding output characteristic of SVS:PS$_{100K}$(1:2)-based OFETs (a, b, c) and EGOFETs (d, e, f) having S/D electrodes functionalized with PFBT. Tetraline has been employed as solvent and the coating speed and temperature are 1 cm/s and 150 °C, respectively.

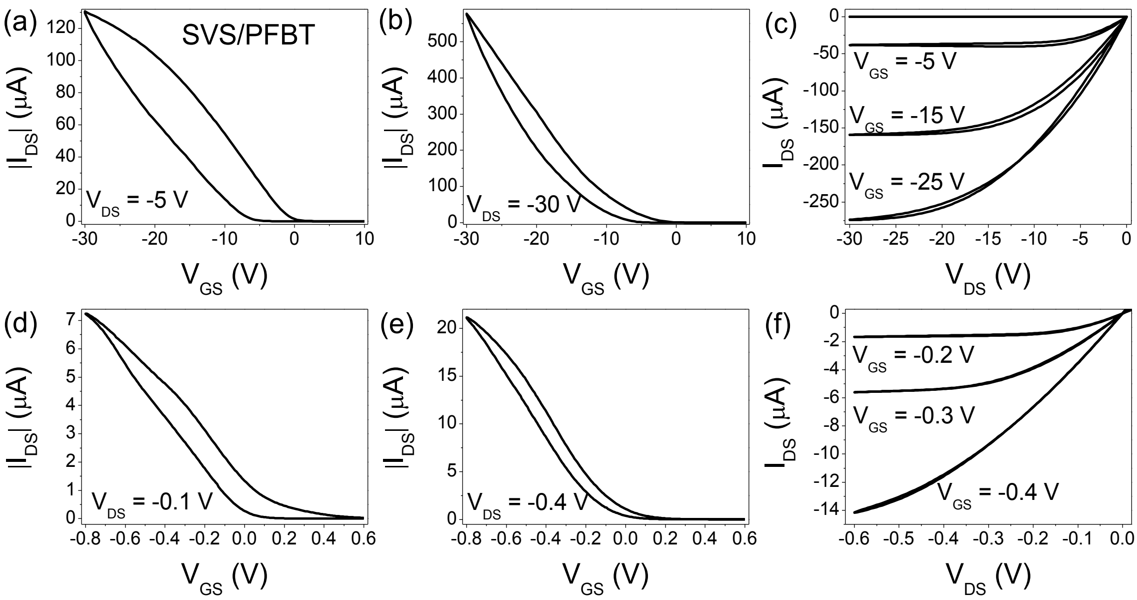

Figure A. 34: Typical *I/V* transfer recorded in linear and saturation regime and the corresponding output characteristic of the SVS/PFBT-based OFETs (a, b, c) and EGOFETs (d, e, f). Tetralin was selected as solvent and the coating speed and temperature are 1 cm/s and 150 °C, respectively.

A.4.4 The Influence of Solvent

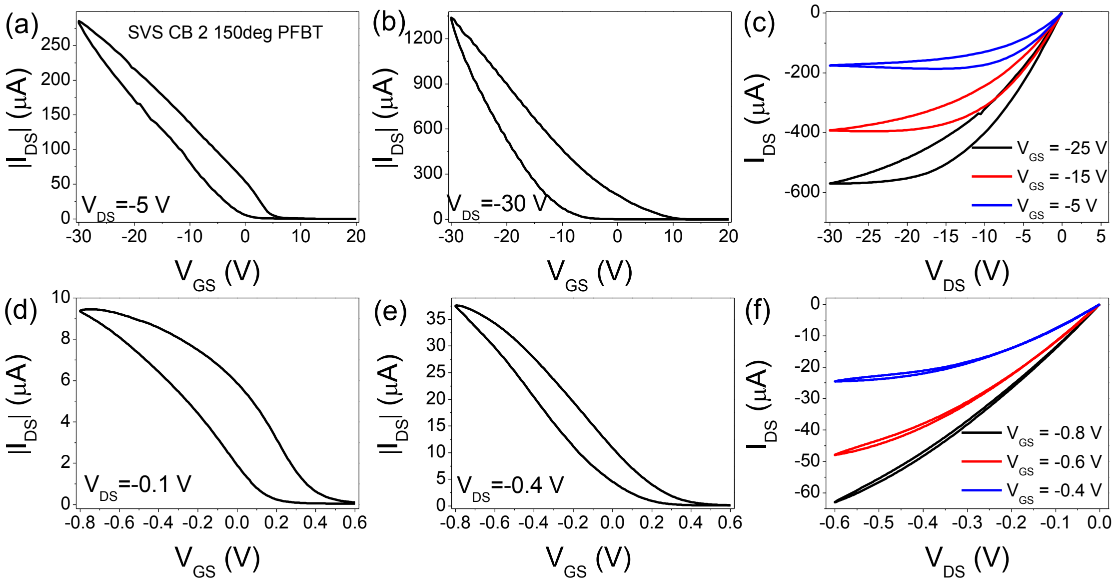

Figure A. 35: Typical *I/V* transfer recorded in linear and saturation regime and the corresponding output characteristic of pristine SVS/PFBT-based OFETs (a, b, c) and EGOFETs (d, e, f) having their S/D electrodes functionalized with PFBT. Chlorobenzene has been used as solvent and the coating speed and temperature are 2 cm/s and 150 °C, respectively.

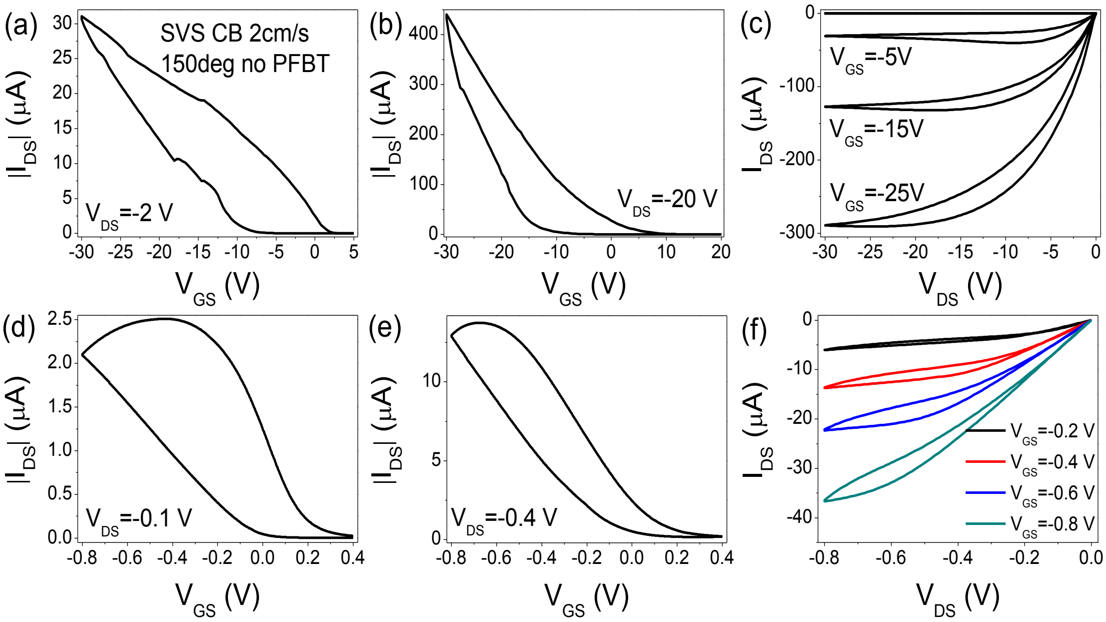

Figure A. 36: Typical *I/V* transfer recorded in linear and saturation regime and the corresponding output characteristic of pristine SVS-based OFETs (a, b, c) and EGOFETs (d, e, f) without applying any PFBT coating on S/D electrodes. Chlorobenzene has been used as solvent and the coating speed and temperature are 2 cm/s and 150 °C.

A.4.5 The Influence of PFBT-functionalization

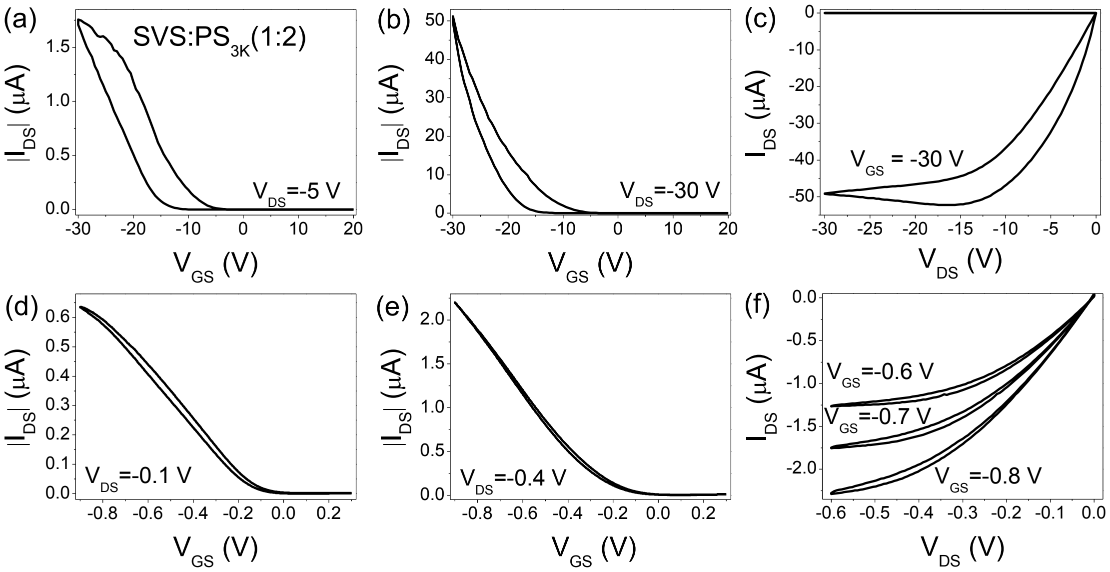

Figure A. 37: Typical *I/V* transfer recorded in linear and saturation regime and the corresponding output characteristic of the SVS:PS$_{3K}$(1:2)-based OFETs (a, b, c) and EGOFETs (d, e, f). Tetralin has been employed as solvent and the coating speed and temperature are 1 cm/s and 150 °C, respectively.

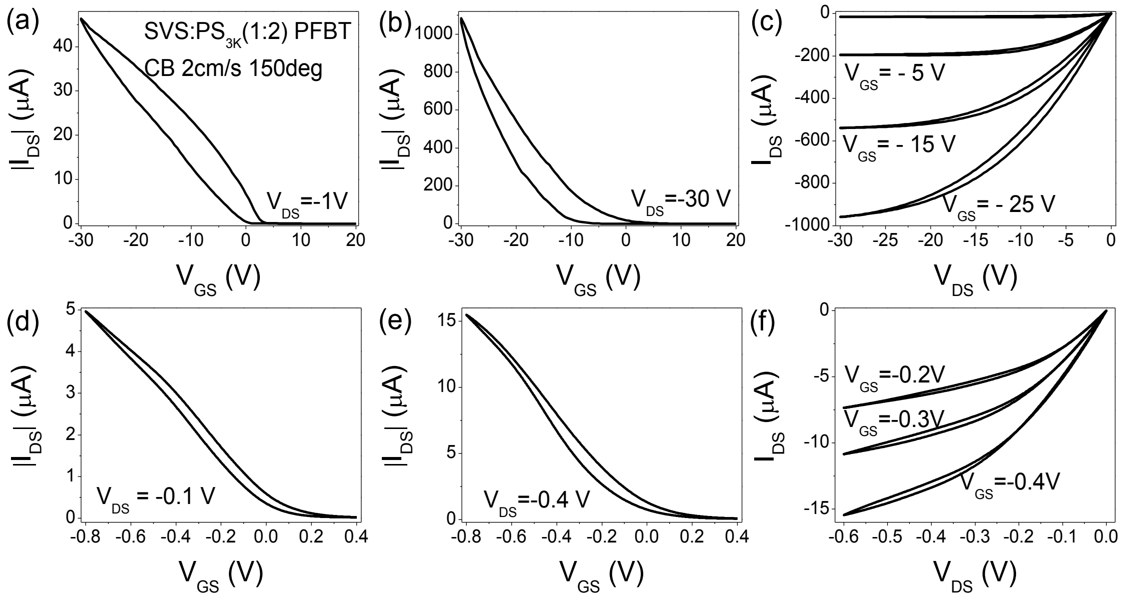

Figure A. 38: Typical *I/V* transfer recorded in linear and saturation regime and the corresponding output characteristic of the SVS:PS$_{3K}$(1:2)-based OFETs (a, b, c) and EGOFETs (d, e, f) with PFBT-functionalization of the S/D electrodes. Chlorobenzene has been used as solvent and the coating speed and temperature are 2 cm/s and 150 °C, respectively.

A.4.6 The Influence of OSC:PS Ratio

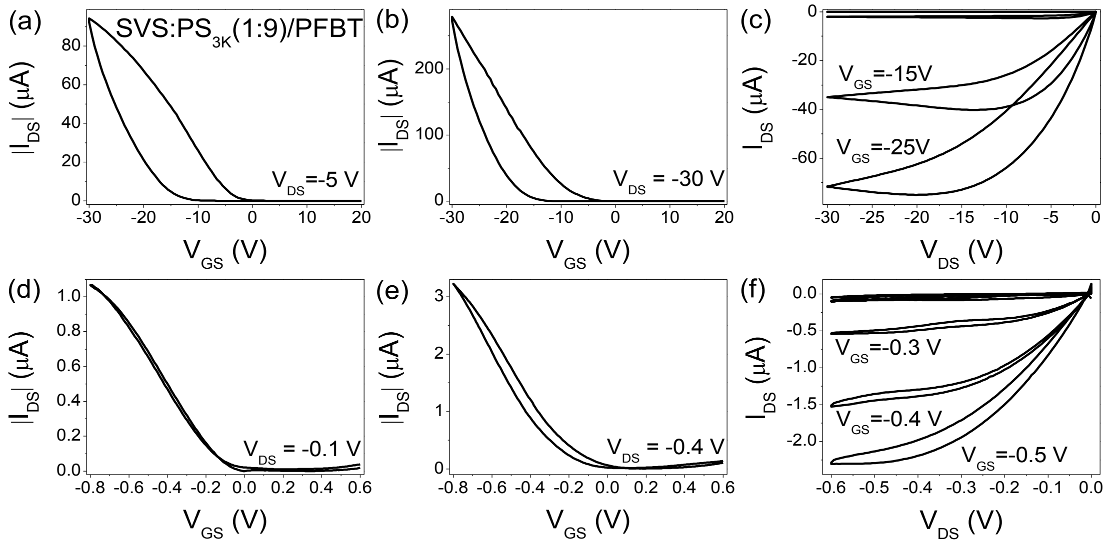

Figure A. 39: Typical *I/V* transfer recorded in linear and saturation regime and the corresponding output characteristic of SVS:PS$_{3K}$(1:9)-based OFETs (a, b, c) and EGOFETs (d, e, f) having S/D electrodes functionalized with PFBT. Tetraline was selected as solvent and the coating speed and temperature are 1 cm/s and 150 °C, respectively.

Table A. 4: The optimization process of PDPP-BTT(1)-SVS(9):PS based device. All the inks were dissolved in chlorobenzene or tetralin with a final concentration of 1 wt% and were deposited on Si/ SiO_2 substrates with the same *W*/*L* ratio (*W*/*L*=690) by BAMS.

#	Mw	ratio	SAM	Solvent	*S* (cm/s)	T (℃)	Acronyms	OFET				EGOFET $_{MilliQ}$				EGOFET $_{NaCl\ 1M}$			
								μ_{sat} ($cm^2V^{-1}s^{-1}$)	V_{th} (V)	I_{on}/I_{off}	*SS* (V/dec)	$\mu_{MilliQ,sat}$ ($cm^2 V^{-1}s^{-1}$)	V_{th} (mV)	I_{on}/I_{off}	*SS* (mV/dec)	$\mu_{NaCl,sat}$ ($cm^2 V^{-1}s^{-1}$)	V_{th} (mV)	I_{on}/I_{off}	*SS* (mV/dec)
1	3K	1:2	YES	Tetralin	1	150	SVS:PS_{3K}(1:2)/PFBT	0.22	-3.42	4.1×10^6	1.72	0.07	52	2.1×10^4	102	0.02	163	2.4×10^3	148
2	3K	1:2	NO	Tetralin	1	150	SVS:PS_{3K}(1:2)/	0.01	-5.13	1.4×10^5	2.52	0.002	10	6.8×10^2	158	/	/	/	/
3	3K	1:2	YES	CB	2	150		0.15	3.13	1.4×10^5	3.84	0.008	410	1.7×10^2	528	/	/	/	/
4	/	/	YES	Tetralin	1	150	SVS/PFBT	0.12	0.28	1.1×10^6	1.21	0.02	84	8.0×10^2	186	/	/	/	/
5	/	/	YES	CB	2	150		0.14	11.81	1.7×10^5	3.13	0.08	319	2.2×10^2	420	/	/	/	/
6	/	/	NO	CB	2	150		0.07	2.75	4.7×10^5	1.83	0.005	208	1.5×10^2	284	/	/	/	/
7	100K	1:2	YES	Tetralin	1	150	SVS:PS_{100K}(1:2)/PFBT	0.05	2.39	1.4×10^3	7.69	0.01	226	8.8×10^2	471	0.008	240	3.6×10^2	209
8	3K	1:9	YES	Tetralin	1	150	SVS:PS_{3K}(1:9)/PFBT	0.07	-2.61	4.8×10^5	1.74	0.002	16	6.2×10^2	318	/	/	/	/

Appendix B. List of Publications

- **Q. M. Zhang**, F. Leonardi, S. Casalini, I. Temino, and M. Mas-Torrent, “High Performing Solution-Coated Electrolyte-Gated Organic Field-Effect Transistors for aqueous Media Operation”, *Scientific Report*, 6, 39623, (2016).
- **Q. M. Zhang**, F. Leonardi, S. Casalini, and M. Mas-Torrent, “Mercury-Mediated Organic Semiconductor Surface Doping Monitored by Electrolyte-Gated Field-Effect Transistors”, *Advanced Functional Materials*, 27,1703899 (2017).
- **Q. M. Zhang**, F. Leonardi, R. Phattner, and M. Mas-Torrent, “A Novel Flexible Hydrogel-based Electrolyte-Gated Field-Effect Transistors as Pressure Sensitive Platform”, 2019, Submitted
- A. Campos[#], **Q. M. Zhang[#]**, M. R. Ajayakumar[#], F. Leonardi, and M. Mas-Torrent, “High Performance Organic Field-Effect Transistors with Solid and Aqueous Dielectric Based on a Solution Sheared Sulfur-Bridged Annulene Derivative”, *Advanced Electronics Materials*, 4,1700349 (2018).
- F. Leonardi[#], **Q. M. Zhang**[#], Yun-Hi Kim, and M. Mas-Torrent, “A novel organic blend based on a DPP- thienothiophene-selenophene vinylene selenophene random copolymer as active material in field-effect transistors”, *Materials Science in Semiconductor Processing*, 93, 105-110, (2019)
- F. Leonardi, S. Casalini, **Q. M. Zhang**, S. Galindo, D. Gutierrez, and M. Mas-Torrent[*], “Electrolyte-Gated Organic Field-Effect Transistor Based on a Solution Sheared Organic Semiconductor Blend”, *Advanced Materials*, 28, 10311, (2016).